THE OHIO STATE UNIVERSITY

GEOMETRICAL OPTICS DESIGN OF A COMPACT RANGE GREGORIAN SUBREFLECTOR SYSTEM BY THE PRINCIPLE OF THE CENTRAL RAY

Giancarlo Clerici
Walter D. Burnside

The Ohio State University
ElectroScience Laboratory

Department of Electrical Engineering
Columbus, Ohio 43212

Technical Report 719493-4
Grant No. NSG 1613
January 1989

National Aeronautics and Space Administration
Langley Research Center
Hampton, VA 22217

NOTICES

When Government drawings, specifications, or other data are used for any purpose other than in connection with a definitely related Government procurement operation, the United States Government thereby incurs no responsibility nor any obligation whatsoever, and the fact that the Government may have formulated, furnished, or in any way supplied the said drawings, specifications, or other data, is not to be regarded by implication or otherwise as in any manner licensing the holder or any other person or corporation, or conveying any rights or permission to manufacture, use, or sell any patented invention that may in any way be related thereto.

TABLE OF CONTENTS

LIST OF FIGURES

LIST OF TABLES

CHAPTER I

INTRODUCTION.

The compact range has always been an attractive alternative to conventional spherical ranges in that it can potentially be used to measure the pattern performance of large antennas or scattering targets in an anechoic chamber. Within the enclosed environment, the measurements are obviously not limited by the prevailing weather conditions, and the security requirements are much easier to satisfy. In addition, the measurement errors are definable and in many cases can be minimized. For example, background subtraction can be used to remove non-target related terms in a scattering measurement, because the room and target mount terms, which dominate the background, remain very stable in such an environment.

The first commercially available compact ranges were introduced by Scientific Atlanta (SA) in the mid 1970's. The SA systems consist of an offset parabolic reflector illuminated by a low gain horn antenna. The purpose of the parabolic reflector is to obtain a uniform plane wave (or an approximation of it) in the quiet zone (or target zone, or sweet spot). The target is located in the quiet zone for scattering measurements, and the antenna under test is positioned there for radiation pattern measurements. It must be noted that the target or antenna is in the near field of the parabolic reflector. This is an important difference as compared to a spherical range, where the target or antenna is in the far field of the transmitting/receiving antenna, which obviously requires much larger ranges.

The SA compact range offers many advantages with respect to the spherical range; however, it presents several problems. The most important of the shortcomings was the serrated edge reflector which caused stray signals that illuminated the target. Next that system used an offset design to reduce aperture blockage errors caused by the feed antenna scattering which in turn illuminated the target or antenna. However, an offset focus fed system causes taper and cross-polarization errors associated with the field reflected by the parabolic reflector. These errors are inherent to the offset focus fed design. In addition, the feed was not offset enough to minimize the aperture blockage errors.

The problem of diffraction was the first one to be addressed at the ElectroScience Laboratory (ESL). An elliptical rolled edge design was introduced to reduce the amount of diffraction. This design was successfully performed using GTD concepts [1] and is shown in Figure 1, while a parabolic reflector with the rolled edges terminations is shown in Figure 2. Figure 3 shows a plot of the total field at 1 GHz for a compact range with elliptical rolled edges. The parabolic reflector under consideration has a focal length of $12'$, and the ellipse semiaxes are $a = 4'$ and $b = 1'$. The field is computed on a vertical cut in the principal plane at $24'$ from the vertex of the parabolic reflector. The feed used is an omnidirectional source (i.e., a source having a uniform pattern). Note that the ripple of the amplitude is about 1 dB, and the phase variation is about 7 degrees across the target zone. This performance was thought to be satisfactory at the time.

The blended rolled edge was introduced later as an improvement over the elliptical rolled edge, in order to further decrease the diffraction from the junction between the parabola and the rolled edge [2]. A blended rolled edge termination for the parabolic reflector is shown in Figure 1. A plot of the total field at 3 GHz for a compact range with blended rolled edges is shown in Figure 4. The

parabolic reflector under consideration has a focal length of $7.25'$, and the ellipse semiaxes are $a = 3.4'$ and $b = 0.75'$ with cosine squared type blending. An omnidirectional source is used as a feed. Again, the field is computed on a vertical cut in the principal plane at $20'$ from the vertex of the parabolic reflector. The ripple variation is about 0.2 dB in amplitude and 1/2 a degree in phase across the target zone. This design meets the desired diffraction performance but the aperture blockage, taper and cross polarization errors remain. The purpose of this work is to determine a design which overcomes these three errors.

As it is well known, aperture blockage happens when an obstacle blocks the plane wave reflected from a parabolic reflector. Typical examples of aperture blockage structures are the feed antenna, waveguide and mounting structure. The plane wave coming from the parabolic reflector is incident on these structures, and a scattered field will then interact with the plane wave in the quiet zone behind these structures, as shown in Figure 5. Consequently, if this error is not eliminated, strong stray signals are present even if care has been taken to minimize the field diffracted by the edges of the parabolic reflector. This stray signal error not only causes ripple in the field illuminating the target, but also undesirable cross-polarized components.

Aperture blockage is typically reduced through an offset design, in that the feed is positioned outside the plane wave reflected from the parabolic reflector (see Figure 6). The aperture blockage effects have been reduced in the SA system through an offset design, but has not been completely eliminated, since the feed antenna is still very close to the beam of the reflected field, as schematically shown in Figure 5. In the ESL compact range, the original SA antenna support has been substituted with one of much smaller blockage dimensions; nevertheless, the aperture blockage stray signal is the largest of all the errors present. Since this

stray signal cannot be time-gated, it remains a serious concern for future designs.

In order to perform effective RCS measurements, it is highly desirable to minimize the amount of cross-polarization present in the target zone. In fact, the importance of the polarization response in RCS measurements and target identification has long been recognized [3]. It is important then to reduce the cross polarization of the plane wave incident on the target so that it is at least 40 dB below the co-polarized level. In this way then the cross-polarized component of the field is below the sensitivity threshold of the system. While diffraction introduces a cross-polarized component, which can be mimimized by reducing diffraction itself, the offset design has an inherent cross-polarization error. Even through the cross-polarization and the taper errors can be reduced by increasing the focal length of the parabolic reflector, this approach in turn dictates a larger room, with a substantial increase in the cost of the facility. Besides, the plane wave obtained in the target zone is a near field effect, which implies that the plane wave deteriorates if the target zone is moved farther away from the main reflector. This can be seen, for instance, from the examples illustrated in Figure 7. In these plots, the total field has been evaluated for a parabolic reflector on a vertical cut at three different distances ℓ_{cm} from the vertex of the parabolic reflector; viz., $12'$, $24'$ and $36'$. The parabolic reflector has a focal distance of $12'$ and elliptical rolled edges with major and minor axis lengths of $4'$ and $1'$, respectively on the upper edge and a "skirt" (i.e., a parabolic cylinder termination) on the lower edge. The computations have been performed using a numerical procedure and GTD techniques. In these plots, it can be seen that the diffraction effects or ripple levels become more significant as the distance from the vertex of the parabolic reflector is increased.

The taper associated with the reflected field is another error present in the compact range. A taper naturally occurs in a focus fed system in that the distance

from the feed to the reflector is not a constant. This fact results in a reduction of the field strength illuminating the reflector at wide angles. Thus, the amplitude of the plane wave illuminating the target is not constant, such that scattering centers near the edge of the target zone are illuminated by a plane wave of lower intensity than that in the middle. Thus, the scattering center is illuminated in the proper direction but with a different field strength. Since the scattering center is being measured in the proper direction, its scattering level is simply changed by the illumination level. Thus, a taper error is still in the direction of the plane wave so its effect on the overall measurement errors is not nearly as significant as a stray signal which illuminates the target at a different angle. This implies that one can tolerate larger taper than ripple errors, as shown by Burnside and Peters [4].

A subreflector system can be used to eliminate the cross-polarized component introduced by the single reflector offset arrangement. At the same time, it can be used to minimize the taper of the reflected field because the equivalent focal length of the subreflector system can be easily made large. In addition, since the main reflector focal length can be designed to be relatively short, the quiet zone can be placed closer to the main reflector, which reduces the diffraction errors as well as the size of the anechoic chamber.

A Cassegrain subreflector system has been considered and discarded [5] in that several undesired effects can seriously degrade its performance. Specifically, there is a triple reflected field; i.e., a field reflected from the subreflector, main reflector, subreflector and finally into the target zone, as shown in Figure 8. This path length is very close to that of the rays of the plane wave illuminating the target, such that this unwanted contribution cannot be time gated out using a pulsed radar system. As a result, this clutter term causes a ripple error associated with the probed field as this mechanism comes in and out of phase with the plane

wave. This error term is normally too large as shown by Rader [5], which makes the Cassegrain subreflector system unacceptable.

Instead, a Gregorian subreflector system with a dual chamber arrangement, as shown in Figure 9, can provide better performance because the subreflector/main reflector interaction errors can be reduced. Note that the geometrical optics field associated with the subreflector system passes through the small aperture opening between the chambers without loss. On the other hand, the diffraction from the subreflector will be attenuated by the absorber surrounding the opening. Thus, the feed does not directly see the main reflector or target, and the subreflector scattered fields cannot directly illuminate the target.

This research is directed toward examining the requirements on a dual chamber, Gregorian subreflector system design. Specifically, the subreflector and main reflector must be specified based on GO considerations in that they dictate the aperture blockage, taper and cross polarization errors of the basic system. The imposed requirements are then satisfied by some design equations which take into consideration the characteristics of the feed. The design equations are derived from the central ray concept introduced by Dragone [6]. This concept allows to determine a geometry which retains the zero cross-polarization property (which holds for a center fed single reflector), in the case of an offset Gregorian subreflector system. The use of the design equations is illustrated by examples, and a design for the next generation of compact ranges is obtained. It is shown that this new design offers better performance, and it is easier to implement than a previous design obtained through a trial-and-error approach. The new design is also compared with a commercially available compact range. The qualitative design of the shaping of the coupling aperture is also discussed.

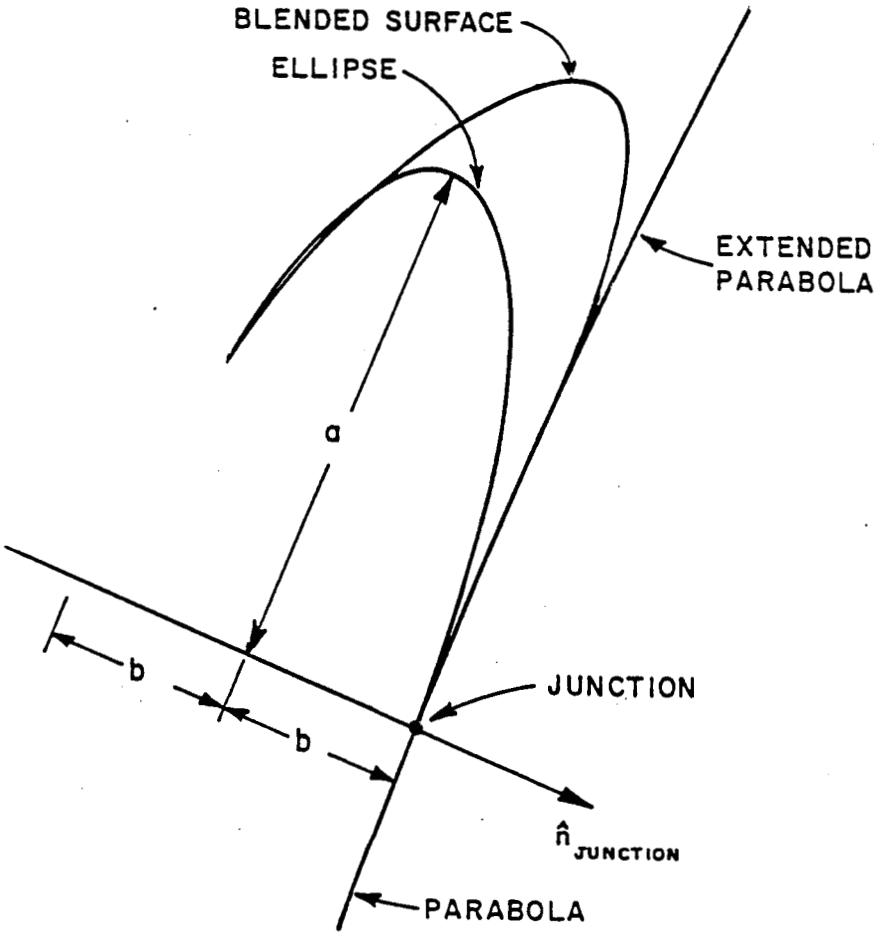

Figure 1: Rolled edge terminations for the parabolic reflector.

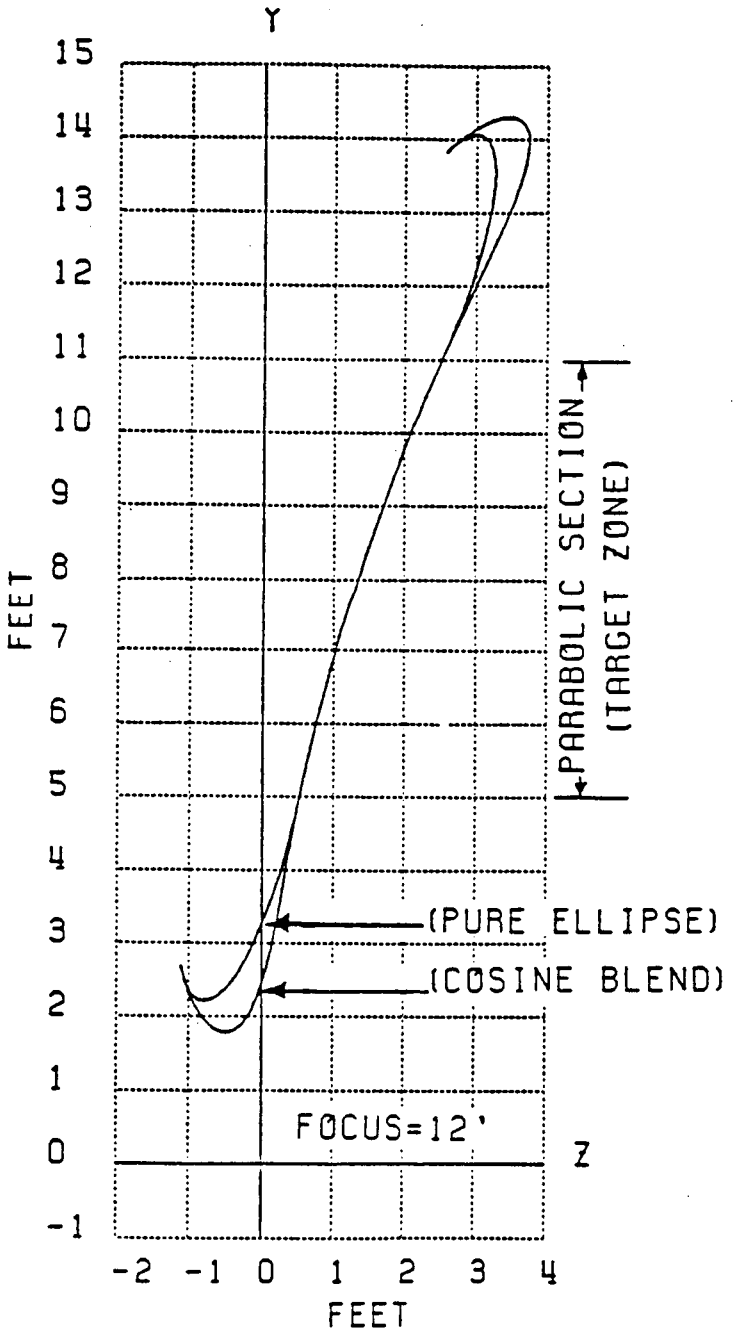

Figure 2: Parabolic reflector with rolled edge terminations.

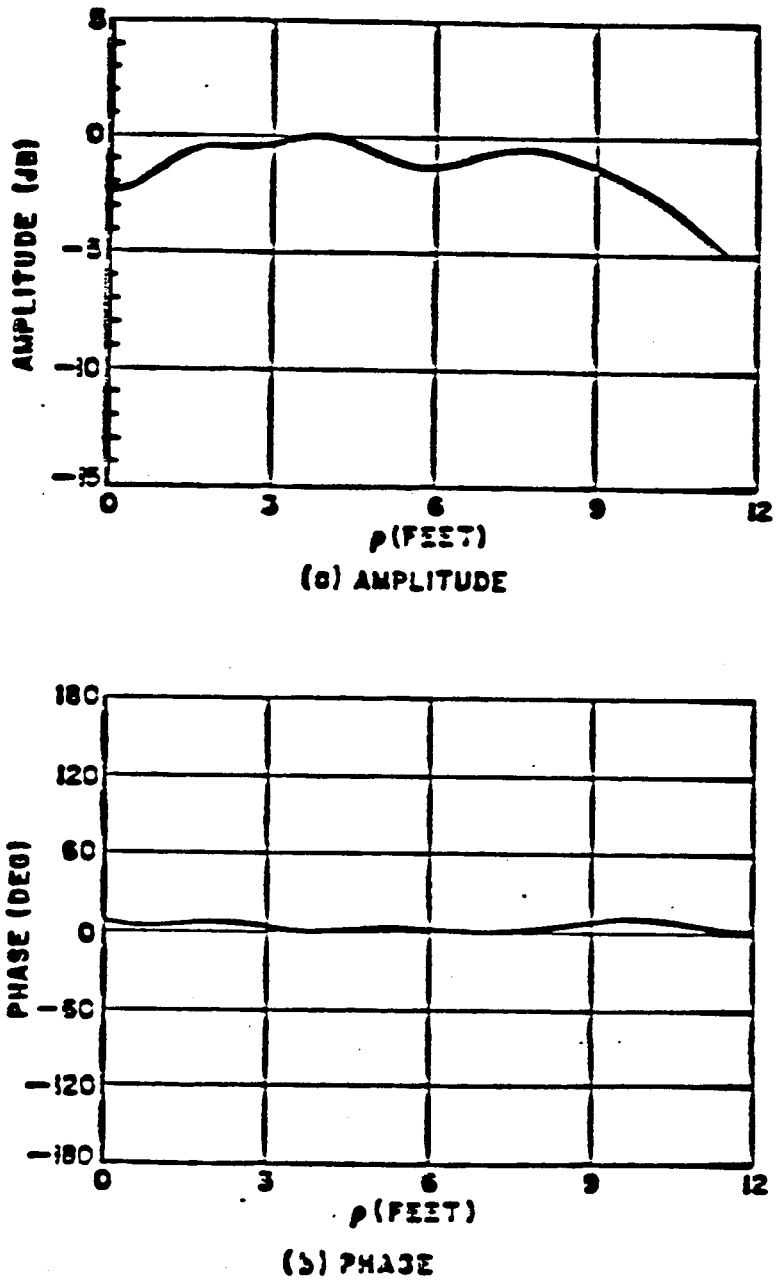

Figure 3: Plot of amplitude and phase of total field for elliptical rolled edge. Focal distance = $12'$, frequency = 1 GHz.

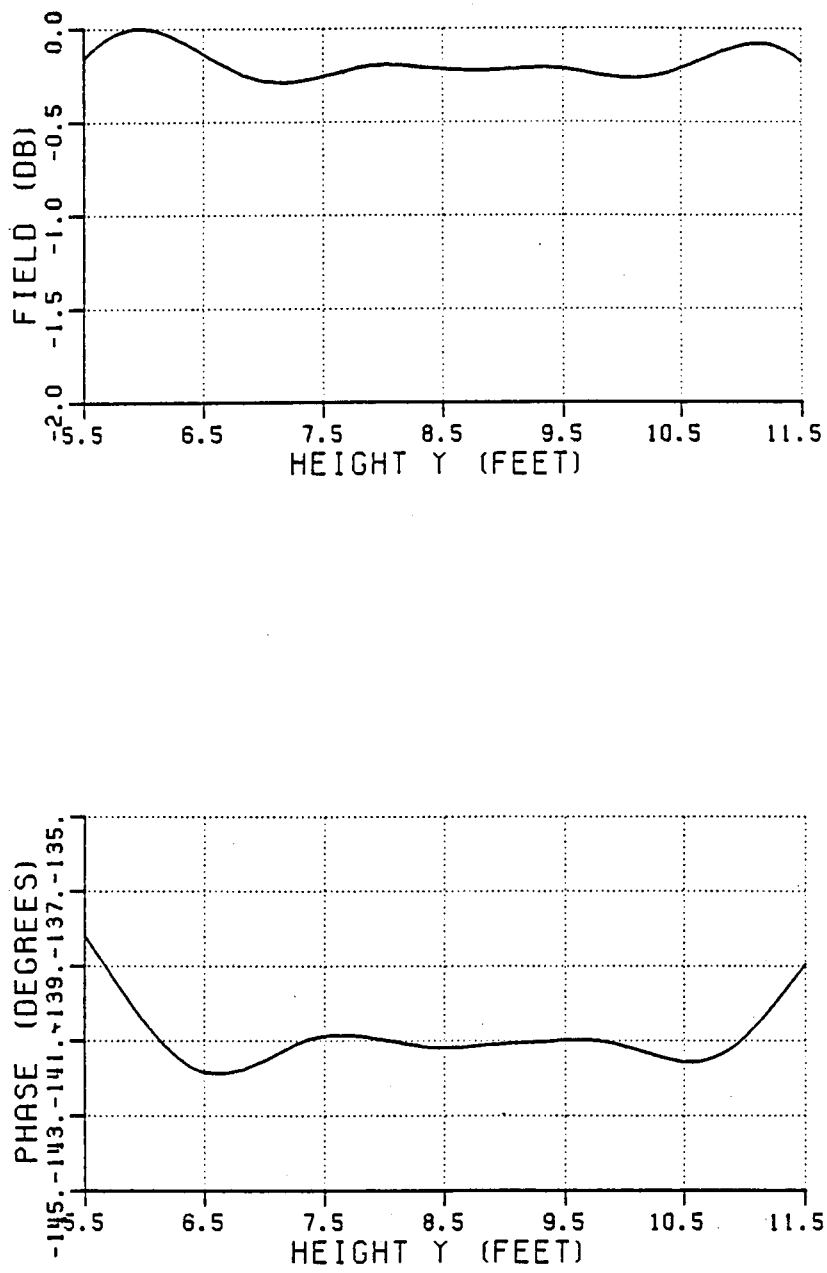

Figure 4: Plot of amplitude and phase of total field for cosine squared blended edge. Focal distance = 7.25′, frequency = 3 GHz.

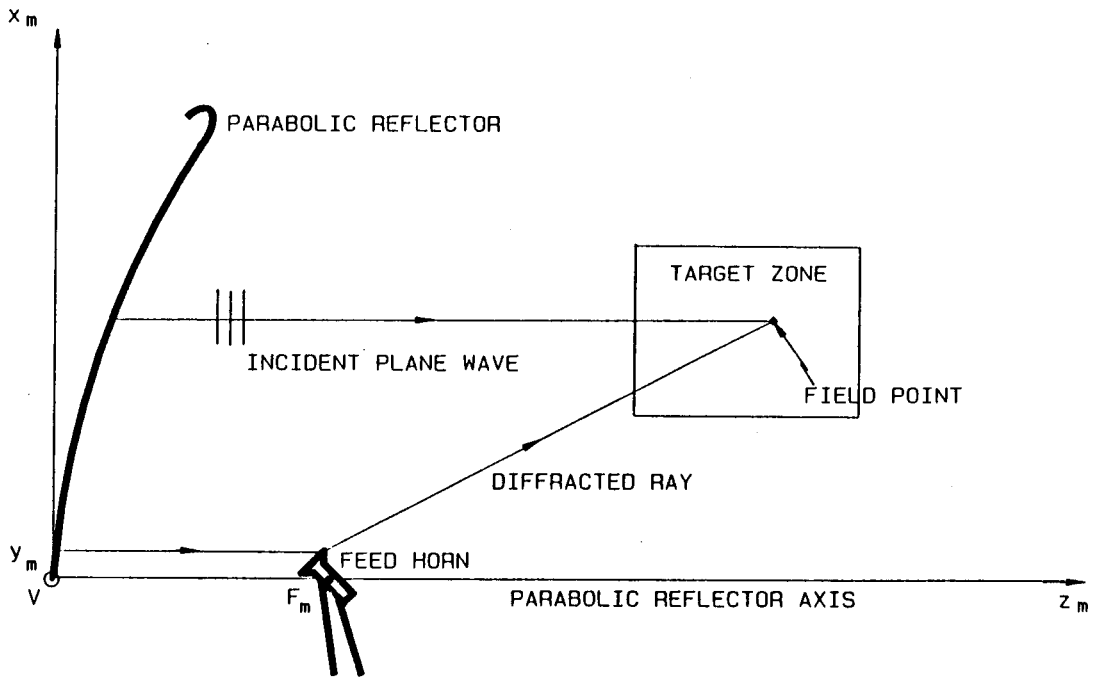

Figure 5: Aperture blockage effect.

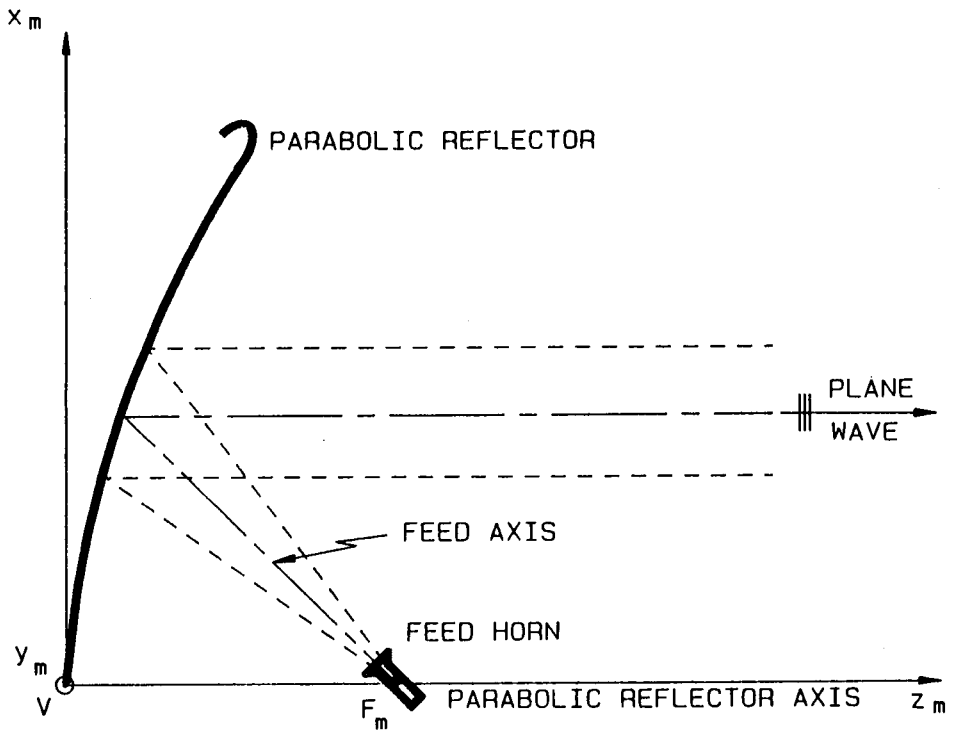

Figure 6: Single reflector offset design.

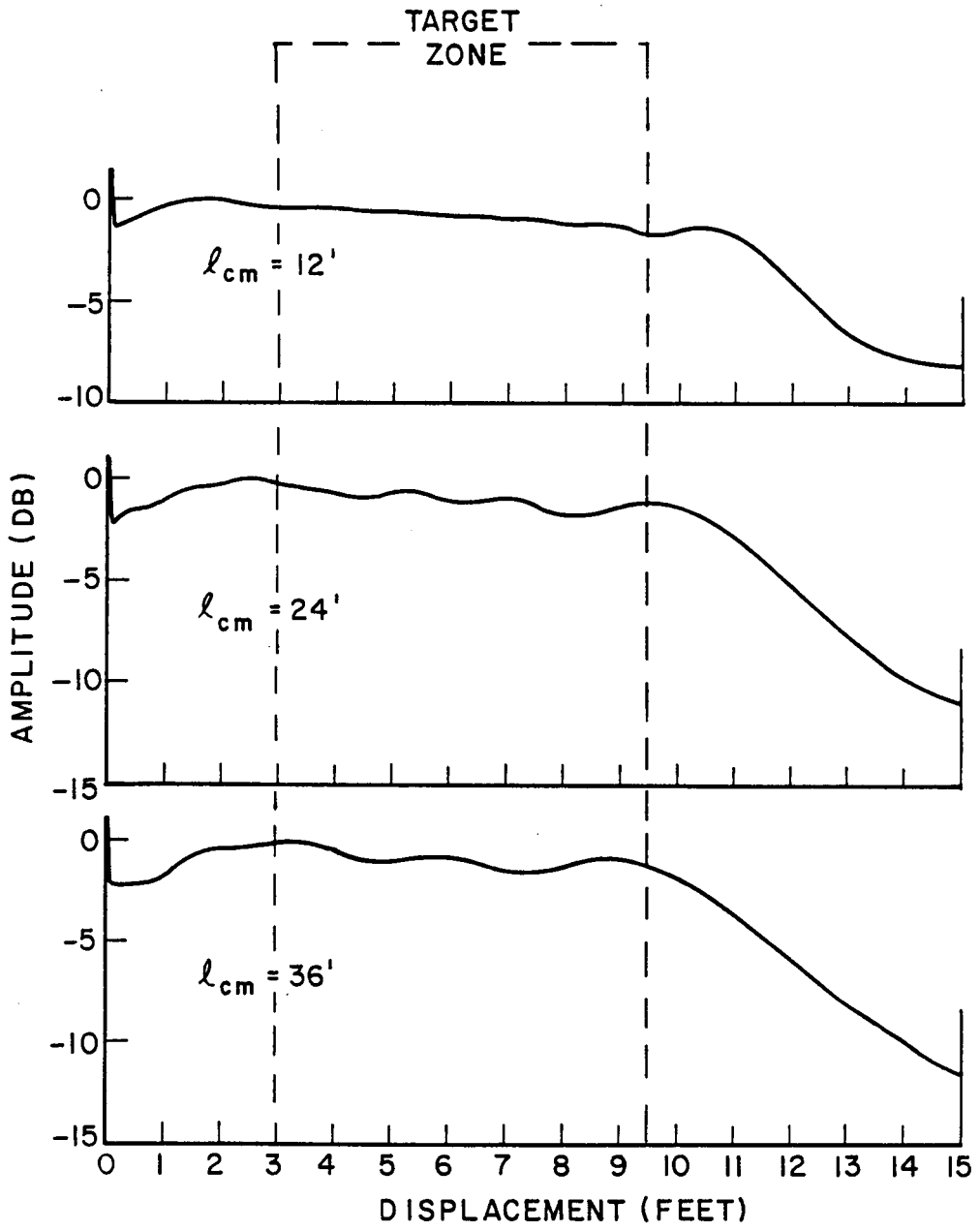

Figure 7: Degradation of the total field with increasing target zone distance (ℓ_{cm}).

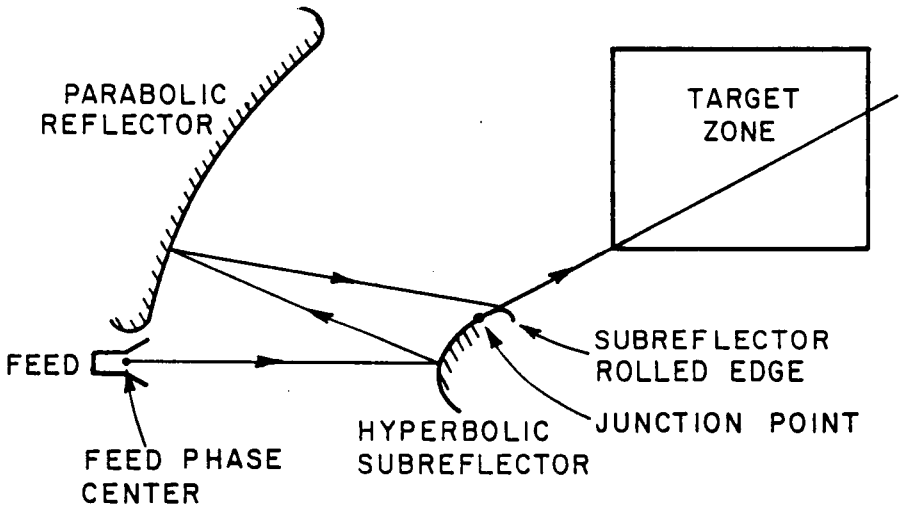

Figure 8: Triple reflected field for a Cassegrain subreflector system.

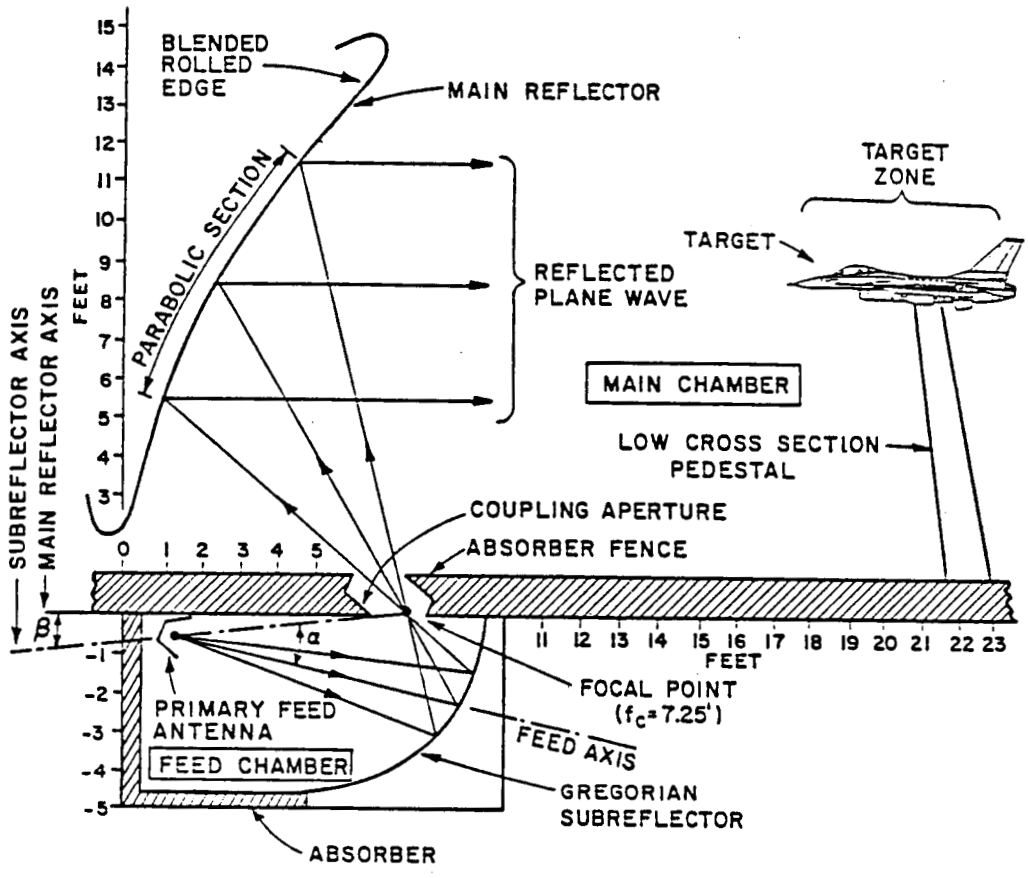

Figure 9: Gregorian subreflector system with a dual chamber arrangement.

CHAPTER II

AN ERROR STUDY OF AN OFFSET SINGLE REFLECTOR COMPACT RANGE

2.1 INTRODUCTION

In Chapter I, it has been mentioned how a single reflector offset design is affected by three problems: aperture blockage, taper of the reflected field and cross-polarization errors. In this chapter a specific single reflector offset design example is considered; viz., the latest (1986) SA compact range, and it is shown how its performance is affected by these errors. The " -40 dB" criterion is used to establish if an error is significant. In other words, an error is considered "acceptable" if it is 40 dB below the intensity of the reflected field. The reflected field is the plane wave illuminating the antenna/target under measurement; consequently, it is the natural reference, and it is approximately constant since its taper is only a fraction of a dB. The value of -40 dB is obtained because it represents an achievable level without unduly restricting the design. Therefore, it is required that the errors present in the design of the compact range be of the same order of magnitude so that one error term is not emphasized over another.

The "-40 dB" criterion gives also a value for the acceptable ripple. This can be seen as follows. By definition, the ripple is given by

$$Ripple = 1 + \frac{U_e}{U_p} \tag{2.1}$$

where U_e is the intensity of the error field, and U_p is the intensity of the plane wave field. Both U_e and U_p are real scalars. By letting

$$20\log\left(\frac{U_e}{U_p}\right) = -40\ , \tag{2.2}$$

one obtains

$$\frac{U_e}{U_p} = 0.01\ . \tag{2.3}$$

Consequently

$$Ripple_{dB} = 20\log\left(1 + \frac{U_e}{U_p}\right) = 0.086442\ \text{dB} \simeq 0.1\ \text{dB} \tag{2.4}$$

and the acceptable ripple, for the "-40 dB" criterion, is approximately -0.1 dB.

For the study of the SA compact range this criterion is relaxed somewhat, and a -0.2 dB value for the ripple was used.

2.2 GEOMETRY OF THE SA REFLECTOR

The cross sectional and front view of the SA reflector are shown in Figure 10. The configuration is an offset semicircular parabolic reflector, and its focal length is $24'$. The height of its parabolic section is $15'$, and it has a blended rolled edge at the top and a "skirt" (i.e., a section of a parabolic cylinder) at the bottom. The shape and dimensions of the target zone have been determined through diffraction considerations [7], and its cross-sectional shape is shown in Figure 11 for an omnidirectional source and in Figure 12 for a Huygens source. The frequency is 2 GHz, and the distance from the center of the target zone to the reflector vertex is $36'$. The criterion adopted is the 0.2 dB ripple level. Since the two shapes are quite similar, a conservative estimate of the target zone is shown in Figure 13, where the skirt sets the lower limit at $4.4'$ and the blended edge sets the upper limit at $12.9'$. In the direction of the reflector axis (z axis), the target zone extends from $36'$ to $50'$.

The reference system adopted is as follows: the origin V is at the parabolic reflector vertex, the x axis is vertical, the y axis is horizontal and the z axis coincides with the reflector axis. The focus is located at F_m, which coincides with the phase center of the feed. The tilt angle of the feed is the angle between the negative z axis and the axis of the feed (see Figure 14).

2.3 REFLECTED FIELD TAPER ERROR ASSOCIATED WITH THE SA REFLECTOR

The taper error of the SA reflector is computed with respect to a omnidirectional source through a numerical implementation of the equations shown in Chapter IV, simplified for the case of a single reflector.

An omnidirectional, or isotropic, source is an idealized, non physical source, since no antenna has a pattern that is independent of angle. This source is introduced in order to separate the effects of the geometry from those of the pattern of the feed.

The amplitude of the GO reflected field in dB with respect to a omnidirectional source is shown in Figure 15. The computations are performed on a grid on a plane perpendicular to the parabolic reflector axis. The data are symmetric with respect to the x axis; therefore, the computations are performed only for $y \geq 0$. The grid is also shown in Figure 15. It is not necessary to specify the distance of the plane cut on which the field is computed from the vertex of the reflector, since the GO field is independent of this distance. In the x direction the computation begins at $x = 4'$ and ends at $x = 13'$; while, in the y direction, it begins at $y = 0'$ and ends at $y = 14'$. The computation is performed over a rectangle, $9' \times 14'$ in the x and y directions, respectively. This rectangle encompasses all of the target zone. The values of the reflected field are normalized to the maximum of the computed

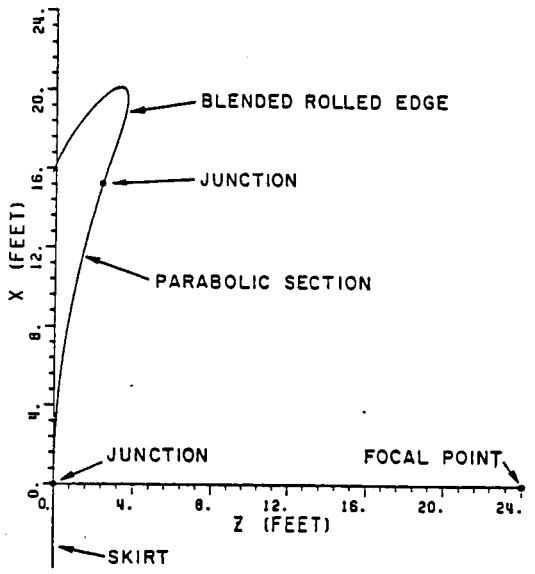

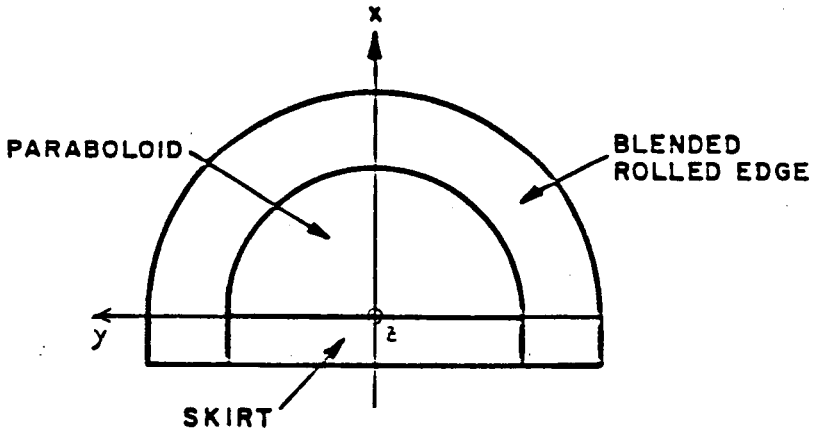

Figure 10: Cross sectional and front view of the SA offset parabolic reflector.

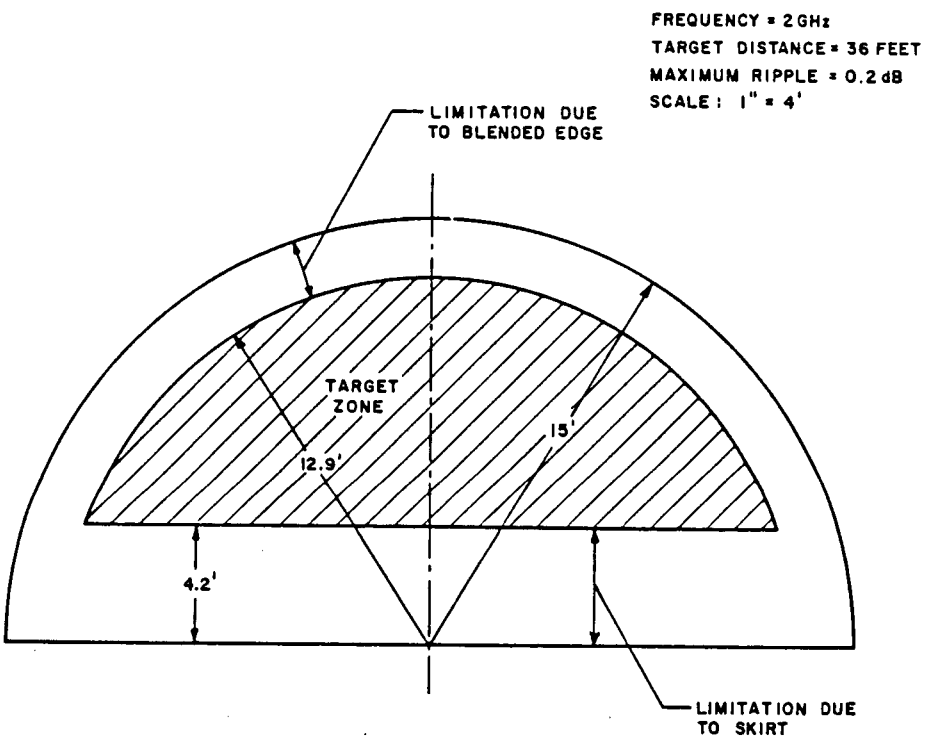

Figure 11: Front view of the target zone (uniform source).

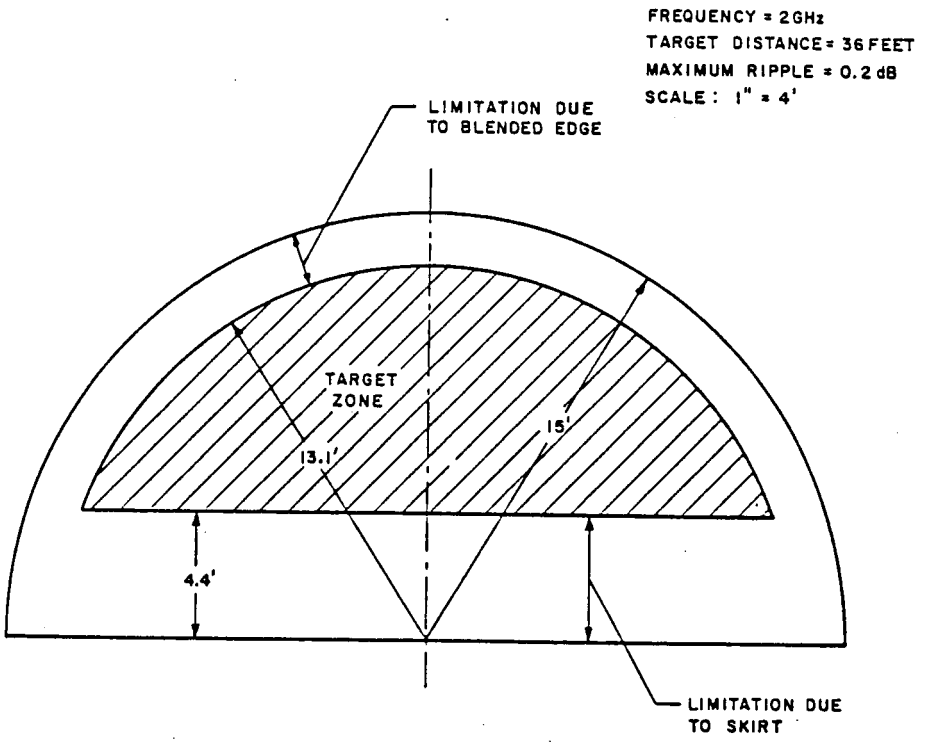

Figure 12: Front view of the target zone (Huygens source).

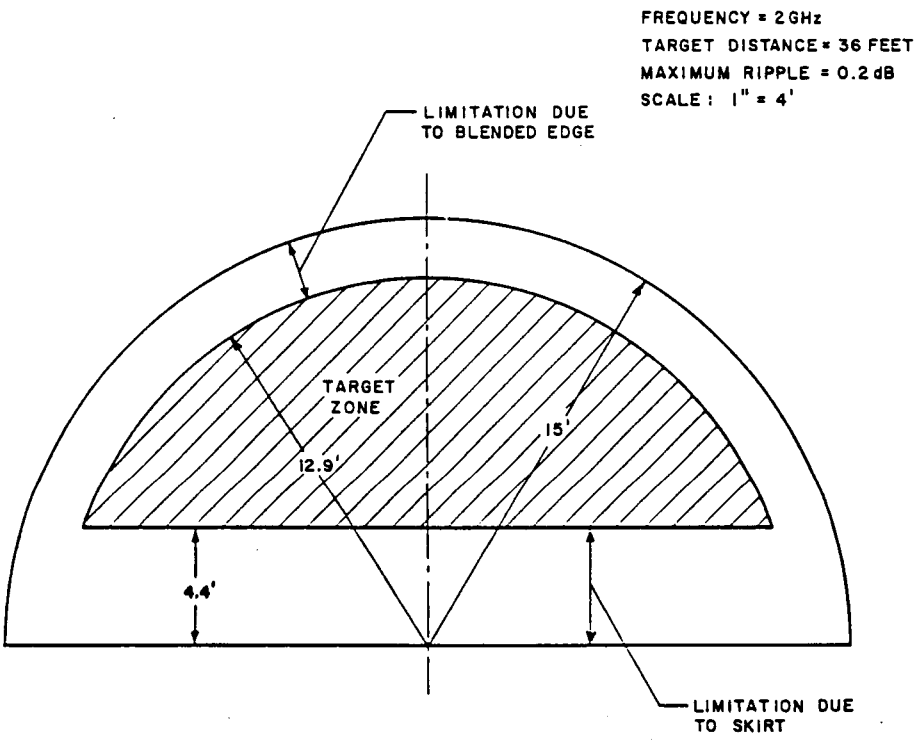

Figure 13: Conservative estimate of the target zone.

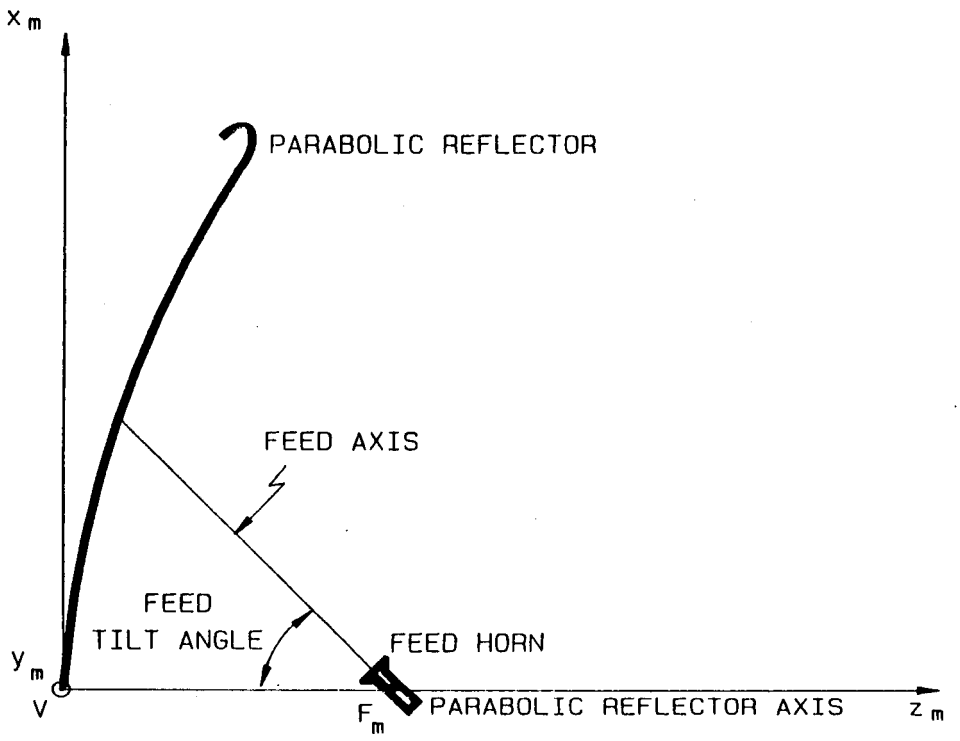

Figure 14: The axis reference system and the tilt angle of the feed.

values, which corresponds to the point at $y = 0'$, $x = 4'$. The overall maximum instead corresponds to the reflector vertex, i.e., to the point $x = 0'$, $y = 0'$. From the values shown in Figure 15, it can be seen that, on the x axis, the normalized reflected field at $x = 13'$ is -0.55 dB. On the y axis instead, the value of the normalized reflected field at $y = 12'$ is -0.52 dB. The value of the reflected field taper error is then -0.55 dB.

The computation of the taper is then repeated with a Huygens source. The Huygens source is defined in Section E, and its pattern is non-uniform. A Huygens source is used to study the polarization properties of reflector antennas and has a pattern which is close to the patterns of an actual feed antenna (for instance, an open ended waveguide). In this case, the total taper of the reflected field is due to the effect of the geometry of the parabolic reflector as well as the feed pattern. By tilting the axis of the source with respect to the axis of the reflector (offset arrangement) it is possible to obtain a partial compensation between these two effects. This is intuitive and is now shown through three examples. The overall taper for a case in which the Huygens source is coincident with the main reflector axis (tilt angle of 0^o) is shown in Figure 16. The values of the reflected field are normalized to the maximum of the computed values, which corresponds to the point at $y = 0'$, $x = 4'$ (the overall maximum instead corresponds to the reflector vertex, i.e., to the point $x = 0'$, $y = 0'$). From this data it can be seen that, on the x axis, the overall reflected field at $x = 13'$ is -1.11 dB, while on the y axis, the overall reflected field at $y = 12'$ is -1.05 dB. The value of the overall taper error then is -1.11 dB. The taper now is larger than the taper with the omnidirectional source discussed earlier due to the sum of effects associated with the geometry and the Huygens source. Next, Figure 17 shows a case in which the axis of the Huygens source is tilted by 20^o with respect to the axis of the parabolic reflector,

which corresponds, approximately, to directing the axis of the feed towards the point on the reflector corresponding to the axis of the target zone. The values of the reflected field are normalized to the overall maximum, which now corresponds, approximately, to the point at $y = 0'$, $x = 4.5'$. On the x axis, the overall reflected field at $x = 4'$ is 0.0 dB, while at $x = 13'$ it is -0.55 dB, on the y axis instead, the overall reflected field is -1.03 dB at $y = 12'$. Thus, the overall taper error is -1.03 dB, which could be reduced if a smaller target zone in the y direction were considered. For instance, for a target zone extending from $-6'$ to $6'$, the overall taper error would be -0.55 dB. In any case, the overall taper error is reduced with respect to the center fed case. These field values show that the offset configuration offers a way to reduce the overall taper by tilting the axis of the feed. For a given target zone it is then of interest to determine the best tilt angle of the feed. In the present case, it has been found that a value of about 39.75^o optimizes the overall taper. The corresponding values of the reflected field are shown in Figure 18. For this tilt angle, the overall normalized reflected field is maximum at about $y = 0'$, $x = 8.4'$; while, on the $x = 8'$ line, at $x = 12'$ it is -0.96 dB, and the overall taper error is -0.96 dB. This tilt angle is the best possible for the offset design in order to minimize the overall taper error. For a different feed, the optimal tilt angle will change, in that it is directly dependent on the feed pattern. It will also depend on the frequency, since the pattern itself is frequency dependent. For this reason a Huygens source (which is frequency independent) has been chosen as a standard reference source. For the optimum tilt angle, the axis of the feed does not correspond to the axis of the target zone, in order to get a better compensation between the feed pattern and the effect of the reflected field taper error. In fact, in the example considered, the axis of the feed corresponds to the axis of the target zone for a tilt angle of 20^o, while a better compensation is obtained for a tilt angle

of 39.75^o.

In conclusion, the performance of the SA compact range does not satisfy the 0.2 dB requirement with respect to the reflected field taper error, despite its large focal length. On the other hand, this taper error could be reduced if the focal length were further increased. However, this would make the chamber much larger than desirable.

2.4 CROSS-POLARIZATION ERROR ASSOCIATED WITH THE SA REFLECTOR

The cross-polarization properties of a reflector or a combination of reflectors are studied with respect to a focussed Huygens source. The definition of cross-polarization is the third definition given by Ludwig [8]. As it is known, the cross-polarization of the reflected field is zero if the axis of the Huygens source coincides with the axis of the parabolic reflector or with the central ray for a combination of reflectors. In a real case, the feed antenna characteristics are not those of a Huygens source, and the cross-polarization is different from zero; nevertheless, the cross-polarization is considered as introduced by the feed alone and not by the geometry of the reflector-feed arrangement (i.e., by the tilt angle of the feed) if the axes are aligned as stated before.

In the offset design, the axis of the feed does not coincide with the axis of the reflector; consequently, a component of cross-polarization is introduced by the geometry of the reflector-feed arrangement. In the real case, the cross-polarization of an offset design is due to both the geometry as well as the cross-polarization of the feed antenna.

The cross-polarization levels are shown in Figure 19 for a 20^o tilt angle. As expected, on the principal plane (plane $y = 0$) the cross polarization is zero

Y coord	14.00	12.00	10.00	8.00	6.00	4.00	2.00	0.00
X coord								
13.00	-1.22	-1.05	-0.90	-0.78	-0.68	-0.61	-0.57	-0.55
12.00	-1.14	-0.96	-0.81	-0.69	-0.59	-0.52	-0.48	-0.47
11.00	-1.06	-0.89	-0.74	-0.61	-0.51	-0.44	-0.40	-0.38
10.00	-0.99	-0.81	-0.66	-0.54	-0.44	-0.37	-0.32	-0.31
9.00	-0.93	-0.75	-0.60	-0.47	-0.37	-0.30	-0.25	-0.24
8.00	-0.87	-0.69	-0.54	-0.41	-0.31	-0.24	-0.19	-0.18
7.00	-0.82	-0.64	-0.48	-0.36	-0.25	-0.18	-0.14	-0.12
6.00	-0.77	-0.59	-0.44	-0.31	-0.21	-0.13	-0.09	-0.07
5.00	-0.74	-0.55	-0.40	-0.27	-0.17	-0.09	-0.05	-0.03
4.00	-0.70	-0.52	-0.37	-0.24	-0.13	-0.06	-0.01	0.00

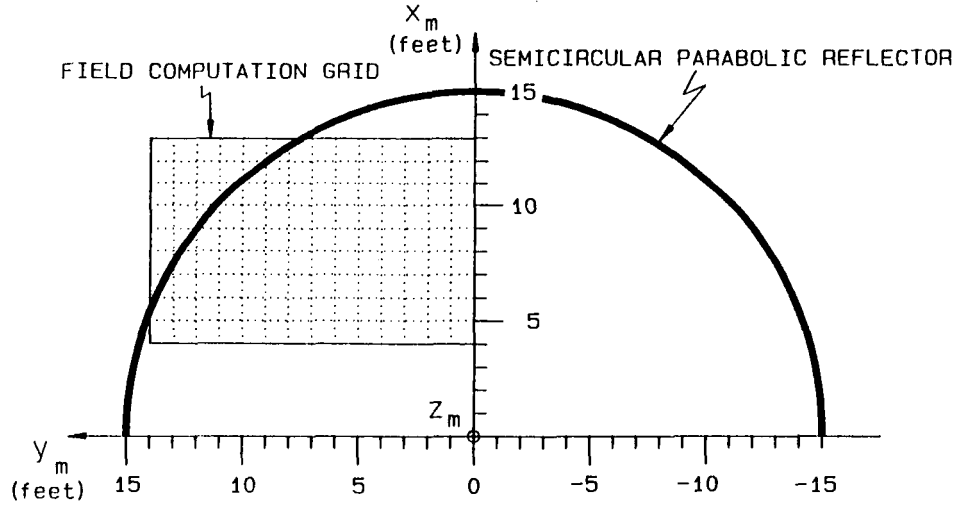

Figure 15: Reflected field taper in dB. Omnidirectional source. Linear dimensions are in feet.

Y coord	14.00	12.00	10.00	8.00	6.00	4.00	2.00	0.00
X coord								
13.00	-2.43	-2.09	-1.80	-1.55	-1.36	-1.22	-1.14	-1.11
12.00	-2.27	-1.93	-1.63	-1.38	-1.19	-1.05	-0.96	-0.93
11.00	-2.12	-1.77	-1.47	-1.22	-1.02	-0.88	-0.80	-0.77
10.00	-1.98	-1.63	-1.33	-1.07	-0.88	-0.73	-0.65	-0.62
9.00	-1.85	-1.50	-1.19	-0.94	-0.74	-0.60	-0.51	-0.48
8.00	-1.74	-1.38	-1.07	-0.82	-0.62	-0.47	-0.39	-0.36
7.00	-1.64	-1.28	-0.97	-0.71	-0.51	-0.36	-0.27	-0.25
6.00	-1.55	-1.19	-0.88	-0.62	-0.41	-0.27	-0.18	-0.15
5.00	-1.47	-1.11	-0.80	-0.54	-0.33	-0.19	-0.10	-0.07
4.00	-1.41	-1.05	-0.73	-0.47	-0.27	-0.12	-0.03	0.00

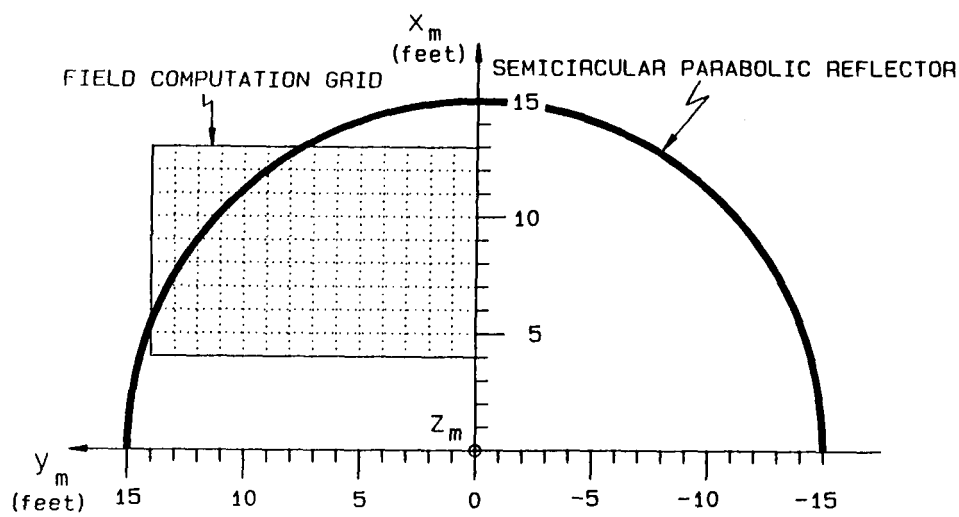

Figure 16: Overall taper in dB. Center fed Huygens source. Linear dimensions are in feet.

Y coord	14.00	12.00	10.00	8.00	6.00	4.00	2.00	0.00
X coord								
13.00	-1.86	-1.52	-1.23	-0.99	-0.80	-0.66	-0.58	-0.55
12.00	-1.75	-1.41	-1.12	-0.88	-0.69	-0.55	-0.46	-0.44
11.00	-1.66	-1.32	-1.03	-0.78	-0.59	-0.45	-0.36	-0.33
10.00	-1.58	-1.24	-0.94	-0.69	-0.50	-0.36	-0.27	-0.24
9.00	-1.52	-1.17	-0.87	-0.62	-0.42	-0.28	-0.20	-0.17
8.00	-1.47	-1.12	-0.81	-0.56	-0.36	-0.22	-0.13	-0.11
7.00	-1.43	-1.07	-0.77	-0.52	-0.32	-0.17	-0.09	-0.06
6.00	-1.40	-1.05	-0.74	-0.49	-0.28	-0.14	-0.05	-0.02
5.00	-1.39	-1.03	-0.72	-0.47	-0.27	-0.12	-0.03	0.00
4.00	-1.39	-1.03	-0.72	-0.47	-0.26	-0.12	-0.03	0.00

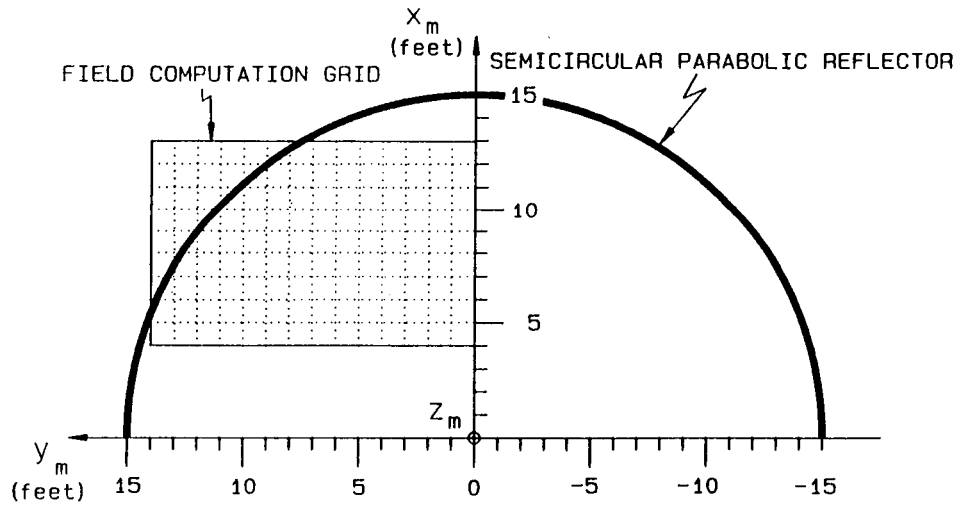

Figure 17: Overall taper in dB with a Huygens source which is tilted 20°. Linear dimensions are in feet.

Y coord	14.00	12.00	10.00	8.00	6.00	4.00	2.00	0.00
X coord								
13.00	-1.39	-1.07	-0.80	-0.57	-0.38	-0.25	-0.17	-0.15
12.00	-1.35	-1.02	-0.74	-0.51	-0.33	-0.20	-0.12	-0.09
11.00	-1.32	-0.99	-0.71	-0.47	-0.29	-0.15	-0.07	-0.05
10.00	-1.30	-0.97	-0.68	-0.45	-0.26	-0.13	-0.04	-0.02
9.00	-1.29	-0.96	-0.67	-0.43	-0.25	-0.11	-0.03	0.00
8.00	-1.30	-0.96	-0.67	-0.44	-0.25	-0.11	-0.03	0.00
7.00	-1.32	-0.98	-0.69	-0.45	-0.26	-0.12	-0.04	-0.01
6.00	-1.35	-1.01	-0.72	-0.48	-0.29	-0.15	-0.07	-0.04
5.00	-1.40	-1.06	-0.77	-0.53	-0.34	-0.20	-0.11	-0.09
4.00	-1.46	-1.12	-0.83	-0.59	-0.40	-0.26	-0.17	-0.14

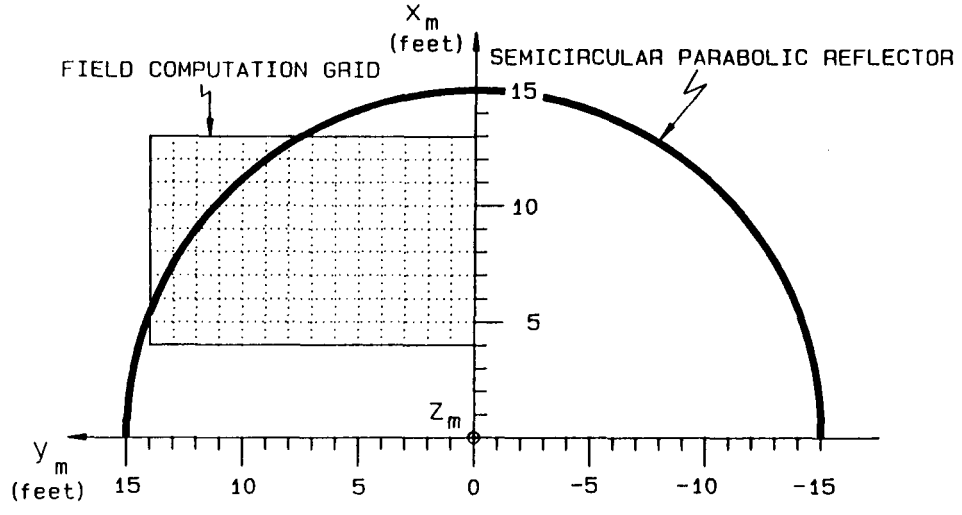

Figure 18: Optimized overall taper in dB with a Huygens source which is tilted 39.75°. Linear dimensions are in feet.

(−100 dB represents zero); whereas, the maximum cross-polarization inside the target zone is −21.2 dB at $x = 4'$, $y = 12'$. As shown in Figure 20, the maximum inside the target zone is −15.05 dB at $x = 4'$, $y = 12'$ for a 39.75^o tilt angle of the feed. By comparing the results from these two tilt angles, it is clear that, the greater the tilt angle of the feed, the worse the cross polarization becomes. Therefore, even if some tilt angle (39.75^o in this case) minimizes the overall taper error, it might not necessarily be the best choice because the corresponding cross-polarization characteristics are not satisfactory.

The performance of the SA compact range with respect to the cross-polarization for both of these angles is poor. It seems necessary then to accept a tilt angle close to 20^o in order to find a compromise between the taper and the cross-polarization errors.

2.5 APERTURE BLOCKAGE ERROR OF THE SA REFLECTOR

The aperture blockage error associated with the SA reflector has been studied in terms of the blockage of the feed [7], which is basically a diffraction problem. The feed itself is simulated as a vertical plate centered at the focal point and illuminated by the plane wave coming from the parabolic reflector (Figure 21). The resulting scattered field is then computed at the end of the target zone because it will be stronger there as can be seen from Figure 21. It is clear from the figure that the points at the end of the target zone are characterized by a smaller ϕ angle (for points with the same x height); consequently, the diffraction coefficient evaluated for P_e is larger than that of P_b, which implies a stronger diffraction. Also, in this case the magnitude of the diffraction coefficient is more significant than the magnitude of the spreading factor (the points at the end have a larger spreading factor than those at the beginning). The distance of the end of the

Y coord	14.00	12.00	10.00	8.00	6.00	4.00	2.00	0.00
X coord								
13.00	-20.14	-21.48	-23.07	-25.01	-27.52	-31.04	-37.06	-100.00
12.00	-20.11	-21.45	-23.04	-24.98	-27.49	-31.01	-37.03	-100.00
11.00	-20.08	-21.42	-23.01	-24.95	-27.46	-30.98	-37.00	-100.00
10.00	-20.05	-21.39	-22.98	-24.92	-27.42	-30.95	-36.97	-100.00
9.00	-20.02	-21.36	-22.95	-24.89	-27.39	-30.92	-36.94	-100.00
8.00	-19.99	-21.33	-22.92	-24.86	-27.36	-30.89	-36.91	-100.00
7.00	-19.95	-21.30	-22.89	-24.83	-27.33	-30.86	-36.88	-100.00
6.00	-19.92	-21.27	-22.86	-24.80	-27.30	-30.82	-36.85	-100.00
5.00	-19.89	-21.24	-22.82	-24.77	-27.27	-30.79	-36.81	-100.00
4.00	-19.86	-21.20	-22.79	-24.74	-27.24	-30.76	-36.78	-100.00

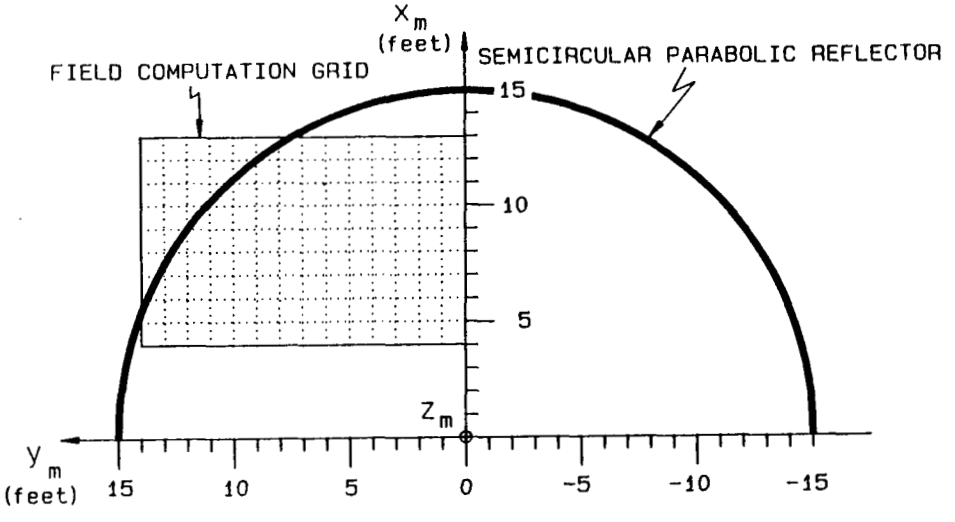

Figure 19: Cross-polarized field in dB with a Huygens source which is tilted 20°. Linear dimensions are in feet.

Y coord	14.00	12.00	10.00	8.00	6.00	4.00	2.00	0.00
X coord								
13.00	-14.25	-15.61	-17.21	-19.17	-21.68	-25.21	-31.23	-100.00
12.00	-14.19	-15.55	-17.15	-19.11	-21.62	-25.15	-31.17	-100.00
11.00	-14.13	-15.49	-17.09	-19.04	-21.56	-25.09	-31.11	-100.00
10.00	-14.07	-15.43	-17.03	-18.98	-21.49	-25.02	-31.05	-100.00
9.00	-14.00	-15.37	-16.97	-18.92	-21.43	-24.96	-30.99	-100.00
8.00	-13.94	-15.30	-16.91	-18.86	-21.37	-24.90	-30.93	-100.00
7.00	-13.88	-15.24	-16.84	-18.80	-21.31	-24.84	-30.87	-100.00
6.00	-13.81	-15.18	-16.78	-18.74	-21.25	-24.78	-30.80	-100.00
5.00	-13.75	-15.11	-16.72	-18.67	-21.18	-24.71	-30.74	-100.00
4.00	-13.69	-15.05	-16.65	-18.61	-21.12	-24.65	-30.68	-100.00

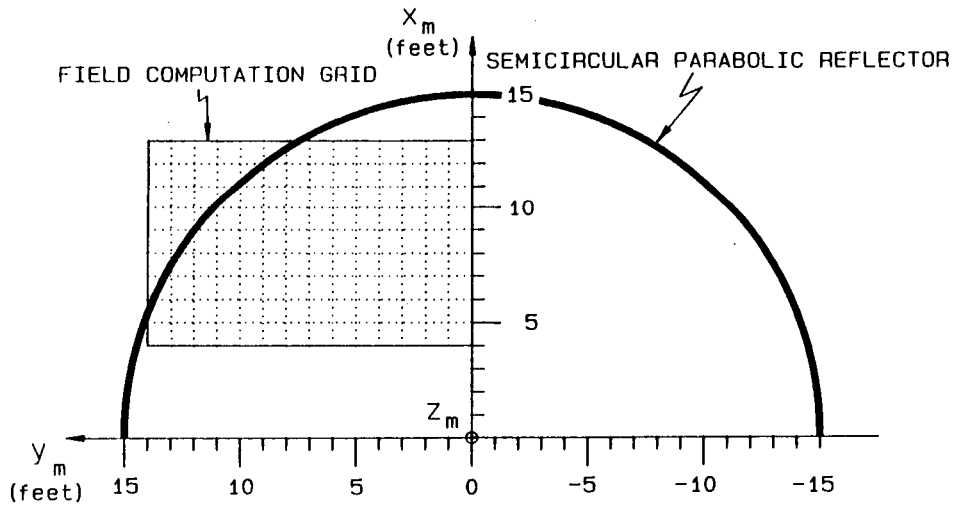

Figure 20: Cross-polarized field in dB with a Huygens Source which is tilted 39.75^o. Linear dimensions are in feet.

target zone from the reflector vertex is $50'$; while, the distance of the beginning is $36'$. The source considered is the omnidirectional source.

The aperture blockage scattered field illuminates the target in directions different than the plane wave so the superposition of these terms results in ripple associated with the total field in the target zone. This error term has both co- and cross-polarized components. Since this is a diffraction effect, it is frequency dependent. The aperture blockage error at 500 MHz is shown in Figure 22 together with the GO reflected field (solid line), where the aperture dimensions $15'' \times 15''$ (long dash plot), $12.5'' \times 12.5''$ (short dash plot) and $10'' \times 10''$ (dotted plot) are considered. The aperture blockage scattered field levels are obtained by subtracting the plotted values of the aperture blockage error from the corresponding value of the GO plot. They are the following:

- for the $20'' \times 20''$ aperture, the scattered field is about 25.5 dB below the level of the GO reflected field at $x = 4'$, and about 29 dB below at $x = 13'$
- for the $15'' \times 15''$ aperture, the scattered field is about 30.5 dB below the level of the reflected field at $x = 4'$, and about 33.5 dB below at $x = 13'$ and
- for the $10'' \times 10''$ aperture, the field is about 37 dB below the level of the reflected field at $x = 4'$, and about 40.5 dB below at $x = 13'$.

The plot for 10 GHz is shown in Figure 23 where the aperture dimensions $4'' \times 4''$, $3'' \times 3''$ and $2'' \times 2''$ are considered. The scattered field levels are:

- for the $4'' \times 4''$ aperture, the field is about 30.5 dB below the level of the reflected field at $x = 4'$, and about 42.5 dB below at $x = 13'$,
- for the $3'' \times 3''$ aperture, the field is about 34.5 dB below the level of the reflected field at $x = 4'$, and about 56.5 dB below at $x = 13'$,

Table 1: Allowable feed aperture versus frequency

Frequency (GHz)	Approximate aperture blockage dimensions	
0.5	$12'' \times 12''$	$(\lambda/2) \times (\lambda/2)$
10.0	$2.4'' \times 2.4''$	$2\lambda \times 2\lambda$

- for the $2'' \times 2''$ aperture, the field is about 40.5 dB below the level of the reflected field at $x = 4'$, and about 50.5 dB below at $x = 13'$.

As specified in Reference [7], in order to meet the 0.2 dB ripple requirement, the field diffracted from the aperture should be about 34 dB below the GO field. From the previous list it follows that, at 500 MHz, the aperture should be somewhat smaller than $10'' \times 10''$ and at 10 GHz, the aperture should be about $2'' \times 2''$. This last requirement then should be applied to obtain satisfactory behaviour over the entire band of operation. The results for these two frequencies are summarized in Table 1, where the acceptable dimensions are expressed in terms of wavelengths. For more details one is referred to Reference [7].

The importance of this aperture blockage error is better understood if one considers that the compact range is used to measure and process RCS data, for example. The numerical processing of the RCS data must determine the size and position of the scattering centers of the target. The RCS measurement is defined in terms of a uniform plane wave incident on the target. A diffracted wave incident on the target comes instead from a direction different from that of the plane wave and has a ray path of different length as shown in Figure 24. As a result, the corresponding time domain plot of the echoes from a scattering center might look like the plot shown in Figure 25. The first impulse is due to the response of

the scattering center to the incident plane wave, and represents the true response. The second echo instead is an error and is due to the response of the scattering center to the diffracted ray. This error response is delayed in time because its ray path is longer. The data processing algorithms then determine two scattering centers instead of one. It is clear then how important it is to reduce the amount of diffraction to a minimum. Consequently it would be very useful to completely eliminate the aperture blockage, if possible.

It is worth noticing that, while a diffraction error introduces spurious scattering centers, a taper instead introduces errors in the relative sizes of the various scattering centers. While this is an error to be avoided; nevertheless, its consequences are less serious than those associated with the diffraction errors in that a diffraction error introduces false echoes which can be associated with the target. As a consequence, one might attempt to modify the target to remove this echo, which instead cannot be eliminated, since it is not associated with the target.

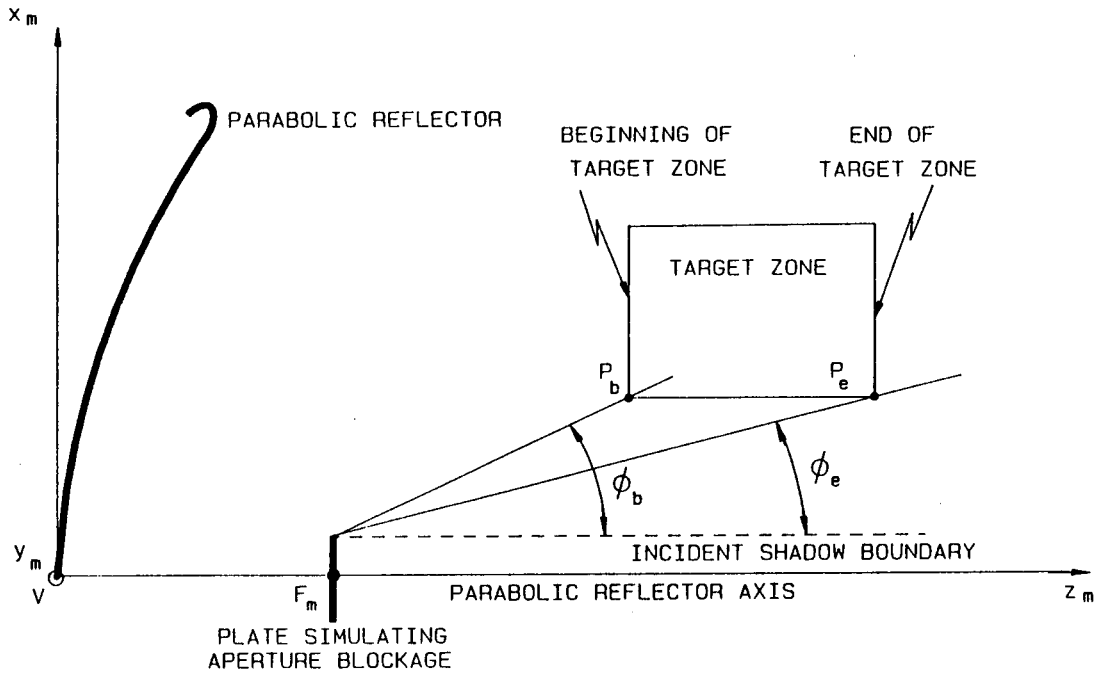

Figure 21: Incident shadow boundary for aperture blockage.

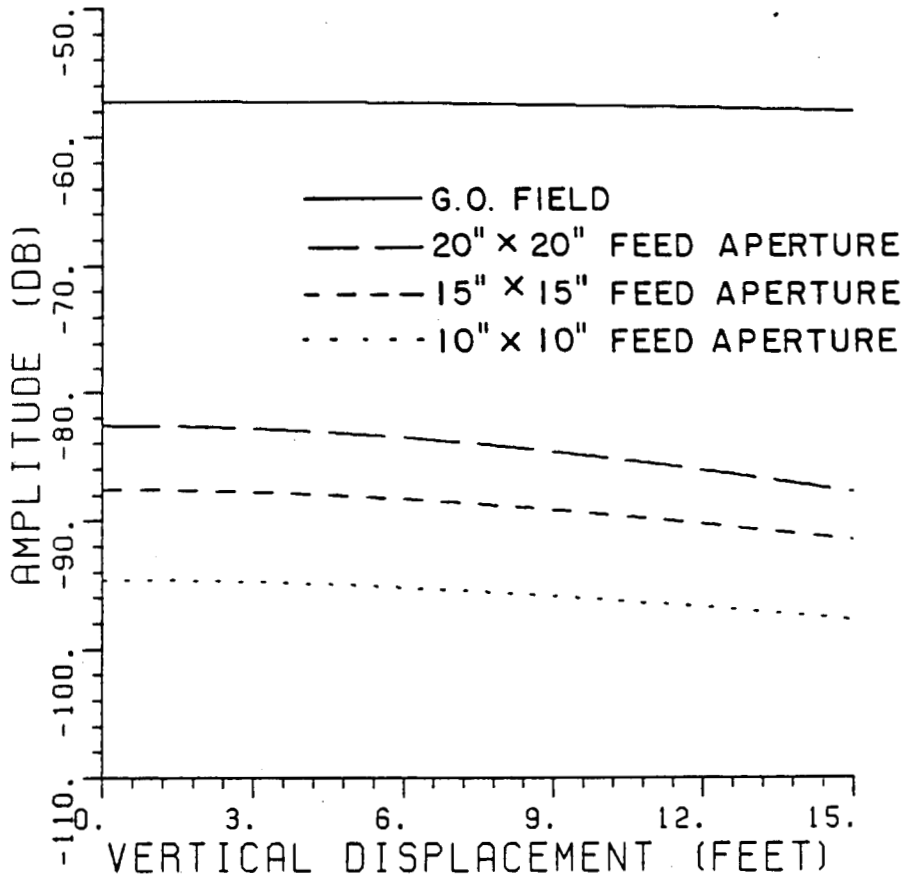

Figure 22: Aperture blockage versus vertical displacement. Frequency = 500 MHz. Distance from the reflector = 50′.

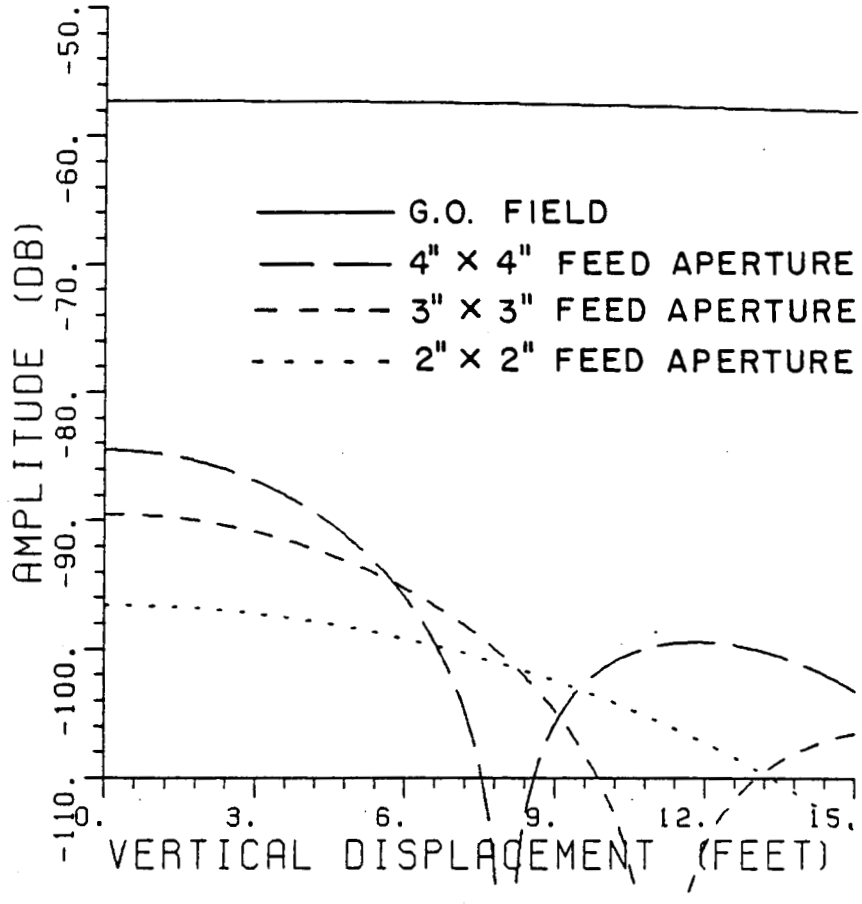

Figure 23: Aperture blockage versus vertical displacement. Frequency = 10 GHz. Distance from the reflector = 50′.

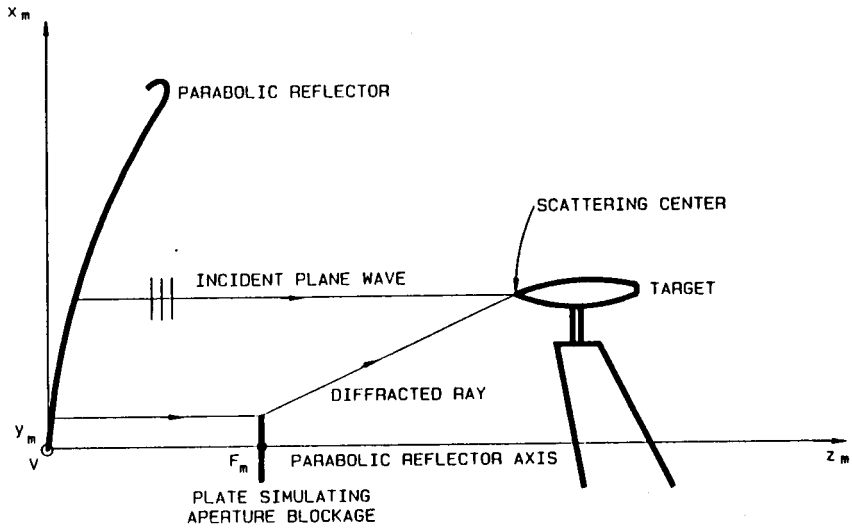

Figure 24: Reflected and diffracted rays incident on a diffraction center.

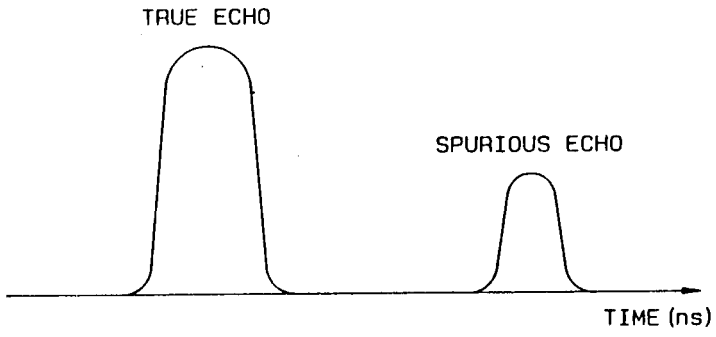

Figure 25: True and spurious echoes for a scattering center.

CHAPTER III

DESIGN CONSIDERATIONS

3.1 INTRODUCTION

In this chapter the physical and geometrical foundations of the design of a compact range subreflector system are presented in a simple way. For clarity and convenience, the single reflector case is discussed first because the subreflector system can be reduced to the single parabolic reflector case through the equivalent reflector principle developed by Dragone [6].

A description of the geometry of the subreflector system and of the associated reference systems is presented in Section 3.2. The principle of the central ray is illustrated in Section 3.3. The problems of the taper of the reflected field and of the cross-polarization error, mentioned in Chapter I, are treated from a quantitative viewpoint in Sections 3.4 and 3.5. A discussion of cross-polarization with respect to the characteristics of the feed antenna, as well as the properties of the Huygens source is presented in Section 3.6. The factors affecting the GO design of a compact range are examined in Section 3.7. Finally, the ambiguities often present in the definition of the target zone are shown in Section 3.8.

3.2 GEOMETRY OF THE SUBREFLECTOR SYSTEM

The subreflector system involves many parameters, which are shown in Figures 26 and 27, where all angles are positive if counterclockwise (ccw). As a result,

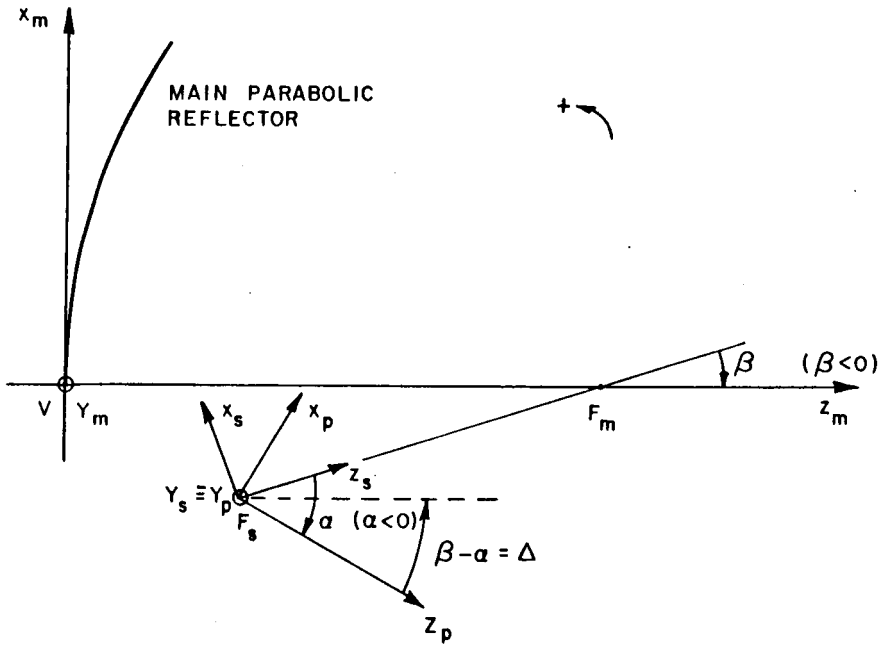

Figure 26: Subreflector system reference axes.

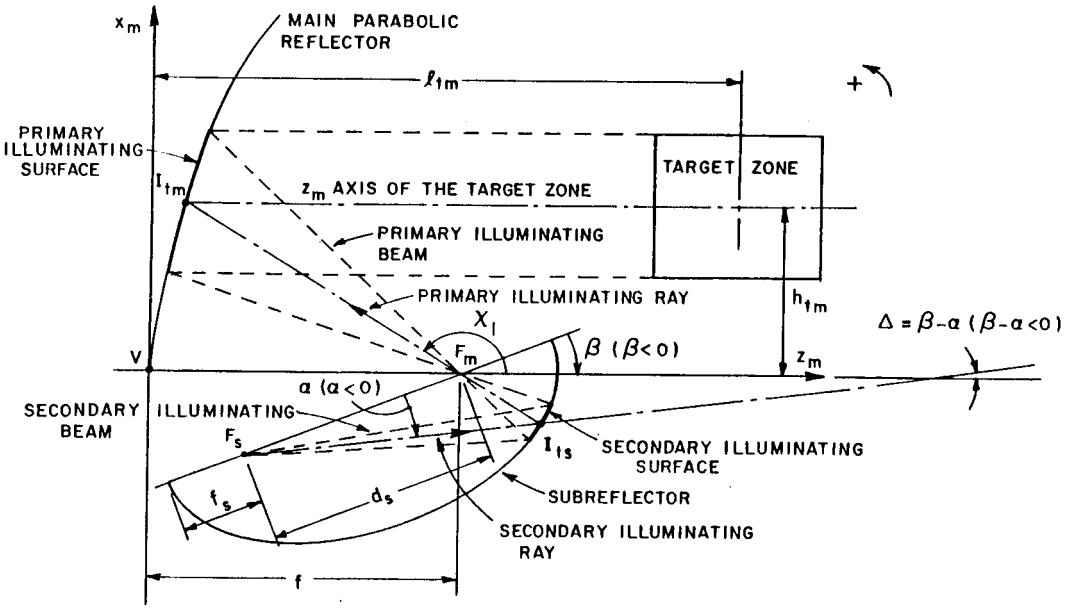

Figure 27: Subreflector system geometry.

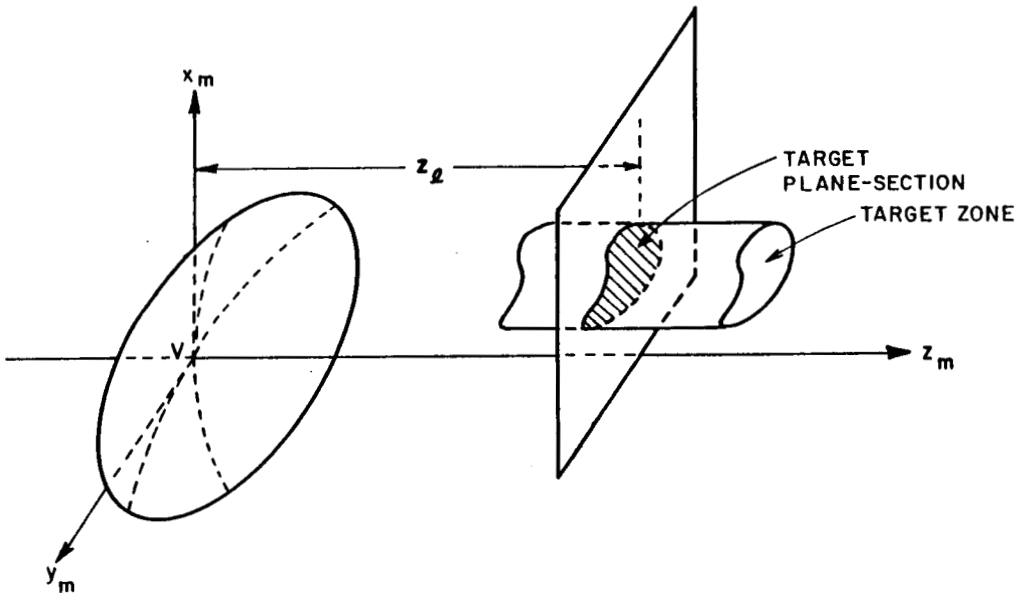

Figure 28: Geometry of the target zone.

several reference systems are used (see Figure 26):

1) The parabolic reflector reference system (also called main for short) $V(x_m, y_m, z_m)$ has its origin at the vertex, V, of the paraboloidal reflector. The z_m axis is coincident with the reflector axis, the x_m axis is vertical, and the y_m axis is horizontal. The polar reference system, $F_m(r_m, \theta_m, \phi_m)$ has its origin at the focus, F_m, of the paraboloidal reflector, and the corresponding cartesian axes are parallel to the $V(x_m, y_m, z_m)$ reference system. The polar quantities are defined in the usual fashion. The focus, F_m, of the parabolic reflector coincides with one of the two focii of the subreflector.

2) The subreflector reference system $F_s(x_s, y_s, z_s)$ has its origin at the focus, F_s, of the subreflector which is the location of the feed antenna, while the second focus coincides with the focus, F_m, of the parabolic reflector. The z_s axis is coincident with the subreflector axis, the y_s axis is horizontal, the x_s axis lies in the plane perpendicular to y_m, and β is the tilt angle from z_s to z_m. The corresponding polar reference system is F_s (r_s, θ_s, ϕ_s).

3) The source reference system F_s (x_p, y_p, z_p) refers to a source having a circularly symmetric pattern, for instance, a Huygens source (Section E). It has the origin at the focus, F_s, of the subreflector, where the z_p axis is coincident with the principal ray (direction of maximum of the pattern of the source), the y_p axis is horizontal and the x_p axis lies in the plane perpendicular to y_m, also α is the tilt angle from z_s to z_p, and $\Delta = \beta - \alpha$ is the tilt angle from z_p to z_m.

Both the parabolic reflector and the subreflector are parts of a conical surface of revolution (also called conic of revolution, i.e., paraboloid, hyperboloid, ellipsoid of revolution).

The parabolic reflector is a part of a paraboloid with its vertex at V, and f is its focal length. The subreflector is a part of an ellipsoid (Gregorian system) or hyperboloid (Cassegrain system). A conic of revolution has two focii (note that for the parabolic reflector, a paraboloid, the second focus is at infinity and F_m is the unique focus). The distance between the two focii of the subreflector is d_s, and f_s denotes the distance between a vertex of the subreflector and the closest focus. The subreflector is also characterized by the parameters ϵ_s and p_s.

The geometry shown in Figure 27 is considered next. The angle β is the tilt angle from the subreflector axis to the paraboloid axis (i.e., between the oriented axes z_s and z_m, from z_s to z_m). The feed is located at the second focus of the subreflector, F_s, and α is the tilt angle of the subreflector axis relative to the z_p axis (feed axis, also called secondary principal ray). The feed boresight direction is then tilted by the angle $\Delta = \beta - \alpha$, which is the angle between the principal ray and the parabolic reflector axis, i.e., from z_p to z_m.

In Figure 27, it is shown that the phase center of the feed is located at the focus F_s of the subreflector, which has coordinates $F_s \equiv (-h_{pc},\ 0,\ z_{pc})$ in the parabolic reflector reference system, where h_{pc} is the vertical (in the x_m direction) distance from the phase center of the feed to the ceiling of the lower chamber; while, l_{pc} is the horizontal (in the z_m direction) distance of the phase center of the feed from the focus F_m of the parabolic reflector.

The target zone (also called quiet zone or sweet spot) is the zone where the targets are located and where a uniform plane wave is required. Geometrically, a target zone is defined as a finite volume delimited by a cylinder having generatrices parallel to the parabolic reflector axis and by two planes, both perpendicular to the parabolic reflector axis (z_m axis). The surface intersection of a plane perpendicular to the parabolic reflector axis with the target zone (Figure 28) is characterized by

its distance z_l from the paraboloid vertex V, while all such sections are identical. In the present case these sections have a rectangular shape: the sides of the target zone are straight lines parallel to the coordinate axes, (x_m, y_m, z_m). A further discussion of the shape of the target zone is presented in Section 3.8. The distance of the center point of the target zone from the reflector vertex, V, in the z_m axis direction is z_{tm}, and h_{tm} is the vertical height (i.e., in the x_m direction) of its center point from the parabolic reflector axis; while, the distance of the beginning of the target zone from V is denoted by z_{tb}.

The target zone is projected onto the parabolic reflector by lines parallel to the z_m axis. The part of the paraboloidal surface so determined is called the primary illuminating surface. The axis of the target zone parallel to the z_m axis intersects the primary illuminating surface at the point I_{tm}, as shown in Figure 27. This axis is called the z_m axis of the target zone. The primary illuminating surface is projected by a beam from the subreflector converging onto the focal point, F_m, and finally intersecting the parabolic reflector. This ideal beam is called the primary illuminating beam. This beam illuminates the target zone after reflection from the parabolic reflector. The ray through F_m and I_{tm} is called the primary illuminating ray and intersects the subreflector at the point, P_{ts}. This ray is oriented from F_m to I_{tm}. The angle between the z_m axis and the primary illuminating ray is called χ_i. If h_{tm} is the x_m coordinate of the point, I_{tm}, the following relationship holds [9]:

$$h_{tm} = 2f \cot\left(\frac{\chi_i}{2}\right) . \tag{3.1}$$

The intersection of the primary illuminating beam with the subreflector defines a surface called the secondary illuminating surface. The ray through the points, F_s and P_{ts}, is called the secondary illuminating ray, and is oriented from F_s to P_{ts}.

Then the illuminating ray is defined as the ray through F_s, I_{ts}, F_m, I_{tm} and from I_{tm} into the target zone, where (by definition) it coincides with the z_m axis of the target zone. The illuminating ray is related primarily to the position of the target zone with respect to the parabolic reflector.

3.3 THE CENTRAL RAY

The principles of the equivalent reflector and of the central ray are very important in the present GO design. For completeness of presentations, the arguments introduced by Dragone [6] are now summarized.

It is known [10] that, in the case of a single conical (elliptical, parabolical, or hyperbolical) reflector, zero cross-polarization is achieved if the following conditions are satisfied:

- A focussed Huygens source feed is used.
- The axis of the feed (called the principal ray) coincides with the axis of the conical reflector (center fed case), in other words, the feed is pointing towards the vertex of the conical reflector.
- The ratio of the intensities of the electric and magnetic currents in the Huygens source is equal to the eccentricity of the conical reflector (Section E). For the case of a paraboloidal reflector, the eccentricity is one, and the two currents are equal.

This zero cross-polarization property refers to the GO field only, not to higher order effects, like edge diffraction.

The issue presently addressed is to determine how this zero cross-polarization property can be achieved for the case of a sequence of confocal reflectors. In Figure

29 a sequence of N confocal conical reflectors is shown, the reflectors are called Σ_1, Σ_2, ... Σ_N. They are called confocal because the second focus of Σ_1 and the first focus of Σ_2 coincide at the point, F_1, the second focus of Σ_2 and the first focus of Σ_3 coincide at the point, F_2, and so forth. The source is located at the first focus F_0 of Σ_1; while, the second focus of Σ_N is located at F_N and does not coincide with any other focus. As shown in [6], it is possible to establish an equivalence principle for such a sequence of confocal subreflectors. In fact, it is possible to show that any sequence of confocal conical reflectors is equivalent, for the purpose of GO computations, to one focussed conical reflector. The theorem proved is just an existence theorem, in other words, it is proved that such an equivalent reflector exists, but it is not shown how to compute its parameters. Nevertheless, this existence theorem is the first step to actually determine the equivalent reflector. It is also possible to show that, if the last reflector, Σ_N, is parabolic, the equivalent reflector is parabolic.

In order to determine the equivalent reflector, it is necessary to determine its equivalent axis. This is important because it is possible to obtain zero cross-polarization by satisfying the three conditions listed above, if the principal ray coincides with the equivalent axis. The equivalent axis is a concept related to the feed, and it coincides with the first segment of the central ray.

The argument to determine the equivalent axis is done in two steps. In the first step a single reflector case is considered, and then the result is extended to a sequence of confocal reflectors.

A single reflector case is considered. If the conical reflector together with only one of the focii are given, while the second focus is unknown, it is still possible to determine the equivalent axis (axis of symmetry of the conic) with a trial-and-error procedure. This is shown as follows (see Figure 30). A test direction, $\hat{\mathbf{s}}$, is

considered, and the corresponding ray through the focus F_0 is reflected twice by the reflector, obtaining the direction $\hat{\mathbf{s}}''$ after the second reflection. In the general case $\hat{\mathbf{s}} \neq \hat{\mathbf{s}}''$ (as in case (a) of Figure 30), unless $\hat{\mathbf{s}}$ coincides with the direction of the geometric axis of the conic (which is supposed to be unknown). Then $\hat{\mathbf{s}} = \hat{\mathbf{s}}''$, and $\hat{\mathbf{s}}$ determines the direction of the equivalent axis, which is a line through the focus, F_0, and in the $\hat{\mathbf{s}}$ direction (cases (b) and (c) of Figure 30). Therefore, the equivalent axis can be determined, at least in principle, through a trial-and-error procedure for a single reflector case. The ray corresponding to the direction of the equivalent axis retraces itself after the first two reflections, and it is the only ray which has this property. The central path is defined as the path back and forth from any of the two focii and corresponding to the equivalent axis. The central path corresponds to either of the two central rays. The central rays have a direction of travel associated with them, which are opposite. In other words, any of the two central rays corresponds to the central path with associated a direction of travel.

This result can be extended to a combination of N confocal reflectors. In this case 2N reflections must be considered, 2 from each reflector. By the equivalent reflector principle, the combination of the N reflectors is equivalent, for all the GO purposes, to just one reflector, for which the previous argument can be applied. It follows that the equivalent axis exists and can be determined through the retracing property of the central path. The central path is unique (except for a few degenerate cases which are presently of no concern), and therefore there are only two central rays, corresponding to the two possible opposite orientations of the central path. As an example, Figure 31 shows a sequence of N confocal reflectors, with $N = 3$. Part (a) of the figure shows a ray (not coincident with the central ray). This ray starts at the focus, F_0, with direction $\hat{\mathbf{s}}$, is reflected by Σ_1, goes through

F_1, which is the second focus of Σ_1 and the first focus of Σ_2, is then reflected by Σ_2 and goes through F_2, which coincides with the second focus of Σ_2 and the first focus of Σ_3, is then reflected by Σ_3, goes through F_3, is reflected for the second time by Σ_3, goes through the focus F_2, and all the way back, being reflected for the second time by each conical reflector in reverse order. After the last reflection from Σ_1, the direction of the ray is $\hat{\mathbf{s}}''$, which is different from $\hat{\mathbf{s}}$,and it does not retrace itself. In Figure 31 (b) instead is shown the case in which $\hat{\mathbf{s}}$ is directed as the equivalent axis, the ending direction, $\hat{\mathbf{s}}''$, coincides with the starting direction, $\hat{\mathbf{s}}$, and the ray can retraces itself indefinitely. Therefore, the ray traced is the central ray. Again, at least in principle, the central ray can be determined through a trial-and-error procedure.

This trial-and-error procedure is very important from a theoretical viewpoint, but in practice it is not very satisfactory. Nevertheless, it is not difficult to find geometrical or analytical criteria to determine the equivalent axis for many cases of interest.

In the case of a Gregorian subreflector system, there are two conic reflectors ($N = 2$) i.e., a parabola and an ellipse. It is now shown how the equivalent axis and the central ray can be determined through a simple geometrical construction, once the geometry (i.e., the two reflectors and their mutual positions) is given.

In the case of a parabolic reflector, it can be shown that the direction, $\hat{\mathbf{s}}''$, of the ray after the second reflection, at the point at infinity of the parabolic reflector, is independent from the direction, $\hat{\mathbf{s}}$. The direction $\hat{\mathbf{s}}''$ is parallel to the axis of the parabola, and the corresponding ray goes through the focus F_{N-1} of the parabola. The proof of this can be seen through Figure 32 and a limiting argument, where the parabola is obtained by moving the second focus, F_N, of an ellipse to infinity. The angle, ψ, then goes to 0 accordingly, for any direction of $\hat{\mathbf{s}}$. Then the reflected

ray is directed as the axis of the limiting parabola, and must go through the focus, F_{N-1}, and therefore it must coincide with the axis itself and is directed from the focus at infinity, F_N, towards F_{N-1}.

By using this property, it is easy to determine the equivalent axis of the Gregorian subreflector system by considering Figure 33. The central ray starts at F_s (the focus of the subreflector where the feed is located) with direction $\hat{\mathbf{s}}$, is reflected by the subreflector at I_s, goes through the focus, F_m, which is common to both the main reflector and the subreflector, is reflected by the parabolic reflector at I_m, goes through the focus at infinity of the parabola $F_{m\,\infty}$ (as limiting case of an ellipse with the second focus at infinity), is then reflected at the point at infinity of the parabola, $I_{s\,\infty}$, is reflected for the second time by the subreflector at I'_s, as in Figure 33, and the path is closed back at F_s. Since the axis of the parabola is known, the point I'_s is known, and the central ray is known. The equivalent axis corresponds to the segment $F_s\,I'_s$. The equivalent axis can also be found through an equation relating the angles α_c and β_c [6], as follows

$$\tan\left(\frac{\alpha_c}{2}\right) = m\,\tan\left(\frac{\beta_c}{2}\right) \tag{3.2}$$

where the axial magnification factor m is given by

$$m = \frac{1+\epsilon_s}{1-\epsilon_s} \tag{3.3}$$

ϵ_s is the eccentricity of the subreflector, and the angles α_c and β_c are defined in Figure 33.

It has been mentioned that, if the last reflector is parabolic, the equivalent reflector is parabolic. The equivalent axis has been found, then this equivalent reflector is determined if the corresponding focal distance, called the equivalent focal distance, f_e, is determined. It can be shown [12], [13] that, for the Gregorian

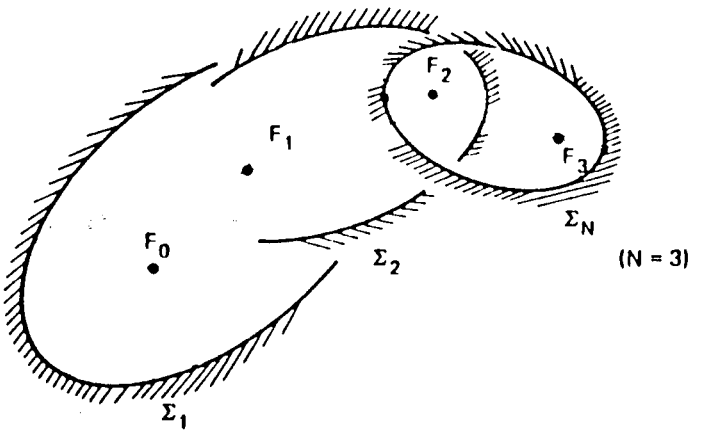

Figure 29: Sequence of N confocal reflectors with $N = 3$.

subreflector system, the following equation holds:

$$f_e = M\, f \tag{3.4}$$

where f is the focal length of the parabolic reflector and M is the magnification factor, given by

$$M = \frac{1 - \epsilon_s^2}{1 + \epsilon_s^2 - 2\epsilon_s \cos\beta_c} \,. \tag{3.5}$$

At this point all the quantities of interest (i.e., the direction of the equivalent axis, the central ray and the equivalent focal length) can be determined in terms of the geometry of the Gregorian subreflector system.

3.4 TAPER OF THE REFLECTED FIELD

A parabolic reflector illuminated by a focussed omnidirectional source is considered here in order to simply evaluate the geometry effects associated with the geometric taper errors. The polar reference system $F_m(r_m,\, \theta_m,\, \phi_m)$ introduced

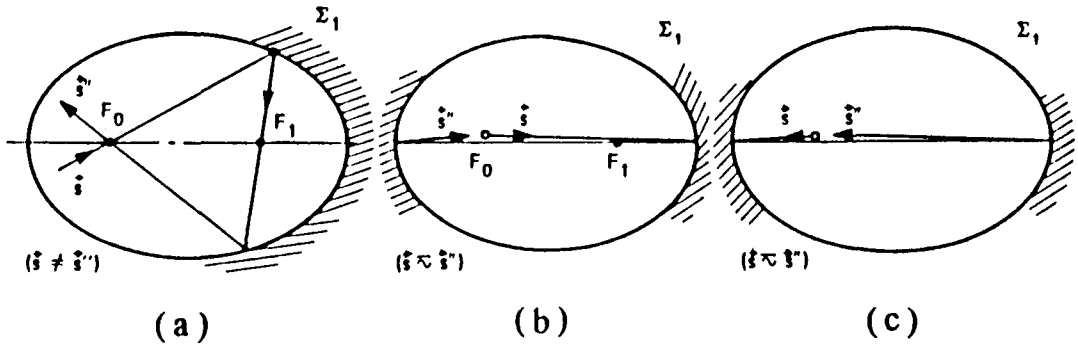

Figure 30: Determination of the equivalent axis for a single reflector. The reflector and the focus, F_0, are known, while, the focus, F_1, is unknown.

in Section 3.2 is considered. An intersection of the target zone with a plane perpendicular to the parabolic reflector axis (as defined in Section 3.2) is considered. This section is rectangular in the present case, but its actual shape is unimportant in the following considerations.

The field reflected from the parabolic reflector is a nonuniform plane wave (see Section G), and in a plane perpendicular to the parabolic reflector axis, its amplitude varies as

$$|\mathbf{U}^r(R)| \propto \frac{1}{r_m} \quad \text{or} \quad |\mathbf{U}^r(R)| \propto \sin^2\left(\frac{\theta_m}{2}\right) \tag{3.6}$$

where R is the field point, and $(r_m,\ \theta_m,\ \phi_m)$ are the polar coordinates of the reflection point, I_m, image of R in the $F_m(r_m,\ \theta_m,\ \phi_m)$ reference system (see Figure 34). The amplitude of the reflected field is maximum for $\theta_m = 180^o$ and decreases as θ_m decreases toward 0^o or increases toward 360^o. Since a uniform

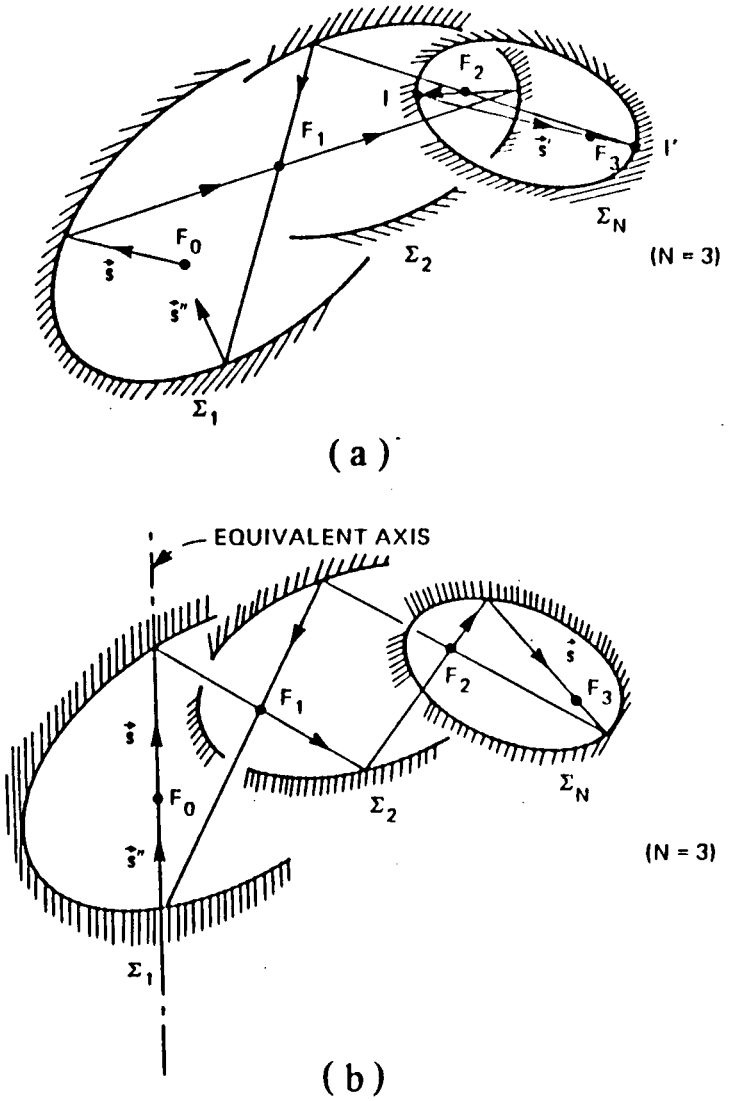

Figure 31: Ray paths for a generic ray (a) and for the central ray (b) for N confocal reflectors with $N = 3$.

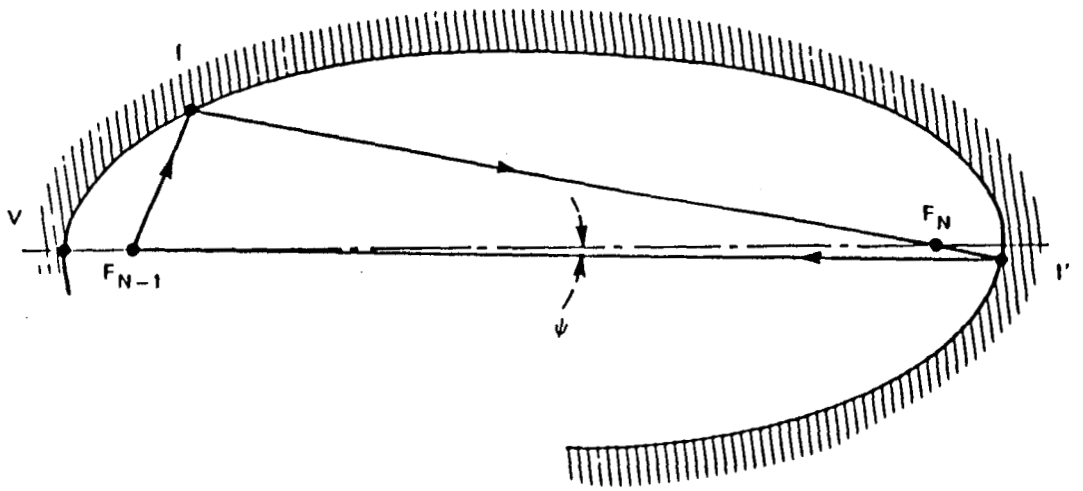

Figure 32: Limit argument to show that the direction, $\hat{\mathbf{s}}''$, is independent from the direction, $\hat{\mathbf{s}}$, for a parabolic reflector.

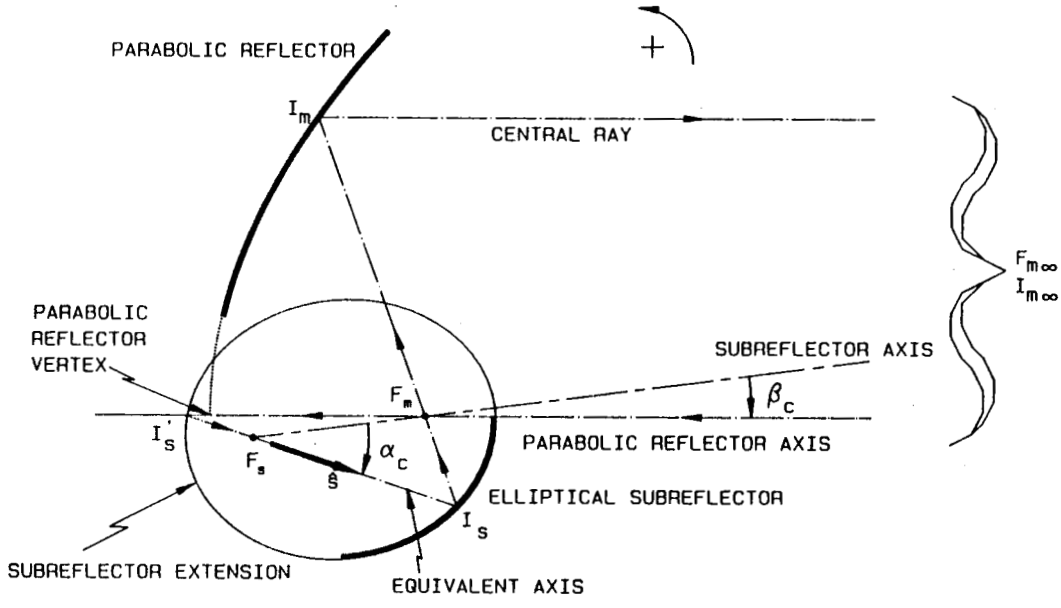

Figure 33: Determination of the equivalent axis and central rays for a Gregorian subreflector system through a geometrical construction.

plane wave is highly desirable in the target zone, a geometric taper is undesirable.

A typical plot of the geometric taper of a parabolic reflector is shown in Figure 35. The coordinate, ρ, represents the distance (with sign) from the parabolic reflector axis along an oriented straight line intersecting the parabolic reflector axis and perpendicular to it, and $\rho = 0$ corresponds to the intersection of the line with the reflector axis.

An arrangement of the target zone is called on-axis when the z_m axis of the target zone coincides with the parabolic reflector axis; otherwise, the arrangement is called off-axis (see Figure 36). By considering this plot, it is easy to realize that an on-axis arrangement of the target zone always gives a better geometric taper than an off-axis arrangement.

The reflected field is also dependent on the pattern of the source. Thus, the total taper of the reflected field is due to the geometric taper combined with the taper associated to the pattern of the source. For an omnidirectional source, the geometric taper and the total taper are the same. An off-axis arrangement for the parabolic reflector and the target zone, with a focussed source having a non-uniform axially symmetrical pattern (a Huygens source, for instance), is considered next. If the pattern axis of the source (i.e., the principal ray) is directed toward the vertex, V, of the reflector, the total taper becomes greater everywhere with respect to the total taper of an omnidirectional source (which coincides with the geometric taper). In fact, another degrading factor is added to the geometric taper; i.e., the decrease of the pattern of the source away from its own axis. Instead, if the pattern axis of the source is aimed towards the upper part of the parabolic reflector, the total taper is reduced by the compensating increase of the source pattern. This argument does not apply to a on-axis arrangement of the reflector and target zone. For an on-axis arrangement no compensation of the geometric

taper can be made by tilting the principal ray, because what is gained on one side, is lost on the other side.

For a subreflector system and for a single reflector offset configuration, the geometric taper can be compensated by a tilt of the feed axis (principal ray) with respect to the subreflector axis.

As shown by Dragone [6], the subreflector system is equivalent to a single parabolic reflector having the central ray as an axis. Consequently, the best geometric taper of the reflected field is obtained for an on-axis arrangement of the target zone with respect to the equivalent reflector; i.e., when the z_m axis of the target zone and the central ray coincide. Zero cross-polarization is obtained if the principal ray of the feed coincides with the central ray (Section 3.6). Therefore, the following condition

$$\chi_p = \chi_i = \chi_c \tag{3.7}$$

which expresses that the axis of the target zone, the equivalent axis and the principal ray all coincide, guarantees at the same time zero cross-polarization and the minimum for the geometric taper for a subreflector system and a target zone.

How the tilt of the pattern axis (the principal ray) affects the cross polarization is examined in Section 3.6, for the single reflector and for the subreflector system in the case of a Huygens source feed.

3.5 REDUCTION OF THE GEOMETRIC TAPER BY AN INCREASE OF THE FOCAL DISTANCE

It was shown in Section 3.4 how the position of the z_m axis of the target zone with respect to the parabolic reflector axis affects the geometric taper of the reflected field, and how it can be minimized if the axis coincides with the central ray. Another factor affecting the geometric taper is the focal distance of

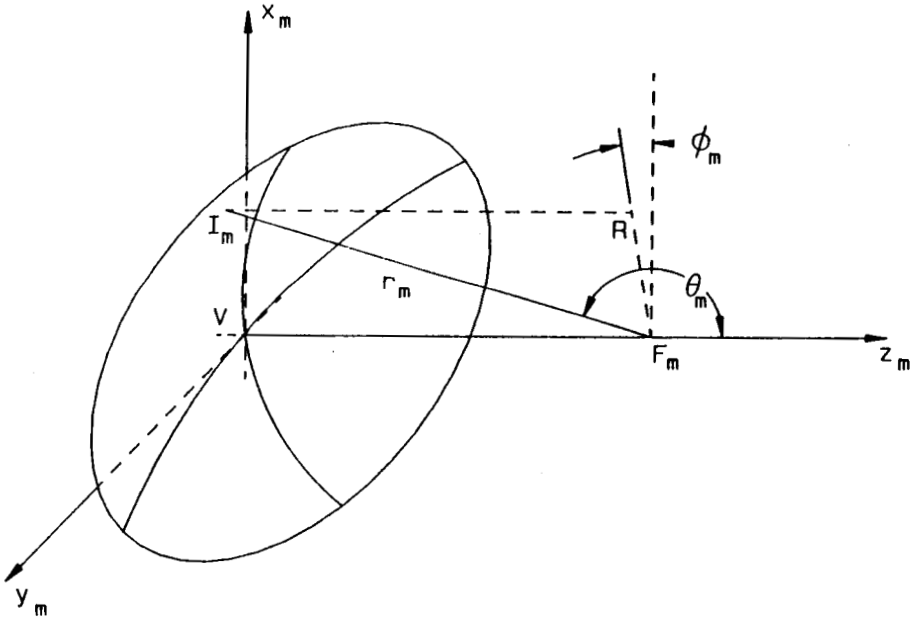

Figure 34: Polar coordinate system for the parabolic reflector.

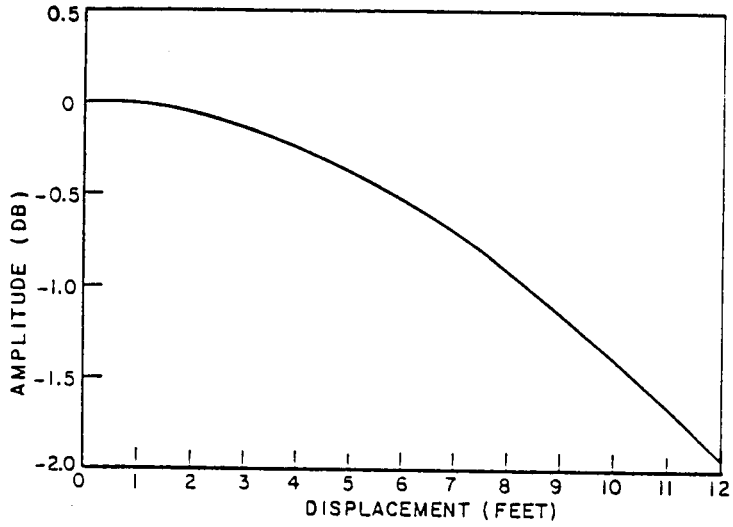

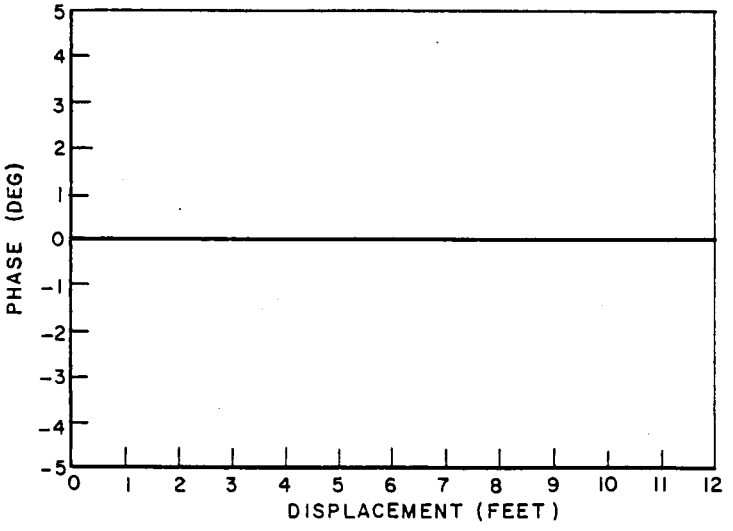

Figure 35: Typical geometric taper of the reflected field.

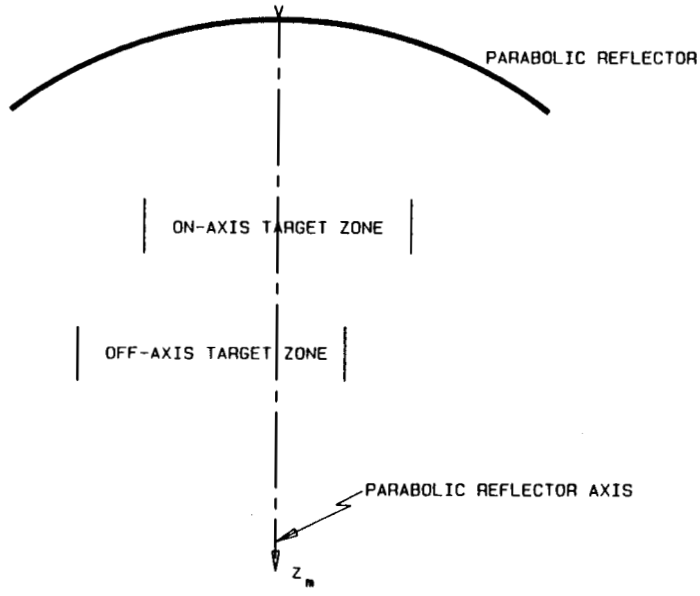

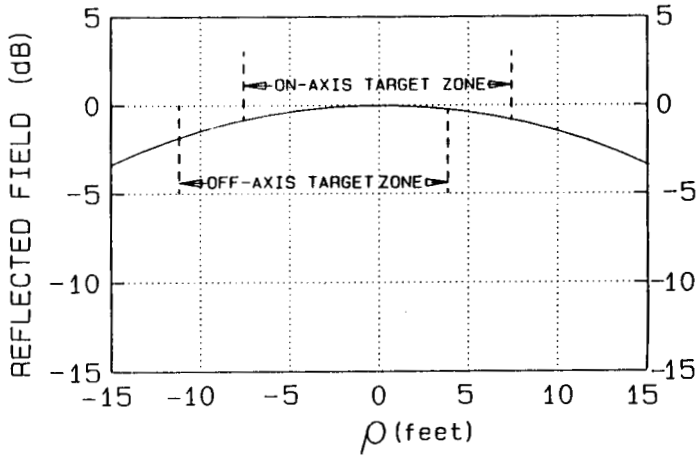

Figure 36: On-axis and off-axis arrangements of the target zone.

the parabolic reflector for a single reflector system, or the equivalent focal distance for a subreflector system. The following considerations make reference to a single parabolic reflector, but they are immediately extended to a subreflector system via the concept of the equivalent reflector.

For a single parabolic reflector, a way to reduce the geometric taper is suggested by Equation (3.6), such that (see Figure 37)

$$|\mathbf{U}^r| \propto \sin^2(\frac{\theta_m}{2}) \ . \tag{3.8}$$

The reference systems considered are the polar coordinate systems $F_{mi}(r_{mi}, \theta_{mi}, \phi_{mi})$ already defined, with $i = 1, 2$. The maximum value of the geometric taper is related to θ_m^{max}, polar coordinate of the upper point of the primary illuminating surface. If θ_m^{max} is increased towards 180^o, the geometric taper decreases. Note that θ_m^{max} increases toward 180^o with increasing focal length; therefore, the taper of the reflected field decreases with increasing focal length. In Figure 37, $f_1 < f_2$, $\theta_{m1}^{max} < \theta_{m2}^{max}$, and reflector 2 has a smaller geometric taper than reflector 1. In the limiting case where the focal length becomes infinite, the parabolic reflector becomes a flat plate, a plane wave is incident on the reflector and a plane wave is reflected; thus, the geometric taper is zero, and the total taper is zero if the incident plane wave is uniform.

An increase of f seems an attractive way to reduce the geometric taper, but there is a drawback for a single reflector system. The distance z_{tm} of the center of the target zone in the z_m direction from the vertex of the reflector must increase with increasing focal distance, as a rule of thumb: $z_{tm} \simeq 2f$. This relationship must be satisfied in order to decouple the target from the feed and to allow the use of time-gating techniques. Due to diffraction from the reflector, z_{tm} must be kept to a minimum; in fact, with increasing z_{tm}, the near-field behaviour of the

total field disappears and approaches the far-field pattern. This results in larger ripple levels in the target zone due to the increased effect of diffraction. This is shown in Figure 7, where the total field for a "typical" compact range is shown at three different values of the distance z_{tm}, i.e., at $12'$, $24'$ and $36'$ feet away from the reflector vertex. It is easy to see how the ripple due to diffraction progressively increases. Consequently, in the design of a single reflector compact range, there must be a trade-off between z_{tm} and f.

The same considerations hold for the subreflector system. Again, z_{tm} must satisfy $z_{tm} \simeq 2f$ in order to decouple the target from the coupling aperture, and z_{tm} must be kept small to avoid deterioration of the wavefront from the parabolic reflector. But, for a subreflector system, the focal distance f is substituted by the equivalent focal length f_e (as explained in Section 3.7.2), therefore, in the subreflector system case, the principle of the equivalent reflector shows that it is possible to have a system with a large equivalent focal length without having large focal length and target distance. It is possible then to reduce the geometric taper without introducing in the total field a large ripple due to diffraction (see Section 3.7.2).

3.6 REFLECTED FIELD CROSS-POLARIZATION

The definition of cross-polarization depends on the application considered [8]. A plane wave is desired in the target zone for compact range applications; consequently, the cross-polarization ratio (cross-polarization for short) is defined as

$$\frac{U_{\perp}}{U_{||}} \tag{3.9}$$

where $U_{\perp}$ and $U_{||}$ are, respectively, the field components perpendicular and parallel to the desired polarization direction, which is perpendicular to the parabolic

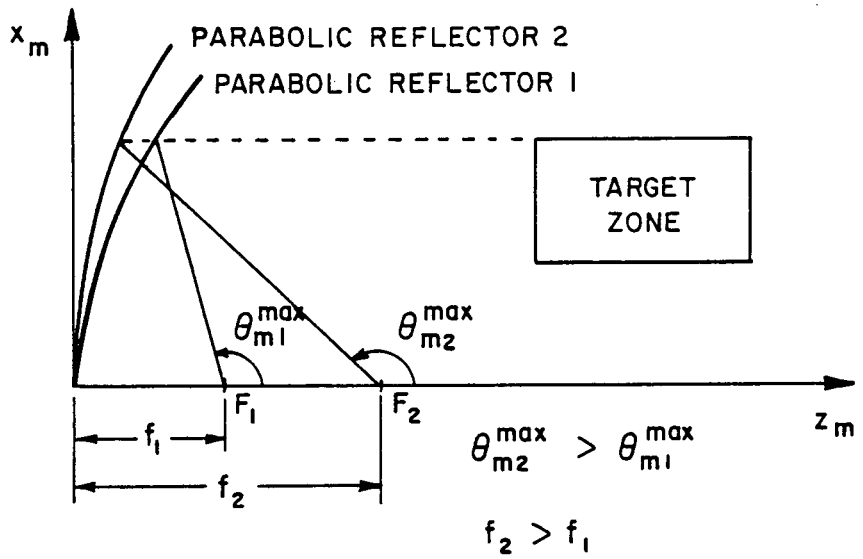

Figure 37: Effect of the focal distance on θ_m^{max}.

reflector axis.

It is very desirable to have a plane wave with zero (or at least very small) cross-polarization in the target zone. In fact, some of the applications of a compact range require excellent polarization purity, such as:

- RCS measurements and target identification, where the received signal is highly influenced by the interaction of the polarization direction of the incident wave with the target geometry [3].
- Measurements of radiation patterns of communication antennas with polarization diversity.

In order to control the cross-polarization of the wavefront in the target zone, one must understand the different factors that affect it:

1) Aperture blockage.

2) Diffraction from edges.

3) Choice of the tilt angles of subreflector and feed.

4) Cross-polarization characteristics of the feed.

5) Mechanical misalignments.

The GO design is concerned with factor number 3). Factor 4) also can be considered with a numerical procedure where the real feed is modeled by data interpolation. The first two factors involve diffraction effects which are not considered here.

It is customary to refer to a Huygens source as a feed to discuss the cross-polarization of a single reflector or subreflector system [10], for the following reasons:

- It is necessary to make reference to a common, standard source in order to compare the performance of different reflector systems.
- The Huygens source fairly realistically models the behaviour of several simple feeds.
- With a Huygens source it is possible to achieve zero cross-polarization of the reflected field with a center fed arrangement.

With a Huygens source it is possible then to conceptually separate the effects due to the reflector (or reflectors) from the effects due to the source on the total cross-polarization. For a single reflector, zero cross-polarization is achieved if the principal ray of the Huygens source coincides with the negative z_m axis (the axis of the reflector); i.e., with a center fed arrangement, where the Huygens source is

pointing towards the vertex of the paraboloid. For a subreflector system, zero cross-polarization is achieved if the principal ray of the Huygens source coincides with the central ray of the subreflector system (see Section E). Under this hypothesis, the tilt angles α and β, denoted by α_c and β_c, satisfy the following relationship (zero cross-polarization equation) [6]:

$$\tan\left(\frac{\alpha_c}{2}\right) = m \tan\left(\frac{\beta_c}{2}\right) \tag{3.10}$$

where for a concave elliptical subreflector, the axial magnification factor m is given by

$$m = \frac{1+\epsilon_s}{1-\epsilon_s} \,. \tag{3.11}$$

The angle, α_c, is the tilt angle from the subreflector axis to the central ray, and β_c is the tilt angle from the subreflector axis to the parabolic reflector axis. These angles are defined in the x_m, y_m plane having y_m as normal. The parameter ϵ_s is the eccentricity of the subreflector.

In the previous section, it has been shown that, for an off-axis target zone, it is advisable to tilt the axis of the feed to compensate for the geometric taper. Referring to a Huygens source it follows that:

- For a single reflector, as the tilt angle χ_p is reduced from 180^o, the cross-polarization error increases.

- For a subreflector system, zero cross-polarization can be achieved by satisfying Equation (3.10). Therefore, it is possible to tilt the feed axis without compromising the cross-polarization.

One of the goals of the GO design is to determine the two angles α and β which satisfy Equation (3.10) together with the other design constraints.

3.7 FACTORS AFFECTING THE GO DESIGN OF A COMPACT RANGE

In this section several factors affecting the design of reflector antennas and compact ranges are analyzed.

3.7.1 SOURCE REQUIREMENTS FOR A COMPACT RANGE

A feed located at the point, F_s, for a subreflector system is shown in Figure 38. The direction corresponding to the maximum of the source pattern is called the principal ray. This ray is oriented from the source towards the reflectors. For the subreflector system, the intersection of the principal ray (in this context also called the secondary principal ray) with the subreflector is the point I_{ps}. The line through the points I_{ps} and F_m is called the primary principal ray. It is oriented from I_{ps} to F_m. It intersects the parabolic reflector at the point I_{pm}. The x_m coordinate of I_{pm} is called h_{pm}. The angle in the x_m, z_m plane from the z_m axis to the primary principal ray is called χ_p. The angle from the subreflector axis to the secondary principal ray is called β.

The part of the central ray between the source and the subreflector is called the secondary central ray, instead the part between the subreflector and the parabolic reflector is called the primary central ray. The central ray is oriented from the source towards the reflectors. The angle in the x_m, z_m plane from the z_m axis to the central ray is called χ_c. The angle on the same plane from the subreflector axis to the secondary central ray is called α_c. The intersection of the central ray with the parabolic reflector is the point I_{cm}; its intersection with the subreflector is the point I_{cs}, and h_{cm} is the x_m coordinate of the point I_{cm}.

One of the objectives of the GO design is to determine the angles α and β so as to achieve zero cross-polarization, i.e., to make the principal ray coincide with

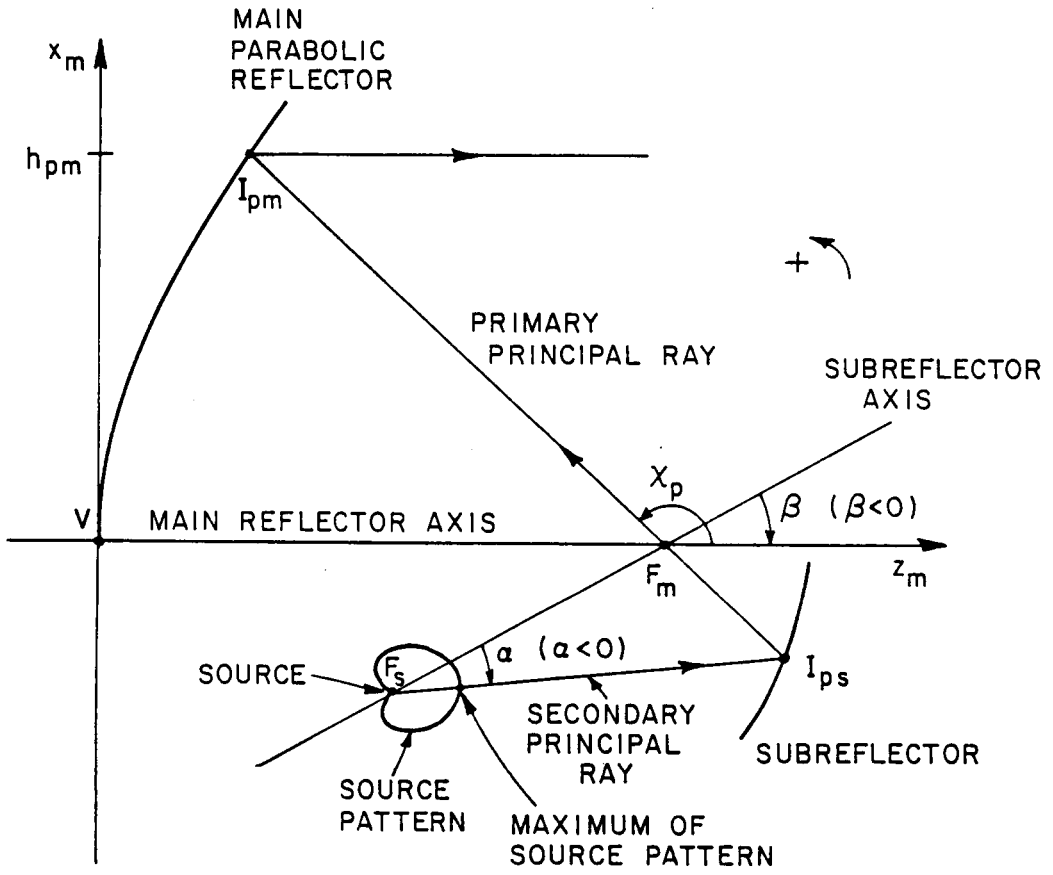

Figure 38: Huygens source parameters.

the central ray. Consequently, to achieve zero cross-polarization, the ideal source for a compact range should have the field distribution of a Huygens source and its principal ray should coincide with the central ray of the subreflector system. It is also important to establish which pattern this ideal source should have. In the ideal case, and neglecting the diffraction that such a beam would introduce through its own shadow boundaries, the source set at the focal point, F_s, should have a pattern different from zero in directions corresponding to the secondary illuminating surface and zero in any other direction. Naturally this is impossible to achieve. Instead, a real feed antenna has a pattern function having a (more or less) symmetric main lobe and several side lobes. The pattern itself is a function of frequency and polarization, and generally is more narrow at the higher frequencies and broadens at the lower frequencies. Since it is desirable to use the same feed over a wide frequency range (2-18 GHz), it is necessary to dimension the subreflector and the feed so that the pattern considered for the GO design corresponds to the narrowest of all the patterns of the feed, i.e., to the pattern at the highest frequency of operation (18 GHz in the present case). It follows that it is unavoidable to have spillover from the feed itself; therefore, the subreflector is overextended (to reduce the amount of diffraction by reducing the field incident on the edges, which are made to correspond in the pattern to directions of lower radiation), and the absorber on the walls of the lower chamber must be properly designed.

As it is shown in Section E, a truncated rectangular waveguide has radiation characteristics very close to those of a Huygens source, and its phase center is stable with direction (i.e., with θ_p, ϕ_p); therefore, these source requirements are not unrealistic. On the other side, the use of a feed with a Cassegrain or Gregorian configuration without the dual chamber arrangement would lead to a large amount of spill-over and strong illumination of diffracting edges, with serious performance

degradation. Thus, for the present purposes it is assumed that the Huygens source realistically models the actual feed antenna.

An important requirement on the source is the stability of the position of its phase center with respect to the angular directions in the pattern. In fact, the position of the phase center is a very critical parameter in the design of the subreflector system, which could seriously degrade its performance for too wide variations of h_{pc} or z_{pc} or both.

The beamwidth of the feed is now related to some geometrical parameters. In fact, the section of the primary illuminating beam with the x_m, z_m plane, as shown in Figure 39, is considered. The ray corresponding to the angle χ_u with the z_m axis illuminates the upper point, I_{um}, of the section of the primary illuminating surface with the x_m, z_m plane, this ray is called the upper illuminating ray, and α_u is the corresponding angle of the ray with the subreflector axis. The point, I_{um}, has x_m coordinate given by h_{um}. The ray corresponding to the angle χ_l with the z_m axis illuminates the lower point, I_{lm}, of the section of the primary illuminating surface with the x_m, z_m plane, this ray is called the lower illuminating ray, and α_l is the corresponding angle with the subreflector axis. The point, I_{lm}, has x_m coordinate given by h_{lm}. The quantity

$$BMW_i^{xz} = \alpha_u - \alpha_l \tag{3.12}$$

characterizes the beamwidth of the feed in the x_m, z_m plane, and the feed pattern is expected to be fairly constant inside this angular sector. For a circular target zone, the illuminating beamwidth of the feed is completely determined by BMW_i^{xz}; it is not so for a rectangular target zone, since the beamwidth in planes through the subreflector axis different from the x_m, z_m plane is not equal to BMW_i^{xz}. Another quantity characterizing the feed in the x_m, z_m plane is BMW^{xz}, which

is the beamwidth inside which the radiation pattern intensity is greater than some specified dB level, called X. The feed pattern is lower than X dB outside this angular sector. Since the feed used has a circular symmetry, the beamwidths BMW_i^{xz} and BMW^{xz} characterize the feed, for the purposes considered here.

For the single reflector case, the previous definitions hold with the changes due to the lack of the subreflector and with the source located at F_m.

3.7.2 EQUIVALENT FOCAL LENGTH FOR A SUBREFLECTOR SYSTEM

As shown by Dragone [6], a sequence of confocal reflectors is equivalent to a single reflector, which has the same GO reflected field as the given sequence of reflectors . The axis of the equivalent reflector is called the equivalent axis, and coincides with the central ray after the reflection from the last reflector in the given reflector sequence. In the present case, the equivalent reflector is a paraboloid, and the equivalent axis is parallel to the parabolic reflector axis z_m and goes through the point I_{cm}. The equivalent paraboloid is centered on the equivalent axis, and its equivalent focal length, f_e, is given by

$$f_e = M\ f \tag{3.13}$$

where f is the focal length of the parabolic reflector, and M is the magnification of the subreflector system. For a concave elliptical subreflector, the magnification is given by [12]

$$M = \frac{1 - \epsilon_s^2}{1 + \epsilon_s^2 - 2\epsilon_s \cos\beta_c} \tag{3.14}$$

where

- ϵ_s is the eccentricity of the elliptical subreflector, and

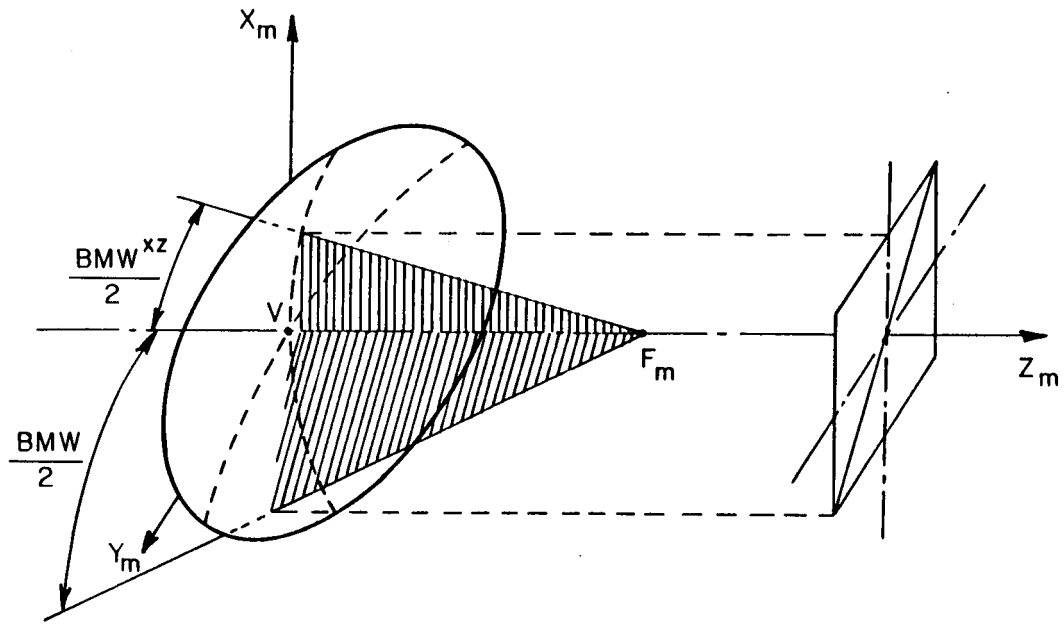

Figure 39: Feed beamwidths.

- β_c is the angle from the subreflector axis to the parabolic reflector axis [12], [13].

In the case $\beta_c = 0$, M is equal to the axial magnification, m, given by

$$m = \frac{1 + \epsilon_s}{1 - \epsilon_s} \tag{3.15}$$

which is the maximum value obtained for M. Also,

$$M > 1 \qquad \text{for} \qquad (-\overline{\beta} < \beta < \overline{\beta}) \tag{3.16}$$

where

$$\overline{\beta} = \arccos \epsilon_s \ , \qquad 0 < \overline{\beta} < \pi \tag{3.17}$$

and that, in this range of values of β, one finds that

$$\infty > M > 1 \tag{3.18}$$

according to the choice of ϵ_s.

These considerations show how a subreflector system can achieve a large equivalent focal length without having a parabolic reflector with a large focal length.

3.7.3 APERTURE BLOCKAGE AND UNWANTED INTERACTIONS

Aperture blockage is a well known problem in the design of reflectors. As the name suggests, it happens when an object (typically the feed, the subreflector, or the supporting struts) blocks the path of the rays reflected from the parabolic reflector. Thus, aperture blockage structures create a shadow and strong diffractions which degrade the amplitude, phase and cross-polarization characteristics of the reflector antenna; also, this field again illuminates the reflector and is reflected back into the feed with degradation of its SWR. Sometimes aperture blockage is

accepted in return for mechanical simplicity. In other cases, where good performance is important, an offset arrangement of the reflector or subreflector system is necessary. This arrangement, in turn, dictates a tilt of the pattern axis of the feed with respect to the axis of the reflector. If a Huygens source is assumed as a feed, for a single reflector case, the tilt of the feed axis can compensate (at least partially) for the geometric taper in the case of an off-axis target zone, but degrades the cross-polarization performance. For a subreflector system, an offset arrangement with a proper choice of the tilt angles improves the geometric taper without compromising the cross-polarization, if the axis of the feed coincides with the central ray of the subreflector system.

There might be objects which are not on the path of the incident rays, but are close to the reflector system and interact with it through diffraction and multiple reflection rather than through direct shadowing, as an example, the walls of the anechoic chamber of a compact range. These interactions can degrade the performance of a reflector antenna. The strict requirements on a compact range dictate not only an offset arrangement for the reflector (and for the subreflector system combination), but also the use of time domain techniques in order to minimize unwanted interactions [14]. Not all unwanted interactions can be eliminated in this way, for instance, for a Cassegrain configuration, the diffraction from the edges of the subreflector into the reflector and from here into the target zone cannot be time-gated. These interactions can be minimized by a Gregorian configuration and by a dual chamber approach, as shown in Figure 9. The lower chamber contains the feed and the subreflector; whereas, the upper chamber contains the parabolic reflector, the pedestal and the target zone. The two chambers are coupled through an opening centered around the focal point of the parabolic reflector, to allow the illumination of the main reflector by the rays coming from the subreflector

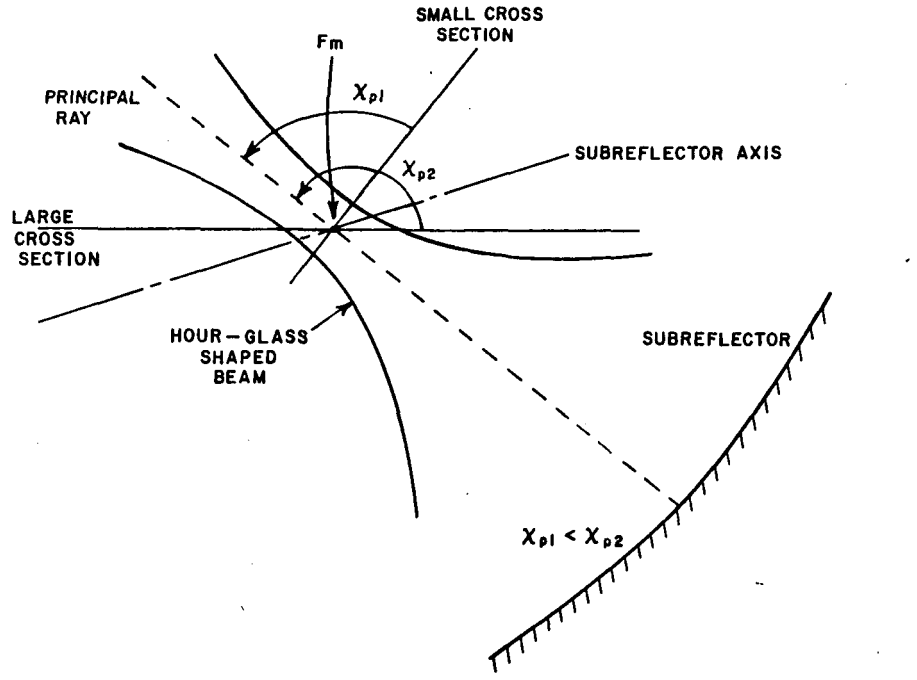

Figure 40: Hour-glass shape of illuminating beam and its sections with planes.

and feed. This aperture is called the coupling aperture and must be as small as possible to eliminate unwanted interactions, but also must be large enough not to perturb the beam illuminating the parabolic reflector at the minimum operating frequency. A careful design of the offset subreflector system with the dual chamber and the coupling aperture eliminates aperture blockage and reduces interactions and the amount of unwanted diffractions in the target zone to a minimum.

3.7.4 FIELD IN THE FOCAL REGION

The choice of the angle χ_p (or χ_c, in the case that the principal ray coincides with the central ray, as it is done to obtain zero cross-polarization) between the parabolic reflector axis and the source principal ray is presently addressed. A choice of χ_p (see Figure 40) close to 90^o minimizes the size of the coupling aperture. In fact, ideally the parabolic reflector is fed by a beam (called the primary illuminating beam) coming from the subreflector and converging into the

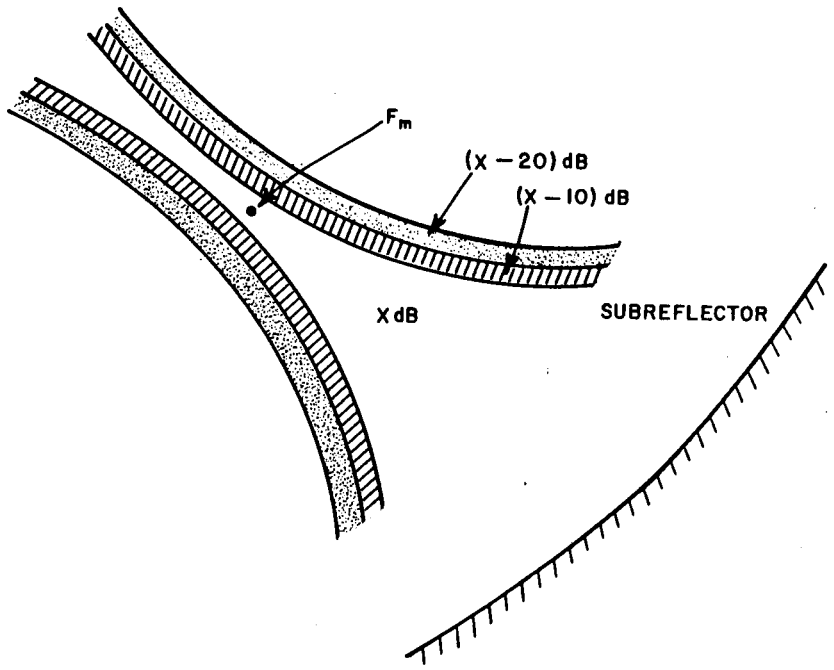

Figure 41: More realistic illuminating beam.

focal point, F_m. The ideal GO beam converges exactly at the point F_m and can be modeled as being zero outside the primary illuminating beam, i.e. as having a box-like shape with sharp edges. The real beam instead has properties still close to this ideal beam, but is focussed through a finite size area with a diameter of approximately one wavelength. This area is made to correspond to the coupling aperture, for which a diameter of about five wavelengths at the lowest frequency can be safely assumed. This choice guarantees that the beam is not disturbed by the sides of the coupling aperture itself. The real beam does not go abruptly to zero outside the primary illuminating beam, but it spreads out somewhat. A more realistic beam pattern is shown in Figure 40, and has an hour-glass shape. The bottleneck of the hour-glass is centered at the focal point, F_m, but it does not shrink to a point. Instead, its cross sectional area is different from zero. The coupling aperture then approximately corresponds to a section of the bottleneck

with the y_m, z_m plane. The section becomes larger when the angle χ_p increases from 90^o to 180^o, or decreases to 0^o (see Figure 40). Figure 41 instead gives the qualitative behaviour of the field contour in the focal region, where X is the field strength in the central zone. As it can see, the gradient of the field is very high in the focal region. It is important than that the contour of the coupling aperture are removed from the region of fast variation of the field, to avoid slope diffraction effects.

3.7.5 TIME GATING OF RAYS DIFFRACTED FROM THE COUPLING APERTURE

The pulsed operation of a Compact Range allows one to time-gate out many error terms. In this section some considerations on the time gating are presented which refer to the GO design of the subreflector system and of the coupling aperture.

In the subreflector system it is desired to time-gate the rays diffracted from the edges of the coupling aperture into the target zone, like the ray $\mathcal{D}^*_{C_l''}$ shown in Figure 42. This ray illuminates the edge, S_u, from the feed, F_s, is diffracted to the absorber wedge tip, C_l'', and it is rediffracted to the point, T_u. The point, T_u, belongs to the plane, II, which is perpendicular to the parabolic reflector axis and set at the beginning of the target zone. The distance $|T_u - C_l''|$ is close to the distance $|T_u - F_m|$, while the distance $|C_l'' - S_u|$ is close to the distance $|F_m - S_u|$; consequently, for the purposes of time delay computations, this diffracted ray can be substituted, with good approximation, with the pseudo-ray, $\mathcal{D}^*_{F_m}$. This pseudo-ray does not correspond to any real ray, but instead it is introduced for convenience and ease of computation. Its path is from F_s to S_u to F_m and finally to T_u. The reason for using the ray, $\mathcal{D}^*_{F_m}$, in the time delay considerations is that the time

delay of the ray, $\mathcal{D}^*_{C_l''}$, is dependent on the location of the point C_l'', which is determined through the design of the coupling aperture; while, the timing of the ray, $\mathcal{D}^*_{F_m}$, is related to the location of the focal point, F_m, which is determined through the design of the subreflector system alone. In this way then the design of the subreflector system can be better separated from the design of the coupling aperture, and the resulting design procedures are greatly simplified. It can be shown similarly that this approximation is reasonably accurate for any of the rays diffracted by the tips of the wedges in the coupling aperture. The reason for choosing the point, T_u, and not any other point on the plane, Π, is shown later.

The ray, $\mathcal{I}_r$, is then considered, which is a representative of any ray illuminating the target zone from the feed through reflection from the subreflector and the main reflector. Its path is from F_s to I_s to F_m to I_m and finally to T_r, up to the "forward" part of the target zone (i.e., to the plane Π). There is no reason to choose this specific ray, but it is convenient to choose one for the sake of an explanation; in any event, the result obtained does not depend from the choice of this ray. The length, $\ell_{f\mathcal{I}_r}$, of the ray, $\mathcal{I}_r$, up to the plane Π is given by (where the subscript "f" refers to the "forward" part of the coupling aperture)

$$\ell_{f\mathcal{I}_r} = |I_s - F_s| + |F_m - I_s| + |I_m - F_m| + |T_r - I_m| \tag{3.19}$$

and by the properties of the parabola and of the ellipse, one finds that

$$|I_s - F_s| + |F_m - I_s| = 2\,a \tag{3.20}$$

$$|I_m - F_m| + |T_r - I_m| = f + z_{bt} \tag{3.21}$$

where

- $2\,a$ is the length of the major axis of the elliptical subreflector
- f is the focal length of the parabolic reflector

- z_{bt} is the z component of the distance $|T_r - V|$; i.e., of the distance of the plane Π from the vertex V of the parabolic reflector, as shown in Figure 42.

One then obtains

$$\ell_{f\mathcal{I}_r} = 2\,a + f + z_{bt} \tag{3.22}$$

and the corresponding time delay is given by

$$t_f = \frac{1}{c}\,[2\,a + f + z_{bt}]\ . \tag{3.23}$$

Notice that the length, $\ell_{f\mathcal{I}_r}$, and the time delay, t_f, do not depend on the point, T_r, but rather on the distance of the plane Π from V. Any point on that plane has the same distance and the same time delay.

The length of the ray path, $\mathcal{D}^*_{F_m}$, up to the plane Π, is given by

$$\ell_{f\mathcal{D}^*_{F_m}} = |S_u - F_s| + |F_m - S_u| + |T_u - F_m| = 2\,a + |T_u - F_m| \tag{3.24}$$

which is based on the proprieties of the ellipse. The corresponding time delay is given by

$$t_d = \frac{1}{c}\,[2\,a + |T_u - F_m|]\ . \tag{3.25}$$

The two time delays, t_f and t_d, are not the same in general. It is possible to take advantage of this to time-gate out the unwanted diffraction contribution. This can be understood by considering the timing diagram of the received pulses shown in Figure 43. The transmitted pulse is shown in (a). The pulse corresponding to the ray $\mathcal{D}^*_{F_m}$ is shown in (b). The pulse corresponding to the forward part of the target zone (plane Π) is shown in (c), while the one corresponding to the back of the target zone is shown in (d). Cases (c) and (d) correspond to the ray $\mathcal{I}_r$ (or any such ray). Finally in (e) the effect of the gating is shown: the portion of the pulse from t_b to $t_f + T$ corresponds to the ray $\mathcal{I}_r$ and is accepted by the switches

into the receiver; while, everything else is gated out, in particular the diffracted ray $\mathcal{D}^*_{Fm}$. From the Figure 43 one obtains

- T is the length of the transmitted pulse
- $\Delta t = t_f - t_d$ is the time delay differential between the rays $\mathcal{I}_r$ and $\mathcal{D}^*_{Fm}$
- $\Delta\tau = t_b - t_f$ corresponds to twice the length ℓ_{tz} of the target zone: $\Delta\tau = 2\,\ell_{tz}/2$
- $T_g = t_f + T - t_b$ is the duration of the gating; also, $T_g = T - \Delta\tau$.

Recall that

$$t_f = 2\frac{1}{c}\ell_{f\mathcal{I}_r} \qquad t_d = 2\frac{1}{c}\ell_{f\mathcal{D}^*_{Fm}} \qquad t_b = 2\frac{1}{c}(\ell_{f\mathcal{I}_r} + \ell_{tz}) \tag{3.26}$$

and the time delay differential, Δt, is given by

$$\Delta t = t_f - t_d = 2\frac{1}{c}\left(\ell_{f\mathcal{I}_r} - \ell_{f\mathcal{D}^*_{Fm}}\right) \tag{3.27}$$

$$\Delta t = 2\frac{1}{c}\left(f + z_{bt} - |T_u - F_m|\right) . \tag{3.28}$$

In order to perform the time gating, it is required that

$$t_d + T < t_b \tag{3.29}$$

this inequality must be satisfied with some margin, to take into account the finite switching time of the switches, therefore one can set

$$t_d + T \leq t_b + T_{sw} \tag{3.30}$$

where T_{sw} is related to the switching speed and determines the minimum separation between the end of the diffracted pulse and the beginning of the gate. Therefore, one obtains

$$T - T_{sw} \leq t_b - t_d \tag{3.31}$$

but

$$t_b - t_d = \Delta t + \Delta\tau \tag{3.32}$$

and one then obtains

$$T - T_{sw} - \Delta\tau \leq \Delta t \tag{3.33}$$

$$T - T_{sw} - \Delta\tau \leq 2\frac{1}{c}(f + z_{bt} - |T_u - F_m|) \,. \tag{3.34}$$

In the present system one has

$$T = 20 \text{ ns} \qquad T_{sw} \simeq 6 \text{ ns} \qquad \Delta\tau \simeq 16 \text{ ns} \tag{3.35}$$

and one then obtains

$$T_g \simeq 4 \text{ ns} \qquad \Delta t \simeq 10 \text{ ns} \tag{3.36}$$

and the value actually obtained in the design is $\Delta t \simeq 9.5$ ns, which can be considered satisfactory.

From Inequality (3.34) it is clear why the point, T_u, must be considered to properly determine the time delays. In fact, for any other point, T', one considers the ray, $\mathcal{D}'_{F_m}$. The ray path is from F_s to S_u to F_m to T'. By comparing the length of this ray with the length of the ray, $\mathcal{D}^*_{F_m}$, one obtains

$$|T' - F_m| < |T_u - F_m| \tag{3.37}$$

and a shorter time delay is associated with the ray, $\mathcal{D}'_{F_m}$. The Inequality (3.34) must be satisfied for any point on the plane Π; therefore, the minimum of the right hand side must be considered. This minimum corresponds to the ray, $\mathcal{D}^*_{F_m}$.

3.8 SHAPE OF THE CROSS SECTION OF THE TARGET ZONE

The target zone is defined in Section 3.2 as a portion of a solid cylinder having generatrices parallel to the parabolic reflector axis and delimited by two

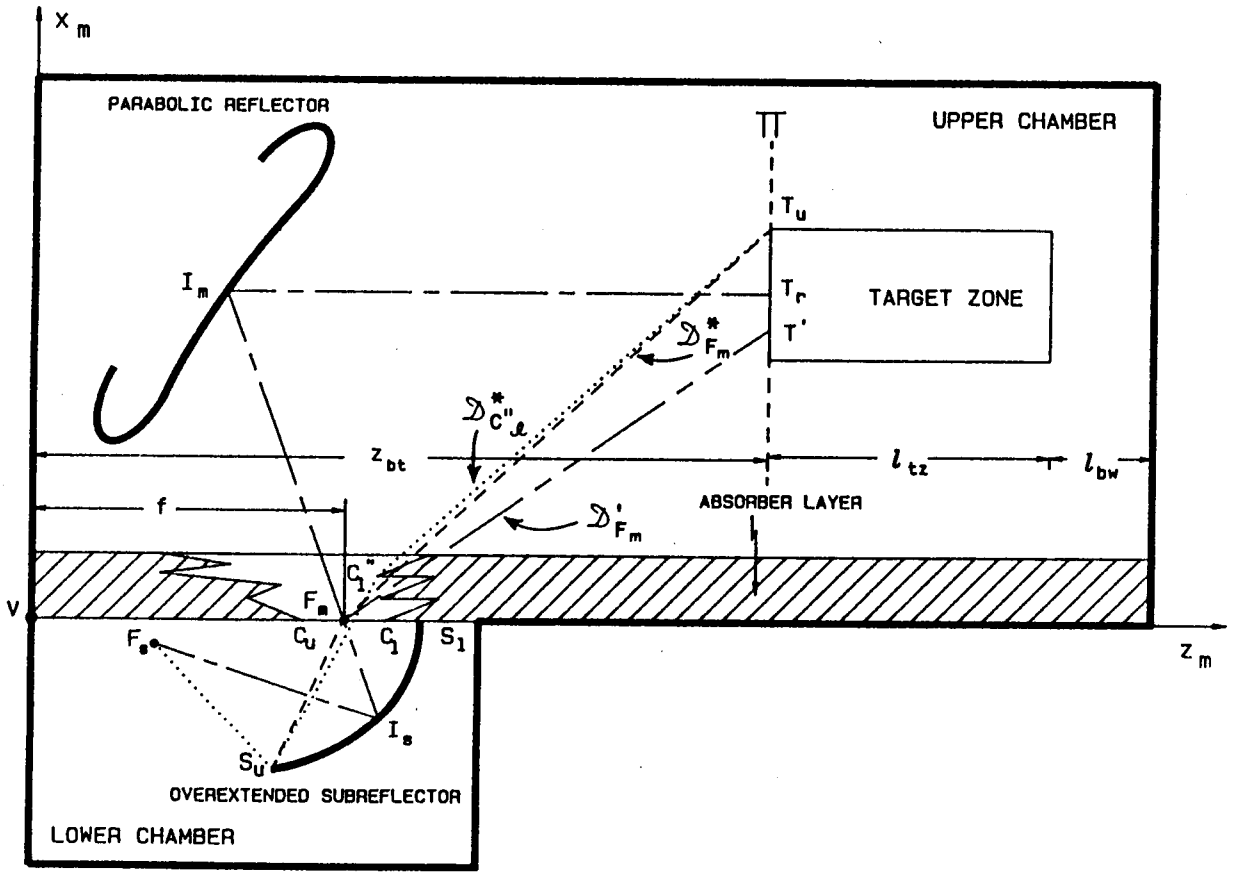

Figure 42: Geometrical quantities related to the time delays of different rays.

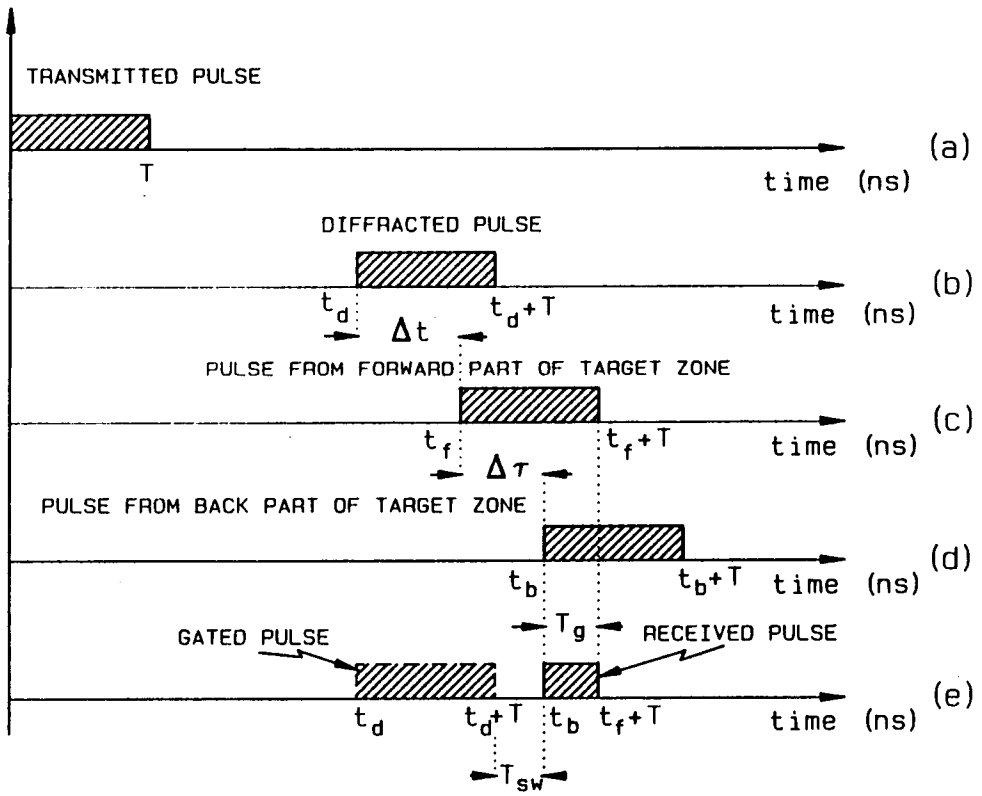

Figure 43: Timing diagram relating time delays and swithching times.

planes perpendicular to the parabolic reflector axis. A target zone is called circular, rectangular, elliptical, etc., according to the shape of its cross section in a plane perpendicular to the parabolic reflector axis. In the present section, it is discussed which shape is the most appropriate to define the cross section of the target zone with a plane perpendicular to the main reflector axis. In Section 3.2, a rectangular cross section has been considered, but this is not the only possible shape.

Most targets have an elongated shape, like the model of an airplane; therefore, it might seem that an elliptical cross section is a more natural one.

The feed considered (typically, a conical corrugated horn) has a radiation pattern circularly symmetrical with respect to the axis of the horn. If this axis coincides with the principal ray, as it is assumed in the present design, the circular symmetry of the beam is preserved after the reflection from the subreflector and the parabolic reflector. Consequently, from a GO viewpoint, a circular shape of the target zone is the most appropriate, since it allows the maximum utilization of the feed.

The shape of the upper room, where the measurements are performed, is rectangular. The room itself is a major element in the design of the compact range (it is by far its most expensive component), this fact then suggests a rectangular cross-section.

Finally, the limiting factor in the compact range design is the diffraction from the edges of the parabolic reflector. This is the factor degrading the otherwise (almost perfect) plane wave reflected from the parabolic reflector. From the purity of the field then, the most natural shape would be the same shape as that of the edges of the parabolic reflector.

It is necessary, on the other side, to specify some shape for the target zone while drafting the specification for the compact range. For instance, it is necessary

to specify the admissible geometric taper of the reflected field and also the taper of the feed, which in turn becomes a specification on the beamwidth of the feed antenna itself. Suppose, for instance, that the target zone is specified as rectangular, and that the maximum admissible taper for the feed is, for the sake of an example, 0.2 dB. In a sense, this represents an excessive requirement on the feed: in order to satisfy this requirement at the corner points, an excessively heavy requirement is imposed on the design of the feed itself and on the GO design. Very likely, this specification is not really necessary, since the corner points are seldom if ever used.

The same argument can also be applied to the geometric taper in the case of a rectangular cross section of the target zone. In practice instead, the requirements on the geometeric taper are easy to satisfy; consequently, it seems acceptable to satisfy the requirement at the four vertexes of the target zone, even if this is not a requisite strictly necessary.

CHAPTER IV

ITERATIVE SUBREFLECTOR SYSTEM DESIGN

The purpose of the geometrical optics (GO) design of a compact range subreflector system is to establish the basic dimensions of the main reflector and subreflector, the size of the primary and secondary illuminating surfaces, the tilt angles of the subreflector and feed, an estimate for the feed beamwidth and an evaluation of the polarization characteristics. All of these issues are addressed in this chapter for a given reflector system.

4.1 EQUATIONS FOR GO FIELD COMPUTATIONS FOR A FOCUSSED SUBREFLECTOR SYSTEM

The GO field equations for a compact range subreflector system are presented in this section and they are related to the appropriate geometrical parameters. These equations allow one to model either an elliptic (Gregorian) or an hyperbolic (Cassegrain) subreflector system and evaluate the following:

- Field intensity, in amplitude and phase, for both vertical and horizontal polarization. Since the distance from the source to the field point is constant based on the focal properties of conics, the phase is known to be constant.

- Polarization ratio, for horizontal/vertical and vertical/horizontal components. The definition of cross-polarization is the third of Ludwig [8].

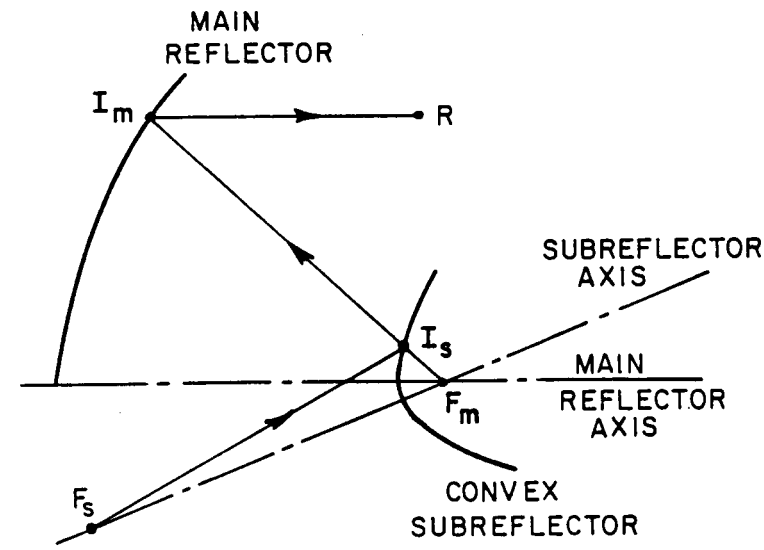

Figure 44: Convex subreflector.

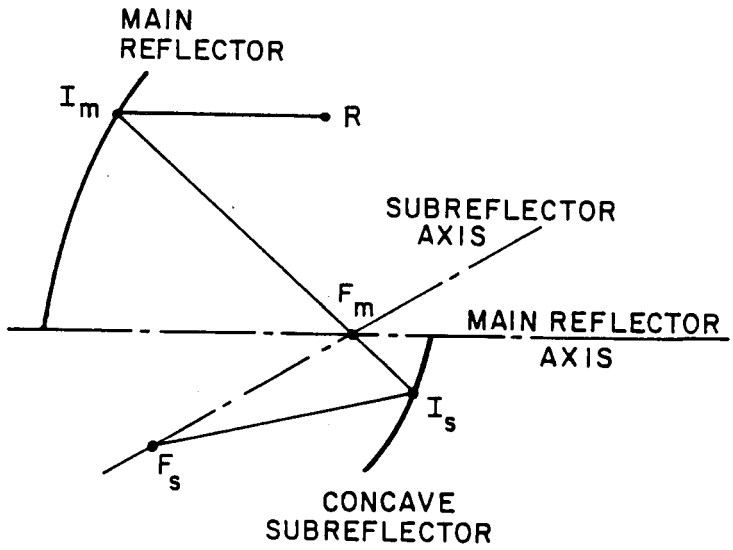

Figure 45: Concave subreflector.

In both subreflector cases, the field values or the polarization ratios are best computed on a rectangular grid in a plane perpendicular to the main reflector.

Three different sources are useful while modeling a subreflector system:

1) Uniform source having field horizontally or vertically polarized.

2) Huygens source, horizontally or vertically polarized (Section E).

3) Interpolated source, to model a real source through the interpolation of pattern values between an appropriate number of data points [15].

In most cases the uniform source is used to perform field computations, and the Huygens source to perform polarization computations, but it is convenient to be able to perform any computation with any source.

A simple ray-tracing technique can be used to perform the computations. Starting from the field point, R, a ray, ℓ, is traced all the way back to the source located at the focus of the subreflector, F_s (see Figures 44 and 45). Two coordinate systems are used. One is the main reflector coordinate system, $F_m(x_m, y_m, z_m)$, and the other is the subreflector coordinate system, $F_s(x_s, y_s, z_s)$. These coordinate systems are shown in Figure 26. The field point is $R \equiv (x_R, y_R, z_R)$ and the corresponding reflection point on the main reflector is I_m, which has coordinates (x_m, y_m, z_m) such that $x_m = x_R$, $y_m = y_R$ and z_m satisfies the equation of the reflecting surface. In other words, all the rays reflected from the parabola propagate in the z direction; consequently, one obtains that

$$x_m = x_R \tag{4.1}$$

$$y_m = y_R \tag{4.2}$$

$$z_m = \frac{1}{4f}\sqrt{x_m^2 + y_m^2} \tag{4.3}$$

where f is the focal length of the parabolic reflector.

The ray ℓ goes through the point I_m and the focal point, F_m. This part of the ray is called ℓ_m; while, the part between F_s and I_s is called ℓ_s. The reflection point on the subreflector I_s can be determined by intersecting ℓ_m with the subreflector itself. This is done as follows. The coordinates (x_m, y_m, z_m) of the point I_m are transformed from the main reflector coordinate system to the subreflector coordinate system, obtaining (x'_m, y'_m, z'_m). This can be accomplished through matrix multiplication, as follows [15]:

$$\begin{bmatrix} x'_m \\ y'_m \\ z'_m \end{bmatrix} = \begin{bmatrix} x'_V \\ y'_V \\ z'_V \end{bmatrix} + \mathbf{R}' \begin{bmatrix} x_m \\ y_m \\ z_m \end{bmatrix} \tag{4.4}$$

where the matrix $\mathbf{R}'$ represents a rotation around the y_m axis by the angle β

$$\mathbf{R}' = \begin{bmatrix} 1 & 0 & 0 \\ 0 & \cos\beta & \sin\beta \\ 0 & -\sin\beta & \cos\beta \end{bmatrix} \tag{4.5}$$

and the vector position of the point V, vertex of the parabolic reflector, in the subreflector coordinate system is given by

$$\begin{bmatrix} x'_V \\ y'_V \\ z'_V \end{bmatrix} = \begin{bmatrix} f\ \sin\beta \\ 0 \\ d_s - f\cos\beta \end{bmatrix}. \tag{4.6}$$

By knowing the points F_m and I_m, the equation of the ray ℓ_m can be determined (see Section B).

The radial distance from the focal point F_s to the reflection point I_s is defined by the polar equation of the subreflector such that

$$r_s = \frac{p_s}{1 - \epsilon_s \cos\theta_s} \tag{4.7}$$

where $F_s(r_s, \theta_s, \phi_s)$ is the spherical coordinate system corresponding to the cartesian subreflector coordinate system, $F_s(x_s, y_s, z_s)$. This description of a conical surface allows one to model an elliptical (Gregorian configuration) or a hyperbolical (Cassegrain configuration) subreflector with the same equation (see Section B).

The coordinates of $I_s \equiv (x_s^I, y_s^I, z_s^I)$ can then be determined through the equations of the ray and the equation of the subreflector. The straight line through the points F_s and I_s can be expressed in parametric form in terms of the distance parameter t of the current point on the line from any of the two points, F_s or I_s. A second order equation in t can be obtained from the equations of the coordinates of the line and the equation of the conic. This second order equation has two, one or no solutions, according to the number of intersection points. In the present case the point F_s is internal to the conic, hence the equation should always have two solutions. It is then necessary to discard the spurious solution and to retain the solution which corresponds to the physical subreflector. This can be done, for instance, by verifying if the angles θ_s, ϕ_s are inside a prescribed range. The solution is derived in detail in Section B.

Knowing the points I_m and I_s, the GO reflected field at R, $\mathbf{U}^r(R)$, can then be computed, where the notation $\mathbf{U}$ represents either the electric ($\mathbf{E}$) or magnetic ($\mathbf{H}$) field.

The following notation is introduced. Given two points, P and Q, the symbol $P - Q$ indicates the displacement vector starting at Q and ending at P, similarly $|P - Q|$ indicates the magnitude of the vector $P - Q$.

A source having unitary strength and a vector pattern function $\mathbf{PF}$ (function of the direction of radiation $\hat{\mathbf{s}}^i$) is considered here. The pattern function is discussed

in Section A, and the unit vector $\hat{\mathbf{s}}^i$ is given by

$$\hat{\mathbf{s}}^i = \frac{I_s - F_s}{|I_s - F_s|} \ . \tag{4.8}$$

Note that $\hat{\mathbf{s}}^i$ is the direction of propagation; i.e., the direction of the ray ℓ_s. The field incident at I_s, $\mathbf{U}^i(I_s)$, is then given by

$$\mathbf{U}^i(I_s) = \mathbf{PF}(\hat{\mathbf{s}}^i)\frac{e^{-jk|I_s - F_s|}}{|I_s - F_s|} \tag{4.9}$$

and the field reflected at I_s and evaluated at I_m is the field $\mathbf{U}^i(I_m)$ incident on the main reflector, and it is given by

$$\mathbf{U}^i(I_m) = \sqrt{\frac{\rho_1^r(I_s)}{\rho_1^r(I_s) + |I_m - I_s|}\,\frac{\rho_2^r(I_s)}{\rho_2^r(I_s) + |I_m - I_s|}}\ \mathbf{U}^i(I_s) \cdot \overline{\overline{\boldsymbol{R}}}(I_s)\, e^{-jk|I_m - I_s|} \ . \tag{4.10}$$

The reflection coefficient dyad $\overline{\overline{\boldsymbol{R}}}(I_s)$ is evaluated at I_s, and is given by (see Section D)

$$\overline{\overline{\boldsymbol{R}}} = R_{\|}\,\hat{\mathbf{e}}_{\|}^i\,\hat{\mathbf{e}}_{\|}^r + R_{\perp}\,\hat{\mathbf{e}}_{\perp}\,\hat{\mathbf{e}}_{\perp} \tag{4.11}$$

where (see Figure 46)

$$R_{\|} = 1 \ , \tag{4.12}$$

$$R_{\perp} = +1 \ , \qquad \text{if} \qquad \mathbf{U} = \mathbf{H} \tag{4.13}$$

$$R_{\perp} = -1 \ , \qquad \text{if} \qquad \mathbf{U} = \mathbf{E} \tag{4.14}$$

$$\hat{\mathbf{e}}_{\perp} = \frac{\hat{\mathbf{s}}^i \times \hat{\mathbf{n}}}{|\hat{\mathbf{s}}^i \times \hat{\mathbf{n}}|} \tag{4.15}$$

$$\hat{\mathbf{e}}_{\|}^i = \hat{\mathbf{s}}^i \times \hat{\mathbf{e}}_{\perp} \tag{4.16}$$

$$\hat{\mathbf{e}}_{\|}^r = \hat{\mathbf{s}}^r \times \hat{\mathbf{e}}_{\perp} \ , \text{and} \tag{4.17}$$

$$\hat{\mathbf{n}} = \frac{1}{\sqrt{1 + \epsilon_s^2 - 2\epsilon_s \cos\theta_s}}[\sin\theta_s(\cos\phi_s\,\hat{\mathbf{x}}_s + \sin\phi_s\,\hat{\mathbf{y}}_s) + (\cos\theta_s - \epsilon)\,\hat{\mathbf{z}}_s] \tag{4.18}$$

where θ_s and ϕ_s are the polar coordinates of I_s in the $F_s(r_s, \theta_s, \phi_s)$ coordinate system. The expression for $\hat{\mathbf{n}}$ is derived in Section C. The direction of the incident ray, $\hat{\mathbf{s}}^i$, is known, the direction of the reflected ray $\hat{\mathbf{s}}^r$ could be determined through the law of reflection such that

$$\hat{\mathbf{s}}^r = \hat{\mathbf{s}}^i - 2(\hat{\mathbf{s}}^i \cdot \hat{\mathbf{n}})\,\hat{\mathbf{n}} \tag{4.19}$$

but in the present case it is already known. The point of reflection and the vectors $\hat{\mathbf{s}}^i$ and $\hat{\mathbf{n}}$ define the plane of incidence.

The terms with the square root represent the spreading factors. The caustic distance ρ_1^r is the radius of curvature of the reflected wavefront in the plane of incidence. This plane contains the radius of curvature R_{c1} of the surface. The caustic distance ρ_2^r is the radius of curvature of the reflected wavefront in the plane normal to the plane of incidence. This plane contains the radius of curvature R_{c2} of the surface.

In the present case, an incident spherical wave is considered because the feed is modeled as a point source, and the plane of incidence coincides with one of the principal planes of the conical surface. The caustic distances are given by the equations

$$\rho_1^r = \frac{1}{s^i} + \frac{2}{R_{c1}\cos\theta^i} \tag{4.20}$$

$$\rho_2^r = \frac{1}{s^i} + \frac{2\cos\theta^i}{R_{c2}} \tag{4.21}$$

where s^i is the distance from the source (real or virtual) to the reflection point, and $\cos\theta^i$ is given by

$$\cos\theta^i = -\,\hat{\mathbf{s}}^i \cdot \hat{\mathbf{n}}\,. \tag{4.22}$$

where $\hat{\mathbf{n}}$ is the normal to the surface.

The spreading factors, the caustic distances (ρ_1^r and ρ_2^r) and the radii of curvature ($R_{c\,1}$ and $R_{c\,2}$) are evaluated at the reflection point, I_s, on the subreflector with the source at F_s.

The field $\mathbf{U}^r(R)$ reflected at I_m and evaluated at the field point R is given by

$$\mathbf{U}^r(R) = \sqrt{\frac{\rho_1^r(I_m)}{\rho_1^r(I_m)+|R-I_m|}\,\frac{\rho_2^r(I_m)}{\rho_2^r(I_m)+|R-I_m|}}\;\mathbf{U}^i(I_m)\cdot\overline{\overline{\boldsymbol{R}}}(I_m)e^{-jk|R-I_m|}\,. \tag{4.23}$$

The dyad, $\overline{\overline{\boldsymbol{R}}}(I_m)$, and the caustic distances are all evaluated at I_m with the (virtual) source at F_m. In fact, the two caustic points are coincident at F_m by the properties of the conics. Consequently, the field incident on I_m is a spherical wave, and it is still legitimate to use the Equations (4.20), (4.21) to compute the caustic distances.

In the present case, it is not necessary to compute the caustic distances of the reflected field in order to evaluate $\mathbf{U}^i(I_m)$ and $\mathbf{U}^r(R)$. For $\mathbf{U}^i(I_m)$, all the rays reflected from the subreflector converge to the focal point, F_m. By definition, then F_m is the caustic point for the field reflected from the subreflector (both caustics are at the same point); consequently, one finds that

$$\rho_1^r(I_s) = \rho_2^r(I_s) = \pm|I_s - F_m| \tag{4.24}$$

where the plus sign holds if the subreflector is convex, and the minus sign if it is concave (Figures 44 and 45).

Let $i = \{1,2\}$, then

- if the subreflector is convex (Figure 44), one obtains that

$$\rho_i^r(I_s) + |I_m - I_s| = |I_s - F_m| + |I_m - I_s| = |I_m - F_m|\,, \quad \text{or} \tag{4.25}$$

- if the subreflector is concave (Figure 45), one obtains instead

$$\rho_i^r(I_s) + |I_m - I_s| = -|I_s - F_m| + |I_m - I_s| = |I_m - F_m|\,. \tag{4.26}$$

In both cases, one finds that

$$\rho_i^r(I_s) + |I_m - I_s| = |I_m - F_m| \ . \tag{4.27}$$

Therefore, the expression for the spreading factor of the field reflected from the subreflector is given by

$$\sqrt{\frac{\rho_1^r(I_s)}{\rho_1^r(I_s) + |I_m - I_s|} \ \frac{\rho_2^r(I_s)}{\rho_2^r(I_s) + |I_m - I_s|}} = \pm \frac{|I_s - F_m|}{|I_m - F_m|} \tag{4.28}$$

where the plus sign holds if the subreflector is convex, and the minus sign if it is concave.

Again it is not necessary to compute the caustic distances in order to evaluate the field $\mathbf{U}^r(R)$ reflected from the parabola. In fact, it is known that, for a parabola, the focal points coincide at infinity, such that

$$\rho_i^r(I_m) = \infty \tag{4.29}$$

then

$$\sqrt{\frac{\rho_1^r(I_m)}{\rho_1^r(I_m) + |R - I_m|} \ \frac{\rho_2^r(I_m)}{\rho_2^r(I_m) + |R - I_m|}} = 1 \ . \tag{4.30}$$

In other words, the field, once reflected from the parabolic reflector, has no spreading attenuation; i.e., it is a plane wave.

Therefore, the following equation is obtained for the GO reflected field at the field point:

$$\begin{aligned} \mathbf{U}^r(R) \ = \ & \pm \mathbf{PF}(\hat{\mathbf{s}}^i) \cdot \overline{\overline{\mathbf{R}}}(I_s) \cdot \overline{\overline{\mathbf{R}}}(I_m) \ \frac{|I_s - F_m|}{|I_m - F_m| \ |I_s - F_s|} \\ & e^{-jk(|I_s - F_s| + |I_m - I_s| + |R - I_m|)} \end{aligned} \tag{4.31}$$

where the plus sign holds if the subreflector is convex, and the minus sign if it is concave.

The equations derived in this section allow one to write a numerical solution to perform computations of field strength and polarization ratios.

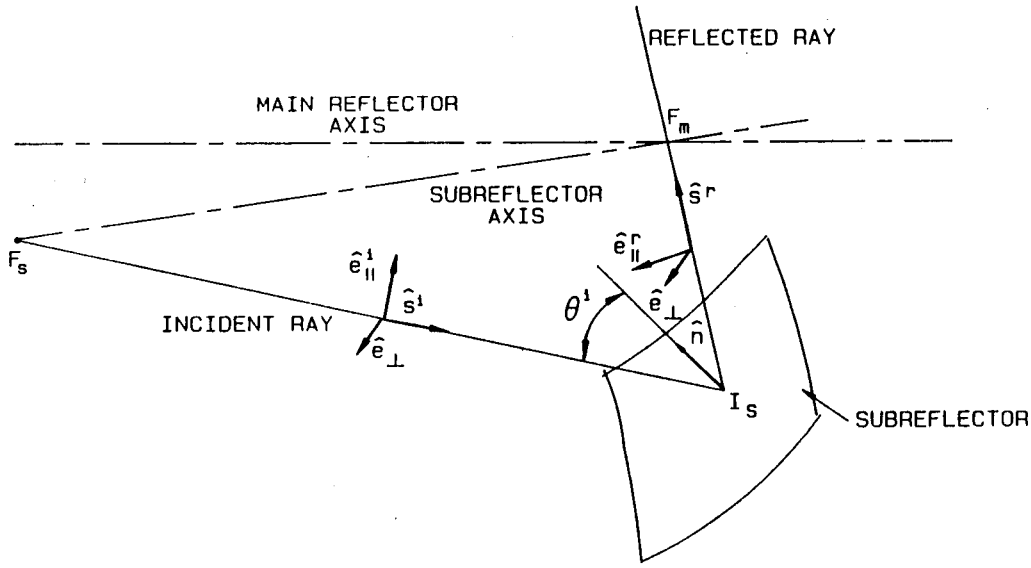

Figure 46: Geometry of the incident and reflected ray.

4.2 ITERATIVE DESIGN INITIAL VALUES

The geometrical parameters of this section are shown in Figure 47. The size of the target zone is determined by the size of the targets to be measured in the compact range, which must be defined in terms of the performance specifications required for the measurements. The first design step is to give an estimate of the focal length, f, of the main reflector. A value for the angle, χ_u, close to 90^o minimizes diffraction from the edges of the coupling aperture, and also makes its actual implementation easier. The beamwidth of the primary illuminating beam is estimated to be approximately 30^o; consequently, a value of χ_p close to 105^o is a good start. Let h_{pm} be the height (the x_m coordinate) of the intersection of the primary principal ray with the parabolic reflector. The gro (taper of the reflected field) and the cross-polarization are minimized if the principal ray of the feed, the equivalent axis (central ray) and the illuminating ray (ray corresponding to the axis of the target zone) all coincide, that is, if $\chi_p = \chi_i = \chi_c$. Under this hypothesis, one finds that $h_{tm} = h_{pm}$. Then, as shown by Dragone [9], it follows that

$$h_{tm} = 2f \cot\left(\frac{\chi_p}{2}\right) \tag{4.32}$$

where h_{tm} is the x_m coordinate of the intersection of the z_m axis of the target zone with the main reflector. There is some flexibility in choosing the height, h_{tm}, because the focal point, F_m, must be at the floor level of the anechoic chamber, but the axis of the target zone can be moved up or down one foot or so. A first estimate of h_{tm} can be made by common sense, then Equation (4.32) and the previous considerations suggest a first choice of f and χ_p.

The eccentricity of the subreflector can be estimated as follows. The specifications on the compact range performance dictate the amount of admissible gro. By

using a numerical solution in the single reflector configuration and with a uniform source it is possible to determine by a trial and error procedure an equivalent focal length f_e of an equivalent parabolic reflector with the desired gro. Notice that a choice of f_e determines the beamwidth of the feed. Once f_e has been estimated, the corresponding eccentricity of the elliptical subreflector, ϵ_s, can be computed by solving the following equation:

$$f_e = M(\beta_c = 0)\, f = m\, f = \frac{1+\epsilon_s}{1-\epsilon_s}\, f \tag{4.33}$$

and obtaining

$$\epsilon_s = \frac{f_e - f}{f_e + f}\,. \tag{4.34}$$

In fact, it is not possible to use the expression for the magnification factor M given by

$$M = \frac{1-\epsilon_s^2}{1+\epsilon_s^2 - 2\epsilon_s \cos\beta_c} \tag{4.35}$$

since the tilt angle, β_c, still needs to be determined. Initially, the angle β_c can be set to zero in that β_c will be small which makes this a good approximation.

A second parameter is necessary to determine the subreflector, for instance, the interfocii distance, d_s. Its choice is suggested by the following considerations:

- There must be a minimum separation between the focii of the subreflector, F_s and F_m. If they are too close, some of the energy is reflected back from the subreflector into the feed, the minor lobes of the feed antenna might radiate through the coupling aperture into the upper chamber or cause strong diffraction by illuminating the edges of the coupling aperture with a strong signal without much space attenuation.

- The size of the secondary illuminating surface cannot be made too small for mechanical reasons: the system acts as a lens; consequently, the mechanical

tolerances on the subreflector are even more strict than those on the main reflector.

- The subreflector must be in the far field of the feed, giving a minimum distance between the feed and subreflector.

- It is shown (see Section 3.2, Figure 47) that the following relationships must be satisfied:

$$h_{pc} = -d_s \sin\beta \text{ , and} \tag{4.36}$$

$$l_{pc} = d_s \cos\beta \tag{4.37}$$

where h_{pc} is the vertical (i.e., in the x_m direction) distance from the phase center of the feed (i.e., the focus F_s of the subreflector) to the ceiling of the lower chamber, and l_{pc} is the horizontal (i.e., in the z_m direction) distance of the phase center of the feed from the focus, F_m, of the main reflector. Equation (4.36) gives a minimum value for the product $d_s \sin\beta$, and β should be small, in order to make the magnification factor M close to its maximum, minimizing in turn the gro; consequently, d_s should be made large, in order to keep the product equal to or larger than its minimum value. On the other hand, it is desirable that the upper and lower room have a common wall. For this purpose the choice of

$$l_{pc} = f \tag{4.38}$$

appears very reasonable, then Equation (4.37) shows that d_s cannot be made too large. In any case, one finds that

$$d_s \leq f \text{ .} \tag{4.39}$$

These considerations suggest an estimate for the distance between focii, d_s, thus, completing the estimate for the parameters of the subreflector.

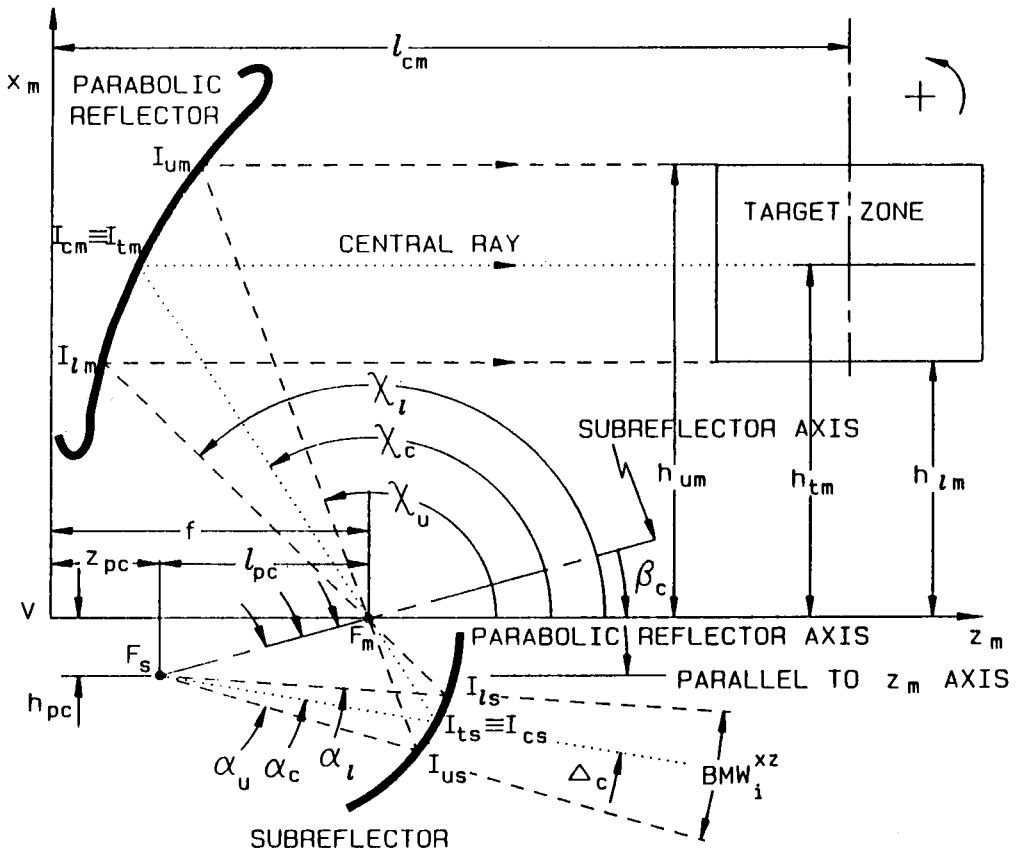

Figure 47: Geometrical quantities defining the subreflector system design

4.3 ITERATIVE DESIGN VIA GO COMPUTATIONS

The previous estimate of the geometric parameters of the subreflector system must be refined to give an initial GO design. A sequence of operations to achieve a GO design for a Huygens source by the use of a numerical solution can be devised as follows.

- Input the geometry of the reflector and subreflector, enter the estimates of the Huygens source tilt angle, α, and the subreflector axis tilt angle, β, as previously computed from the angle, χ_p, of the primary principal ray.

- Check if the overall taper error of the reflected field is satisfactory. Eventually the height, h_{tm}, of the z_m axis of the target zone can be adjusted somewhat corresponding to the center of the surface having a satisfactory taper error. If the taper error is not satisfactory, find a new value of the tilt angle of the feed axis α to satisfy the requirement on the overall taper error.

- Check if the cross-polarization, although no longer zero, is still satisfactorily small.

- If not, try a value of the tilt angle of the feed axis α intermediate between the previous two cases.

- Check if the overall taper error and cross-polarization performance are satisfactory.

- If any or both of the two is not satisfactory, change the subreflector axis tilt angle, β.

- Compute the corresponding angle α to achieve zero cross-polarization.

- Check if the angle χ_p is close to 105^o. This angle can be computed through the equation:

$$\chi = \pi - \beta + \arctan\left[\frac{(1+\epsilon_s^2)\cos\alpha - 2\epsilon_s}{(1-\epsilon_s^2)\sin\alpha}\right] . \tag{4.40}$$

  which holds for any angle χ in terms of the corresponding angles α and β. It might be very difficult to make this angle equal to 105^o through this iterative approach; consequently, this condition is relaxed by assuming χ_p to be between 110^o and 120^o.

- Start again if χ_p is not between 110^o and 120^o.

Since this is a trial-and-error approach, the values of χ_p, α and β are close but not exactly equal to χ_c, α_c and β_c, the tilt angles corresponding to the central ray. The changes of values in reiterating the previous sequence should be small, so that the broad requirements of Section 4.2 are still met. If the requirements cannot be met satisfactorily with the chosen geometry, it is necessary to change the parameter, d_s, and begin the design sequence again. This last parameter in fact allows some flexibility in the design.

It is necessary, once a design has been achieved, to verify that the cross-polarization values are not too sensitive to small changes of the angles α and β, as it has been found in some cases. If this happens for several combinations of α and β satisfying Equation (3.10), it might be necessary to change the distance between the focii, d_s, and to go through all the previous steps.

If possible, it is advisable to model the actual source's polarization and amplitude to see if the performance with the actual source is satisfactory at this point in the design.

The design obtained in this way is still a first-cut configuration. A more complete and accurate model of the system is necessary to evaluate how other factors

(like diffraction) affect the total field in the target zone. It might be necessary then to modify the values of the GO design according to the indications of the more complete model, but all the previous requirements still have to be satisfied.

Once all the parameters of the reflector and subreflector are determined, the projection of the target zone on the main reflector determines the primary illuminating surface. This projection is made with rays parallel to the main reflector axis. The secondary illuminating surface in turn is defined by projecting the primary illuminating surface from the main reflector on the subreflector with rays through the focus F_m which is in common to the reflector and subreflector. The primary and secondary illuminating surfaces give a first indication on the physical sizes of main reflector and subreflector.

4.4 ITERATIVE DESIGN SUMMARY

In summary, it has been shown that several of the design requirements for a compact range, although not related to the GO field, must be taken into account to obtain a good GO design. It is impossible to make a clear cut separation and relate each design parameter to one and only one requirement, but the following guidelines can be established for a Gregorian system with a parabolic reflector and concave elliptical subreflector:

- The choice of the focal length, f, of the main reflector is dictated both by a choice of the height, h_{tm}, to the center of the target zone and by a choice of χ_u, the angle of the upper illuminating ray with the main reflector axis, which should be close to 90^o. This in turn defines χ_p to be close to 105^o, since the beamwidth of the primary illuminating beam is assumed to be close to 30^o.

- The geometric taper requirement is satisfied through the choice of the axial magnification factor m, and the choice of m, in turn, determines the eccentricity, ϵ_s, of the subreflector.

- The second parameter of the subreflector (the interfocii distance d_s) is determined by the necessity of keeping a minimum distance between the feed and the coupling aperture, of having the subreflector in the far field of the feed, of having a minimum size of the subreflector, and of making the null of the cross-polarized field as insensitive as possible to small changes of the angles α and β. Recall that α is the angle from the subreflector axis to the secondary principal ray of the source, and β is the angle from the subreflector axis to the main reflector axis. Then, the following relationships are obtained:

$$h_{pc} = -d_s \sin\beta \tag{4.41}$$

$$l_{pc} = d_s \cos\beta \tag{4.42}$$

where

$$l_{pc} \leq f \ . \tag{4.43}$$

These equations suggest a value of d_s close but smaller than f.

- The choice of χ_p determines either α or β.

- The cross-polarization requirement determines the second one (β or α).

- The beamwidth of the feed BMW_i^{xz} is determined through the angles α_u and α_l.

Consequently, reflector and subreflector, tilt angles of feed and subreflector, beamwidth and cross-polarization characteristics of the feed, and primary and secondary illuminating surfaces are determined.

4.5 ITERATIVE DESIGN EXAMPLE

In this section, a design example is given to show how to use the principles just discussed to effectively satisfy the design specifications of a compact range such as shown in Figure 9.

The desired target zone has a rectangular cross section having a vertical height of $6'$ and a horizontal length of $8'$. By setting the lower line delimiting the primary illuminating surface at $5.5'$, allowance is made for the lower rolled edge. This in turn sets the height, h_{tm}, of the center of the rectangular target plane-sections at $8.5'$, and the upper line delimiting the primary illuminating surface at $11.5'$.

The following relationship relates the angle from the main reflector axis to the primary principal ray, χ_p, to the focal distance, f:

$$h_{pm} = 2f \cot\left(\frac{\chi_p}{2}\right) . \tag{4.44}$$

The value $\chi_p = 120^o$ is chosen, then a value for f is obtained

$$f = \frac{1}{2}\frac{8.5'}{\cot(60^o)} = 7.36' \tag{4.45}$$

and $f = 7.25'$ is chosen.

Through the use of a numerical solution in the single reflector mode with a uniform source, it was found that a value of f_e of $26.5'$ gives an acceptable value ($< .1$ dB) for the geometric taper. The values of the field strength are shown in Figure 48. The field is computed on a target plane-section. The field strength is normalized to its maximum, and the values are given in dB. For convenience, the values are given on one side only of the target plane-section, because symmetry holds.

From the value of the focal length the eccentricity of the subreflector is determined. In fact, the axial magnification, m, is given initially by

$$m \cong f_e/f = 26.5'/7.25' = 3.662 \tag{4.46}$$

because, for small β, one obtains

$$m \cong M \ . \tag{4.47}$$

Then, ϵ_s can be determined from the following equation:

$$m = \frac{1+\epsilon_s}{1-\epsilon_s} \tag{4.48}$$

which can be solved for ϵ_s

$$\epsilon_s = \frac{m-1}{m+1} \tag{4.49}$$

then

$$\epsilon_s = \frac{3.66-1}{3.66+1} = 0.5708 \ . \tag{4.50}$$

The distance between the focii is then chosen such that $d_s = 6'$, which is close, but smaller than $f = 7.25'$.

The semiaxes, a and b, of the elliptical subreflector are determined as follows. Since $2c = d_s$ then $c = 3'$. Also, one finds that

$$\epsilon_s = \frac{c}{a} \tag{4.51}$$

consequently

$$a = \frac{c}{\epsilon_s} \ . \tag{4.52}$$

This gives

$$a = \frac{3'}{.571} = 5.25' \ . \tag{4.53}$$

Since $c^2 = a^2 - b^2$, then $b^2 = a^2 - c^2$ and b can be computed such that

$$b = \sqrt{(5.25')^2 - (3')^2} = 4.308' \ . \tag{4.54}$$

The parameter p is also computed through the following relationship:

$$p = a(1 - \epsilon^2) \tag{4.55}$$

then

$$p = 5.25'(1 - 0.5708^2) = 3.539' \ . \tag{4.56}$$

The tilt angles, α and β, are determined through the trial and error procedure already described. The following values are then obtained:

$$\beta = -5.5^o \qquad \text{and} \qquad \alpha = -19.95^o \ . \tag{4.57}$$

The values of χ_u and χ_l are computed through the following equation:

$$\chi = 2 \arctan\left(\frac{2f}{h}\right) \tag{4.58}$$

and one obtains

$$\chi_u = 2 \arctan\left(\frac{2 \times 7.25'}{11.5'}\right) = 103.164^o \tag{4.59}$$

and

$$\chi_l = 2 \arctan\left(\frac{2 \times 7.25'}{5.5'}\right) = 138.454^o \ . \tag{4.60}$$

The beamwidth BMW^{xz}_{max} (Section 3.7.1) is given by

$$BMW^{xz}_{max} = 2\,(\beta - \alpha) \tag{4.61}$$

such that one obtains

$$BMW^{xz}_{max} = 2(-5.5^o + 19.95^o) = 28.9^o \ . \tag{4.62}$$

Then, the values of h_{pc} and l_{pc} can be obtained by

$$h_{pc} = -6' \times \sin(-5.5^o) = 0.575' \tag{4.63}$$

and

$$l_{pc} = 6' \times \cos(-5.5^o) = 5.972' \tag{4.64}$$

which are satisfactory, while the coordinate z_{pc} of the phase center in the x_m, y_m, z_m coordinate system is

$$z_{pc} = f - l_{pc} = 7.25' - 5.972' = 1.278' \ . \tag{4.65}$$

The actual magnification factor can now be computed through the following expression:

$$M = \frac{1 - \epsilon_s^2}{1 + \epsilon_s^2 - 2\epsilon_s \cos\beta} \tag{4.66}$$

which gives

$$M = \frac{1 - 0.571^2}{1 + 0.571^2 - 2 \times 0.571 \cos(-5.5^o)} = 3.5583 \tag{4.67}$$

which is close to the value of the axial magnification factor, $m = 3.662$.

Through the use of a numerical solution in the subreflector system mode with a Huygens source it can be checked if the total reflected field taper is acceptable. The field is computed on a target plane-section (defined in Appendix G). The computed values are given in Figure 49. As before, the field strength is normalized to its maximum, the values are given in dB and on one side only of the section of the target zone, because symmetry holds. The total taper error is still acceptable, since it is less then 0.2 dB.

The angles α_u and α_l (defined in Section 3.7.4) are obtained through the following equation (see Section F):

$$\alpha = -\arctan\left[\frac{(1 - \epsilon_s^2)\sin(\chi + \beta)}{2\epsilon_s - (1 + \epsilon_s^2)\cos(\chi + \beta)}\right] \tag{4.68}$$

which gives

$$\alpha_u = -\arctan\left[\frac{(1 - 0.5708^2)\sin(103.164^o - 5.5^o)}{2 \times 0.5708 - (1 + 0.5708^2)\cos(103.164^o + -5.5^o)}\right] \tag{4.69}$$

and

$$\alpha_l = -\arctan\left[\frac{(1-0.5708^2)\sin(138.454^o - 5.5^o)}{2\times 0.5708 - (1+0.5708^2)\cos(138.454^o - 5.5^o)}\right] \quad (4.70)$$

The beamwidth is given by

$$BMW_i^{xz} = \alpha_l - \alpha_u \quad (4.71)$$

such that

$$BMW_i^{xz} = -13.5654318^o + 26.87557^o = 13.3101382^o\ . \quad (4.72)$$

As a summary, the given design quantities are as follows:

$$h_{tm} = 8.5' \quad (4.73)$$

$$h_{um} = 11.5' \quad (4.74)$$

$$h_{lm} = 6' \quad (4.75)$$

$$Y = 8'\ , \qquad \text{and} \quad (4.76)$$

$$\chi_p = 120.0^o \quad (4.77)$$

where Y is the amplitude of the target zone in the y_m direction. The resulting quantities for this design (called design ID) are shown in Table 2 (see Figure 47) together with the given quantities.

Y coord	4.00	3.00	2.00	1.00	0.00
X coord					
11.50	-0.08	-0.06	-0.04	-0.04	-0.03
10.50	-0.07	-0.04	-0.03	-0.02	-0.01
9.50	-0.06	-0.03	-0.02	-0.01	0.00
8.50	-0.05	-0.03	-0.01	0.00	0.00
7.50	-0.05	-0.03	-0.02	-0.01	0.00
6.50	-0.06	-0.04	-0.02	-0.01	-0.01
5.50	-0.08	-0.06	-0.04	-0.03	-0.03

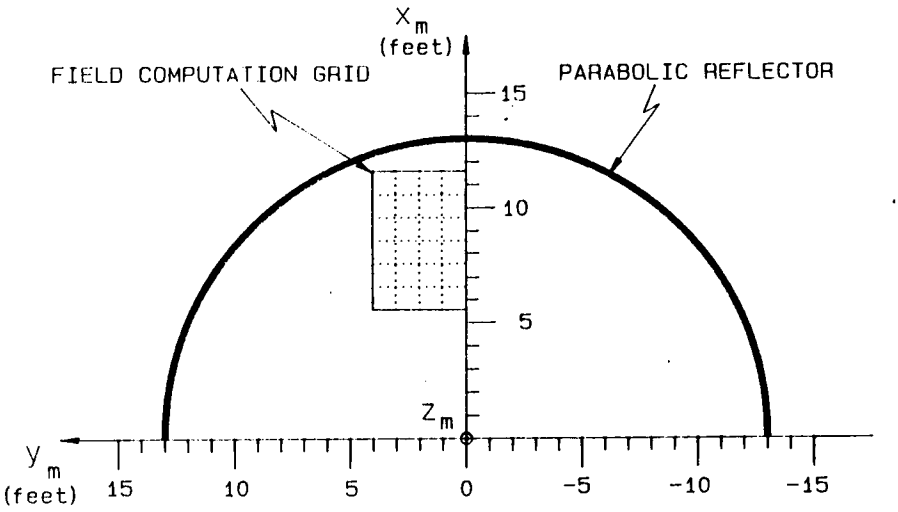

Figure 48: Values of the GO reflected field for the equivalent reflector with uniform source. Linear dimensions are in feet.

Y coord	4.00	3.00	2.00	1.00	0.00
X coord					
11.50	-0.17	-0.12	-0.09	-0.07	-0.06
10.50	-0.13	-0.09	-0.06	-0.04	-0.03
9.50	-0.11	-0.07	-0.03	-0.01	-0.01
8.50	-0.10	-0.06	-0.03	-0.01	0.00
7.50	-0.11	-0.06	-0.03	-0.01	0.00
6.50	-0.13	-0.08	-0.05	-0.03	-0.02
5.50	-0.16	-0.11	-0.08	-0.06	-0.05

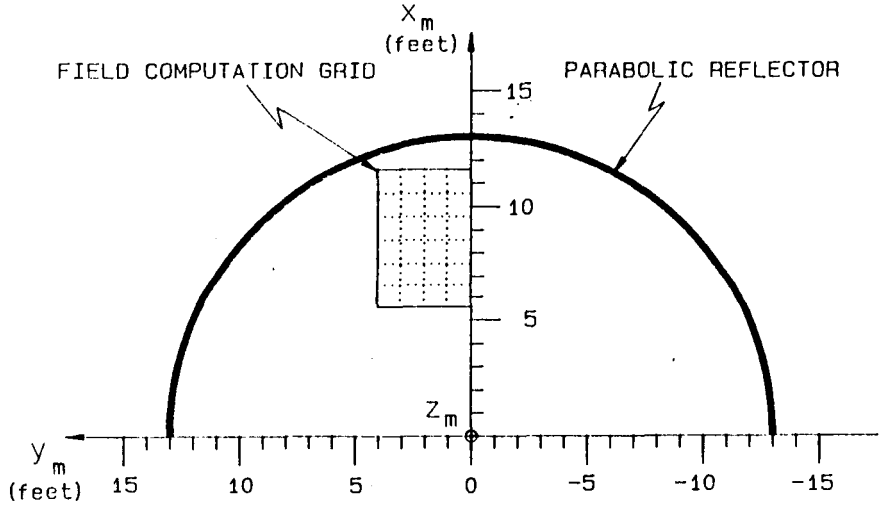

Figure 49: Values of the GO reflected field for the subreflector system with a Huygens source. Linear dimensions are in feet.

Table 2: Design parameters for design ID

$h_{pc} = 0.575'$	$z_{pc} = 1.278'$	$h_{um} = 11.5'$
$h_{lm} = 5.5'$	$\chi_p = 119.24^o$	$Y = 8.0'$
$\alpha = -19.95^o$	$\beta = -5.5^o$	$\Delta = 14.45^o$
$\alpha_u = -26.875^o$	$\alpha_l = -13.565^o$	$\chi_u = 103.164^o$
$\chi_l = 138.454^o$	$\Delta t = 10.248$ ns	$BMW^{xz}_{max} = 28.9^o$
$BMW^{xz}_{i} = 13.31^o$	$f = 7.25'$	$\epsilon_s = 0.5708$
$d_s = 6.0'$	$p_s = 3.639'$	$m = 3.662$
$M = 3.5583$	$\text{gro}_{dB} = -0.0819$ dB	

CHAPTER V

DIRECT DESIGN THEORY

5.1 INTRODUCTION

Four design procedures are derived in this chapter to perform the GO design of the dual chamber compact range. These procedures use the geometrical and electrical requirements to obtain an uniquely defined compact range reflector system. Three of the design procedures assume that the quantity z_{pc} (see Figure 50) is set to zero (see Figure 51) in order to obtain more simple equations. In the fourth design procedure instead z_{pc} can assume any value. Any of the first three design procedures then can be used to obtain an initial estimate of the design, which is then refined through the fourth procedure.

5.1.1 GEOMETRICAL CONSTRAINTS

In this section some relations between the geometrical quantities of the compact range are established.

Since the zero cross-polarization condition is enforced, the angles α, β and χ are denoted as α_c, β_c and χ_c. The angle α is the tilt angle of the feed axis with respect to the subreflector axis, β is the tilt angle of the subreflector axis with respect to the main reflector axis, and χ is the angle of the corresponding primary ray with the main reflector axis.

It has been established (see Section 4.2) that

$$\frac{h_{tm}}{2f} = \cot\left(\frac{\chi_c}{2}\right) . \tag{5.1}$$

The height h_{tm} is the vertical coordinate (x_m coordinate) of the intersection of a line parallel to the main reflector axis and through the center of the target zone with the parabolic reflector. This line presently coincides with the central ray. The angle χ_c is the corresponding angle of the primary central ray with the main reflector axis. Two different arrangements for the upper chamber have been adopted.

The first arrangement has been adopted for the "iterative" design. In this design the absorber layer has been equally divided between the two rooms, the mid plane of the absorber corresponds to the plane $x_m = 0$. The equations for this arrangement are the same as the equations for the second arrangement with $h_a = 0$. This arrangement is shown in Figure 52.

The second arrangement is adopted instead for the new design, and is shown in Figure 53. The absorber layer which separates the upper and lower chamber is set all in the upper chamber, in other words, the lower x_m coordinate of the absorber layer is zero. The absorber thickness is denoted by h_a. Then the total height of the upper chamber is given by $h_a + h$, where h represents the height of the upper chamber from the "floor" of the absorber layer. The actual floor of the upper chamber is a plane coincident with the ceiling of the lower chamber and is set to $x_m = 0$. The height h of the upper chamber is, in first approximation, divided as follows:

- $h/3$ = height of the target zone = height of the primary illuminating surface on the main reflector,
- $h/6$ = height of each of the two rolled edges,

- $h/6$ = vertical distance between the top of the upper rolled edge and the ceiling of the upper chamber, and
- $h/6$ = vertical distance between the bottom of the lower rolled edge and the "floor" of the absorber layer.

In this fashion, the central ray after reflection from the main reflector, the z_m axis of the target zone and the z_m axis of the upper chamber all coincide such that

$$h_{tm} = \frac{h}{2} + h_a \ . \tag{5.2}$$

This way to dimension the target zone and the room is common to all procedures, and Equation (5.1) holds for any value z_{pm}.

The following geometrical relationships have been established (Figure 50)

$$h_{pc} = -d_s \sin\beta_c \tag{5.3}$$

$$l_{pc} = d_s \cos\beta_c \ , \text{ and} \tag{5.4}$$

$$f = d_s \cos\beta_c + z_{pc} = l_{pc} + z_{pc} \ . \tag{5.5}$$

The phase center of the feed antenna has x_m, y_m, z_m coordinates given by (h_{pc}, 0, z_{pc}). The quantity h_{pc} is the vertical (in the x_m direction) distance from the phase center of the feed to the ceiling of the lower chamber, it must be greater than a minimum value to take into account the physical size of the feed, its mechanical support and the electrical connections. The quantity l_{pc} is the horizontal (in the z_m direction) distance of the phase center of the feed from the focus F_m of the main reflector. The quantity d_s is the distance between the focii of the subreflector. It should be as large as possible to achieve the maximum decoupling between the feed and the edges of the subreflector as well as the coupling aperture, and to avoid spill-over of the feed into the target zone through the coupling aperture.

On the other hand, it is desirable that both chambers have a wall in common in order to achieve an optimal layout of the upper and lower rooms. In order to satisfy these two contrasting requirements the choice $l_{pc} = f$ appears to be very appealing, but it has been found that this choice does not optimize the remaining parameters of the compact range. On the other side, the choice $l_{pc} = f$ simplifies the mathematics necessary to derive some design procedures. Then, at present, it is assumed that $l_{pc} = f$ (which corresponds to $z_{pc} = 0$), as shown in Figure 51, for three design procedures, while the more general case is treated later for the fourth procedure. The following relationship is obtained by taking the ratio of Equations (5.3) and (5.4) such that

$$\frac{h_{pc}}{f} = -\tan\beta_c \ . \tag{5.6}$$

By taking the ratio of Equations (5.6) and (5.1) the focal distance f can be eliminated, and one obtains

$$\frac{2h_{pc}}{h_{tm}} = -\tan\beta_c \tan\left(\frac{\chi_c}{2}\right) \ . \tag{5.7}$$

This equation expresses the geometrical constraints on the design, holds only for $z_{pm} = 0$ and is used in the first, second and third design procedures.

5.1.2 ELECTRICAL CONSTRAINTS

In this section the electrical constraints for the GO design are expressed through some equations, which hold for any value of z_{pm} and are common to all four design procedures.

The minimum admissible geometric taper error, gro_{min}, is a part of the specifications of the compact range. From Equation (G.41) of Section G, the corresponding minimum focal length for the main reflector is

$$f_{min} = \frac{\rho_d}{2M}\sqrt{\frac{\mathrm{gro}_{min}}{1-\mathrm{gro}_{min}}} \tag{5.8}$$

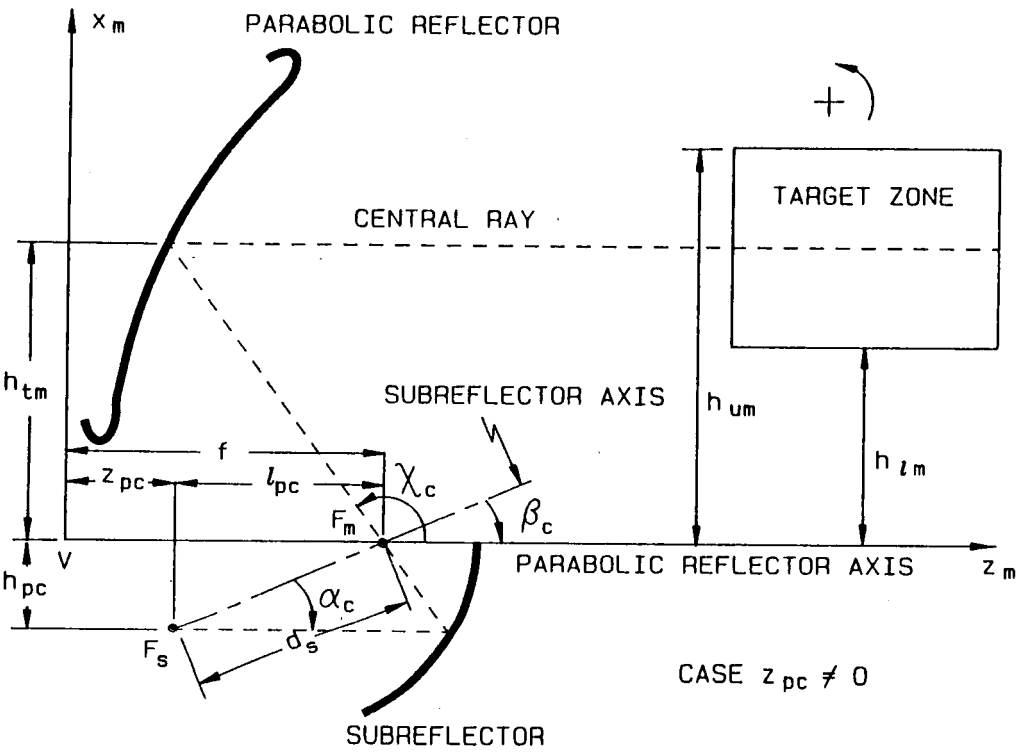

Figure 50: Geometry for Equations (5.1), (5.3), (5.4) and (5.5) ($z_{pc} \neq 0$).

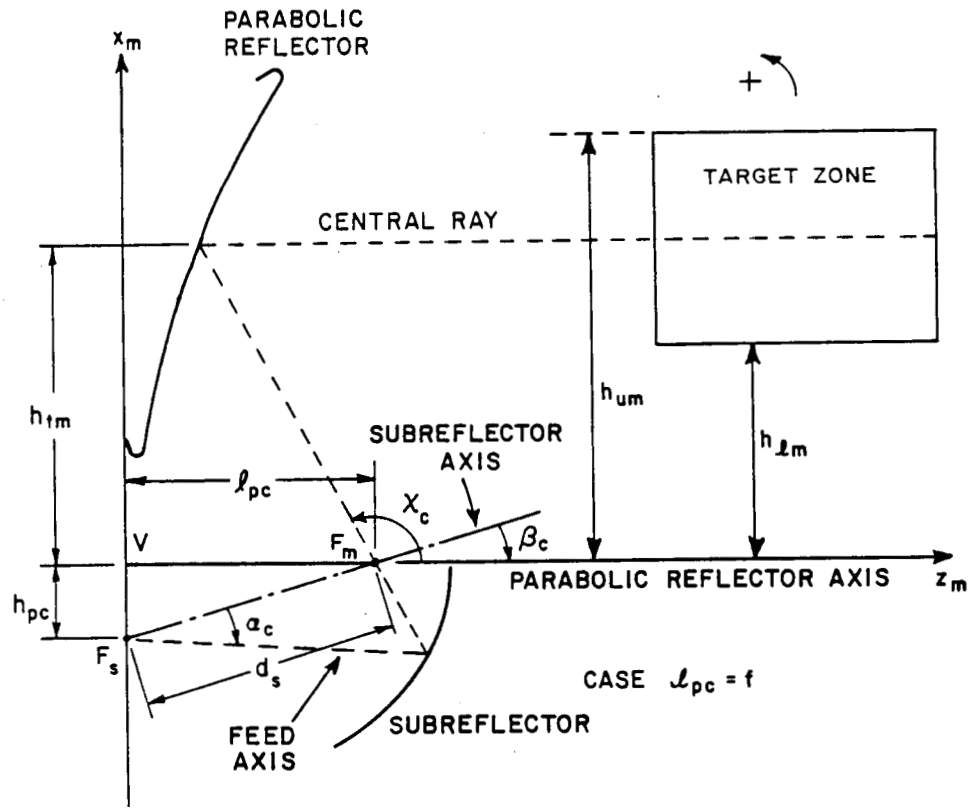

Figure 51: Geometry for Equations (5.1), (5.3), (5.4), and (5.5) ($z_{pc} = 0$).

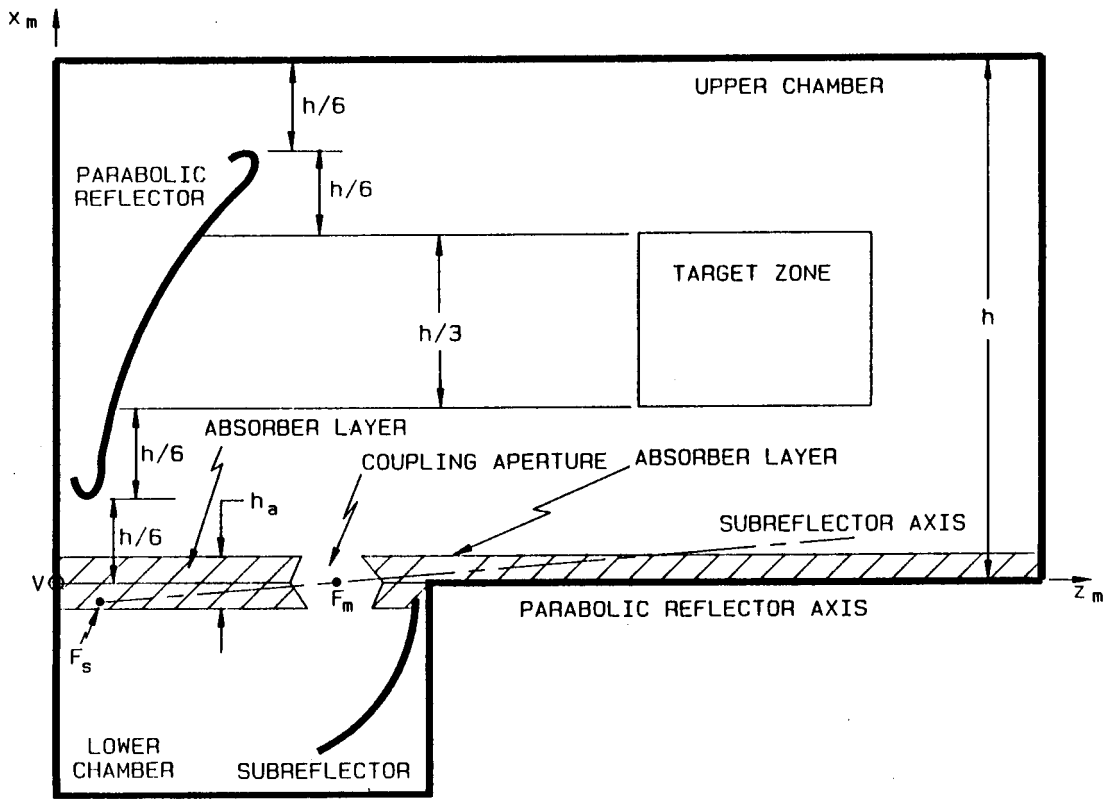

Figure 52: Vertical dimensions of compact range upper room for the "iterative design" arrangement.

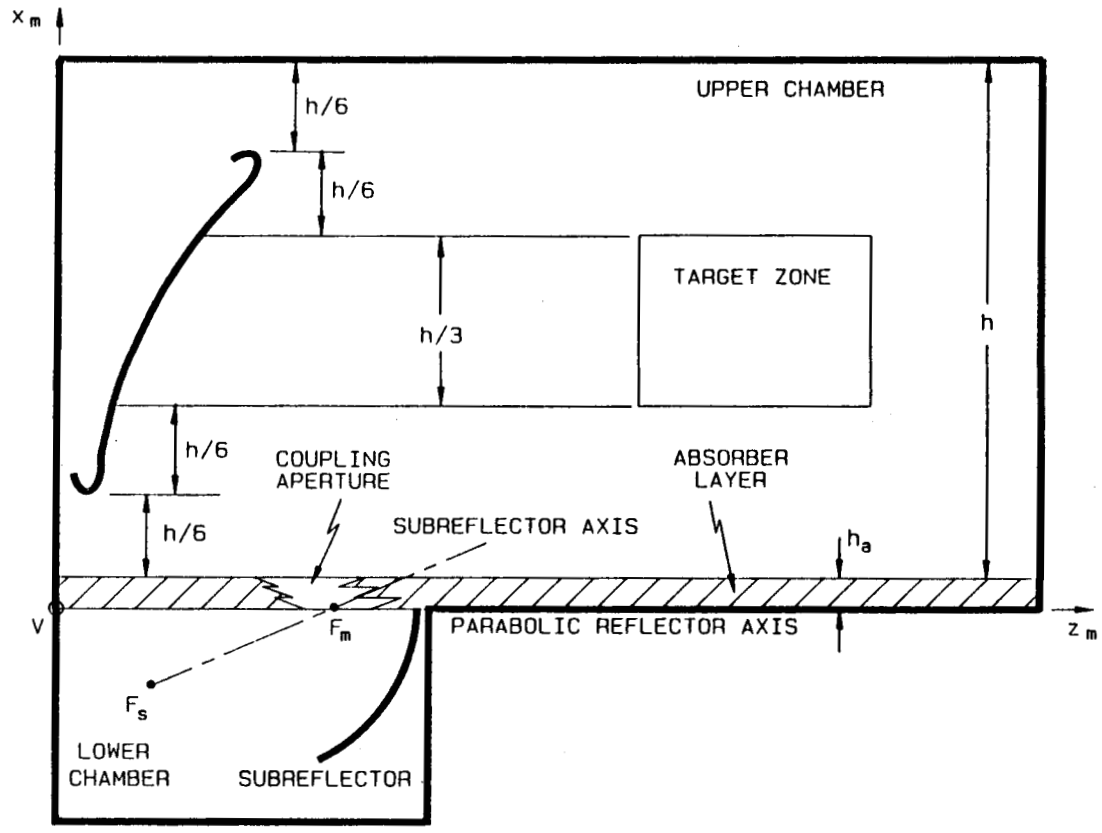

Figure 53: Vertical dimensions of compact range upper room for the new design FD.

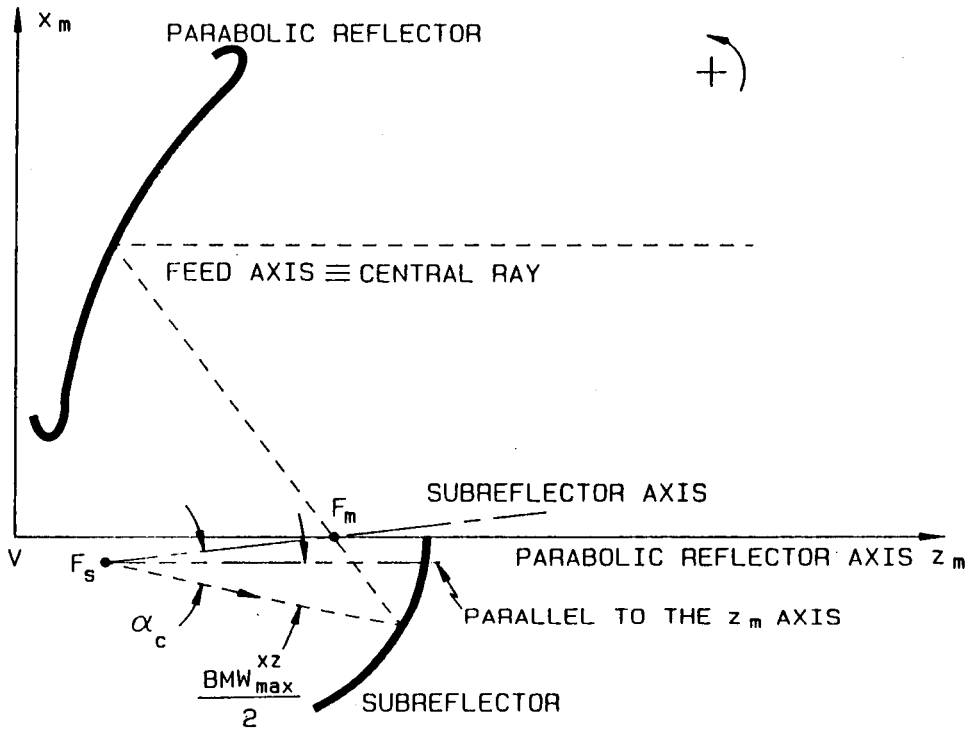

Figure 54: Condition on α_c and β_c to avoid diffraction from coupling aperture.

where ρ_d is the length of the semidiagonal of the rectangular target zone cross-section. On the other hand, M is a function of ϵ_s, still to be determined, then f_{min} is also a function of ϵ_s. Then, any $f \geq f_{min}$ satisfies the taper requirements for the reflected field. Then, in the first design procedure it has been set such that $f \doteq f_{min}$ and therefore gro = gro_{min} is obtained. In the remaining design procedures instead it is necessary to verify if the gro obtained from the design satisfies the gro_{min} requirement.

The pattern behaviour of the feed is characterized through two beamwidths, BMW^{xz} and BMW_i^{xz}, which correspond to two different requirements that the feed must satisfy.

The beamwidth, BMW^{xz}, is defined (Section 3.2) with reference to the angles at which the pattern intensity of the feed becomes smaller than a given value X in dB, where X is an appropriate small value obtained from diffraction considerations in that the feed illuminates the coupling aperture. This illumination of the coupling aperture by the feed is a very undesirable effect for two reasons. For certain angles, there could be a direct illumination of the target zone by the feed. This is undesirable, but can be time-gated. The second and more important reason is that, through the lower portion of its main lobe or its side lobes, the feed illuminates the edges of the coupling aperture, with subsequent diffraction by the edges themselves. Some of the diffracted rays are reflected by the main reflector into the target zone, and cannot be time-gated. Consequently, in order to reduce this diffraction to a minimum, the field incident on the target zone must be minimized. The appropriate value for the quantity X is determined through diffraction considerations and is not discussed here. Since in actuality the coupling aperture is an extended surface and not a point, it is not easy to define exactly the beamwidth, BMW_{max}^{xz}, as the maximum acceptable value of BMW^{xz}. Two

possible definitions are considered here, although, these are not the only ones possible. In actuality, one should consider in detail the field incident on the edge of the coupling aperture and perform a diffraction computation in order to verify if the level of the sidelobes of the feed considered is acceptable. The quantity BMW^{xz}_{max} is only a first cut parameter to help in the design of the feed.

One could define BMW^{xz}_{max} with reference to the central point of the coupling aperture; i.e., with respect to F_m. In this case, one would set $BMW^{xz}_{max} = 2|\alpha_c|$.

It seems instead a more conservative approach to define BMW^{xz}_{max} with respect to the parallel to the main reflector axis through the phase center of the feed (i.e., the focus of the subreflector, F_s). In this case, the following inequality must be satisfied to avoid a strong illumination of the edges of the coupling aperture (see Figure 54):

$$\frac{BMW^{xz}_{max}}{2} = \alpha_c - \beta_c \geq \frac{BMW^{xz}}{2} \ . \tag{5.9}$$

This is the definition used in the design procedures presently discussed. The second design procedure is then obtained by letting

$$\frac{BMW^{xz}_{max}}{2} = \alpha_c - \beta_c = \frac{BMW^{xz}}{2} \tag{5.10}$$

and by computing accordingly the design parameters.

A second requisite on the feed is that it must illuminate uniformly (or with some suitable roll-off correction) the target zone, and BMW^{xz}_i is the secondary illuminating beamwidth defined in Section 3.2. This beamwidth is equal to the angle subtended at the focal point F_s by the secondary illuminating surface in the x, z plane (see Figure 55). The third design procedure is then obtained by enforcing the requirement that this beamwidth corresponds to the target zone through the reflections from the subreflector and the main reflector, and by computing the design parameters accordingly.

From the previous constraints then, together with the zero cross-polarization condition, it is possible to obtain four design procedures, which are summarized here.

5.1.3 FIRST DESIGN PROCEDURE (METHOD 1)

The quantities h_{pc}, h_{um}, h_{lm}, ρ_d, and gro_{min} are specified in this design procedure, and z_{pc} is set to zero. The following parameters are computed: BMW^{xz}_{max}, α_c, β_c, χ_c, f, ϵ_s, d_s, M, m, and BMW^{xz}_i. In this procedure, gro_{min} (the minimum admissible taper of the reflected field) is an input, and a value of the feed beamwidth, BMW^{xz}_{max}, is obtained, such that the actual feed beamwidth, BMW^{xz}, must satisfy the following inequality:

$$BMW^{xz} \leq BMW^{xz}_{max} \; . \tag{5.11}$$

This procedure allows one to obtain the parameters BMW^{xz}_{max} and BMW^{xz}_i necessary for the design of the feed.

5.1.4 SECOND DESIGN PROCEDURE (METHOD 2)

The quantities h_{pc}, h_{um}, h_{lm}, ρ_d, and BMW^{xz} are assumed, and z_{pc} is set to zero. The following quantities are computed: gro, α_c, β_c, χ_c, f, ϵ_s, d_s, M, m, and BMW^{xz}_i.

In this procedure the feed beamwidth, BMW^{xz}, is an input, and the corresponding value of the gro is obtained. This procedure allows one to verify how a given feed (for instance, a horn with given characteristics) performs if used as a compact range feed. This second procedure can be alternated with the first and third to obtain a satisfactory design for a given application.

5.1.5 THIRD DESIGN PROCEDURE (METHOD 3)

The quantities h_{pc}, h_{tm}, h_{um}, ρ_d, and BMW_i^{xz} are assumed, and z_{pc} is set to zero. The following quantities are computed: gro, α_c, β_c, χ_c, f, ϵ_s, d_s, M, m, and BMW^{xz}.

In this procedure the feed beamwidth BMW_i^{xz} is an input. The corresponding value of the gro is obtained. Again this procedure allows one to verify how a given feed performs if used as a compact range feed.

5.1.6 FOURTH DESIGN PROCEDURE (METHOD 4)

The quantities z_{pc}, h_{pc}, h_{um}, h_{lm}, ρ_d and χ_c are specified in this design procedure, and z_{pc} can be different from zero. The following parameters are computed: BMW_{max}^{xz}, α_c, β_c, f, ϵ_s, d_s, ρ_d, M, m, and BMW_i^{xz}. In this procedure, the tilt angle, χ_c, and the height of the axis of the target zone, h_{tm}, are assumed. This determines the focal length f. The quantities t_β and m are then computed, together with all the remaining quantities.

These design procedures are examined in detail in the following sections.

5.2 AN EQUATION USED IN THE FIRST, SECOND AND THIRD DESIGN PROCEDURES

The following basic equation has been derived in Section 5.1.1 under the condition $z_{pc} = 0$:

$$\frac{2h_{pc}}{h_{tm}} = -\tan\beta_c \tan\left(\frac{\chi_c}{2}\right) . \tag{5.12}$$

From this equation, one can obtain an equation used in the first, second and third design procedures.

Equation (5.12) is written as

$$\tan\left(\frac{\chi_c}{2}\right) = -2\,\frac{h_{pc}}{h_{tm}}\,\frac{1}{\tan\beta_c} \tag{5.13}$$

then

$$t_{\chi c} = H \frac{t_{\beta_c}^2 - 1}{t_{\beta_c}} \tag{5.14}$$

where

$$H = \frac{h_{pc}}{h_{tm}} , \qquad t_{\chi c} = \tan\left(\frac{\chi_c}{2}\right) , \text{ and } \quad t_{\beta_c} = \tan\left(\frac{\beta_c}{2}\right) . \tag{5.15}$$

By making use of the cross-polarization equation, one obtains immediately

$$m^2 = \frac{H t_{\beta_c}^2 - (1+H)}{(1+H) t_{\beta_c}^2 - H} . \tag{5.16}$$

Since $m^2 > 0$, the range of validity of the solutions must be established such that the following inequality:

$$\frac{H t_{\beta_c}^2 - (1+H)}{(1+H) t_{\beta_c}^2 - H} \geq 0 \tag{5.17}$$

is satisfied. This inequality in turn is satisfied if

$$\begin{cases} H t_{\beta_c}^2 - (1+H) \geq 0 , \text{ and} \\ (1+H) t_{\beta_c}^2 - H > 0 \end{cases} \tag{5.18}$$

or if

$$\begin{cases} H t_{\beta_c}^2 - (1+H) \leq 0 , \text{ and} \\ (1+H) t_{\beta_c}^2 - H < 0 . \end{cases} \tag{5.19}$$

The first set of inequalities gives

$$\begin{cases} t_{\beta_c}^2 \geq (1+H)/H = 1 + 1/H , \text{ and} \\ t_{\beta_c}^2 > H/(1+H) = 1 - 1/(1+H) \end{cases} \tag{5.20}$$

which is satisfied if

$$t_{\beta_c}^2 \geq 1 + \frac{1}{H} \tag{5.21}$$

and the second set of inequalities gives

$$\begin{cases} t_{\beta_c}^2 \leq (1+H)/H = 1 + 1/H , \text{ and} \\ t_{\beta_c}^2 < H/(1+H) = 1 - 1/(1+H) \end{cases} \tag{5.22}$$

which is satisfied if

$$t_{\beta_c}^2 < 1 - \frac{1}{1+H} \ . \tag{5.23}$$

Therefore, any solution of Equation (5.16) is acceptable if $t_{\beta_c}^2$ belongs to the following union of intervals:

$$\left(0 \leq t_{\beta_c}^2 < 1 - \frac{1}{1+H}\right) \cup \left(1 + \frac{1}{H} \leq t_{\beta_c}^2\right) \ . \tag{5.24}$$

These inequalities are important. In fact, the design equations are higher order equations (second and fourth order) which have more than one solution. It is necessary then to be able to discard the spurious solutions by verifying which of the solutions satisfies both the Inequalities (5.21) and (5.23).

5.3 DIRECT DESIGN METHOD 1

The first design equation is derived in this section. The following quantities are initially specified by the designers:

$$\rho_d, \quad \text{gro, and } H = \frac{h_{pc}}{h_{tm}} \ . \tag{5.25}$$

An expression (called the design equation) for $\tan(\beta_c/2)$ in terms of the given quantities ρ_d, gro and H is derived and then the other parameters are expressed in terms of $\tan(\beta_c/2)$ and the specified quantities.

By expressing the magnification factor [12] in terms of $\tan(\beta_c/2)$, one finds that

$$M = \frac{m(t_{\beta_c}^2 + 1)}{m^2 t_{\beta_c}^2 + 1} \qquad \text{where} \qquad t_{\beta_c} = \tan\left(\frac{\beta_c}{2}\right) \ . \tag{5.26}$$

From Equation (G.41), the focal distance f is given by

$$f = \frac{\rho_d}{2M}\sqrt{\frac{\text{gro}}{1-\text{gro}}} \tag{5.27}$$

at the same time, f is given by

$$f = -\frac{h_{pc}}{\tan\beta_c} = h_{pc}\frac{t_{\beta_c}^2 - 1}{2t_{\beta_c}} \,. \tag{5.28}$$

Then, by equating the two expressions, one obtains that

$$\frac{h_{pc}}{\rho_d}\sqrt{\frac{1-\mathrm{gro}}{\mathrm{gro}}} = \frac{t_{\beta_c}}{M(t_{\beta_c}^2 - 1)} \,. \tag{5.29}$$

The quantity, Q, is presently defined by the following equation:

$$\sqrt{Q} = \frac{h_{pc}}{\rho_d}\sqrt{\frac{1-\mathrm{gro}}{\mathrm{gro}}} \tag{5.30}$$

then one finds that

$$\sqrt{Q} = \frac{t_{\beta_c}}{M(t_{\beta_c}^2 - 1)} \,. \tag{5.31}$$

This equation is presently used to obtain t_{β_c} such that

$$\sqrt{Q}M\,(t_{\beta_c}^2 - 1) - t_{\beta_c} = 0 \tag{5.32}$$

$$\sqrt{Q}m(t_{\beta_c}^4 - 1) - t_{\beta_c}(m^2 t_{\beta_c}^2 + 1) = 0 \,. \tag{5.33}$$

Note that the term m^2 has been already obtained in terms of H and t_{β_c}, so that

$$m^2 = \frac{Ht_{\beta_c}^2 - (1+H)}{(1+H)t_{\beta_c}^2 - H} \,. \tag{5.34}$$

Consequently, Equation (5.33) can be rearranged so that

$$(m^2 t_{\beta_c}^2 + 1)t_{\beta_c} = m\sqrt{Q}(t_{\beta_c}^4 - 1) \quad \text{or} \tag{5.35}$$

$$(m^2 t_{\beta_c}^2 + 1)^2 t_{\beta_c}^2 = m^2 Q(t_{\beta_c}^4 - 1)^2 \,. \tag{5.36}$$

One obtains from Equation (5.34)

$$m^2 t_{\beta_c}^2 + 1 = \frac{Ht_{\beta_c}^2 - (1+H)}{(1+H)t_{\beta_c}^2 - H} t_{\beta_c}^2 + 1 \text{ , and} \tag{5.37}$$

$$m^2 t_{\beta_c}^2 + 1 = \frac{1}{(1+H)t_{\beta_c}^2 - H} \times$$
$$\times \{[Ht_{\beta_c}^2 - (1+H)]t_{\beta_c}^2 + (1+H)t_{\beta_c}^2 - H\} \tag{5.38}$$

where the term inside the braces gives

$$\{[Ht_{\beta_c}^2 - (1+H)]t_{\beta_c}^2 + (1+H)t_{\beta_c}^2 - H\} = H(t_{\beta_c}^4 - 1)\ . \tag{5.39}$$

Therefore, one obtains

$$m^2 t_{\beta_c}^2 + 1 = \frac{H(t_{\beta_c}^4 - 1)}{(1+H)t_{\beta_c}^2 - H} \tag{5.40}$$

and Equation (5.36) becomes

$$\left[\frac{H(t_{\beta_c}^4 - 1)}{(1+H)t_{\beta_c}^2 - H}\right]^2 t_{\beta_c}^2 = \frac{Ht_{\beta_c}^2 - (1+H)}{(1+H)t_{\beta_c}^2 - H} Q(t_{\beta_c}^4 - 1)^2\ . \tag{5.41}$$

Both sides of the previous expression can be divided by $(t_{\beta_c}^4 - 1)^2$ and multiplied by $[(1+H)t_{\beta_c}^2 - H]^2$ such that one obtains

$$Q[Ht_{\beta_c}^2 - (1+H)][(1+H)t_{\beta_c}^2 - H] = H^2 t_{\beta_c}^2 \tag{5.42}$$

or

$$QH(1+H)t_{\beta_c}^4 - [H^2(1+Q) + Q(1+H)^2]t_{\beta_c}^2 + QH(1+H) = 0\ . \tag{5.43}$$

If one sets $t = t_{\beta_c}^2$, Equation (5.43) can be written as a second order equation in t, as follows:

$$\boxed{B_0 t^2 + B_1 t + B_2 = 0} \tag{5.44}$$

where the coefficients B_i are given by

$$B_0 = QH(1+H) \tag{5.45}$$

$$B_1 = -H^2(1+Q) - Q(1+H)^2 = -H^2(1+2Q) - Q(1+2H) \tag{5.46}$$

$$B_2 = QH(1+H)\ , \text{and} \tag{5.47}$$

$$t_{\beta_c} = \sqrt{t} \tag{5.48}$$

and $t > 0$. This second order expression is the design equation. The coefficients of this equation are expressed in terms of the input quantities, and hence are known. The equation can then be solved. If there is more than one solution, the actual value of t_{β_c} can be found by substituting the roots back into the original equations and by checking if the Inequalities (5.21) and (5.23) are satisfied.

5.4 DIRECT DESIGN METHOD 2

The second design equation is derived in this section using the following specified quantities:

$$BMW^{xz}, \text{ and } H = \frac{h_{pc}}{h_{tm}} . \tag{5.49}$$

As seen before, the beamwidth, BMW^{xz}, describes how fast the radiation pattern of the feed is reduced (i.e., becomes lower than a certain chosen amount of dB) outside its main beam. An expression for $\tan(\beta_c/2)$ in terms of the given quantities is derived (the design equation). All the other quantities can then be derived in terms of $\tan(\beta_c/2)$, the specified quantities and the length of the semidiagonal of the target zone, ρ_d.

The geometry for this design procedure is shown in Figure 55, and the following relationship has been derived in Section 5.1.2:

$$\beta_c - \alpha_c = \frac{BMW^{xz}}{2} . \tag{5.50}$$

By dividing both sides by two and taking the tangent, one obtains

$$\tan\left(\frac{\beta_c - \alpha_c}{2}\right) = \tan\left(\frac{BMW^{xz}}{4}\right) = G \tag{5.51}$$

and then G is a known quantity, since BMW^{xz} is known. One then obtains

$$m = \frac{t_{\beta_c} - G}{G t_{\beta_c}^2 + t_{\beta_c}} . \tag{5.52}$$

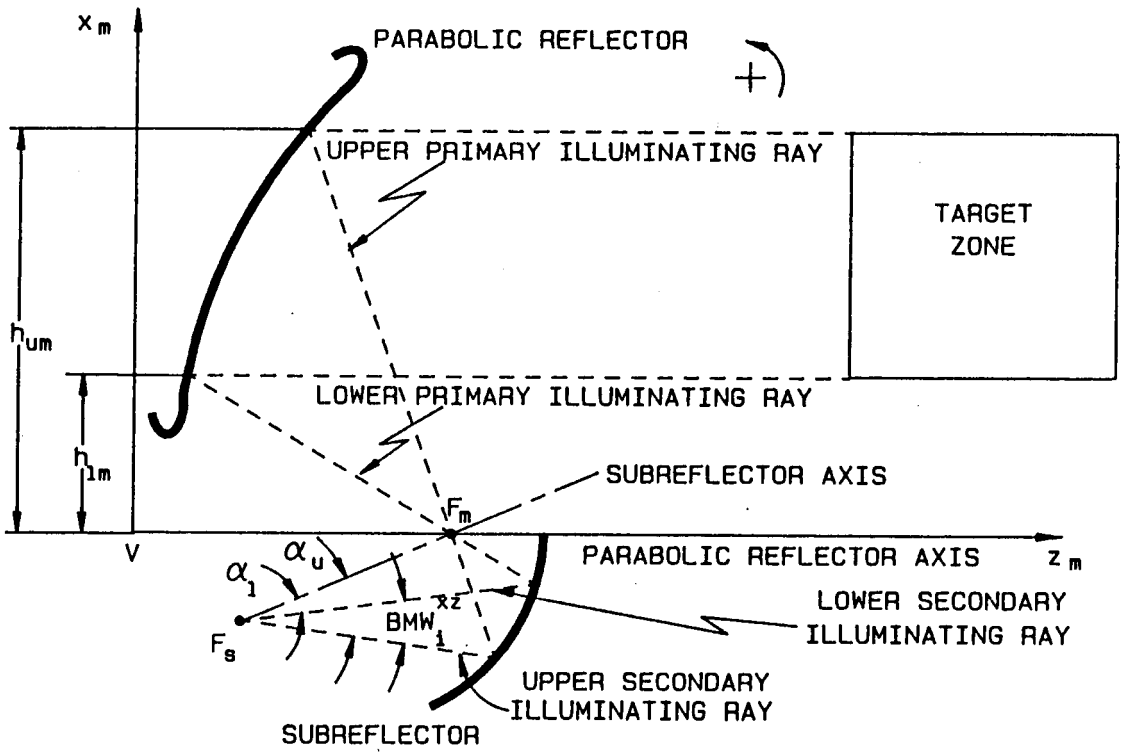

Figure 55: Geometry of Direct Design, Method 2.

From Equation (5.16), one recalls that

$$m^2 = \frac{Ht_{\beta_c}^2 - (1+H)}{(1+H)t_{\beta_c}^2 - H} \tag{5.53}$$

as it has been determined in Section 5.2, with the condition that $t_{\beta_c}^2$ belongs to the unions of intervals

$$\left(0 \leq t_{\beta_c}^2 < 1 - \frac{1}{1+H}\right) \cup \left(1 + \frac{1}{H} < t_{\beta_c}^2\right) . \tag{5.54}$$

Equating Equation (5.53) with Equation (5.52) squared, one obtains that

$$\frac{Ht_{\beta_c}^2 - (1+H)}{(1+H)t_{\beta_c}^2 - H} = \frac{(t_{\beta_c} - G)^2}{(Gt_{\beta_c}^2 + t_{\beta_c})^2} . \tag{5.55}$$

By multiplying both sides by

$$[(1+H)t_{\beta_c}^2 - H](Gt_{\beta_c}^2 + t_{\beta_c})^2 \tag{5.56}$$

one obtains

$$[Ht_{\beta_c}^2 - (1+H)](Gt_{\beta_c}^2 + t_{\beta_c})^2 - [(1+H)t_{\beta_c}^2 - H](t_{\beta_c} - G)^2 = 0 \tag{5.57}$$

or

$$\begin{aligned} &HG^2t_{\beta_c}^6 + 2HGt_{\beta_c}^5 - [1 + (1+H)G^2]t_{\beta_c}^4 - \\ &[1 + (1+H)G^2]t_{\beta_c}^2 - 2HGt_{\beta_c} + HG^2 = 0 . \end{aligned} \tag{5.58}$$

This last expression can be factored as follows:

$$\begin{aligned} (t_{\beta_c}^2 + 1)(HG^2t_{\beta_c}^4 + 2HGt_{\beta_c}^3 - [1 + (1+2H)G^2]t_{\beta_c}^2 \\ -2HGt_{\beta_c} + HG^2) = 0 . \end{aligned} \tag{5.59}$$

Then, dividing by the factor $t_{\beta_c}^2 + 1$ (which has only imaginary solutions), one finally obtains that

$$HG^2t_{\beta_c}^4 + 2HGt_{\beta_c}^3 - [1 + (1+2H)G^2]t_{\beta_c}^2 - 2HGt_{\beta_c} + HG^2 = 0 . \tag{5.60}$$

This results in the following fourth order equation in the unknown term t_{β_c}

$$\boxed{A_0 t_{\beta_c}^4 + A_1 t_{\beta_c}^3 + A_2 t_{\beta_c}^2 + A_3 t_{\beta_c} + A_4 = 0} \tag{5.61}$$

where the coefficients are given by

$$A_0 = HG^2 \tag{5.62}$$

$$A_1 = 2HG \tag{5.63}$$

$$A_2 = -[1 + (1 + 2H)G^2] \tag{5.64}$$

$$A_3 = -A_1 \text{ , and} \tag{5.65}$$

$$A_4 = A_0 \text{ .} \tag{5.66}$$

These coefficients are known in terms of the specified design parameters, so that the design equation can be solved. A solution for t_{β_c} can be found using known search procedures (Raphson-Newton, for instance) or by using the known expressions for solving a fourth order equation, or a combination of both to improve the numerical precision. The solution must belong to the following union of intervals:

$$\left(0 \leq t_{\beta_c}^2 < 1 - \frac{1}{1+H}\right) \cup \left(1 + \frac{1}{H} < t_{\beta_c}^2\right) \tag{5.67}$$

which completes the design.

5.5 DIRECT DESIGN METHOD 3

The third design equation is derived in this section. The following quantities:

$$BMW_i^{xz} \text{ , } h_{um} \text{ , } h_{lm} \text{ , and } H = \frac{h_{pc}}{h_{tm}} \tag{5.68}$$

are assumed to be specified by the designer. The quantity, BMW_i^{xz}, is the illuminating beamwidth which characterizes the main beam of the feed. Again, an expression for $\tan(\beta_c/2)$ in terms of the given quantities is derived (the design

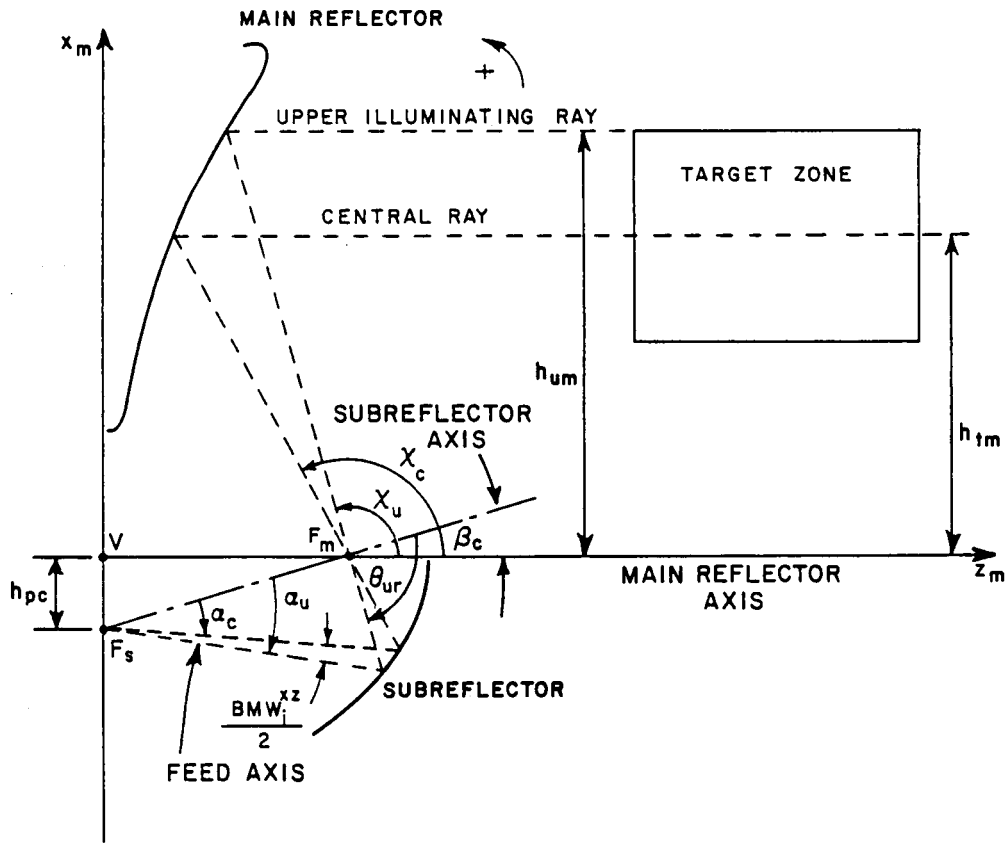

Figure 56: Geometry of Direct Design, Method 3.

equation). All other quantities can then be computed in terms of t_{β_c}, the specified quantities and ρ_d.

Let h_{um} be the height (the x_m coordinate) of the upper edge of the primary illuminating area, χ_u be the angle of the corresponding upper illuminating ray with the axis of the main reflector, and α_u be the polar angle of the corresponding secondary illuminating ray with respect to the subreflector polar coordinate system as shown in Figure 56. Then, the following relationships hold:

$$\frac{h_{um}}{2f} = \cot\left(\frac{\chi_u}{2}\right) \tag{5.69}$$

$$\alpha_c - \alpha_u = \frac{BMW_i^{xz}}{2} \tag{5.70}$$

where the geometry is shown in Figure 56. One then obtains

$$t_{\alpha_u} = \frac{1}{m}\frac{t_{\chi_u} t_{\beta_c} - 1}{t_{\chi_u} + t_{\beta_c}} \tag{5.71}$$

where

$$t_{\alpha_u} = \tan\left(\frac{\alpha_u}{2}\right), \quad t_{\chi_u} = \tan\left(\frac{\chi_u}{2}\right), \text{ and } t_{\beta_c} = \tan\left(\frac{\beta_c}{2}\right). \tag{5.72}$$

From Equation (3.1) and Equation (5.14) one obtains

$$t_{\chi_u} = R t_{\chi_c} \qquad \text{where} \qquad R = \frac{h_{tm}}{h_{um}}. \tag{5.73}$$

Then, Equation (5.71) becomes

$$t_{\alpha_u} = \frac{1}{m} t_{\beta_c} \frac{RHt_{\beta_c}^2 - (1 + RH)}{(1 + RH)t_{\beta_c}^2 - RH}. \tag{5.74}$$

By letting

$$\tan\left(\frac{\alpha_c - \alpha_u}{2}\right) = \tan\left(\frac{BMW_i^{xz}}{4}\right) = G_i \tag{5.75}$$

where G_i is a known quantity, since BMW_i^{xz} is known, one obtains

$$m^2 t_{\beta_c}[(1 + RH)t_{\beta_c}^2 - RH] - t_{\beta_c}[RHt_{\beta_c}^2 - (1 + RH)] + \\ -mG_i RH(t_{\beta_c}^4 - 1) = 0. \tag{5.76}$$

This expression can be solved for m as follows:

$$m = \frac{t_{\beta_c}}{G_i RH(t_{\beta_c}^4 - 1)} \left\{ m^2[(1 + RH)t_{\beta_c}^2 - RH] - [RHt_{\beta_c}^2 - (1 + RH)] \right\} \quad (5.77)$$

which can be written as

$$m = X \left\{ m^2 Y - Z \right\} . \quad (5.78)$$

By squaring, one obtains

$$m^2 = X^2 \left\{ m^4 Y^2 - 2m^2 YZ + Z^2 \right\} \quad (5.79)$$

then

$$(m^2)^2 X^2 Y^2 - m^2(1 + 2X^2 YZ) + X^2 Z^2 = 0 \quad (5.80)$$

and, by Equation (5.16)

$$m^2 = \frac{Ht_{\beta_c}^2 - (1 + H)}{(1 + H)t_{\beta_c}^2 - H} . \quad (5.81)$$

Then, using these results, one obtains

$$\begin{aligned} \left[\frac{Ht_{\beta_c}^2 - (1 + H)}{(1 + H)t_{\beta_c}^2 - H} \right]^2 \frac{t_{\beta_c}^2}{(G_i RH)^2(t_{\beta_c}^4 - 1)^2} [(1 + RH)t_{\beta_c}^2 - RH]^2 \; + \\ - \frac{Ht_{\beta_c}^2 - (1 + H)}{(1 + H)t_{\beta_c}^2 - H} \; \times \\ \left\{ 1 + 2 \frac{t_{\beta_c}^2}{(G_i RH)^2(t_{\beta_c}^4 - 1)^2} [(1 + RH)t_{\beta_c}^2 - RH][RHt_{\beta_c}^2 - (1 + RH)] \right\} \; + \\ + \frac{t_{\beta_c}^2}{(G_i RH)^2(t_{\beta_c}^4 - 1)^2} [RHt_{\beta_c}^2 - (1 + RH)]^2 \; = \; 0 . \end{aligned} \quad (5.82)$$

By multiplying by

$$[(1 + H)t_{\beta_c}^2 - H]^2 (G_i RH)^2 (t_{\beta_c}^4 - 1)^2 \quad (5.83)$$

one obtains

$$\begin{aligned} t_{\beta_c}^2[Ht_{\beta_c}^2-(1+H)]^2[(1+RH)t_{\beta_c}^2-RH]^2 \; &+ \\ -[(1+H)t_{\beta_c}^2-H][Ht_{\beta_c}^2-(1+H)] \; &\times \\ \{(G_iRH)^2(t_{\beta_c}^4-1)^2+2t_{\beta_c}^2[(1+RH)t_{\beta_c}^2-RH][RHt_{\beta_c}^2-(1+RH)]\} \; &+ \\ t_{\beta_c}^2[(1+H)t_{\beta_c}^2-H]^2[RHt_{\beta_c}^2-(1+RH)]^2 \; &= \; 0 \end{aligned} \tag{5.84}$$

or

$$\begin{aligned} t_{\beta_c}^2\{[Ht_{\beta_c}^2-(1+H)]^2[(1+RH)t_{\beta_c}^2-RH]^2 \; &+ \\ [(1+H)t_{\beta_c}^2-H]^2[RHt_{\beta_c}^2-(1+RH)]^2 \; &+ \\ -2[(1+H)t_{\beta_c}^2-H][Ht_{\beta_c}^2-(1+H)] \; &\times \\ [(1+RH)t_{\beta_c}^2-RH][RHt_{\beta_c}^2-(1+RH)]\} \; &+ \\ -(G_iRH)^2[(1+H)t_{\beta_c}^2-H][Ht_{\beta_c}^2-(1+H)](t_{\beta_c}^4-1)^2 \; &= \; 0\,. \end{aligned} \tag{5.85}$$

This can be written as follows:

$$t_{\beta_c}^2(T_1^2T_2^2+T_3^2T_4^2-2T_1T_2T_3T_4)-(G_iRH)^2T_3T_1(t_{\beta_c}^4-1)^2=0 \tag{5.86}$$

where

$$T_1 \; = \; Ht_{\beta_c}^2-(1+H) \tag{5.87}$$

$$T_2 \; = \; (1+RH)t_{\beta_c}^2-RH \tag{5.88}$$

$$T_3 \; = \; (1+H)t_{\beta_c}^2-H \text{ , and} \tag{5.89}$$

$$T_4 \; = \; RHt_{\beta_c}^2-(1+RH)\,. \tag{5.90}$$

Then, it follows that

$$t_{\beta_c}^2(T_1T_2-T_3T_4)^2-(G_iRH)^2T_1T_3(t_{\beta_c}^4-1)^2=0 \tag{5.91}$$

with

$$T_1T_2 = [Ht^2_{\beta_c} - (1+H)][(1+RH)t^2_{\beta_c} - RH] \quad (5.92)$$

$$T_1T_2 = H(1+RH)t^4_{\beta_c} - RH^2t^2_{\beta_c} - (1+H)(1+RH)t^2_{\beta_c} + (1+H)RH \quad (5.93)$$

$$T_1T_2 = H(1+RH)t^4_{\beta_c} - [RH^2 + (1+H)(1+RH)]t^2_{\beta_c} + (1+H)RH \quad (5.94)$$

$$T_3T_4 = [(1+H)t^2_{\beta_c} - H][RHt^2_{\beta_c} - (1+RH)] \quad (5.95)$$

$$T_3T_4 = (1+H)RHt^4_{\beta_c} - (1+H)(1+RH)t^2_{\beta_c} - RH^2t^2_{\beta_c} + H(1+RH) \quad (5.96)$$

$$T_3T_4 = (1+H)RHt^4_{\beta_c} - [(1+H)(1+RH) + RH^2]t^2_{\beta_c} + H(1+RH) \quad (5.97)$$

$$T_1T_3 = [Ht^2_{\beta_c} - (1+H)][(1+H)t^2_{\beta_c} - H] \quad (5.98)$$

$$T_1T_3 = H(1+H)t^4_{\beta_c} - H^2t^2_{\beta_c} - (1+H)^2t^2_{\beta_c} + H(1+H) \quad (5.99)$$

$$T_1T_3 = H(1+H)t^4_{\beta_c} - [H^2 + (1+H)^2]t^2_{\beta_c} + H(1+H) \quad (5.100)$$

and

$$T_1T_2 - T_3T_4 = H(1+RH)t^4_{\beta_c} - [RH^2 + (1+H)(1+RH)]t^2_{\beta_c} + (1+H)RH - (1+H)RHt^4_{\beta_c} + [(1+H)(1+RH) + RH^2]t^2_{\beta_c} - H(1+RH) \quad (5.101)$$

$$T_1T_2 - T_3T_4 = (H + RH^2 - RH - RH^2)t^4_{\beta_c} - (RH^2 + 1 + RH + H + RH^2 - 1 - RH - H - RH^2 - RH^2)t^2_{\beta_c} + RH + RH^2 - H - RH^2 \quad (5.102)$$

$$T_1T_2 - T_3T_4 = H(1-R)t^4_{\beta_c} - H(1-R) \quad (5.103)$$

$$T_1T_2 - T_3T_4 = H(1-R)(t_{\beta_c}^4 - 1)\,. \tag{5.104}$$

Therefore, one obtains the following equation by performing the substitutions and by dividing Equation (5.86) by $H^2(t_{\beta_c}^4 - 1)^2$, such that

$$\begin{aligned} t_{\beta_c}^2(1-R)^2 \; + \\ -(G_iR)^2\{H(1+H)t_{\beta_c}^4 - [H^2 + (1+H)^2]t_{\beta_c}^2 - H(1+H)\} \;&=\; 0 \end{aligned} \tag{5.105}$$

$$\begin{aligned} (G_iR)^2H(1+H)t_{\beta_c}^4 \; + \\ -\{(G_iR)^2[H^2 + (1+H)^2] + (1-R)^2\}t_{\beta_c}^2 \; + \\ +(G_iR)^2H(1+H) \;&=\; 0\,. \end{aligned} \tag{5.106}$$

By letting $t = t_{\beta_c}^2$ one obtains the following design equation:

$$\boxed{C_0t^2 + C_1t + C_2 = 0} \tag{5.107}$$

where the coefficients C_i are given by

$$C_0 = (G_iR)^2H(1+H) \tag{5.108}$$

$$C_1 = -(G_iR)^2[H^2 + (1+H)^2] - (1-R)^2 \text{ , and} \tag{5.109}$$

$$C_2 = (G_iR)^2H(1+H) = C_0\,. \tag{5.110}$$

5.6 DIRECT DESIGN METHOD 4

The fourth design equation is derived in this section, using the following specified quantities:

$$h_{pc}\,,\; z_{pc}\,,\; h_{um}\,,\; h_{lm}\,,\text{ and }\chi_c\,. \tag{5.111}$$

The general case for which the phase center of the feed antenna is not vertically aligned with the vertex of the parabolic reflector is considered in this design procedure. The geometry is shown in Figure 50.

The focal length f is determined in terms of the tilt angle χ_c and the height of the axis of the target zone, h_{tm}. All the other quantities can be derived in terms of $\tan(\beta_c/2)$, the specified quantities and the length of the semidiagonal of the target zone, ρ_d. The phase center has x_m, y_m, z_m coordinates given by $(h_{pc}, 0, z_{pc})$.

This equation has been previously derived

$$h_{tm} = 2\, f\, \cot\left(\frac{\chi_c}{2}\right) \tag{5.112}$$

and one obtains for f

$$f = \frac{1}{2}\, h_{tm}\, t_{\chi_c}\ . \tag{5.113}$$

The following equations are derived from Figure 50

$$h_{tm} = h_{lm} + \frac{1}{2}(h_{um} - h_{lm}) \tag{5.114}$$

$$f = d_s \cos\beta_c + z_{pc} \tag{5.115}$$

$$h_{pc} = -d_s \sin\beta_c\ . \tag{5.116}$$

Equation (5.115) can be solved for $d_s \cos\beta_c$

$$d_s \cos\beta_c = f - z_{pc} \tag{5.117}$$

and, by taking the ratio of (5.116) and (5.117) one obtains

$$\boxed{\tan\beta_c = \frac{h_{pc}}{z_{pc} - f}} \tag{5.118}$$

which expresses the unknown tilt angle β_c in terms of h_{pc}, z_{pc} and f. The quantities h_{pc} and z_{pc} are assumed to be known, while f is computed in terms of the angle χ_c through Equation (5.113). The quantity t_{β_c} is then known, since $t_{\beta_c} = \tan(\beta_c/2)$.

5.7 EVALUATION OF VARIOUS DESIGN PARAMETERS

Having evaluated t_{β_c} with any of the design equations, the remaining quantities can be computed accordingly. Some of the quantities (viz. χ_c, f, m) are

evaluated differently for methods 1, 2, 3 from method 4, while the remaining are evaluated in the same way for all methods.

5.7.1 METHODS 1, 2 AND 3

Having evaluated t_{β_c} with any of the design equations (method 1, 2 or 3), the remaining quantities can be computed accordingly. It has been found that

$$m^2 = \frac{H t_{\beta_c}^2 - (1+H)}{(1+H) t_{\beta_c}^2 - H} \tag{5.119}$$

where $t_{\beta_c}^2$ belongs to the union of intervals

$$\left(0 \leq t_{\beta_c}^2 < 1 - \frac{1}{1+H}\right) \cup \left(1 + \frac{1}{H} \leq t_{\beta_c}^2\right) . \tag{5.120}$$

Since $m > 0$ (convex ellipsoidal subreflector), one writes the following:

$$m = \sqrt{m^2} \tag{5.121}$$

where the square root is understood in the arithmetic sense.

Also, one finds that

$$t_{\chi_c} = H \frac{t_{\beta_c}^2 - 1}{t_{\beta_c}} \tag{5.122}$$

$$\chi_c = 2 \arctan(t_{\chi_c}) \tag{5.123}$$

$$f = -\frac{h_{pc}}{\tan \beta_c} \tag{5.124}$$

5.7.2 METHOD 4

The angle χ_c is an input. The focal length f is immediately derived from Equation (5.113), and does not depend on t_{β_c}, such that

$$f = \frac{1}{2} h_{tm} t_{\chi_c} \tag{5.125}$$

the axial magnification m is obtained from this equation

$$m = \sqrt{\frac{|\sin\beta_c|\sqrt{1-\cos\chi_c} + (1+\cos\beta_c)\sqrt{1+\cos\chi_c}}{|\sin\beta_c|\sqrt{1-\cos\chi_c} - (1-\cos\beta_c)\sqrt{1+\cos\chi_c}}} \tag{5.126}$$

where only the positive sign has been considered.

5.7.3 REMAINING QUANTITIES

All the remaining quantities are computed in the same way for all design procedures. One finds that

$$t_{\alpha_c} = m\, t_{\beta_c} \tag{5.127}$$

$$\alpha_c = 2\arctan(t_{\alpha_c}) \tag{5.128}$$

$$\beta_c = 2\arctan(t_{\beta_c}) \tag{5.129}$$

$$\epsilon_s = \frac{m-1}{m+1} \tag{5.130}$$

$$d_s = -\frac{h_{pc}}{\sin\beta_c} \tag{5.131}$$

$$p_s = \frac{1}{2}\frac{d_s}{\epsilon_s}(1-\epsilon_s^2) \tag{5.132}$$

$$M = \frac{1-\epsilon_s^2}{1+\epsilon_s^2-2\epsilon_s\cos\beta_c} \tag{5.133}$$

$$BMW_{max}^{xz} = 2(\beta_c - \alpha_c) \text{ using method 1, 3 or 4} \tag{5.134}$$

$$\text{gro}_{dB} = 20\ \log_{10}\left\{(2M\,f/\rho_d)^2 \Big/ \left[1+(2M\,f/\rho_d)^2\right]\right\} \text{ using method 2, 3 or 4.} \tag{5.135}$$

The secondary illuminating beamwidth in the $x_m z_m$ plane, BMW_i^{xz}, can be computed through the following equations, such that

$$BMW_i^{xz} = \alpha_u - \alpha_l \tag{5.136}$$

where

$$\chi_u = 2\arctan\left(\frac{2f}{h_{um}}\right) \tag{5.137}$$

$$\chi_l = 2\arctan\left(\frac{2f}{h_{lm}}\right) \tag{5.138}$$

$$\alpha_u = -\arctan\left[\frac{(1-\epsilon_s^2)\sin(\chi_u+\beta_c)}{2\epsilon_s-(1+\epsilon_s^2)\cos(\chi_u+\beta_c)}\right], \text{ and} \tag{5.139}$$

$$\alpha_l = -\arctan\left[\frac{(1-\epsilon_s^2)\sin(\chi_l+\beta_c)}{2\epsilon_s-(1+\epsilon_s^2)\cos(\chi_l+\beta_c)}\right]. \tag{5.140}$$

Recall the following parameters:

- α_u is the angle from the subreflector axis to the secondary illuminating ray corresponding to the upper point of the primary illuminating surface in the x_m, z_m plane
- χ_u is the angle from the main reflector axis to the primary illuminating ray corresponding to the upper point of the primary illuminating surface in the x_m, z_m plane, and
- h_{um} is the x_m coordinate of the upper point of the primary illuminating surface in the x_m, z_m plane.

Similar definitions correspond to α_l, χ_l, h_{lm} for the lower point of the primary illuminating surface (see Figure 47). In this way all quantities are determined, and the GO design is complete.

5.8 CONCLUSIONS

Several simple design equations have been derived in this chapter, which allow one to compute in an exact way all the geometrical parameters of a compact range subreflector system in terms of suitable input variables, which represent the specifications for the design. These equations have been easily converted into a computer program, called WAYLAND, which allow one to perform the design simply, quickly and efficiently, without the iterations and uncertainties which are unavoidable with an iteration procedure like the one described in Chapter IV.

CHAPTER VI

COUPLING APERTURE DESIGN

6.1 BEHAVIOUR OF WEDGE SHAPED ABSORBER

The qualitative behaviour of wedge shaped absorber is briefly described to better understand the design of the coupling aperture. A more complete discussion is available in [16]. The wedge absorber is modeled as a dielectric wedge such as shown in Figure 57. It is assumed that a uniform plane wave is incident on the wedge. As for a conducting wedge, an incident shadow boundary and a reflection shadow boundary are present, and the diffracted field has to compensate for the discontinuities of the GO field. The reflected field is equal to the incident field multiplied by the reflection coefficient, which is considerably less than one for a good absorber. Consequently, the reflected field for an absorber wedge is considerably less than for a conducting wedge, and the corresponding diffracted field is proportionally weaker. A transmitted field is also present, and its intensity is given by the incident field multiplied by the transmission coefficient and an exponentially decaying term depending on the actual thickness of absorber crossed by the ray. Also, the transmitted ray changes direction. Again the diffracted field has to compensate for the discontinuity between the incident field and the transmitted field. If the transmitted field is weak, the diffracted field at the shadow boundary is strong. In other words, the more effective the wedge absorber is in blocking the incident field, the stronger is the diffraction at the incident shadow

boundary. Thus to minimize diffraction it is necessary to use low loss absorbing materials or, alternatively, to use a wedge with a small wedge angle. On the other side, it is also desired that the absorber attenuates the transmitted signal.

These considerations also suggest a design criterion for absorbing materials, for which the absorbing properties should gradually increase from zero (free space) to high absorption.

6.2 GO DESIGN OF THE OVERSIZED SUBREFLECTOR AND THE COUPLING APERTURE

In this section the GO design of the coupling aperture is illustrated through a specific design example. The example considered is design FD, shown in Figure 66 and in Table 5.

The main parabolic reflector has rolled edges to minimize the diffraction from its terminations. This diffraction, in fact, would corrupt the plane wave reflected field. For the subreflector, it is necessary to avoid the diffractions from its terminations which can illuminate either the main reflector or the target zone and cause undesirable errors. This is achieved by overextending the subreflector and by designing the coupling aperture so that the diffracted rays are absorbed in a proper way. This is a better approach than using rolled edges on the subreflector itself, which are difficult to design for a very concave surface. In fact, a subreflector with rolled edges would be as large as an overextended subreflector, while being more complex to design and manufacture. The motivations and design of the overextension of the subreflector can be better seen in two steps. The design is performed in the x_m, z_m plane. Let ℓ_s be the length, in the x_m, z_m plane, of the part of the subreflector illuminated by the secondary illuminating beam (i.e., by the beam from the feed antenna corresponding to the target zone) from the

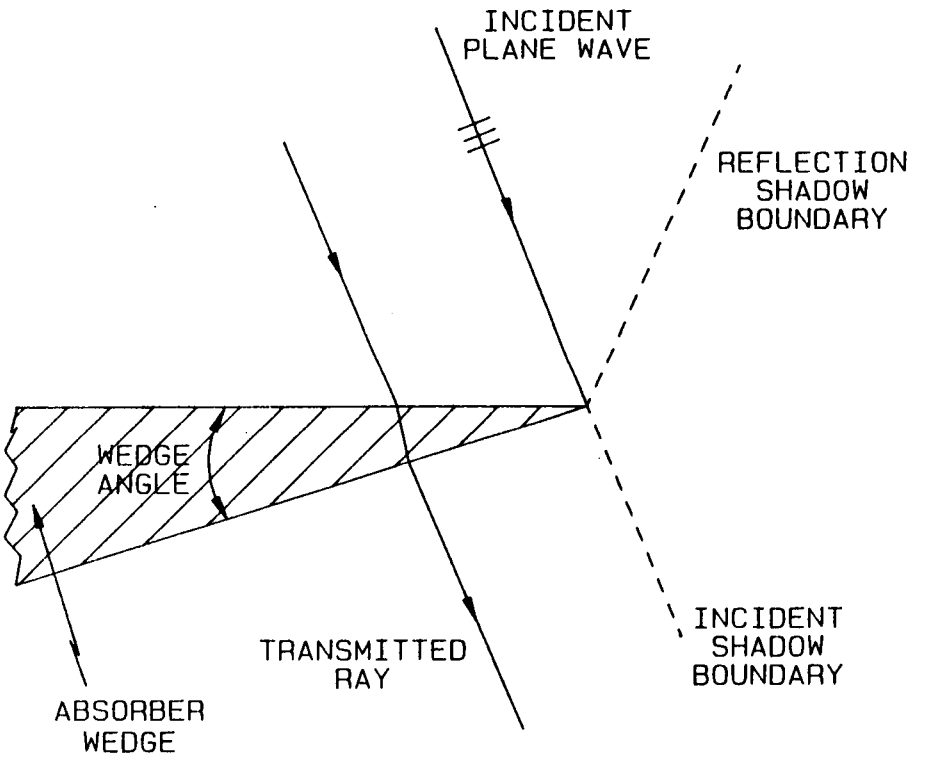

Figure 57: Wedge absorber illuminated by a plane wave.

feed antenna, and delimited by the points, I_{us} and I_{ls}, as shown in Figure 58. Then, on all sides, the subreflector is extended by an amount of about ℓ_s, obtaining a subreflector having, in the x_m, z_m plane, a total length of about $3\,\ell_s$, as shown in Figure 58. This subreflector is called the extended subreflector. From the same figure it can be seen that the reflection shadow boundary at the edge S_l' is given by the ray, $\mathcal{R}_{S_l'}$; while, the reflection shadow boundary at the edge S_u' is given by the ray, $\mathcal{R}_{S_u'}$. These rays are separated anglewise from the rays, $\mathcal{R}_l$ (from I_{ls} to I_{lm}) and $\mathcal{R}_u$ (from I_{us} to I_{um}), which coincide with the lower and upper illuminating rays and correspond to that part of the subreflector which is actually illuminating the target zone. Still, in order to increase this separation, and consequently to reduce the amount of diffraction from the lower into the upper chamber, it is desirable to further extend the subreflector by, for instance, about ℓ_s, on all sides, obtaining new edges (called S_u and S_l in the x_m, z_m plane) and new corresponding shadow boundaries (called $\mathcal{R}_{S_u}$ and $\mathcal{R}_{S_l}$) as shown in Figure 60. This is called an overextended subreflector. In performing this extension, it is important that the rays reflected from the subreflector avoid going directly into the target zone through the coupling aperture; in other words, it is important not to extend the subreflector too much on the side of the edge, S_u. Instead, on the side of S_l, the extension of the subreflector is limited by the fact that the subreflector must be all inside the lower chamber. These new shadow boundaries, $\mathcal{R}_{S_u}$ and $\mathcal{R}_{S_l}$ are farther removed from the rays, $\mathcal{R}_l$ and $\mathcal{R}_u$. The reason to introduce this overextension of the subreflector becomes apparent from the design of the coupling aperture, which is described later. In fact, it is advantageous to let the rays, $\mathcal{R}_{S_u'}$ and $\mathcal{R}_{S_l'}$, pass through the coupling aperture without experiencing any absorbtion. These reflected rays, coming from the points, S_u' and S_l', are directed towards areas of the ceiling/walls which are covered by absorber material,

away from the target zone. Therefore, they can be absorbed without perturbing the plane wave in the target zone. If instead they were absorbed in the coupling aperture, a shadow boundary would be introduced close anglewise to the parabolic reflector, with subsequent reflection and diffraction in the target zone. The time delays of these reflected and diffracted rays would be very close to that of the plane wave illuminating the target zone, and no time gating would be possible. Instead, the reflection shadow boundaries, $\mathcal{R}_{S_l}$ and $\mathcal{R}_{S_u}$, are further separated anglewise from the parabolic reflector; therefore, the related diffracted rays, reflected or rediffracted by the parabolic reflector, are much weaker. It is possible then to intercept these rays with the absorber at the coupling aperture, since the incident shadow boundaries introduced by the absorber are sufficiently removed anglewise from the parabolic reflector.

The GO design of the coupling aperture is now described. The minimum diameter of the coupling aperture is determined by the minimum frequency of operation of the range. This diameter, d_c, is safely assumed to be about 5 wavelengths at the lowest frequency of operation, and it is centered around the focal point, F_m. In the design presently considered, this corresponds to a diameter of approximately 75 cm, or about $2.5'$, because the lower frequency of operation is 2 GHz. At the focal point, F_m, the actual field does not shrink to a point, as GO would predict, but instead occupies a finite region of space, as shown in Figures 40 and 41. Since the diameter of the coupling aperture is specified, the points C_l and C_u are located. The thickness of the coupling aperture is determined by evaluating the performance of the absorber material used. In the present design, the absorber thickness, h_a, is $2'$. The absorber layer is all above the main reflector axis, so that the ceiling of the lower chamber is set at $x = 0$. Once the thickness, h_a, of the absorber is determined, it is necessary to determine the shape of the

coupling aperture. It is clear that its shape must be such that the reflected beam from the subreflector can flare out towards the main reflector without attenuation; while, the diffracted rays are attenuated. The absorber around the coupling aperture is shaped as a series of wedges, stacked one above the other, typically two or three wedges, having height approximately of $h_a/3$ each.

The design of the shape of the coupling aperture of the subreflector can be better understood through several steps. It is desired to let the rays, $\mathcal{R}_{S_l'}$ and $\mathcal{R}_{S_u'}$, go through the coupling aperture unimpeded. Otherwise, diffraction shadow boundaries would be introduced, which would be close anglewise to the edges, I_{lm} and I_{um} (lower and upper, respectively), of the parabolic reflector. In fact, the rays, $\mathcal{R}_{S_l'}$ and $\mathcal{R}_{S_u'}$, are not directed towards the target zone, but rather towards the wall on the back of the main reflector or towards the ceiling. Both areas are covered with absorber, and these rays are safely absorbed (perhaps, after reflection from the rolled edges). If the subreflector were terminated at the points, S_l' and S_u', the wedges of the coupling aperture would be shaped with sides parallel to the rays, $\mathcal{R}_{S_l'}$ and $\mathcal{R}_{S_u'}$, and the design shown in Figure 59 would be obtained. But this design is not satisfactory. In fact, it is important that the coupling aperture eliminates the diffracted rays directed from the edges of the subreflector towards the edges of the main reflector. These rays are indicated as $\mathcal{D}_{S_u'}$ and $\mathcal{D}_{S_l'}$ in Figure 59. The diffracted ray, $\mathcal{D}_{S_u'}$, goes from the point, S_u', to the edge point, I_{um}; while, the ray, $\mathcal{D}_{S_l'}$, goes from the point, S_l', to the edge point, I_{lm}. These rays would cause diffraction in the target zone, in that they would be rediffracted in the target zone by the edges of the main reflector, while the diffracted rays which are close anglewise to $\mathcal{D}_{S_u'}$ and $\mathcal{D}_{S_l'}$ and are directed towards the portion of the main reflector between I_{lm} and I_{um}, would be reflected in the target zone. In both cases the plane wave in the target zone would be deteriorated. It can be

seen from Figure 59 that the absorber wedge angles are large (especially at C_l), introducing diffraction, but at the same time the rays, $\mathcal{D}_{S_u'}$ and $\mathcal{D}_{S_l'}$, go through a thin portion of the wedges (if they go through any at all), with little attenuation, and the coupling aperture would fail to accomplish its main purpose. For this reason then it is desirable to extend further the subreflector to the points, S_l and S_u, by an amount of ℓ_s on each side, obtaining the design of Figure 60, where the subreflector has an overall length of about $5\,\ell_s$. In fact, after the corresponding coupling aperture has been designed, it has been found that a length of $4\,\ell_s$ was not sufficient to insure a good attenuation of the rays $\mathcal{D}_{S_u}$ and $\mathcal{D}_{S_l}$. The design of the overextended subreflector is then completed.

To complete the design of the coupling aperture, it is necessary to determine the shapes of the "C_l" and "C_u" sides of the coupling aperture.

On the "C_u" side, the purpose of the coupling aperture is to block the diffracted ray, $\mathcal{D}_{S_u}$, which goes from the point, S_u, to the point, I_{um}. The coupling aperture at C_u is slanted with a slope equal to that of the reflected ray, $\mathcal{R}_l'$, obtaining a wedge-like structure, as shown in Figure 61. The angle of this wedge is sufficiently small to reduce its diffraction to an acceptable value. This wedge introduces a shadow boundary, with subsequent diffraction. It is important then that this diffraction be low in the direction towards the point, I_{lm}, and for this reason the subreflector is overextended on the S_l side. If only one wedge were used on the "C_u" side , the coupling aperture would be too large. A second wedge then is introduced on top of the first. In order to make the transition of the field gradual, this second wedge is inverted. The reason for this choice can be seen through a counterexample; in other words, it is now shown how a bad choice for the shape of the second wedge would introduce a strong diffraction. One should consider in fact Figure 63, where a second wedge has been added, having the same slope as

the first. The two rays, $\mathcal{R}_l'$ and $\mathcal{R}_l''$, which are very close anglewise, are considered. The ray $\mathcal{R}_l''$ goes through a thick piece of absorber, experiencing a strong attenuation (if the absorbing material has high absorbption properties). Instead, the ray $\mathcal{R}_l'$ does not experience any attenuation. This arrangement then introduces a discontinuity in the field directed from the subreflector towards the main reflector, with a resulting strong diffraction with $\mathcal{R}_l'$ as a shadow boundary. Instead, it is not necessary to strongly attenuate the rays like $\mathcal{R}_l''$, which can be absorbed by the absorber on the walls of the upper chamber (perhaps, after reflection from the rolled edge). Thus, this diffraction can be reduced by the inverted wedge arrangement, which does not introduce such a discontinuity. In this way the amount of diffraction reflected by the main reflector into the target zone is reduced. Therefore, the inverted wedge arrangement is better suited for the present purposes, and the design of Figure 61 is obtained, where the details of the coupling aperture are shown in Figure 62. The position of the tip, C_u', of the second wedge is determined as follows. A line parallel to the ray, $\mathcal{R}_l$, is drawn, at a distance of $d_c/2$, obtaining the line b_u, then the tips of the wedges on the "C_u" side of the coupling aperture must not cross b_u. The tip of the second wedge is actually set on the b_u line. In this way, the illuminating beam towards the parabolic reflector is not perturbed by the absorber, which is sufficiently distant from it. This design insures a smooth transition through the use of the inverted wedge and a third wedge on top. The purpose of the third wedge is to make a more smooth transition from unabsorbed to fully aborbed rays. In fact, this third wedge does not have its tip on the b_u line, as the first and second wedge do, instead, it is not intercepted by the ray $\mathcal{R}_l'$. Therefore, since the transition of the field from the coupling aperture from unabsorbed to very absorbed is gradual, the field diffracted is a higher order effect with respect to the diffraction from the edges of the subreflector. Consequently,

through the adoption of the coupling aperture, the strong diffraction from the subreflector edges (S_u and S_l) is greatly attenuated at the expenses of introducing a much weaker diffraction from the tips of the wedge absorbers of the coupling aperture. The vertical heights of these three wedges is about the same, and it is $h_a/3$, where h_a is the thickness of the absorber layer.

For the design of the "C_l" side of the coupling aperture, one should consider that its purpose is to block the diffracted ray, $\mathcal{D}_{S_l}$, which goes from the point, S_l, to the point, I_{lm}. Three absorber wedges are stacked as shown in Figure 61 in order to accomplish this objective. The length of the path of this ray inside the absorber should be enough to insure a proper attenuation. Instead, the length of the path corresponding to the shadow boundary, $\mathcal{R}_{S_u}$, should be such that this reflected ray and the corresponding adjacent diffracted rays are time gated (see Section 3.7.5). If these rays are time gated, it is not important if they are not completely attenuated by the coupling aperture. If instead, the time gating offers a marginal or no attenuation for these rays (as it happens when the angle χ_c is close to 90^o), it becomes necessary to attenuate these rays by shaping accordingly the coupling aperture; i.e., by extending the stacked wedges so that they are crossed by these rays. The slope of these wedges is the same as that of the "C_u" side. The position of the tip, C_l', of the second wedge is determined as follows. A line parallel to the ray, $\mathcal{R}_u$, is drawn at a distance of $d_c/2$, obtaining the line b_l, then the tips of the wedges on the "C_l" side of the coupling aperture must not cross b_l. In this way, the illuminating beam towards the parabolic reflector is not perturbed by the absorber, which is sufficiently distant form it. The position of the tip, C_l'', of the third wedge is determined so as to be as close to the line b_l as possible without perturbing the ray $\mathcal{R}_{S_u'}$. The height of the wedges is the same, $h_a/3$.

With this procedure, the shape of the coupling aperture "follows" the shape

of the illuminating beam, reducing to a minimum the size of the coupling aperture itself, with consequent maximum decoupling between the two chambers. At the same time, the illuminating beam is not perturbed by interactions with the sides of the coupling aperture.

The design of the coupling aperture is then completed. However, it is important to realize that the qualitative explanations presented in this section are just a guideline, and they do not constitute a rigid prescription. Using a similar approach, a different discussion of the design of the coupling aperture is presented in [2].

From these design guidelines it is clear why a rolled edge on the lower part of the parabolic reflector offers a better performance than a continuation of the reflector in its lower part until its edge reaches the absorber on the floor of the upper chamber. In fact, such a parabolic continuation would reflect towards the target zone some of the rays diffracted by the tips of the wedge absorbers in the coupling aperture. Such rays instead are reflected by the rolled edge towards the absorber on the walls. A similar argument applies to the upper edge of the parabolic reflector.

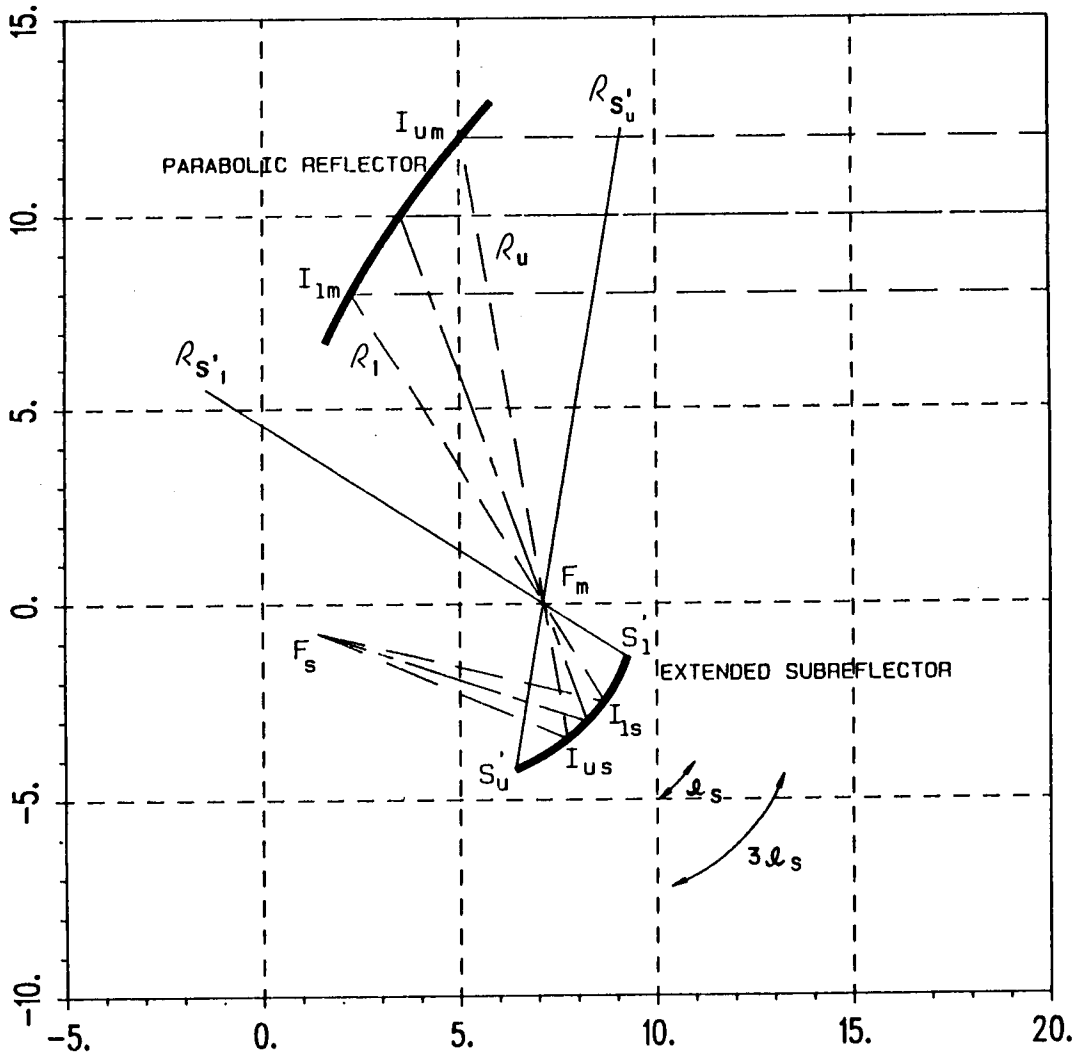

Figure 58: Extended subreflector. Linear dimensions are in feet.

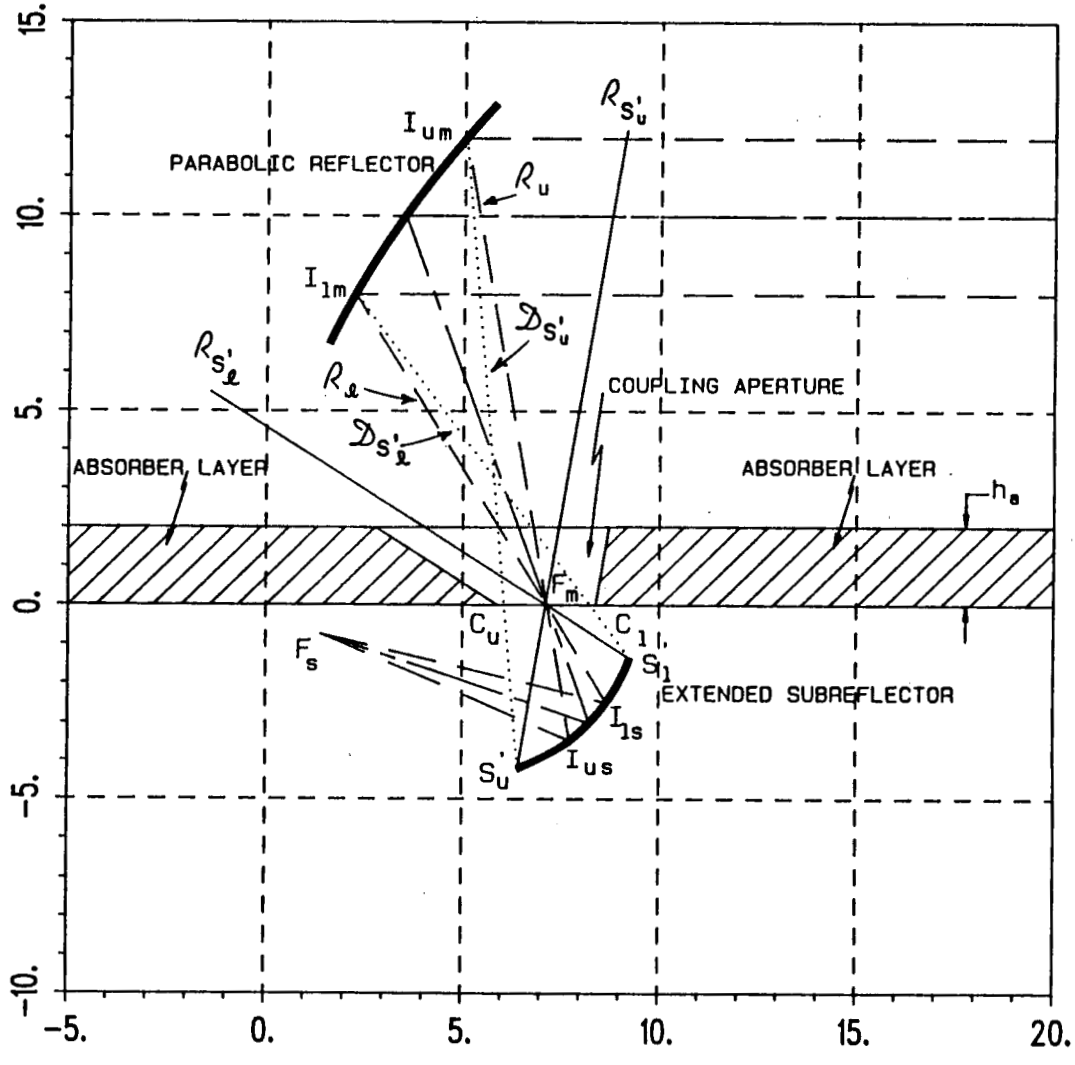

Figure 59: Extended subreflector with coupling aperture. Linear dimensions are in feet.

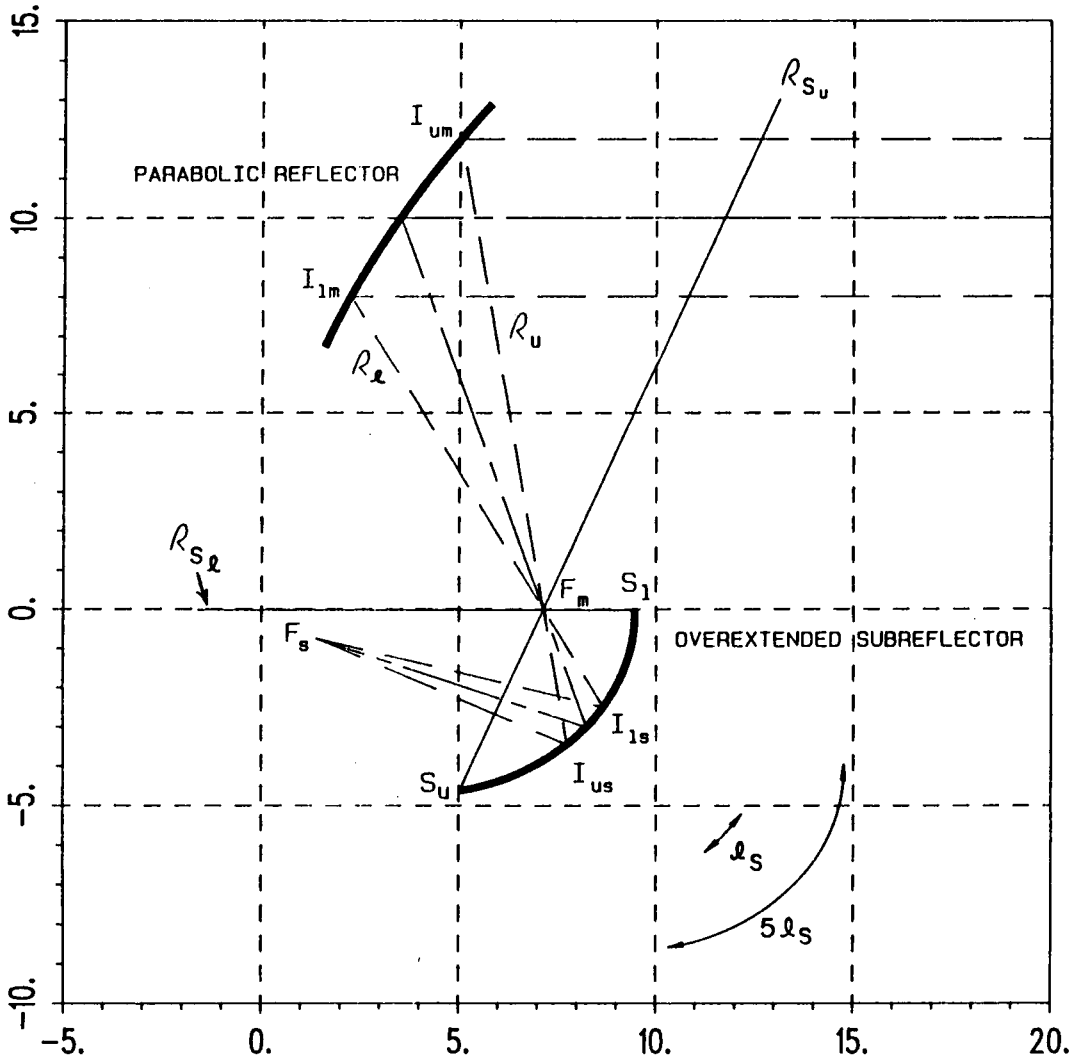

Figure 60: Overextended subreflector. Linear dimensions are in feet.

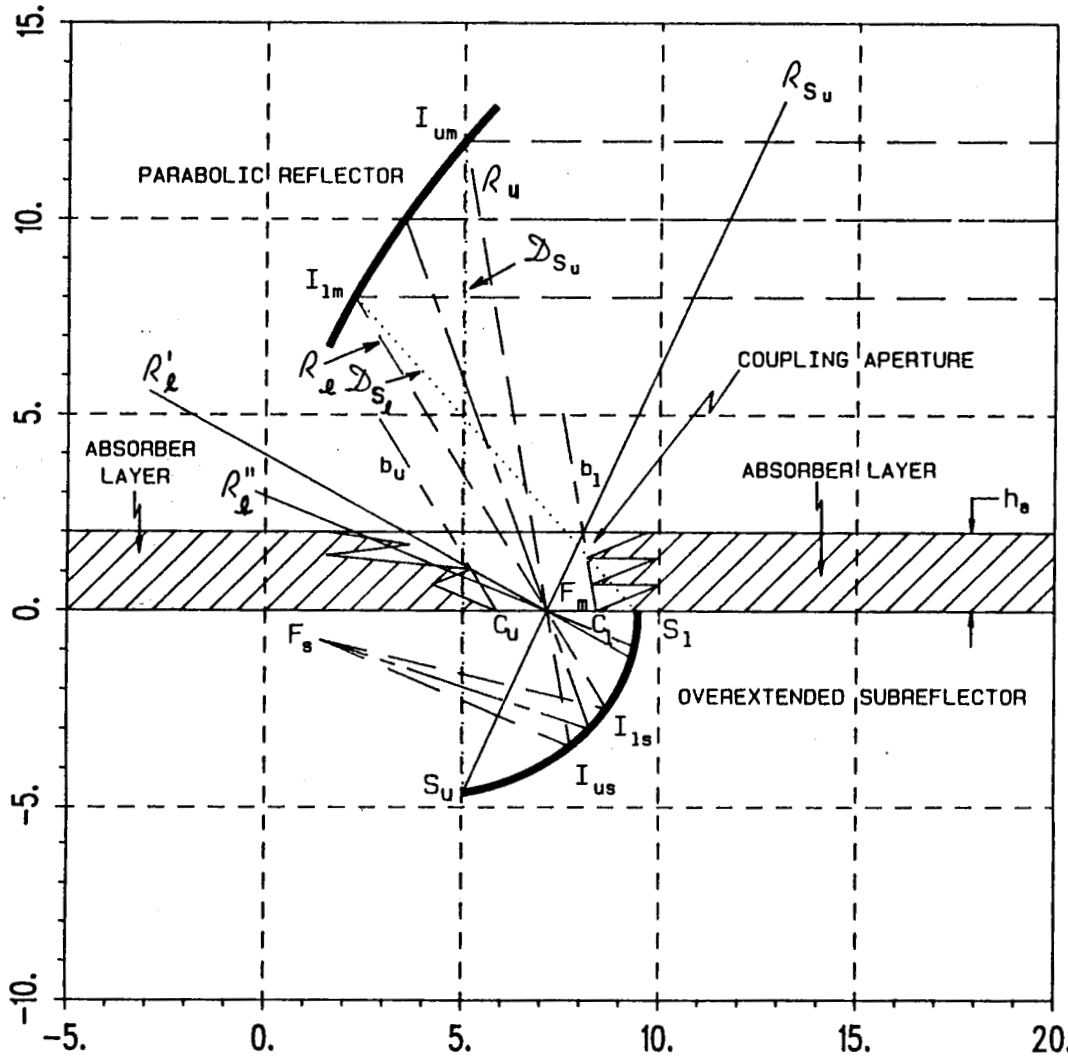

Figure 61: Overextended subreflector with coupling aperture. Linear dimensions are in feet.

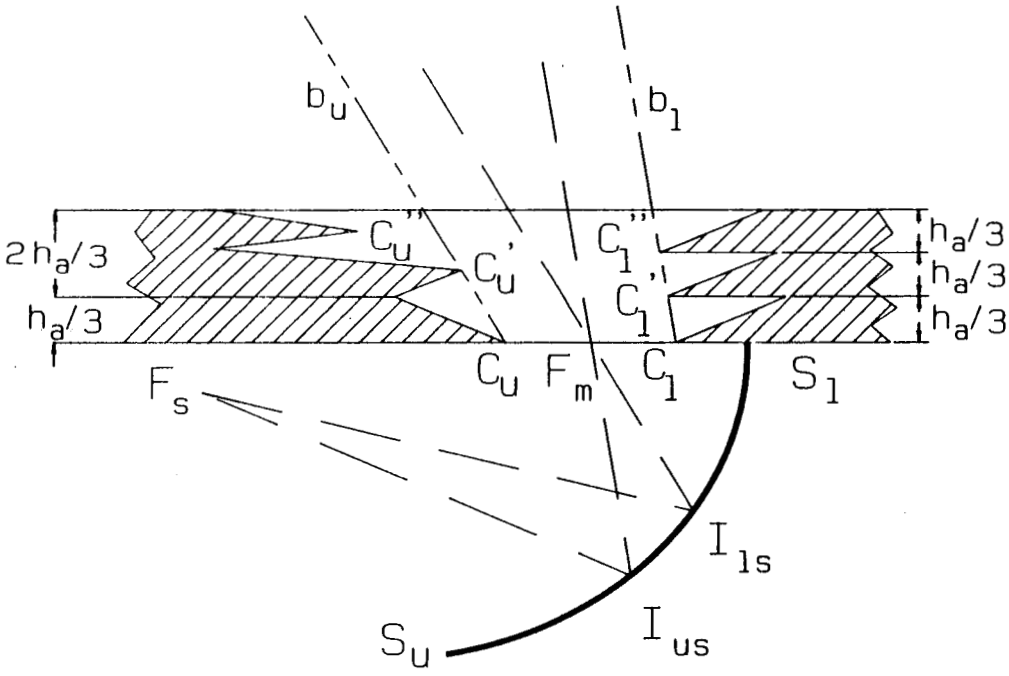

Figure 62: Detail of the coupling aperture.

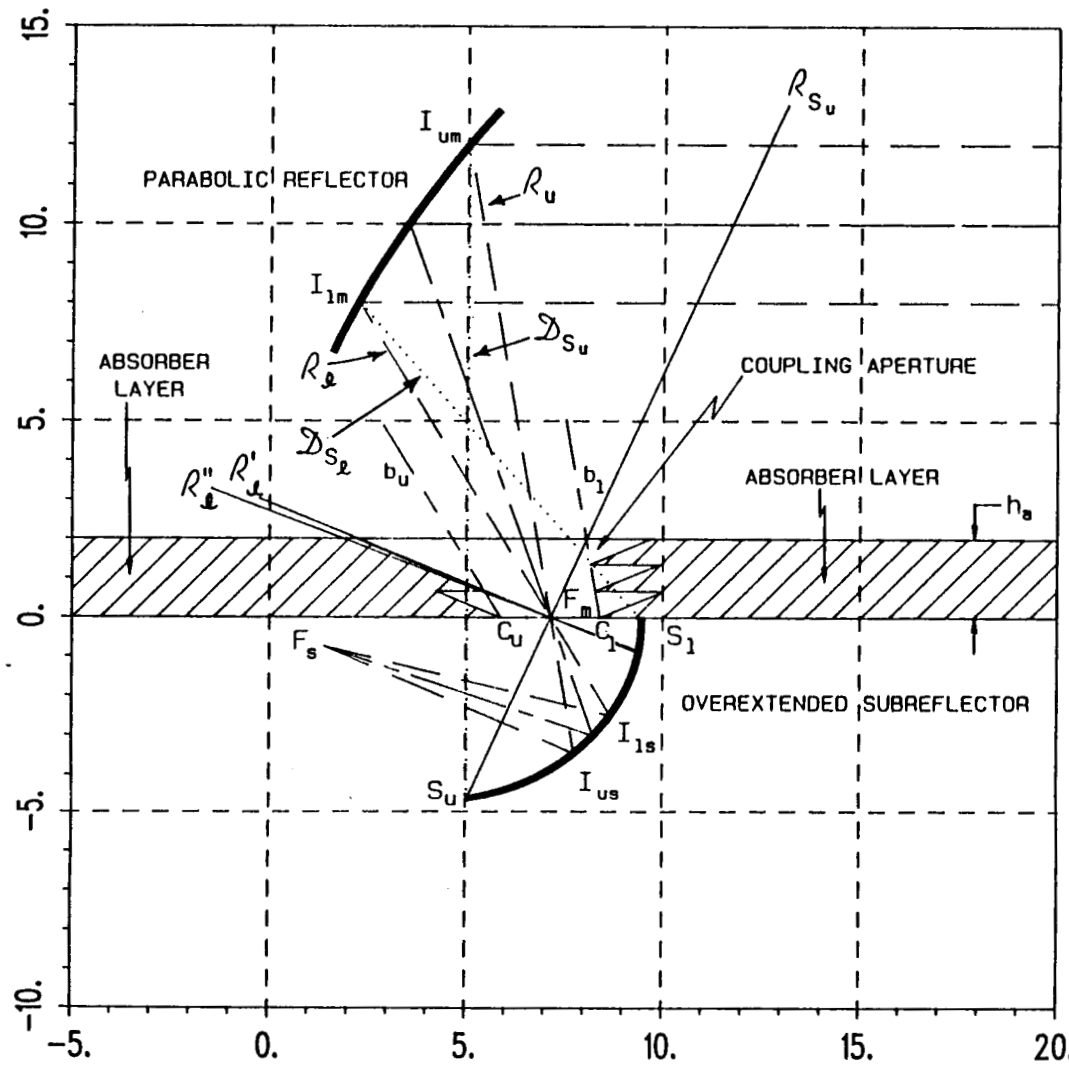

Figure 63: Overextended subreflector with strongly diffracting coupling aperture. Linear dimensions are in feet.

CHAPTER VII

DIRECT DESIGN EXAMPLES

7.1 INTRODUCTION

The GO design of a new compact range is presented in this chapter, and several other examples are discussed. This design is compared with the one obtained iteratively through a numerical procedure in Chapter IV, to show that the procedure called "direct design" gives better results; while, the design is performed in a straightforward way. Several design examples are also presented to show the system dependence associated with the various design parameters as shown in Figure 47. For each design, it is given a table with all the design parameters and an outline of the layout of the parabolic reflector and overextended subreflector. The outline shows a section in the x_m, y_m plane of the subreflector system, the upper and lower illuminating rays and the central ray are also shown, as, for instance, in Figure 64. From this layout it is possible to obtain an idea of the appearance of the design itself as well as of the size of the extended subreflector. Also, the design of the coupling aperture is performed by using this layout.

7.2 DIRECT DESIGN. AN EXAMPLE FOR COMPARISON

In this section a design is performed with the same specifications as the iterative design (ID) of Chapter IV, which was obtained by a trial-and-error procedure. The two different designs are then compared in order to realize how much is gained

by using the design equations instead of an iteration procedure. The specifications considered are as follows:

$$h_{pc} = 0.575' \tag{7.1}$$

$$z_{pc} = 0.0 \tag{7.2}$$

$$h_{um} = 11.5' \tag{7.3}$$

$$h_{lm} = 5.5', \text{ and} \tag{7.4}$$

$$Y = 8.0' \tag{7.5}$$

where Y is the length of the target zone in the y direction. Additionally, this design requires the following:

$$BMW_i^{xz} = 13.31^o \tag{7.6}$$

$$\chi_u = 90^o \text{ , and} \tag{7.7}$$

$$\text{gro}_{dB} = 0.1 \text{ dB .} \tag{7.8}$$

With these design parameters, the direct method computes the values shown in Table 3 (design DD1).

The values of the parameters of the two designs, ID and DD1, are shown side by side in Table 4 in order to perform a comparison.

In the DD1 design the focal distance has been reduced from $7.25'$ to about $6.58'$; consequently, the target zone can be slightly closer to the paraboloidal reflector vertex, and the upper chamber can be slightly smaller by the same amount. In this way, the effect of diffraction in the target zone from the junctions between the parabolic reflectors and the rolled edges are reduced, and the cost of the room should be reduced. The angles χ_u, χ_c and χ_l are reduced by about 4.0^o. This in turn reduces the diffraction from the coupling aperture, and simplifies the construction of the coupling aperture itself. The beamwidth BMW_{max}^{xz} is increased by

Table 3: Parameters for design DD1

$h_{pc} = 0.575'$	$z_{pc} = 0.0'$	$h_{um} = 11.5'$
$h_{lm} = 5.5'$	$BMW_i^{xz} = 13.31^o$	$Y = 8.0'$
$\alpha_c = -19.94765^o$	$\beta_c = -4.99295^o$	$\Delta_c = 14.9547^o$
$\alpha_u = -26.60265^o$	$\alpha_l = -13.29265^o$	$\chi_u = 97.71603^o$
$\chi_l = 134.6466^o$	$\Delta t = 9.058338$ ns	$BMW_{max}^{xz} = 29.90941^o$
$\chi_c = 114.2962^o$	$f = 6.581607'$	$\epsilon_s = 0.6026589$
$d_s = 6.606677'$	$p_s = 3.490487'$	$m = 4.033459$
$M = 3.919901$	$\text{gro}_{dB} = -0.08118021$ dB	

about 1.0^o, reducing, albeit slightly, the direct illumination of the coupling aperture by the feed, with consequent reduction of the related diffraction. The sizes of the subreflectors are very similar. On the other hand, the DD1 design has at least one shortcoming: a decrease in the time delay differential Δt of about 1 ns. An adequate duration of this differential is very important in order to insure the correct time-gating of the rays diffracted by the edges of the coupling aperture into the target zone, consequently, this time delay differential must be greater than a minimum value, which, in the present case, is of about 9 ns. One major advantage of the DD1 design is that the design is accomplished easily and in a very short time, while the trial-and-error approach requires a major effort, and is prone to errors, in other words, the designer could easily miss the optimal design. Notice that it could be possible to further improve the DD1 design by choosing for the quantity z_{pc} a value different from zero, as it is done in the examples of the next sections.

Table 4: Comparison between the ID design obtained via an iterative procedure and the DD1 design obtained via the direct method

ID	DD1
$h_{pc} = 0.575'$	$h_{pc} = 0.575'$
$z_{pc} = 1.278'$	$z_{pc} = 0.0'$
$h_{um} = 11.5'$	$h_{um} = 11.5'$
$h_{lm} = 5.5'$	$h_{lm} = 5.5'$
$BMW_i^{xz} = 13.31^o$	$BMW_i^{xz} = 13.31^o$
$Y = 8.0'$	$Y = 8.0'$
$\alpha = -19.95^o$	$\alpha_c = -19.94765^o$
$\beta = -5.5^o$	$\beta_c = -4.99295^o$
$\Delta_c = 14.45^o$	$\Delta_c = 14.9547$
$\chi_p = 119.24^o$	$\chi_c = 114.2962^o$
$\alpha_u = -26.875^o$	$\alpha_u = -26.60265^o$
$\alpha_l = -13.565^o$	$\alpha_l = -13.29265^o$
$\chi_u = 103.164^o$	$\chi_u = 97.71603^o$
$\chi_l = 138.454^o$	$\chi_l = 134.6466^o$
$\Delta\, t = 10.248$ ns	$\Delta\, t = 9.058338$ ns
$BMW_{max}^{xz} = 28.9^o$	$BMW_{max}^{xz} = 29.90941^o$
$f = 7.25'$	$f = 6.581607'$
$\epsilon_s = 0.5708$	$\epsilon_s = 0.6026589$
$d_s = 6.0'$	$d_s = 6.606677'$
$p_s = 3.639'$	$p_s = 3.490487'$
$m = 3.662$	$m = 4.033459$
$M = 3.5583$	$M = 3.919901$
$\text{gro}_{dB} = -0.0819$ dB	$\text{gro}_{dB} = -0.08118021$ dB

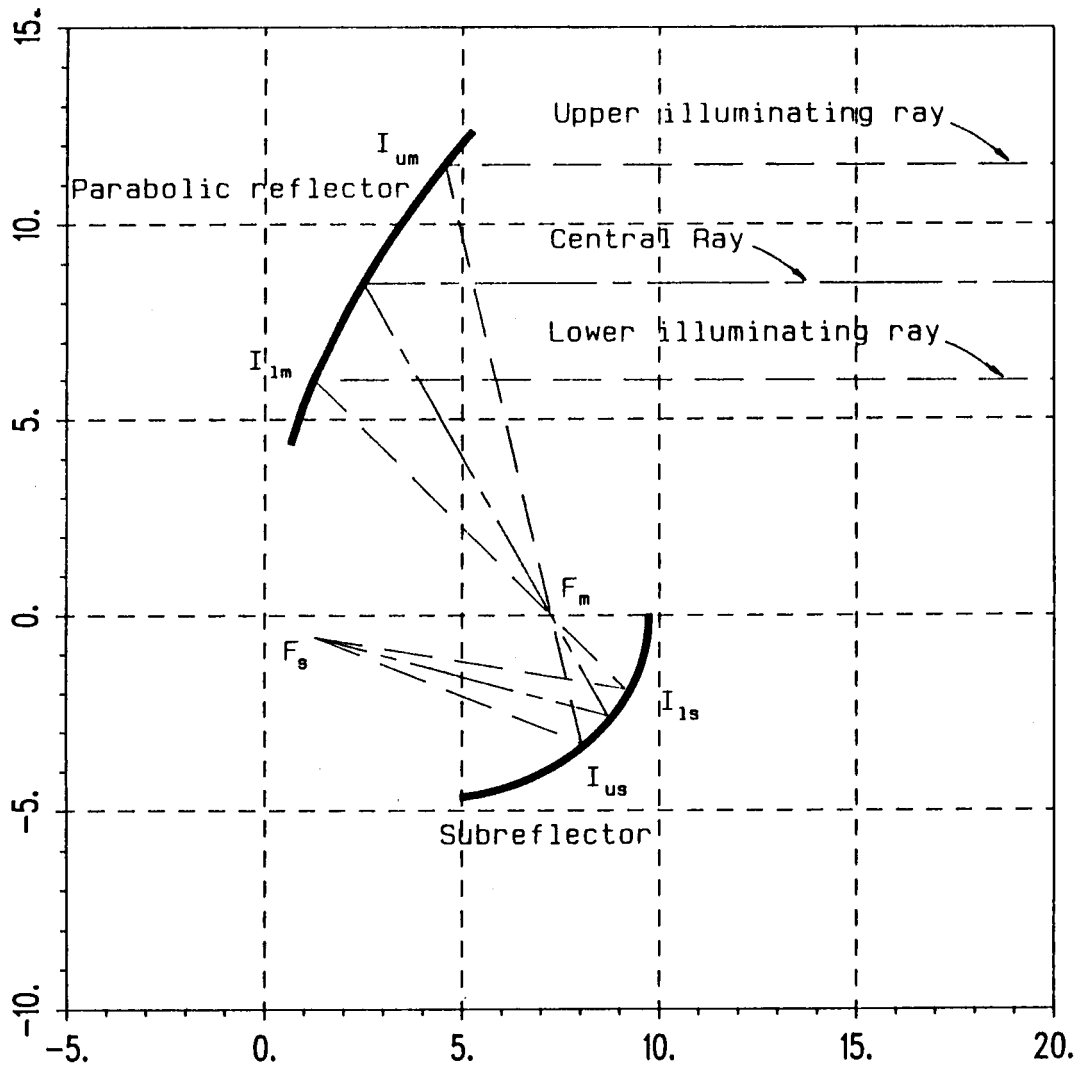

Figure 64: Layout of the ID design in the x_m z_m plane, showing the main reflector, the subreflector, the upper and lower illuminating rays and the central ray. Linear dimensions are in feet.

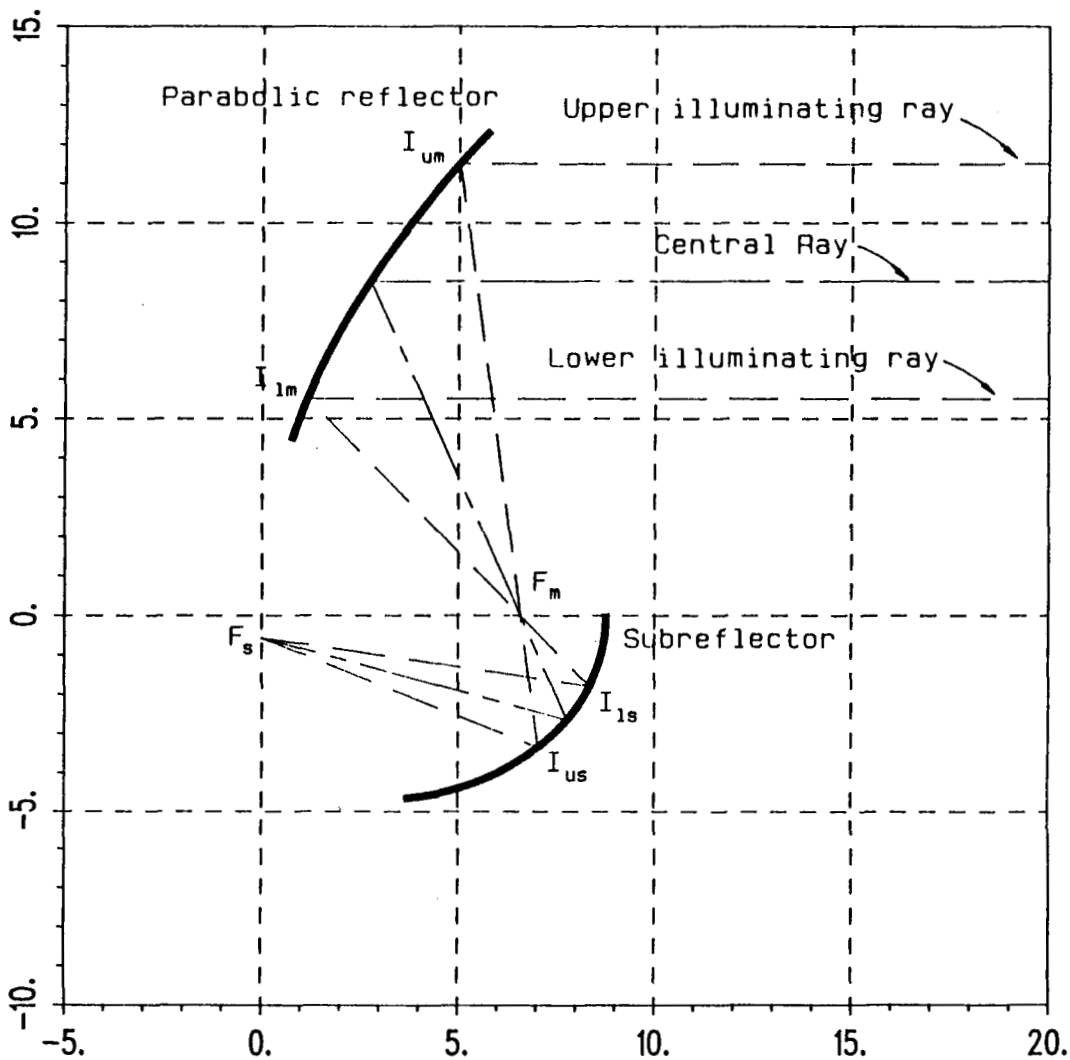

Figure 65: Layout of the DD1 design in the x_m z_m plane, showing the main reflector, the subreflector, the upper and lower illuminating rays and the central ray. Linear dimensions are in feet.

7.3 DIRECT DESIGN. REQUIREMENTS FOR THE GO DESIGN OF A NEW COMPACT RANGE

The requirements on the GO compact range are reviewed in this section in order to improve these designs.

A broadband ridged horn has been designed and built to be used as a feed over the full frequency range of operation (2-18 GHz). Its beamwidth at the highest frequency of operation is about 12^o. It is then desirable that the parameter BMW_i^{xz} be reduced from 13.31^o to a value closer to 12^o in order to match the design to the actual performance of the feed. At the lower frequencies, the beamwidth of the feed is greater and the consequent spillover and higher incident field on the edges of the extended subreflector must be accepted in order to provide the desired bandwidth from just one feed antenna.

In the ID design, the absorber layer between the upper and lower chamber is arranged in a symmetric fashion, so that the plane which represents the boundary between the two chambers (the "ceiling" of the lower chamber and the "floor" of the upper chamber) is half way in the middle of the absorber layer. In the new design instead the absorber layer is moved entirely inside the upper chamber, as shown in Figure 53. This provides two advantages:

- the upper chamber is made higher (which leads naturally to better values for several design parameters) without any waste of room,
- the layout of the lower chamber is much easier, since the feed antenna can be moved farther from the absorber layer.

It is desirable to increase the distance of the phase center of the feed antenna from the "ceiling" of the lower chamber, h_{pc}, in order to make the mechanical arrangement of the feed easier.

It is desirable to increase the angle Δ_c, where $\Delta_c = \alpha_c - \beta_c$. In this way the field incident on the absorber on the walls of the lower chamber from the feed is reduced, which also reduces the field incident from the feed on the edges of the coupling aperture.

It is desirable to decrease the angle χ_c, which represents the tilt angle of the axis of the coupling aperture, in order to make the design of the coupling aperture itself easier and to reduce the interactions of the illuminating beam with the absorber on the sides of the coupling aperture. On this regard, the ideal value of the angle would be 90^o, although this value cannot be adopted because in turn it would reduce the value of the time delay differential Δt to an unacceptable low value by reducing the value of the focal distance f. Recall that Δt is the time differential between rays from the coupling aperture directly to the target zone versus the desired path through the main reflector and then the target zone.

The size of the extended subreflector for the ID design is fairly large, but still acceptable. It would be desirable to reduce the size of the extended subreflector, or, at least, not to increase it.

The taper of the reflected field and the time delay differential Δt of the ID design are very good, and it is desirable to maintain this level of performance in the new design.

7.4 DIRECT DESIGN. GO DESIGN OF A NEW COMPACT RANGE

The design of a new generation compact range, called the FD design, is presented. It is shown how its characteristics satisfy the requirements on the design and represent a reasonable compromise between the conflicting requirements for the compact range itself. In the Section 7.6 instead, several designs are presented, obtained by changing the values of some design parameters around the values of

the FD design. It is shown that, in each case, any improvement is obtained at the expense of some other requirement, and the resulting design is not as acceptable.

The parameters of the FD design are shown in Table 5 and its layout in the x_m, z_m plane is shown in Figure 66.

From the specifications, the height of the target zone is $6'$, while the thickness of the absorber between the two chambers is $2'$. The lower side of the absorber layer is set at $x_m = 0$ as shown in Figure 53. In other words, the absorber layer is all in the upper chamber. By the scheme of Section 5.1.1 then, the height of the upper chamber is $20'$, $h_{um} = 14'$ and $h_{um} = 8'$. The horizontal width of the target zone is $Y = 8'$. The height of the phase center of the feed is set to $h_{pc} = 0.75'$, in fact, a smaller distance would be difficult to achieve in practice due to the physical sizes of the feed horn and the mounting support; while, a larger value would degrade the design. The tilt angle, χ_c, is chosen to be 110^o for two reasons. In fact, the time delay differential Δt is dependent only on the choice of f, the distance z_{tb} of the target zone from the vertex V of the main reflector, and h_{um}. The distance z_{tb} depends on the acceptable amount of diffraction from the edges of the main reflector (especially from the lower edge, which is further away from the target zone and results in the largest diffraction contribution), as well as on the timing of the pulsed radar system [17]. This distance z_{tb} is found to be $20'$ for the present case. The height h_{tm} is obtained by choosing h_{um} and h_{lm}, and the only free parameter left in Equation (5.1) is the tilt angle, χ_c; then, a choice of this angle completely determines f. Therefore, χ_c is chosen to be 110^o in order to make Δt acceptable (i.e., close to the value of 9.5 ns). The parameter BMW_i^{xz} is about 12.3^o, which is close to the value 12^o of the beamwidth at the highest frequency of operation (18 GHz) of the chosen feed horn. At lower frequencies, the feed pattern broadens with resulting spillover, but the system has to be designed

for the smallest value of the beamwidth, in order to insure adequate illumination of the target zone at all frequencies. Since at the lower frequencies the actual feed beamwidth are larger than the design parameter BMW_i^{xz}, the subreflector is overextended to reduce the intensity of the field illuminating its edges, which, in turn, reduces diffraction. The size of the extended subreflector for this design is acceptable, although it is fairly large. The "rule of thumb" adopted is to obtain a subreflector which can be approximately inscribed in a square with $5'$ sides. The tilt angle of the axis of the feed with respect to a horizontal line, Δ_c (where $\Delta_c = \beta_c - \alpha_c$), is about 17.5^o. It would be desirable to increase the value of this parameter, in order to minimize the direct illumination of the coupling aperture from the feed, with consequent diffraction into the target zone and towards the main reflector, but an increase of Δ_c can only be achieved at the expense of other, equally important parameters in the design (for instance, the height h_{pc}, which cannot be reduced below a minimum amount). At the same time, the distance z_{pc} cannot be increased beyond a certain amount, in that the feed might illuminate directly the upper chamber through the coupling aperture. In this design z_{pc} is about $1.4'$, and any spillover is avoided. The taper of the reflected field, gro_{dB}, is about -0.07 dB, better than the required value of -0.1 dB. The design of the coupling aperture is described in Section 6.2, where this case is used as an example. The layout of the FD design is shown In Figure 67 together with the coupling aperture. It can be seen that the ray $\mathcal{D}_{S_u}$, which is the diffracted ray illuminating the upper edge I_{um} of the main reflector, passes through an adequate thickness of absorber to insure adequate attenuation. The attenuation could be increased by further overextending the subreflector. Any other ray diffracted by the edge S_u, which illuminates the main reflector and is reflected into the target zone, passes through an even greater thickness of absorber, and is adequately attenuated.

Table 5: Parameters for the FD design

$h_{pc} = 0.75'$	$z_{pc} = 1.4'$	$h_{um} = 14.0'$
$h_{lm} = 8.0'$	$\chi_c = 110.0^o$	$Y = 8.0'$
$\alpha_c = -24.14653^o$	$\beta_c = -6.627610^o$	$\Delta_c = 17.51892^o$
$\alpha_u = -30.31467^o$	$\alpha_l = -17.97840^o$	$\chi_u = 96.58686^o$
$\chi_l = 126.0258^o$	$\Delta t = 9.47662$ ns	$BMW^{xz}_{max} = 35.03785^o$
$BMW^{xz}_i = 12.33628^o$	$f = 7.854814'$	$\epsilon_s = 0.5739332$
$d_s = 6.498242'$	$p_s = 3.796371'$	$m = 3.694099$
$M = 3.544329$	$\text{gro}_{dB} = -0.06976044$ dB	

The reflection shadow boundary ray $\mathcal{R}_{S_u}$ is sufficiently removed from the target zone, and any diffracted ray from the edge S_u directed towards the target zone is attenuated by the absorber wedges in the coupling aperture. These rays are also time-gated effectively, since the time difference between the diffracted rays and any ray of the plane wave illuminating the coupling aperture is greater than Δt, which, for this design, is about 9.5 ns (nanoseconds). With respect to the edge S_l of the subreflector, the diffracted ray, $\mathcal{D}_{S_l}$, which is directed towards the lower edge I_{lm} of the main reflector, passes a sufficiently thick portion of absorber to be properly attenuated, while all the other diffracted rays, which are reflected by the parabolic reflector into the target zone, passes through an even thicker portion of absorber. There are no problems related to the reflection shadow boundary of the edge S_l, since it is directed towards the wall behind the main reflector or towards the lower rolled edge.

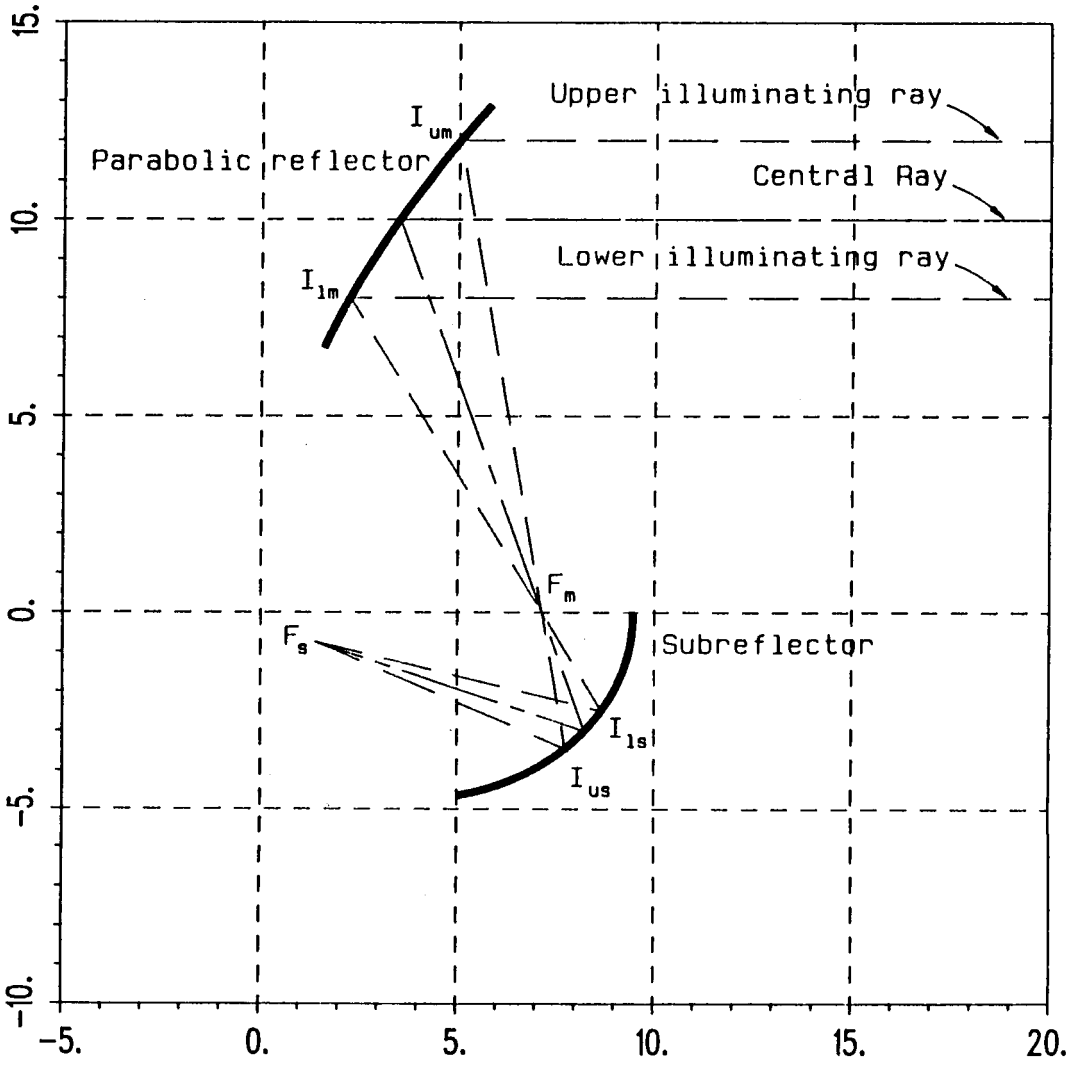

Figure 66: Layout of the final FD design in the x_m z_m plane, showing the main reflector, the subreflector, the upper and lower illuminating rays and the central ray. Linear dimensions are in feet.

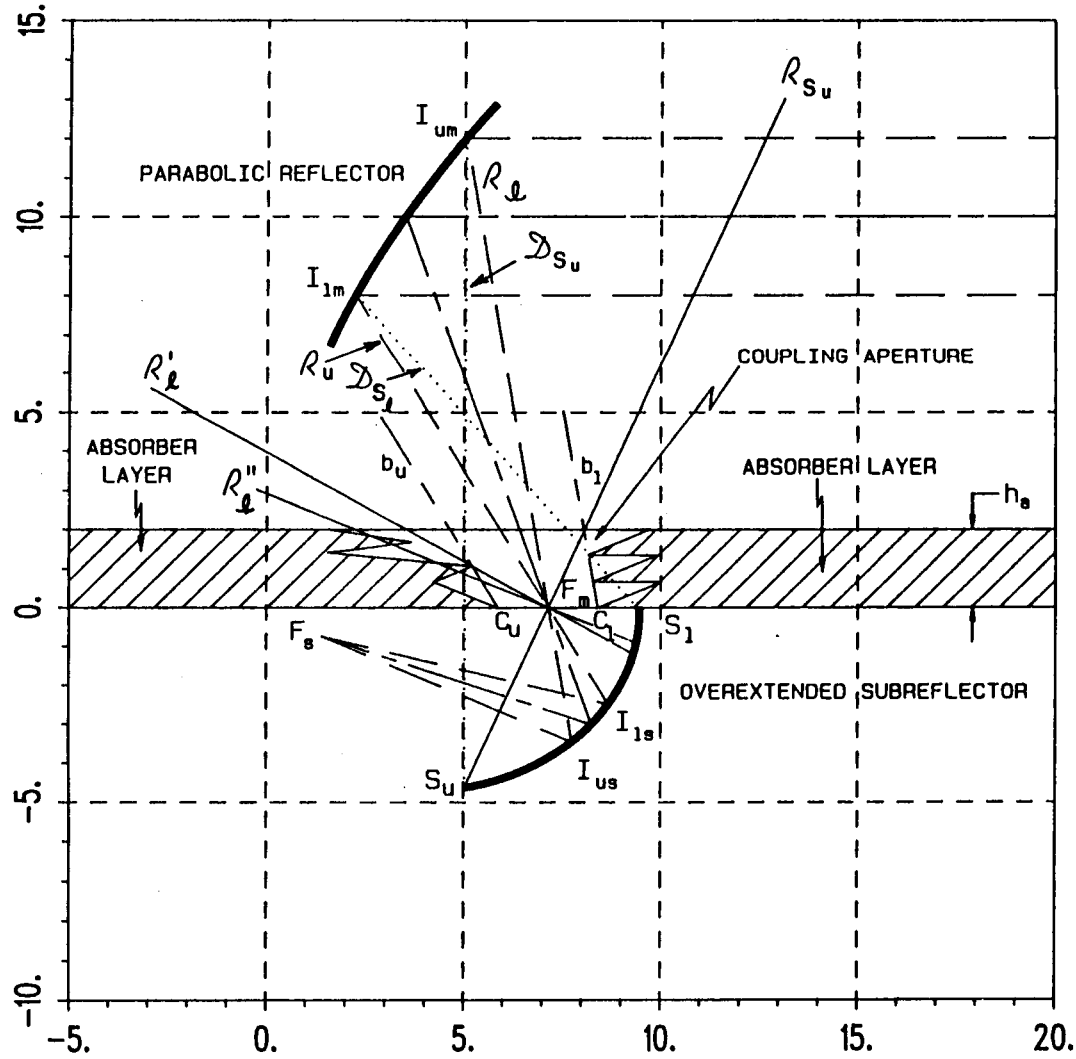

Figure 67: Layout of the final FD design in the x_m z_m plane, with first-cut design of the coupling aperture. Linear dimensions are in feet.

7.5 DIRECT DESIGN. COMPARISON OF THE ID AND FD DESIGNS

In this section a comparison is made between the ID (previous compact range) and FD (new generation compact range) designs. The parameters of two designs are shown, side by side, on Table 6.

From this table it can be seen that the FD design represents an overall improvement over the ID one, and that the requirements of Section 7.3 are satisfied.

The new design represents a major improvement from a constructive viewpoint: the lower chamber is easier to build, having made a sensible choice for the location of the absorber layer, and having chosen a larger value for the distance h_{pc}, so is the coupling aperture, since the central ray coming from the main reflector (which coincides with the axis of the coupling aperture) is closer to vertical by about 9.2^o, and this in turn allows one to use a narrower coupling aperture. The angle Δ_c is increased by about 3^o, while the beamwidth BMW_i^{xz} is decreased by about 1^o, in this way the parameter BMW_i^{xz} is closer to the performance of the actual feed; while, the field incident from the feed on the absorber on the walls of the lower chamber and on the coupling aperture is weaker. The distance of the target zone from the absorbers in the upper chamber is $6'$; while, it is only $4.5'$ for the ID design. Therefore, the clutter from the absorbing material is lower for the new design, and the distance of the rolled edges from the absorber is greater, reducing their illumination. The size of the subreflector for the FD design is larger, but the overextended subreflector itself is more centrally illuminated. In other words, the overextensions on both sides of the subreflector are approximately the same size. On the other hand, the overextension for the ID design is limited on one side by lack of suitable room. The gro (taper of the reflected field) is smaller

Table 6: Comparison between the ID design (previous compact range) and the FD design (new generation compact range)

ID	FD
$h_{pc} = 0.575'$ $z_{pc} = 1.278'$ $h_{um} = 11.5'$ $h_{lm} = 5.5'$ $Y = 8.0'$	$h_{pc} = 0.75'$ $z_{pc} = 1.4'$ $h_{um} = 14.0'$ $h_{lm} = 8.0'$ $Y = 8.0'$
$\alpha = -19.95^o$	$\alpha_c = -24.14653^o$
$\beta = -5.5^o$	$\beta_c = -6.627610^o$
$\Delta_c = 14.45^o$	$\Delta_c = 17.51892$
$\chi_p = 119.24^o$	$\chi_c = 110.0^o$
$\alpha_u = -26.875^o$	$\alpha_u = -30.31467^o$
$\alpha_l = -13.565^o$	$\alpha_l = -17.97840^o$
$\chi_u = 103.164^o$	$\chi_u = 96.58686^o$
$\chi_l = 138.454^o$	$\chi_l = 126.0258^o$
$\Delta\, t = 10.248$ ns	$\Delta\, t = 9.47662$ ns
$BMW^{xz}_{max} = 28.9^o$	$BMW^{xz}_{max} = 35.03785^o$
$BMW^{xz}_{i} = 13.31^o$	$BMW^{xz}_{i} = 12.33628^o$
$f = 7.25'$	$f = 7.854814'$
$\epsilon_s = 0.5708$	$\epsilon_s = 0.5739332$
$d_s = 6.0'$	$d_s = 6.498242'$
$p_s = 3.639'$	$p_s = 3.796371'$
$m = 3.662$	$m = 3.694099$
$M = 3.5583$	$M = 3.544329$
$\text{gro}_{dB} = -0.0819$ dB	$\text{gro}_{dB} = -0.06976044$ dB

for the FD design, but it is satisfactory in both cases. The ID design presents the only advantage of having a larger Δt, but this quantity is still satisfactory for the FD design.

In conclusion, the FD design represents a better compromise, especially from the point of view of ease of construction.

7.6 DIRECT DESIGN. EXAMPLES OF APPLICATION OF THE DESIGN PROCEDURES

Several compact range design examples are evaluated in terms of changing the the input design parameters, one at a time, around the values of the FD design. It is shown that, in each case, any improvement is obtained at the expense of some other requirement, and the design obtained is not as acceptable.

7.6.1 DIRECT DESIGN. EXAMPLES DD2 AND DD3

In the design examples, DD2 and DD3, the quantity h_{pc} is varied by $0.5'$, about the value of the FD design; while, the other input quantities are kept constant. The design values are shown in Table 7, with the layouts illustrated in Figures 68 and 69. The trends of the parameters are shown in Table 8. The advantages and disadvantages offered by each design are briefly summarized.

In design DD2, the height h_{pc} is set to $0.25'$. This in itself represents an unreasonable assumption, since then it would be impossible to place the feed and the supporting structure within this small dimension, but it is useful as an example. The size of the subreflector is reduced, the illuminating beamwidth BMW_i^{xz} is reduced to about 7.22^o, and the $|\text{gro}_{dB}|$ is reduced to about 0.02 dB, which are improvements. Instead, the magnification M has increased to about 6, making the tolerances in the subreflector more critical, and the tilt angle Δ_c has decreased to

about 11.3°, a value completely unacceptable. The other quantities have remained constant.

In design DD3, the height h_{pc} is set to 1.25′. The size of the subreflector is increased to an unacceptable value, the illuminating beamwidth BMW_i^{xz} is increased to about 15.7°, a fairly large value, and the $|\text{gro}_{dB}|$ is increased to about 0.113 dB, which is slightly greater than the specified value of 0.1 dB. Instead, the magnification M has decreased to about 2.7, making the tolerances in the subreflector less critical, and the tilt angle Δ_c has increased to about 21.0°, a very good value. The other quantities have remained constant.

7.6.2 DIRECT DESIGN. EXAMPLES DD4 AND DD5

In the design examples, DD4 and DD5, the quantity z_{pc} is varied by 1.4′ about the value for the FD design; while, the other input quantities have been kept constant. The design values are shown in Table 9, with the layouts illustrated in Figures 70 and 71. The trends of the parameters are shown in Table 10. The advantages and disadvantages offered by each design are shown here. In the DD4 design, the distance z_{pc} is set to 0′. This is a reasonable assumption, and would optimize the layout of the lower chamber. The illuminating beamwidth BMW_i^{xz} is reduced to about 11.2°, and the $|\text{gro}_{dB}|$ is reduced to about 0.058 dB, which are slight improvements. Instead, the size of the subreflector is increased, the magnification M has increased to about 3.9, and the tilt angle Δ_c has decreased to about 16.3°, a small value. The other quantities have remained constant. This design is slightly inferior to the FD design, especially for the larger size of the subreflector. In the DD5 design, the distance z_{pc} is set to 2.8′. This is still a reasonable value. The size of the subreflector is decreased, the magnification M has decreased to about 3.15, and the tilt angle Δ_c has increased to about

Table 7: Comparison between the final FD design and the DD2, DD3 designs obtained by varying the quantity h_{pc}

	DD2	FD	DD3
h_{pc}	$0.25'$	$0.75'$	$1.25'$
z_{pc}	$1.4'$	$1.4'$	$1.4'$
h_{um}	$14.0'$	$14.0'$	$14.0'$
h_{lm}	$8.0'$	$8.0'$	$8.0'$
χ_c	110.0^o	110.0^o	110.0^o
Y	$8.0'$	$8.0'$	$8.0'$
α_c	-13.55333^o	-24.14653^o	-31.93641^o
β_c	-2.217950^o	-6.627610^o	-10.95989^o
Δ_c	11.33538^o	17.51892^o	20.97651^o
α_u	-17.16593^o	-30.31467^o	-39.78915^o
α_l	-9.940739^o	-17.97840^o	-24.08365^o
χ_u	96.58686^o	96.58686^o	96.58686^o
χ_l	126.0258^o	126.0258^o	126.0258^o
Δt	9.47662 ns	9.47662 ns	9.47662 ns
BMW_{max}^{xz}	22.67076^o	35.03785^o	41.95302^o
BMW_i^{xz}	7.225187^o	12.33628^o	15.70551^o
f	$7.854814'$	$7.854814'$	$7.854814'$
ϵ_s	0.7198344	0.5739332	0.4978243
d_s	$6.459805'$	$6.498242'$	$6.574732'$
p_s	$2.162013'$	$3.796371'$	$4.966936'$
m	6.138635	3.694099	2.98267
M	6.055425	3.544329	2.782308
gro_{dB}	-0.02396253 dB	-0.06976044 dB	-0.1129238 dB

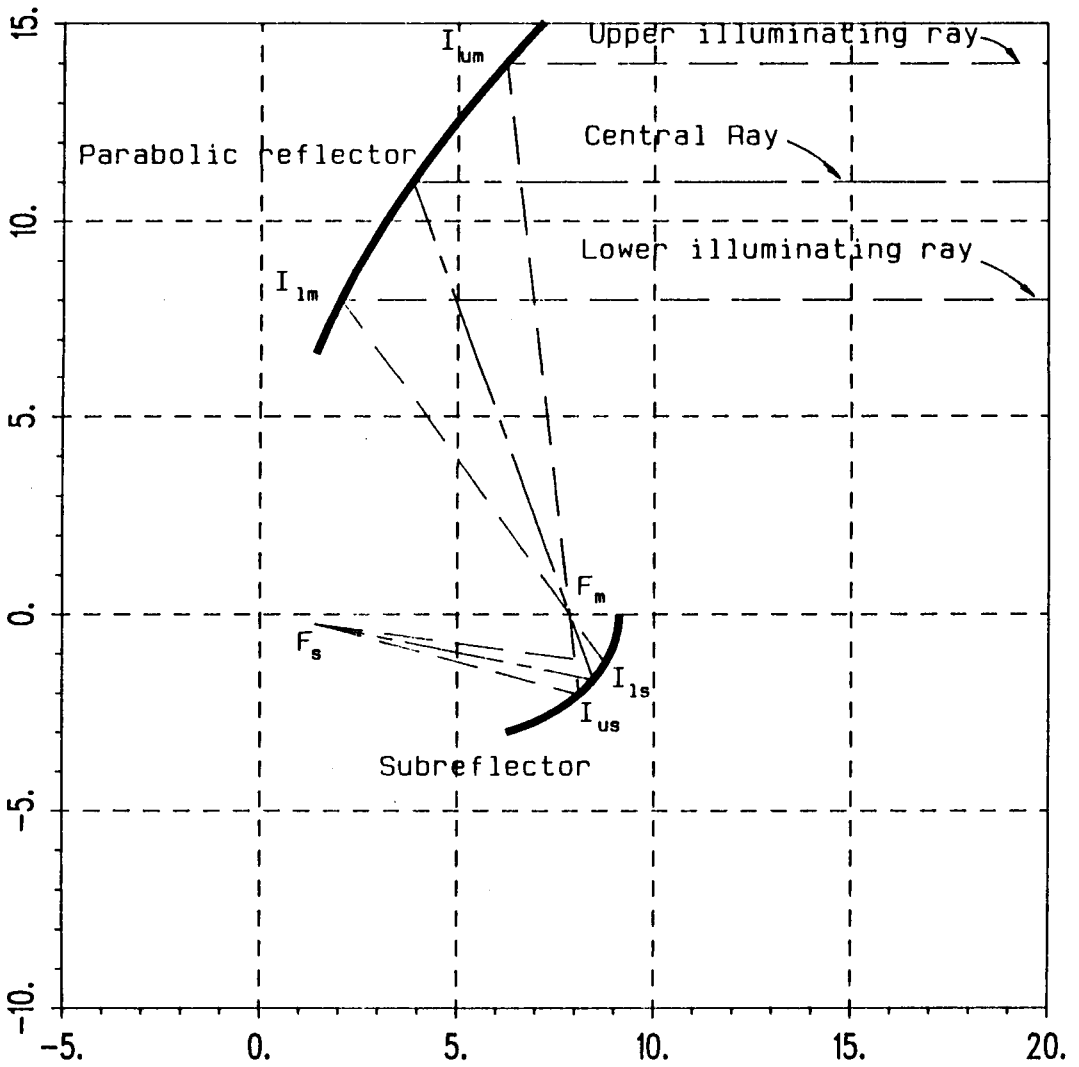

Figure 68: Layout of the DD2 design in the x_m z_m plane, showing the main reflector, the subreflector, the upper and lower illuminating rays and the central ray. Linear dimensions are in feet.

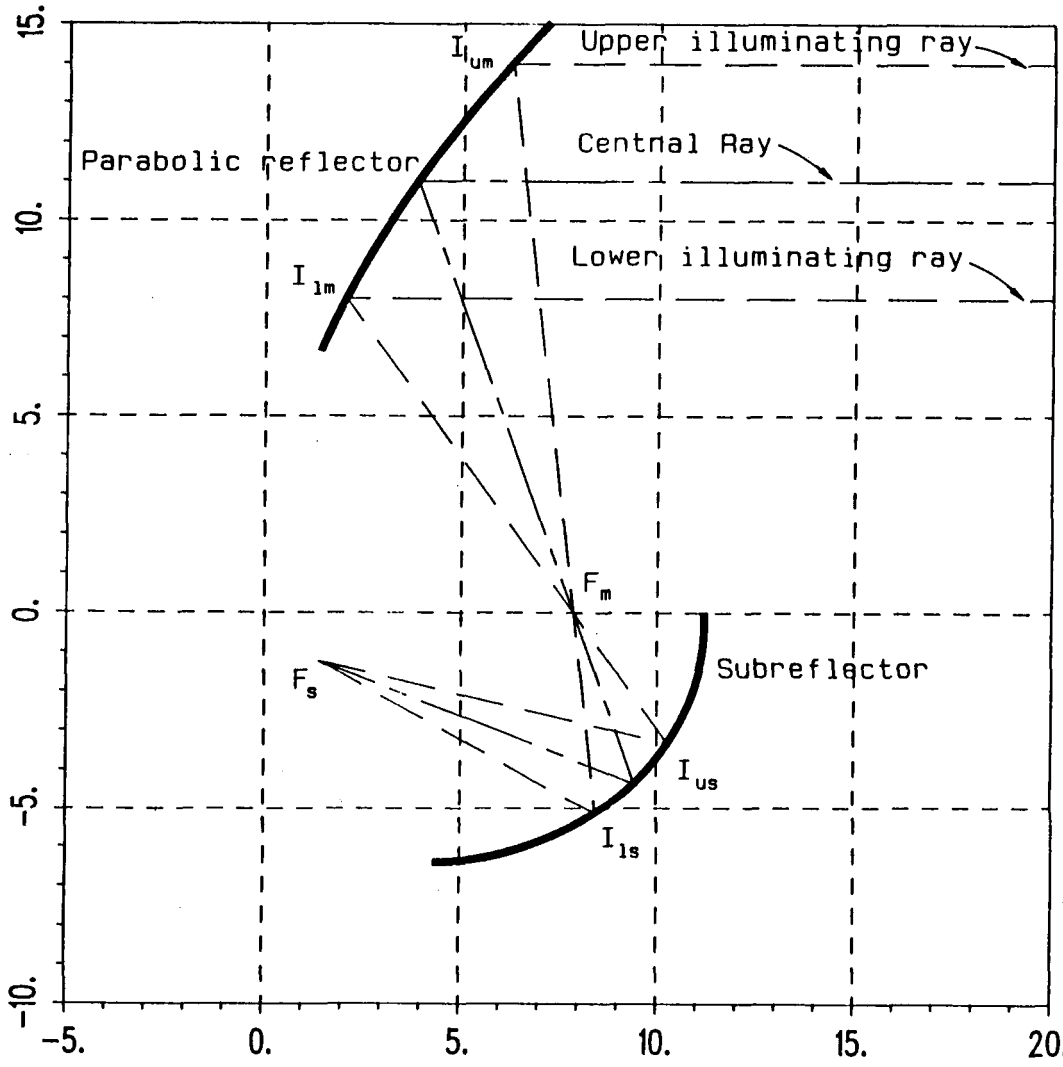

Figure 69: Layout of the DD3 design in the x_m z_m plane, showing the main reflector, the subreflector, the upper and lower illuminating rays and the central ray. Linear dimensions are in feet.

Table 8: Effect of increasing h_{pc} (designs DD2 and DD3)

$\|\alpha_c\|$	increasing	f	constant
$\|\beta_c\|$	increasing	ϵ_s	decreasing
Δt	constant	d_s	increasing
$\|\alpha_u\|$	increasing	p_s	increasing
$\|\alpha_l\|$	increasing	m	decreasing
χ_u	constant	M	decreasing
χ_l	constant	$\|\text{gro}_{dB}\|$	increasing
BMW^{xz}_{max}	increasing	Δ_c	increasing
BMW^{xz}_i	increasing		

19.1^o, a good value, which represent slight improvements. Instead, the illuminating beamwidth BMW^{xz}_i is increased to about 13.8^o, and the $|\text{gro}_{dB}|$ is increased to about 0.088 dB. The other quantities have remained constant. This design offers some advantages over the FD design, but FD is, on the overall, preferable because its value of BMW^{xz}_i is close to the value of 12^o, which is the actual beamwidth of the feed.

7.6.3 DIRECT DESIGN. EXAMPLES DD6 AND DD7

In the DD6 and DD7 design examples the quantities h_{um} and h_{lm} are varied by $1.0'$ from the values of the FD design; while, the other input quantities are kept constant. The design values are shown in Table 11, with the layouts illustrated in Figures 72 and 73. The trends of the parameters are shown in Table 12. The advantages and disadvantages offered by each design are briefly shown.

In the DD6 design, the heights, h_{um} and h_{lm}, are set to $15.0'$ and $9.0'$, respectively. In other words, the height of the target zone is increased by $1'$. This is a reasonable assumption. The illuminating beamwidth, BMW^{xz}_i, is reduced to

Table 9: Comparison between the final FD design and the DD4, DD5 designs obtained by varying the quantity z_{pc}

	DD4	FD	DD5
z_{pc}	$0.0'$	$1.4'$	$2.8'$
h_{pc}	$0.75'$	$0.75'$	$0.75'$
h_{um}	$14.0'$	$14.0'$	$14.0'$
h_{lm}	$8.0'$	$8.0'$	$8.0'$
χ_c	110.0^o	110.0^o	110.0^o
Y	$8.0'$	$8.0'$	$8.0'$
α_c	-21.73335^o	-24.14653^o	-27.57522^o
β_c	-5.454237^o	-6.627610^o	-8.439608^o
Δ_c	16.27911^o	17.51892^o	19.13561^o
α_u	-27.34611^o	-30.31467^o	-34.50481^o
α_l	-16.12058^o	-17.97840^o	-20.64564^o
χ_u	96.58686^o	96.58686^o	96.58686^o
χ_l	126.0258^o	126.0258^o	126.0258^o
$\Delta\, t$	9.47662 ns	9.47662 ns	9.47662 ns
BMW^{xz}_{max}	32.55822^o	35.03785^o	38.27123^o
BMW^{xz}_{i}	11.22553^o	12.33628^o	13.85916^o
f	$7.854814'$	$7.854814'$	$7.854814'$
ϵ_s	0.6023936	0.5739332	0.5376679
d_s	$7.890527'$	$6.498242'$	$5.110146'$
p_s	$4.172710'$	$3.796371'$	$3.378359'$
m	4.030100	3.694099	3.325896
M	3.895684	3.544329	3.154068
gro_{dB}	-0.05778445 dB	-0.06976044 dB	-0.08799943 dB

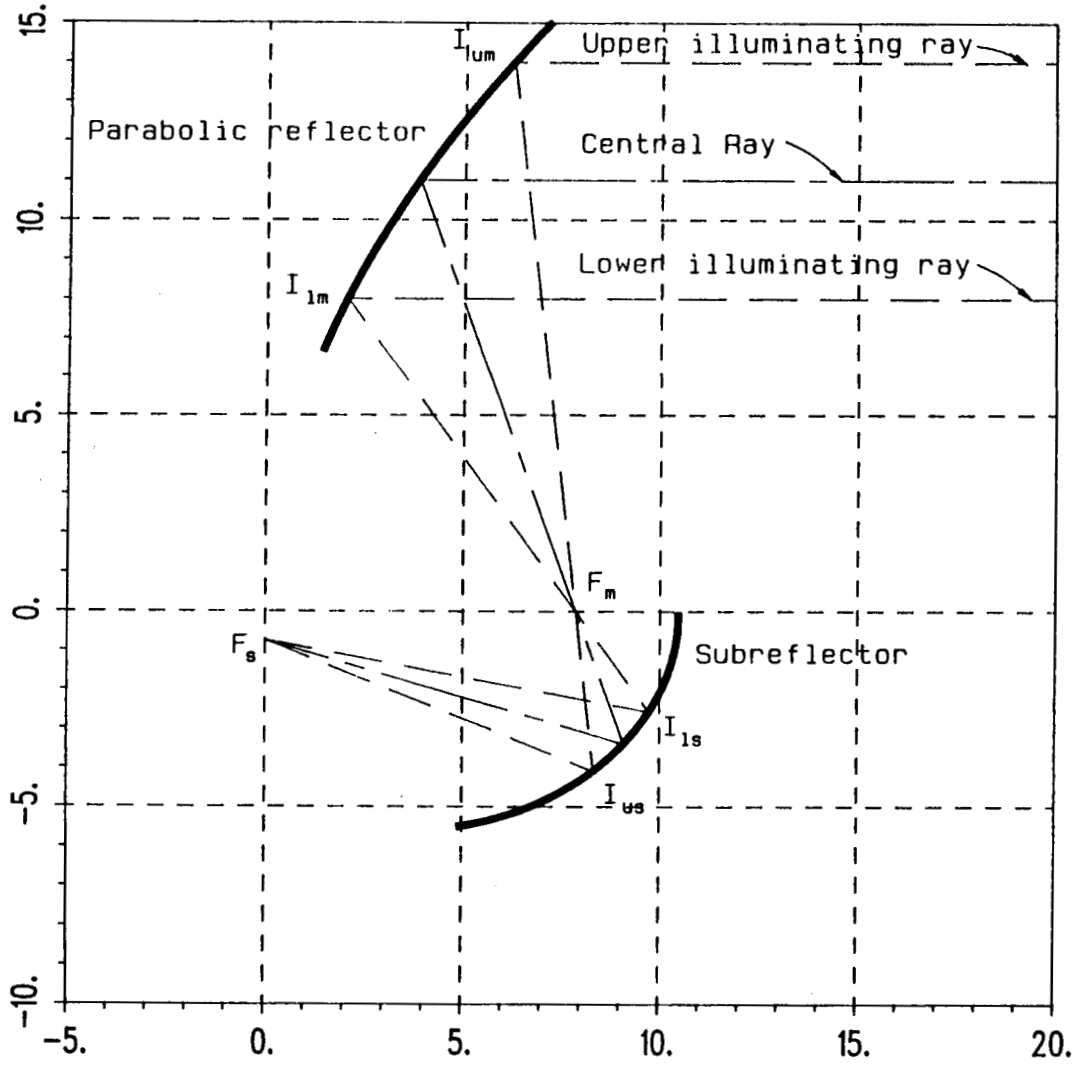

Figure 70: Layout of the DD4 design in the x_m z_m plane, showing the main reflector, the subreflector, the upper and lower illuminating rays and the central ray. Linear dimensions are in feet.

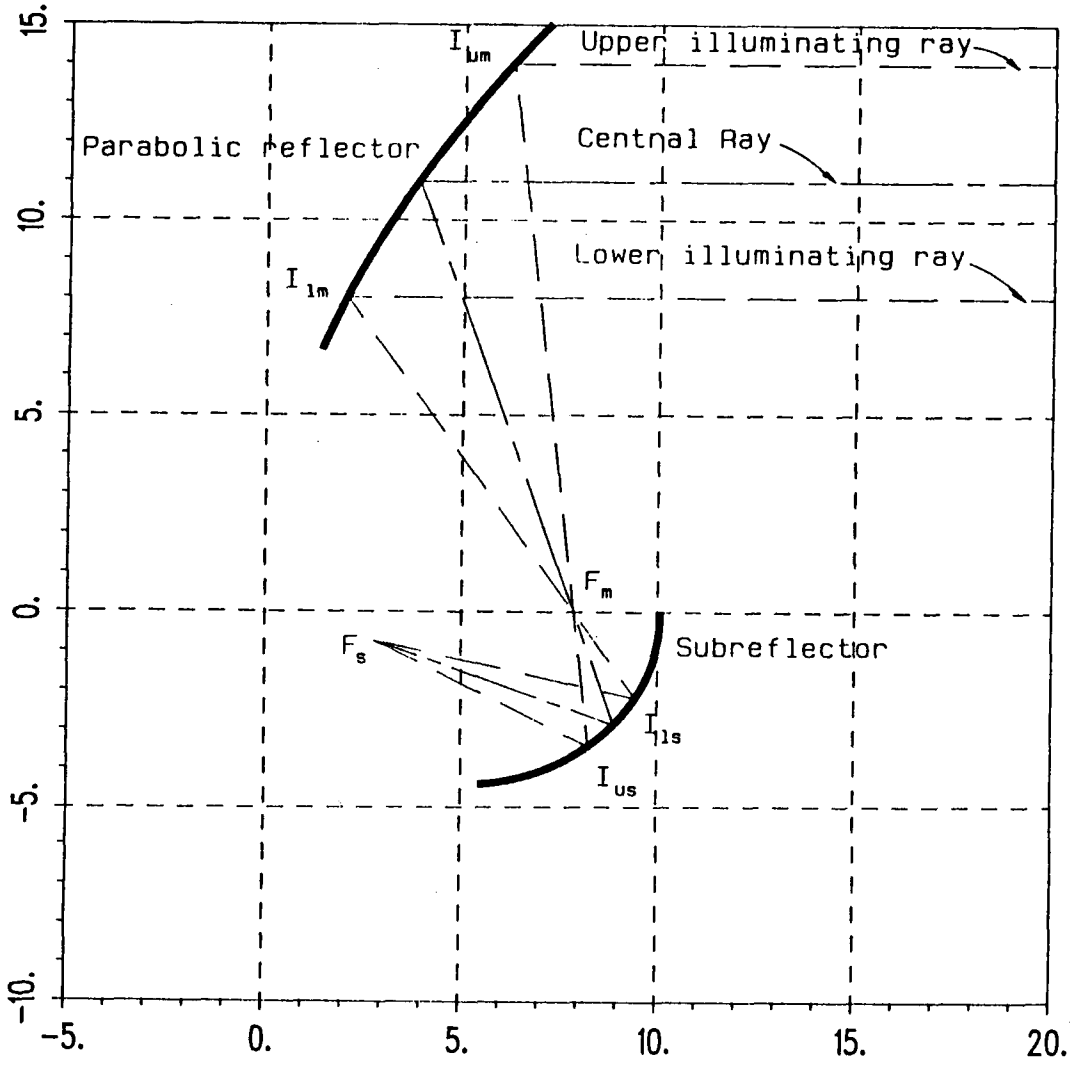

Figure 71: Layout of the DD5 design in the x_m z_m plane, showing the main reflector, the subreflector, the upper and lower illuminating rays and the central ray. Linear dimensions are in feet.

Table 10: Effect of increasing z_{pc} (designs DD4 and DD5)

$\|\alpha_c\|$	increasing	f	constant
$\|\beta_c\|$	increasing	ϵ_s	decreasing
Δt	constant	d_s	decreasing
$\|\alpha_u\|$	increasing	p_s	decreasing
$\|\alpha_l\|$	increasing	m	decreasing
χ_u	constant	M	decreasing
χ_l	constant	$\|\text{gro}_{dB}\|$	increasing
BMW^{xz}_{max}	increasing	Δ_c	increasing
BMW^{xz}_{i}	increasing		

about 10.7^o, and the $|\text{gro}_{dB}|$ is reduced to about 0.053 dB, the time delay Δt is increased to about 9.9 ns, which are improvements. Instead, the size of the subreflector is approximately the same, the focal length is increased to about $8.57'$, the magnification M is increased to about 3.7, and the tilt angle Δ_c is decreased to about 16.8^o. This design offers several advantages over the FD design, but it has the disadvantages of requiring a larger room and of having a slightly smaller value for the tilt angle Δ_c.

In the DD7 design, the heights, h_{um} and h_{lm}, are set to $13.0'$ and $7.0'$, respectively. In other words, the height of the target zone is decreased by $1'$. This is still a reasonable assumption. The $|\text{gro}_{dB}|$ is increased to about 0.094 dB, which is still acceptable, the illuminating beamwidth BMW^{xz}_{i} is increased to about 14.7^o, and the time delay Δt is decreased to about 9 ns, which are degradations in the design. Instead, the size of the subreflector is approximately the same, the focal length is decreased to about $7.14'$, the magnification M is decreased to about 3.5, and the tilt angle Δ_c is increased to about 18.3^o. This design offers the advantages

of a reduced size room and a larger tilt angle Δ_c, at the expense of a deterioration of the remaining parameters, especially of BMW_i^{xz}.

7.6.4 DIRECT DESIGN. EXAMPLES DD8 AND DD9

In the DD8 and DD9 design examples the quantity χ_c is varied by 10^o, about the value of the FD design; while, the other input quantities are kept constant. The design values are shown in Table 13, with the layouts illustrated in Figures 74 and 75. The trends of the parameters are shown in Table 14. The advantages and disadvantages offered by each design are briefly summarized.

In the DD8 design, the tilt angle χ_c is set to 95.0^o. In other words, the beam illuminating the main reflector is becoming more vertical than in the FD design. The illuminating beamwidth BMW_i^{xz} is increased to about 16.9^o, and the $|\text{gro}_{dB}|$ is increased to about 0.131 dB, which is slightly greater than the specified value of 0.1 dB, the time delay Δt is strongly decreased to about 6.3 ns, which are degradations in the design. Instead, the size of the subreflector is slightly smaller, the focal length is greatly decreased to about $6.0'$, the magnification M is decreased to about 3.38, and the tilt angle Δ_c is greatly increased to about 23.6^o. This design offers several advantages over the FD design, especially for the tilt angle of the feed Δ_c, but it also has strong disadvantages, especially for the time delay differential Δt, which is much too low. Also, the feed beamwidth, BMW_i^{xz}, is very large, besides, there are problems related to diffraction from the edges of the main reflector. In fact, this type of design shows a greatly different behaviour of the upper and lower edges of the main reflector with respect to diffraction. While the diffraction from the upper edge is reduced with respect to the FD design, the diffraction from the lower edge is increased. This is due to the fact that the difference of the distances of the upper and lower edges is greater for this design

Table 11: Comparison between the final FD design and the DD6, DD7 designs obtained by varying the quantities h_{um} and h_{lm}

	DD6	FD	DD7
h_{um}	13.0′	14.0′	15.0′
h_{lm}	7.0′	8.0′	9.0′
h_{pc}	0.75′	0.75′	0.75′
z_{pc}	1.4′	1.4′	1.4′
χ_c	110.0°	110.0°	110.0°
Y	8.0′	8.0′	8.0′
α_c	−25.72792°	−24.14653°	−22.82191°
β_c	−7.443272°	−6.627610°	−5.972477°
Δ_c	18.28465°	17.51892°	16.84943°
α_u	−32.90196°	−30.31467°	−28.19917°
α_l	−18.55388°	−17.97840°	−17.44464°
χ_u	95.37871°	96.58686°	97.61132°
χ_l	127.7769°	126.0258°	124.5871°
Δt	9.003141 ns	9.47662 ns	9.871864 ns
BMW^{xz}_{max}	36.56930°	35.03785°	33.69887°
BMW^{xz}_{i}	14.34808°	12.33628°	10.75453°
f	7.140740′	7.854814′	8.568889′
ϵ_s	0.5566258	0.5739332	0.5892388
d_s	5.789516′	6.498242′	7.208023′
p_s	3.589248′	3.796371′	3.992762′
m	3.510863	3.694099	3.869009
M	3.350957	3.544329	3.727683
gro_{dB}	−0.09429957 dB	−0.06976044 dB	−0.05304461 dB

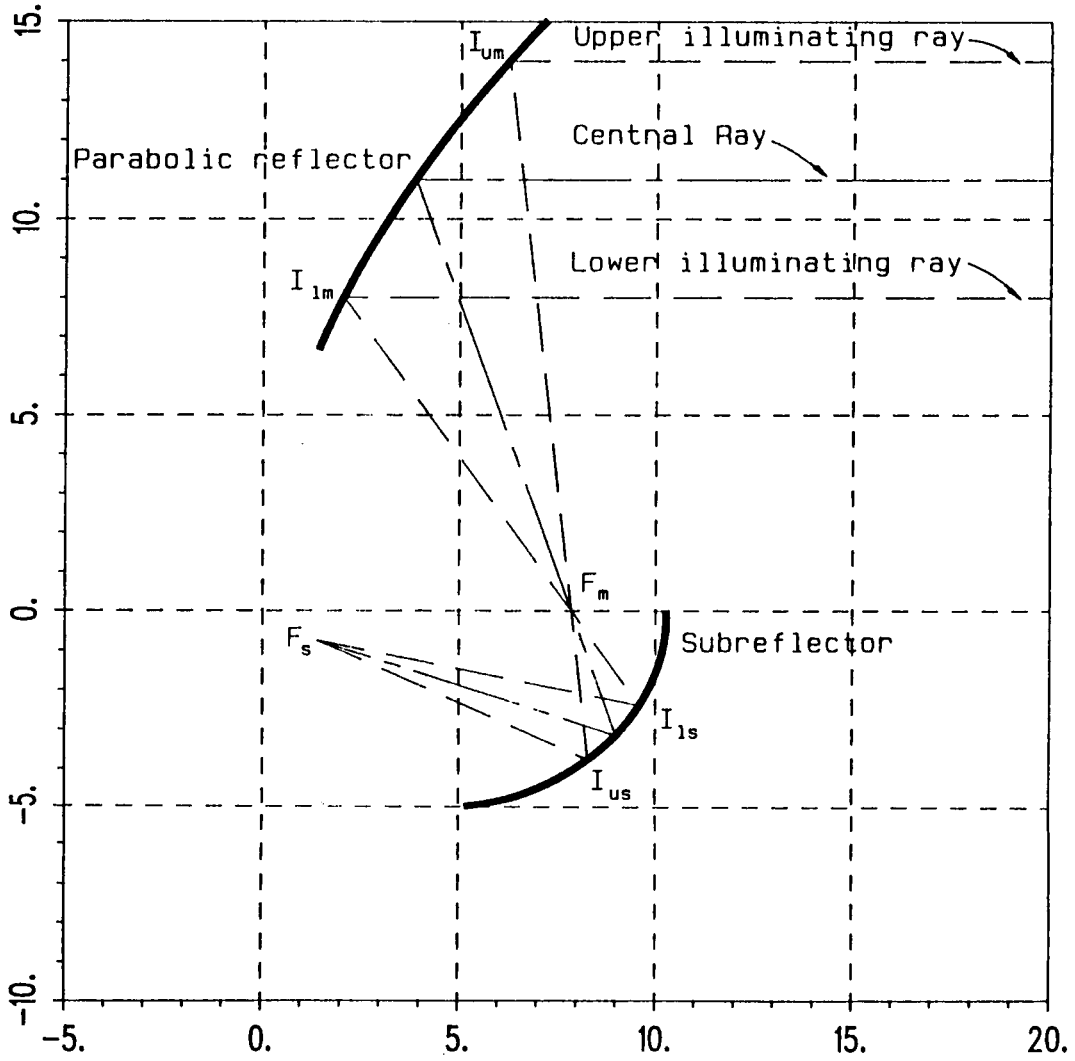

Figure 72: Layout of the DD6 design in the x_m z_m plane, showing the main reflector, the subreflector, the upper and lower illuminating rays and the central ray. Linear dimensions are in feet.

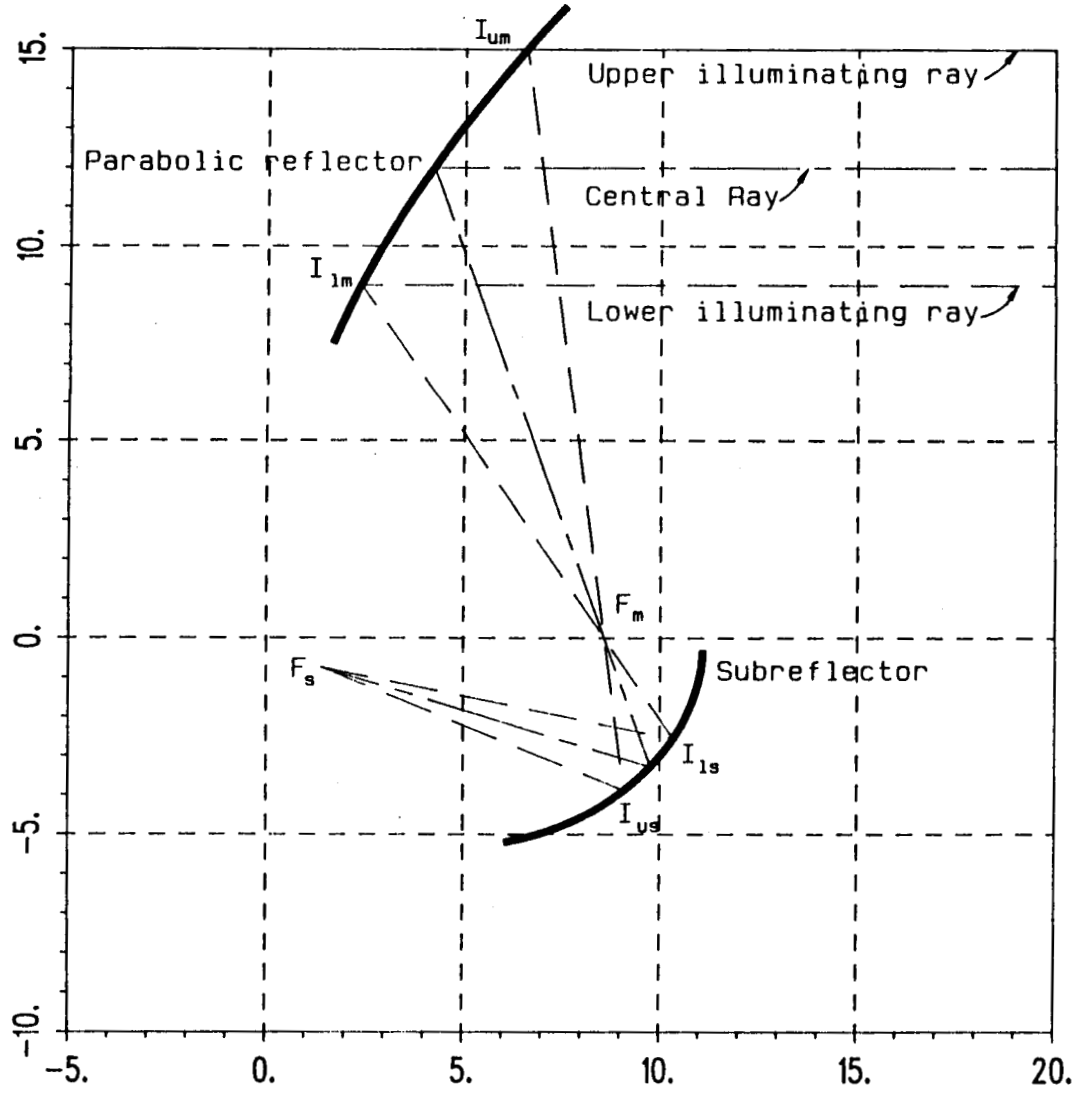

Figure 73: Layout of the DD7 design in the x_m z_m plane, showing the main reflector, the subreflector, the upper and lower illuminating rays and the central ray. Linear dimensions are in feet.

Table 12: Effect of increasing h_{um} and h_{lm} (designs DD6 and DD7)

$\|\alpha_c\|$	decreasing	f	increasing
$\|\beta_c\|$	decreasing	ϵ_s	increasing
Δt	decreasing	d_s	increasing
$\|\alpha_u\|$	decreasing	p_s	increasing
$\|\alpha_l\|$	decreasing	m	increasing
χ_u	increasing	M	increasing
χ_l	decreasing	$\|\text{gro}_{dB}\|$	decreasing
BMW^{xz}_{max}	decreasing	Δ_c	decreasing
BMW^{xz}_i	decreasing		

than for the FD design, and also to the fact that the radii of curvature at the lower edge are smaller for this case than for the FD design. This increases diffraction, since the rolled edge must perform a transition from a concave surface (parabolic section) to a convex one (elliptical section).

In the DD9 design, the tilt angle, χ_c, is set to 125.0^o. In other words, the beam illuminating the main reflector is coming more horizontal than in the FD design. The illuminating beamwidth, BMW^{xz}_i, is decreased to about 8.9^o, and the $|\text{gro}_{dB}|$ is decreased to about 0.036 dB, the time delay differential, Δt, is strongly increased to about 13.9 ns, which are improvements. Instead, the size of the subreflector is larger, the focal length is greatly increased to about $10.56'$, the magnification M is increased to about 3.66, and the tilt angle Δ_c is greatly decreased to about 12.72^o. This design offers several advantages over the FD design, especially for the feed beamwidth BMW^{xz}_i and the time delay differential Δt, but it also has disadvantages, especially for the tilt angle Δ_c, which is much too low, and for the size of the subreflector.

Table 13: Comparison between the final FD design and the DD8, DD9 designs obtained by varying the quantity χ_c

	DD8	FD	DD9
χ_c	95.0°	110.0°	125.0°
h_{pc}	0.75′	0.75′	0.75′
z_{pc}	1.4′	1.4′	1.4′
h_{um}	14.0′	14.0′	14.0′
h_{lm}	8.0′	8.0′	8.0′
Y	8.0′	8.0′	8.0′
α_c	−32.90275°	−24.14653°	−17.40534°
β_c	−9.255871°	−6.627610°	−4.678101°
Δ_c	23.64688°	17.51892°	12.72724°
α_u	−41.36674°	−30.31467°	−21.83883°
α_l	−24.43876°	−17.97840°	−12.97185°
χ_u	81.22332°	96.58686°	112.9479°
χ_l	112.6392°	126.0258°	138.5273°
$\Delta\, t$	6.308411 ns	9.47662 ns	13.91169 ns
BMW^{xz}_{max}	47.29376°	35.03785°	25.45448°
BMW^{xz}_{i}	16.92799°	12.33628°	8.866981°
f	6.002197′	7.854814′	10.56540′
ϵ_s	0.5696951	0.5739332	0.5787164
d_s	4.662912′	6.498242′	9.195958′
p_s	2.764244′	3.796371′	5.284208′
m	3.647867	3.694099	3.747396
M	3.377283	3.544329	3.667713
gro_{dB}	−0.1311165 dB	−0.06976044 dB	−0.03607703 dB

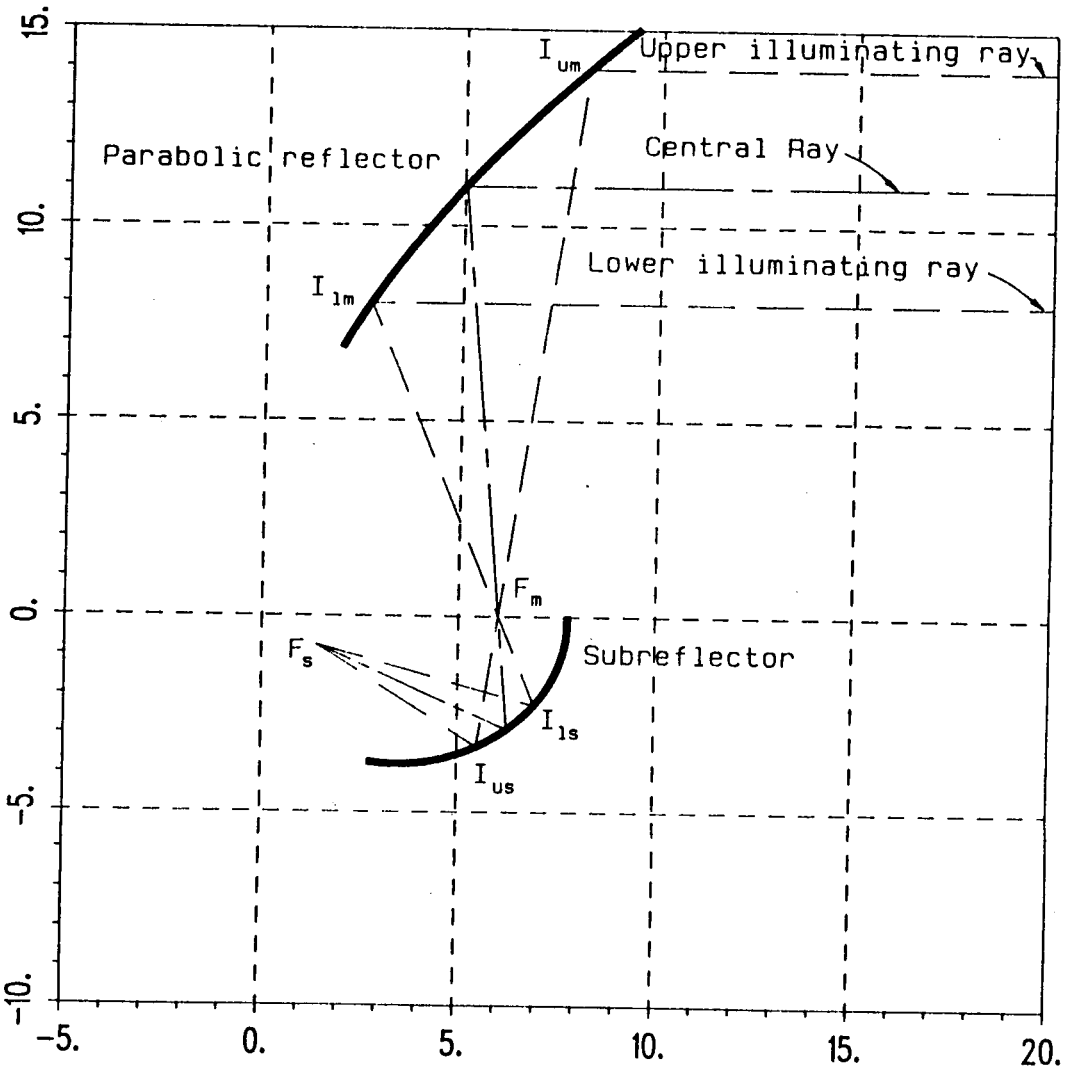

Figure 74: Layout of the DD8 design in the x_m z_m plane, showing the main reflector, the subreflector, the upper and lower illuminating rays and the central ray. Linear dimensions are in feet.

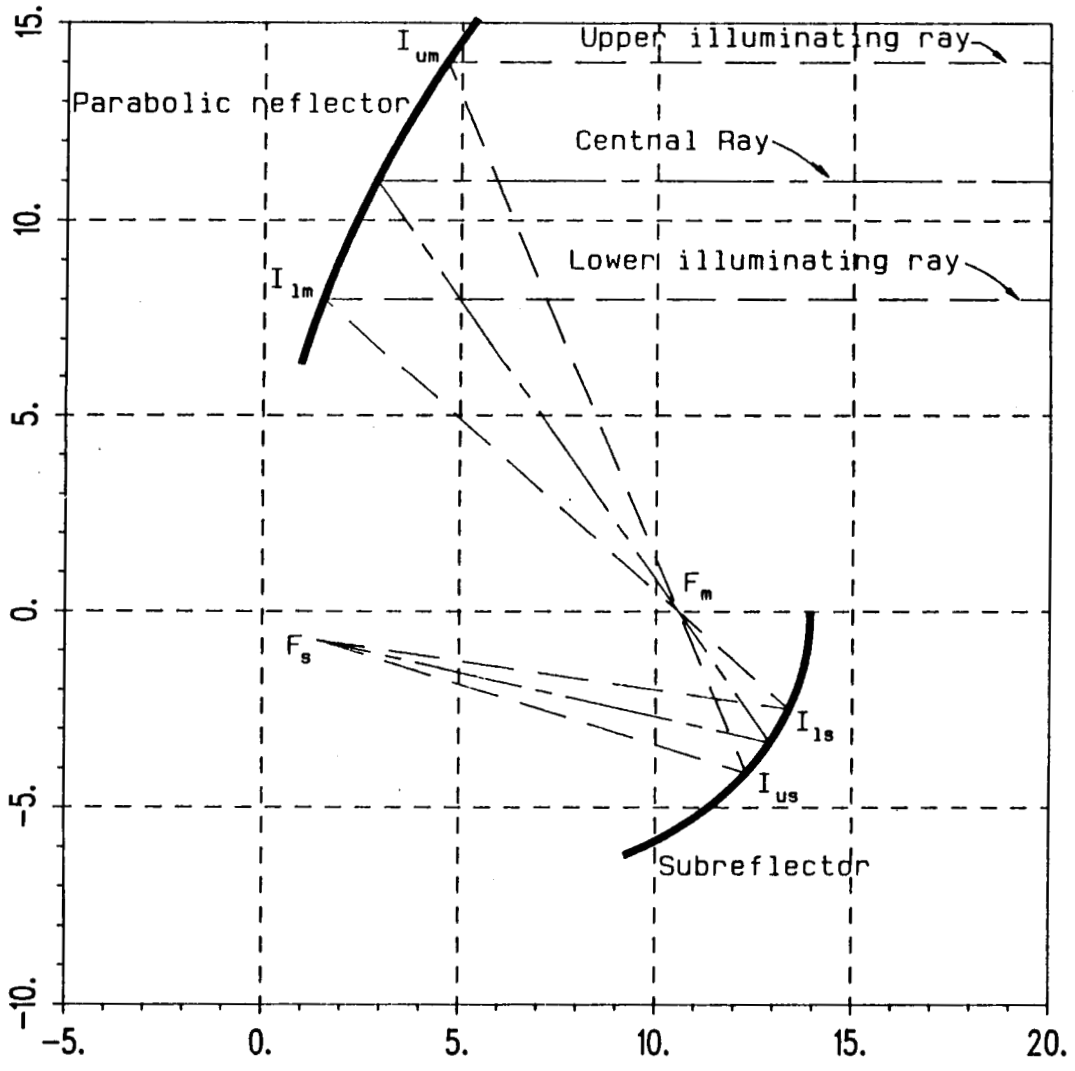

Figure 75: Layout of the DD9 design in the x_m z_m plane, showing the main reflector, the subreflector, the upper and lower illuminating rays and the central ray. Linear dimensions are in feet.

Table 14: Effect of increasing χ_c (designs DD8 and DD9)

$\|\alpha_c\|$	decreasing	f	increasing
$\|\beta_c\|$	decreasing	ϵ_s	increasing
Δt	decreasing	d_s	increasing
$\|\alpha_u\|$	decreasing	p_s	increasing
$\|\alpha_l\|$	decreasing	m	increasing
χ_u	increasing	M	increasing
χ_l	increasing	$\|\text{gro}_{dB}\|$	decreasing
BMW^{xz}_{max}	decreasing	Δ_c	decreasing
BMW^{xz}_{i}	decreasing		

7.7 CONCLUSION

The FD design for the next generation compact range has been achieved through the design procedures introduced in Chapter V. This design, by using Dragone's principle of the central ray, eliminates or minimizes the three problems related to the single reflector offset design, viz. cross-polarization, aperture blockage and taper of the reflected field. At the same time, the design satisfies several geometrical constraints and represents a compromise between different requirements which must be satisfied to minimize diffraction arising from different causes, for instance, the coupling aperture and the edges of the main reflector and subreflector. It has been shown that the new design represents an overall improvement over the previous design. Through several examples it is shown how an improvement for some of the parameters of the FD design is achieved only at the expense of one or more other factors, therefore, the design obtained is a reasonable compromise. While a detailed analysis of diffraction is not the purpose of this study, it has been shown that nevertheless the requirements dictated by

diffraction considerations must be carefully taken into account to obtain a useful GO design.

CHAPTER VIII

CONCLUSIONS

The geometrical optics design of a compact range has been addressed in this report. Through this study it has been shown how an offset single reflector design fails to solve three problems:

- aperture blockage error
- cross polarization error
- geometric taper error of the reflected field.

These three errors are intrinsic to the offset single reflector design. For example, if the axis of the feed coincides with the axis of the parabolic reflector (center fed arrangement), the feed and its supporting structures are illuminated by the reflected plane wave, with a subsequent strong interaction. Then, the total signal in the quiet zone is the sum of the reflected plane wave and the diffracted fields, which result from the feed (and supporting structures) scatter (or aperture blockage). This dictates an offset arrangement, in which the axis of the feed is tilted with respect to the parabolic reflector axis. This reduces (but does not eliminate) the aperture blockage, but it also introduces a strong cross-polarized component. Presently cross-polarization is defined as the ratio of the cross-polarized term over the co-polarized component of the reflected field in the target zone. While an center fed arrangement has no cross-polarization, an offset arrangement has a strong

cross-polarization. In fact, the parabolic surface is a doubly curved surface, which introduces a "twisting" in the polarization of the reflected field with respect to the incident field. A geometric taper error is also present for both the center fed and offset configuration. In fact, since the distance from the focal point to the reflection point is not constant (because the reflector is not spherical), the resulting plane wave from an omnidirectional feed has a non-uniform field distribution. The offset arrangement can be used to partially compensate for the geometric taper, but at the expense of increasing the cross-polarization error.

These errors can be eliminated or reduced with a dual chambers offset Gregorian subreflector system, which has the following advantages:

- greatly reduces the aperture blockage error
- eliminates the cross polarization error
- minimizes the taper of the reflected field through a large equivalent focal length and an optimal choice of the position of the target zone.

By tilting the axis of the feed, and locating the subreflector accordingly, and with a dual chambers arrangement, the aperture blockage can be greatly reduced. The geometric optics cross polarization can be eliminated despite the fact that the feed axis is tilted, since now two surfaces are reflecting, such that the "twisting" of the one can be made to cancel the other. The geometric taper can be made small by having a large equivalent focal length, while reducing the actual focal length of the main reflector.

A comparison between a commercially available offset single reflector and a Gregorian subreflector system shows the following:

For the offset single reflector:

1) Target zone of almost semicircular shape, with lower limit at $4.4'$ and upper limit at $12.9'$, and extending in depth from $36'$ to $50'$.

2) Focal distance of $24'$.

3) Field taper

- taper of the geometric reflected field of 0.55 dB
- taper with Huygens source of 1.03 dB for a tilt angle of 20^o
- taper with Huygens source of 0.96 dB for a tilt angle of 39.75^o.

4) Cross polarization error

- -21.2 dB for a tilt angle of 20^o
- -15.05 dB for a tilt angle of 39.75^o.

For the Gregorian subreflector system:

1) Target zone of rectangular shape, with lower limit at $8'$ and upper limit at $14'$, and extending in depth from $20'$ to $28'$.

2) Focal distance of $7.85'$, equivalent focal distance of $27.84'$.

3) Field taper

- taper of the geometric reflected field of 0.0698 dB
- taper with Huygens source of 0.14 dB.

4) Cross polarization error is zero ($-\infty$ dB).

The GO design of a Gregorian subreflector system can be performed with an iteration procedure, using a numerical solution which evaluates the reflected field and the cross-polarization in the target zone, but this approach is very cumbersome and, even with a great effort, easily misses the optimal design. Instead, some simple algebraic design equations to solve quickly and exactly the design problem have been developed in this report. Besides minimizing the three errors already mentioned, these equations allow one to satisfy several geometrical conditions as well as other conditions which minimize the amount of diffraction in the target zone.

The design of a new generation subreflector system compact range has been determined through these equations. This new design offers better electrical characteristics than the offset single reflector system.

APPENDIX A

THE VECTOR PATTERN FUNCTION

A radiator and its electric or magnetic far field, $\mathbf{E}_{ff}$ or $\mathbf{H}_{ff}$, are considered in an homogeneous lossless medium having propagation constant k and intrinsic impedance Z. It is assumed that the radiator has a well defined phase center at the point O,constant with respect to the direction of radiation. This phase center is assumed as origin of a polar coordinate system $O\{r\,\theta\,\phi\}$. Under these assumptions the wave propagating from O is a spherical wave, and $\hat{\mathbf{r}}$ represents its direction of propagation. Its phase factor is e^{-jkr}, where r is the distance from the phase center O to the field point R. The electric and magnetic fields are perpendicular to each other and to the direction of propagation under the far field assumption (TEM wave), as follows

$$\mathbf{E}_{ff} \cdot \mathbf{H}_{ff} = 0 \tag{A.1}$$

$$\mathbf{E}_{ff} \cdot \hat{\mathbf{r}} = 0 \tag{A.2}$$

$$\mathbf{H}_{ff} \cdot \hat{\mathbf{r}} = 0 \tag{A.3}$$

$$\text{and} \quad \mathbf{E}_{ff} = Z\,\mathbf{H}_{ff}\,. \tag{A.4}$$

Two vector functions can then be defined at each point $P \equiv \{r\,\theta\,\phi\}$ in the far field of the radiator

$$\mathbf{PF}_E(\hat{\mathbf{r}}) \stackrel{\text{def}}{=} \mathbf{E}_{ff}\frac{r}{e^{-jkr}} \tag{A.5}$$

$$\mathbf{PF}_H(\hat{\mathbf{r}}) \stackrel{\text{def}}{=} \mathbf{H}_{ff}\frac{r}{e^{-jkr}}\,. \tag{A.6}$$

These are called vector pattern function for the $\mathbf{E}$ and for the $\mathbf{H}$ fields, respectively. One can be derived from the other by the use of the previous equations.

The vector pattern function is a function of the direction of propagation $\hat{\mathbf{r}}$ only, it does not depend on the distance r. It contains information on the radiation intensity (as the more usual pattern function) as well as on the polarization of the radiator in the direction $\hat{\mathbf{r}}$.

APPENDIX B

INTERSECTION OF A STRAIGHT LINE WITH A CONIC OF REVOLUTION

A conic is defined as a plane curve characterized through the equation in polar coordinates

$$r = \frac{p}{1 - \epsilon \cos\theta} \tag{B.1}$$

where the quantities are shown in Figure 76, and ϵ is the eccentricity of the conic.

In a three dimensional space, a conic of revolution is defined as a surface, as follows.

The axis of the conic connectiong the two focai is considered. One of the focai is at infinity for a parabola, for a circle any axis can be considered. The conic is rotated of 180^o in space around this axis. The surface obtained is a conic of revolution.

A conic of revolution is still described by Equation (B.1)

$$r = \frac{p}{1 - \epsilon \cos\theta} \tag{B.2}$$

where now r and θ are polar coordinates in the three dimensional space, and the origin coincides with the appropriate focus of the conic.

Two points in space, $P_1 \equiv (x_1, y_1, z_1), P_2 \equiv (x_2, y_2, z_2)$, with $P_1 \neq P_2$, and a conic of revolution, are considered. It is desired to determine the intersection

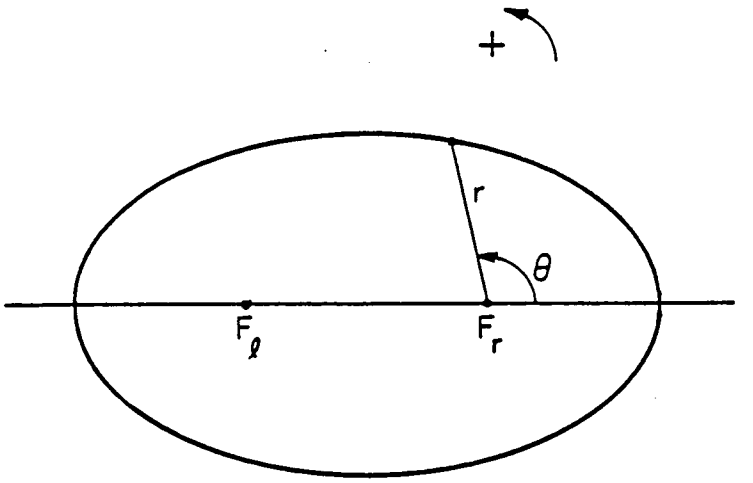

Figure 76: Geometry in polar coordinates of a conic in the plane.

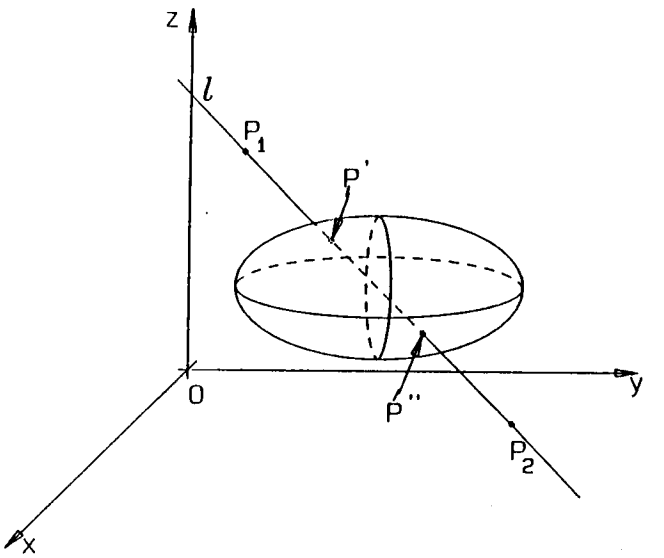

Figure 77: Geometry of the line ℓ intersecting the conic of revolution.

points of the oriented line ℓ through P_1, P_2 with the conic of revolution. The line ℓ is oriented from P_1 to P_2 (see Figure 77).

The equation of the straight line ℓ through the points, P_1 and P_2, is determined first. The direction cosines k, l, m of ℓ are given by

$$k = \frac{x_2 - x_1}{d} \tag{B.3}$$

$$l = \frac{y_2 - y_1}{d} \tag{B.4}$$

$$m = \frac{z_2 - z_1}{d} \tag{B.5}$$

$$\text{where} \quad k^2 + l^2 + m^2 = 1 \tag{B.6}$$

and d is the distance between P_1 and P_2

$$d = \sqrt{(x_2 - x_1)^2 + (y_2 - y_1)^2 + (z_2 - z_1)^2} \; . \tag{B.7}$$

The parametric equation of ℓ is

$$x = k\,t + x_1 \tag{B.8}$$

$$y = l\,t + y_1 \tag{B.9}$$

$$z = m\,t + z_1 \tag{B.10}$$

where t is the signed distance along the line ℓ of a point $P \equiv (x, y, z)$ of ℓ from the point P_1.

The coordinates of a point on ℓ can be expressed in polar form, and Equations (B.8), (B.9), and (B.10) can be used to obtain

$$x = k\,t + x_1 = r \sin\theta \cos\phi \tag{B.11}$$

$$y = l\,t + y_1 = r \sin\theta \sin\phi \tag{B.12}$$

$$z = m\,t + z_1 = r \cos\theta \; . \tag{B.13}$$

From Equation (B.2)

$$r = p + r\epsilon\cos\theta \tag{B.14}$$

hence, using Equation (B.13)

$$r = p + \epsilon(mt + z_1) \tag{B.15}$$

by squaring Equations (B.11), (B.12) and (B.13) this relation follows

$$r^2 = (kt + x_1)^2 + (lt + y_1)^2 + (mt + z_1)^2 \tag{B.16}$$

by performing the squares and ordering with respect to powers of t one obtains

$$r^2 = (k^2 + l^2 + m^2)t^2 + 2(kx_1 + ly_1 + mz_1)t + (x_1^2 + y_1^2 + z_1^2) \tag{B.17}$$

which can be written as

$$r^2 = t^2 + 2At + B \tag{B.18}$$

consequently, using Equation (B.15)

$$t^2 + 2At + B = [p + \epsilon(mt + z_1)]^2 \tag{B.19}$$

expanding the square

$$t^2 + 2At + B - p^2 - 2p\epsilon(mt + z_1) - \epsilon^2(mt + z_1)^2 = 0 \tag{B.20}$$

$$t^2 + 2At + B - p^2 - 2p\epsilon(mt + z_1) - \epsilon^2(m^2t^2 + 2mz_1t + z_1^2) = 0 \tag{B.21}$$

$$(1 - \epsilon^2m^2)t^2 + 2(A - p\epsilon m - \epsilon^2mz_1)t + (B - p^2 - 2p\epsilon z_1 - \epsilon^2z_1^2) = 0 \tag{B.22}$$

a second degree equation of the form:

$$at^2 + 2bt + c = 0 \tag{B.23}$$

where

$$a = 1 - \epsilon^2 m^2 \tag{B.24}$$

$$b = kx_1 + ly_1 + mz_1 - \epsilon m(p + \epsilon z_1) \tag{B.25}$$

$$c = x_1^2 + y_1^2 + z_1^2 - (p + \epsilon z_1)^2 \ . \tag{B.26}$$

Equation (B.23) gives two (one or none) solutions for t, t' and t'', which are the coordinates along ℓ of the intersection points, P' and P'', with the conic of revolution. By inserting these values of t in the equations of the straight line ℓ, the xyz coordinates of the intersection points can easily be found

$$x' = kt' + x_1 \tag{B.27}$$

$$y' = lt' + y_1 \tag{B.28}$$

$$z' = mt' + z_1 \ , \tag{B.29}$$

$$x'' = kt'' + x_1 \tag{B.30}$$

$$y'' = lt'' + y_1 \tag{B.31}$$

$$z'' = mt'' + z_1 \ . \tag{B.32}$$

Some of the solutions might be spurious, and the coordinates of the points, P' and P'', must be substituted into Equation (B.2) to check if they actually are points of the conic of revolution, i.e., actual intersection points.

APPENDIX C

COMPUTATION OF THE NORMAL FOR A CONIC OF REVOLUTION

Let $f(\mu,\nu,\xi) = 0$ be the equation of a surface expressed in the μ,ν,ξ coordinate system. Its normal vector is given by

$$\mathbf{n} = \nabla f(\mu,\nu,\xi) \tag{C.1}$$

where ∇ is the gradient in the μ,ν,ξ coordinate system.

In a polar coordinate system, the gradient is given by

$$\nabla = \hat{\mathbf{r}}\frac{\partial}{\partial r} + \frac{\hat{\theta}}{r}\frac{\partial}{\partial \theta} + \frac{\hat{\phi}}{r\sin\theta}\frac{\partial}{\partial \phi} \tag{C.2}$$

and the equation of a conic of revolution is

$$f(r,\theta) = r - \frac{p}{1-\epsilon\cos\theta} = 0\ . \tag{C.3}$$

Thus, one finds that

$$\frac{\partial}{\partial r}f(r,\theta) = 1 \tag{C.4}$$

$$\frac{\partial}{\partial \theta}f(r,\theta) = \frac{p\epsilon\sin\theta}{(1-\epsilon\cos\theta)^2}\ , \quad \text{and} \tag{C.5}$$

$$\frac{\partial}{\partial \phi}f(r,\theta) = 0 \tag{C.6}$$

consequently

$$\mathbf{n} = \hat{\mathbf{r}} + \frac{1}{r}\frac{p\epsilon\sin\theta}{(1-\epsilon\cos\theta)^2}\,\hat{\theta} \tag{C.7}$$

$$\mathbf{n} = \hat{\mathbf{r}} + \frac{\epsilon \sin\theta}{1 - \epsilon\cos\theta}\,\hat{\theta} \tag{C.8}$$

$$\text{with} \quad |\mathbf{n}| = \frac{1}{1 - \epsilon\cos\theta}\sqrt{1 + \epsilon^2 - 2\epsilon\cos\theta}\ . \tag{C.9}$$

By normalizing $\mathbf{n}$, one obtains the unit vector $\hat{\mathbf{n}}$ such that

$$\hat{\mathbf{n}} = \frac{1}{\sqrt{1 + \epsilon^2 - 2\epsilon\cos\theta}}[(1 - \epsilon\cos\theta)\,\hat{\mathbf{r}} + \epsilon\sin\theta\,\hat{\theta}]\ . \tag{C.10}$$

This is the expression for the unit normal of a conic of revolution in a polar coordinate system.

To determine its expression in a cartesian coordinate system, one can write

$$\hat{\mathbf{r}} = \sin\theta\cos\phi\,\hat{\mathbf{x}} + \sin\theta\sin\phi\,\hat{\mathbf{y}} + \cos\theta\,\hat{\mathbf{z}} \tag{C.11}$$

and

$$\hat{\theta} = \cos\theta\cos\phi\,\hat{\mathbf{x}} + \cos\theta\sin\phi\,\hat{\mathbf{y}} - \sin\theta\,\hat{\mathbf{z}}\ , \tag{C.12}$$

then, the unit normal is given by

$$\hat{\mathbf{n}} = \frac{1}{\sqrt{1 + \epsilon^2 - 2\epsilon\cos\theta}}[\sin\theta(\cos\phi\,\hat{\mathbf{x}} + \sin\phi\,\hat{\mathbf{y}}) + (\cos\theta - \epsilon)\,\hat{\mathbf{z}}]\ . \tag{C.13}$$

A conic of revolution divides all space into two complementary sets, called the inside and the outside of the conic of revolution. The inside of the conic of revolution is defined as the set containing the focus closest to the surface. Then the normal $\hat{\mathbf{n}}$ is pointing towards the outside of the conic of revolution. This is the convention used for a convex subreflector. It might be necessary to change the sign in Equation (C.13) if a concave subreflector is considered.

APPENDIX D

LAW OF REFLECTION

In this section an expression for the reflected field in terms of the incident field and the normal $\hat{\mathbf{n}}$ to a surface Σ is determined [18]. It is assumed here that the normal to the surface is pointing towards the source (real or virtual). The plane of incidence $\Pi_{||}$ is determined by the direction of the incident ray, $\hat{\mathbf{s}}^i$, the normal, $\hat{\mathbf{n}}$, and the point P^i of incidence. This plane contains the two vectors and the point. The plane of reflection is determined by the direction of the reflected ray, $\mathbf{s}^r$, the normal, $\mathbf{n}$, and the point of incidence, P_i. This plane contains the two vectors and the point. The plane of incidence and of reflection coincide.

The reference system of the incident ray is determined by the three perpendicular unit vectors ($\hat{\mathbf{s}}^i, \hat{\mathbf{e}}^i_{||}, \hat{\mathbf{e}}_{\perp}$), such that
the perpendicular unit vector $\hat{\mathbf{e}}_{\perp}$ is normal to the plane of incidence

$$\hat{\mathbf{e}}_{\perp} = \frac{\hat{\mathbf{s}}^i \times \hat{\mathbf{n}}}{|\hat{\mathbf{s}}^i \times \hat{\mathbf{n}}|} , \tag{D.1}$$

the incident parallel unit vector, $\hat{\mathbf{e}}^i_{||}$, is parallel to the plane of incidence and is given by

$$\hat{\mathbf{e}}^i_{||} = \hat{\mathbf{s}}^i \times \hat{\mathbf{e}}_{\perp} . \tag{D.2}$$

One can then determine the reference system of the reflected ray.

Since the reflected and the incident plane coincide, the reflected and incident reference systems have $\hat{\mathbf{e}}_{\perp}$ in common, because it must be perpendicular to both

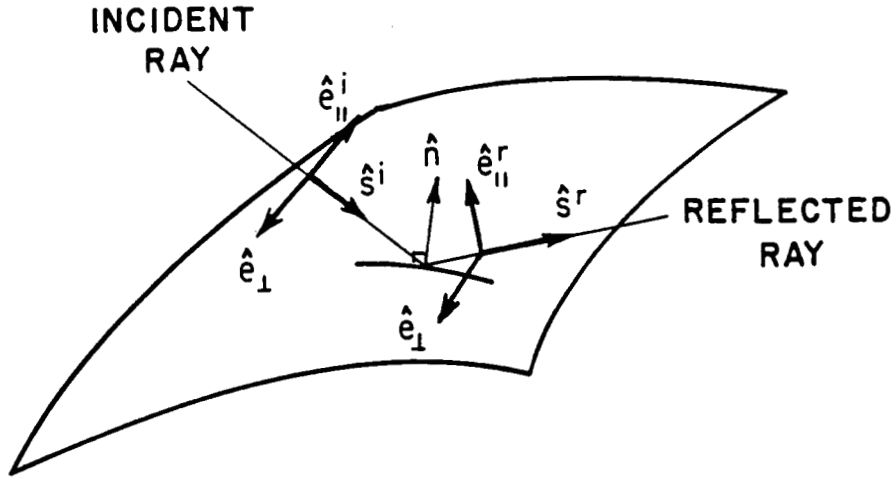

Figure 78: Incident and reflected triads.

planes.

The direction of the reflected ray is given by

$$\hat{\mathbf{s}}^{r} = \hat{\mathbf{s}}^{i} - 2(\hat{\mathbf{s}}^{i} \cdot \hat{\mathbf{n}})\,\hat{\mathbf{n}} \,. \tag{D.3}$$

This equation expresses that the tangential component (with respect to the reflecting surface) of $\hat{\mathbf{s}}^{r}$ is the same as the tangential component of $\hat{\mathbf{s}}^{i}$, while their normal components are opposite in sign.

The reflected parallel unit vector, $\hat{\mathbf{e}}_{\parallel}^{r}$, is parallel to the plane of incidence (coincident with the plane of reflection) and is given by

$$\hat{\mathbf{e}}_{\parallel}^{r} = \hat{\mathbf{s}}^{r} \times \hat{\mathbf{e}}_{\perp} \tag{D.4}$$

in order to have a right handed reference system (Figure 78).

The law of reflection can be expressed as

$$\mathbf{U}^{r} = R_{\parallel}(\mathbf{U}^{i} \cdot \hat{\mathbf{e}}_{\parallel}^{i})\,\hat{\mathbf{e}}_{\parallel}^{r} + R_{\perp}(\mathbf{U}^{i} \cdot \hat{\mathbf{e}}_{\perp})\,\hat{\mathbf{e}}_{\perp} \tag{D.5}$$

where $\mathbf{U}$ represents the field (i.e., the electric field, $\mathbf{E}$, or the magnetic field, $\mathbf{H}$), $\mathbf{U}^i$ is the incident field, $\mathbf{U}^r$ is the reflected field, $R_{||}$ and $R_{\perp}$ are the reflection coefficients

$R_{||} = 1$,

$R_{\perp} = +1$, if $\mathbf{U} = \mathbf{H}$,

$R_{\perp} = -1$, if $\mathbf{U} = \mathbf{E}$.

This reflection law can be expressed in a compact way by the use of a 2x2 dyad $\overline{\overline{R}}$

$$\overline{\overline{R}} = R_{||}\, \hat{\mathbf{e}}_{||}^{i}\, \hat{\mathbf{e}}_{||}^{r} + R_{\perp}\, \hat{\mathbf{e}}_{\perp}\, \hat{\mathbf{e}}_{\perp} \tag{D.6}$$

and the reflected field is expressed in a compact form as

$$\mathbf{U}^r = \mathbf{U}^i \cdot \overline{\overline{R}} \tag{D.7}$$

which expresses the reflected field at the reflection point in term of the incident field at the reflection point.

APPENDIX E

POLARIZATION

A (generalized) Huygens source is used to study the cross-polarization properties of a conical (not necessarily parabolic) focussed reflector or of a combination of conical focussed reflectors [10].

A (generalized) Huygens source consists of an electric and magnetic dipole set at the same point in space and having perpendicular axes. In Figure 79, the electric dipole is directed in the $-x$ direction, the magnetic dipole in the $-y$ direction. In a polar reference system the resulting far field is given by

$$E_\theta = \cos\phi(A\cos\theta + B) = B\cos\phi(X\cos\theta + 1) \tag{E.1}$$

$$E_\phi = -\sin\phi(A + B\cos\theta) = -B\sin\phi(X + \cos\theta) \tag{E.2}$$

$$H_\theta = \frac{1}{\eta}\sin\phi(A + B\cos\theta) = \frac{B}{\eta}\sin\phi(X + \cos\theta) \tag{E.3}$$

$$H_\phi = -\frac{1}{\eta}\sin\phi(A\cos\theta + B) = -\frac{B}{\eta}\cos\phi(X\cos\theta + 1) \tag{E.4}$$

where

$$X = \frac{B}{A} \tag{E.5}$$

and A, B are given by

$$A = \eta j\frac{I_d l}{2\lambda}\frac{e^{-jkr}}{r} \tag{E.6}$$

$$B = \eta\pi\frac{I_l A}{\lambda^2}\frac{e^{-jkr}}{r}\,. \tag{E.7}$$

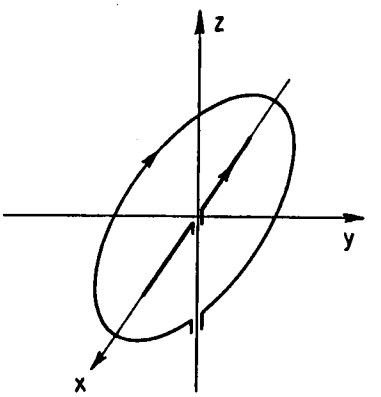

Figure 79: Huygens source

The expression of the field as given by Koffman [10] has a tipographic error in the sign of the E_ϕ components of the field of the electric and magnetic dipole. Note that η is the free-space impedance, $I_d l$ is the electric moment, $I_l A$ is the magnetic moment, λ is the wavelength, r is the distance from the source to the field point.

To obtain zero cross-polarization in the reflected field it is necessary that $X = |\epsilon|$, where ϵ is the eccentricity of the conical reflector (the actual reflector for the single reflector case, or the equivalent reflector for any combination of focussed reflectors). If $X = 1$ the source is called a Huygens source proper. If the field components given by the Equations (E.1) through (E.4) are all multiplied by the same pattern function $f(\theta, \phi)$, the new source retains the zero cross-polarization property of the Huygens source. In the case of a single reflector, the axis of the pattern of the Huygens source and the axis of the paraboloidal reflector must be aligned in order to achieve zero cross-polarization (center fed case). In the case of a subreflector system, it is possible to achieve zero cross-polarization if the angles

α and β satisfy the relationship [6]

$$\tan\left(\frac{\alpha}{2}\right) = m\tan\left(\frac{\beta}{2}\right) \tag{E.8}$$

where

$$m = \frac{1-\epsilon_l}{1+\epsilon_l} \tag{E.9}$$

where

- ϵ is the eccentricity of the subreflector
- α is the angle from the subreflector axis to the feed axis,
- β is the angle from the subreflector to the main reflector axis.

Equation (E.8) is satisfied by $\alpha = 0, \beta = 0$, but there exists a simple infinity of solutions different from zero; i.e., for every α it is possible to determine a β which satisfies Equation (E.8), and vice versa. Therefore, with a subreflector system, it is possible to achieve zero cross-polarization when the subreflector and feed axes are tilted, and to have an extra degree of freedom in choosing one of the tilt angles α or β.

It is legitimate to ask if the Huygens source is a mathematical abstraction or if it can be approximated with an actual feed. As an example it is shown that a truncated waveguide feed approximates a Huygens source. Consequently a Huygens source represents also an physical feed.

An analysis of the truncated rectangular waveguide is available in Silver [19], and, if the waveguide is excited in the TE_{10} mode, the expression for the electric far field radiated by the waveguide is given by

$$E_\theta = -\frac{K}{r}\cos\phi[1+\frac{\beta_{10}}{k}\cos\theta+\Gamma\,(1-\frac{\beta_{10}}{k}\cos\theta)]\Psi_{10}(\theta,\phi)e^{-jkr} \tag{E.10}$$

$$E_\phi = -\frac{K}{r}\sin\phi[\cos\theta+\frac{\beta_{10}}{k}+\Gamma\,(\cos\theta-\frac{\beta_{10}}{k})]\Psi_{10}(\theta,\phi)e^{-jkr}\ , \tag{E.11}$$

where

$$\Psi_{10}(\theta,\phi) = \left\{ \frac{\cos\left[(\pi a/\lambda)\sin\theta\sin\phi\right]}{\left[(\pi a/\lambda)\sin\theta\sin\phi\right]^2 - (\pi/2)^2} \right\} \left\{ \frac{\sin\left[(\pi b/\lambda)\sin\theta\sin\phi\right]}{(\pi b/\lambda)\sin\theta\sin\phi} \right\} \quad \text{(E.12)}$$

$$K = \sqrt{\frac{\mu}{\epsilon}}\,\frac{\pi a^2 b}{2\lambda^2}\,, \quad \text{(E.13)}$$

where (Figure 80), assuming a lossless medium inside the waveguide (i.e., assuming ϵ and μ real),

- μ is the permeability of the medium inside the waveguide (in free space $\mu = 4\pi\ 10^{-7}$ henry meter^{-1}),
- ϵ is the permittivity of the medium inside the waveguide (in free space $\epsilon \cong$ 8.854 farad meter),
- a is the transversal length over which the electric field components inside the waveguide, E_x and E_y, have a half period variation,
- b is the transversal length over which there is no field variation,
- λ is the characteristic wavelength of the medium inside the waveguide

$$\lambda = \frac{2\pi}{\omega\sqrt{\mu\epsilon}} = \frac{1}{f\sqrt{\mu\epsilon}} \quad \text{(E.14)}$$

where f is the frequency,

- β_{10} is the phase constant of the TE_{10} mode in the direction of propagation inside the waveguide

$$\beta_{10} = \sqrt{k^2 - \left(\frac{\pi}{a}\right)^2} \quad \text{(E.15)}$$

where k is the wave number of the medium inside the waveguide,

$$k = \omega\sqrt{\mu\epsilon} = \frac{2\pi}{\lambda}\,, \quad \text{(E.16)}$$

Γ is the reflection coefficient of the waveguide truncation,

- r is the distance from the field point to the center of the waveguide truncation (i.e., to the origin of the coordinate system).

The previous equations have been modified from Silver to take into account the different coordinate system as well as to correct a printing error in the expression of the E_ϕ component. It is clear that, if $\Gamma = 0$, the field components are those of the Huygens source multiplied by a pattern factor, and they are real. The argument of the phase factor is just r, consequently, since the amplitude is entirely real, the phase center is fixed with respect to direction, i.e., with respect to θ, ϕ. Hence, two conditions must be satisfied for the truncated waveguide to behave as a Huygens source

$$\Gamma = 0 \,, \tag{E.17}$$

$$\frac{\beta_{10}}{k} = 1 \quad \text{i.e.} \quad \sqrt{1 - \left(\frac{\pi/a}{k}\right)^2} = 1 \,. \tag{E.18}$$

Clearly this last equality can never be satisfied, and the first too can be satisfied only approximately, hence one obtains the more realistic conditions

$$\Gamma \simeq 0 \,, \tag{E.19}$$

$$1 \gg \frac{\pi}{a\,k} \tag{E.20}$$

or

$$a \gg \frac{\lambda}{2} \,. \tag{E.21}$$

The two requirements (E.19) and (E.21) are not contrasting, i.e., having large dimensions for the waveguide satisfies the condition on small Γ, and, viceversa, in order to obtain a small Γ it is necessary to have large dimensions for the waveguide.

The truncated waveguide example shows that there exist feeds which reasonably approximate the properties of a Huygens source.

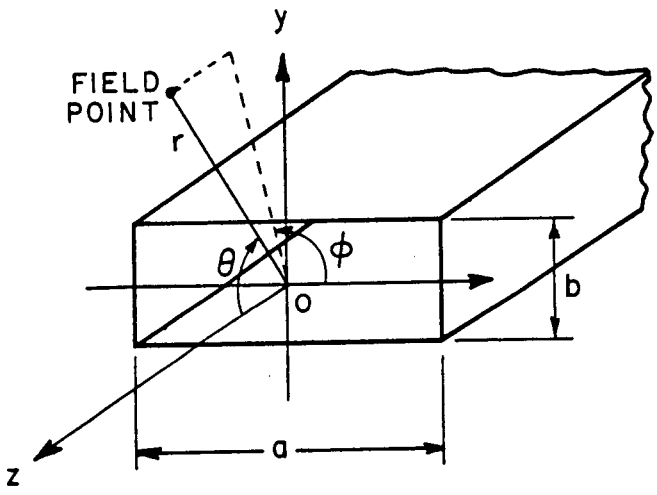

Figure 80: Truncated waveguide

APPENDIX F

ANGULAR EXPRESSIONS

Some expressions between the angles α, β and χ, as shown in Figure 81, are presently derived.

By considering the triangle F_s, F_m and I_s one obtains an expression for α in terms of ϵ_s, β and χ, where ϵ_s is the eccentricity of the subreflector referred to its left focus, as follows,

$$\tan\alpha = \frac{r_r \sin\gamma}{d_s + r_r \cos\gamma} \tag{F.1}$$

where

$$r_r = \frac{p_s}{1 + \epsilon_s \cos\gamma} \tag{F.2}$$

$$d_s = \frac{2\,p_s\,\epsilon_s}{1 - \epsilon_s^2}\ , \text{ and} \tag{F.3}$$

$$\gamma = -\pi + \chi + \beta\ . \tag{F.4}$$

By substitution one obtains

$$\tan\alpha = \frac{(1 - \epsilon_s^2)\sin\gamma}{2\epsilon_s(1 + \epsilon_s\cos\gamma) + (1 - \epsilon_s^2)\cos\gamma} \tag{F.5}$$

and since

$$\sin\gamma = -\sin(\chi + \beta) \tag{F.6}$$

$$\cos\gamma = -\cos(\chi + \beta) \tag{F.7}$$

one finally obtains

$$\alpha = -\arctan\left[\frac{(1-\epsilon_s^2)\sin(\chi+\beta)}{2\epsilon_s-(1+\epsilon_s^2)\cos(\chi+\beta)}\right] . \tag{F.8}$$

By considering the same triangle one obtains an expression for χ (or β) in terms of ϵ_s, α and β (or χ), as follows,

$$\tan\gamma = \frac{r_l\cos\alpha - d_s}{r_l\sin\alpha} \tag{F.9}$$

where

$$r_l = \frac{p_s}{1-\epsilon_s\cos\alpha} \tag{F.10}$$

one then obtains

$$\tan\gamma = \frac{(1+\epsilon_s^2)\cos\alpha - 2\epsilon_s}{(1-\epsilon_s^2)\sin\alpha} \tag{F.11}$$

therefore

$$\chi+\beta = \pi + \arctan\left[\frac{(1+\epsilon_s^2)\cos\alpha - 2\epsilon_s}{(1-\epsilon_s^2)\sin\alpha}\right] \tag{F.12}$$

which can be solved for χ or for β, as desired,

$$\chi = \pi - \beta + \arctan\left[\frac{(1+\epsilon_s^2)\cos\alpha - 2\epsilon_s}{(1-\epsilon_s^2)\sin\alpha}\right] \tag{F.13}$$

$$\beta = \pi - \chi + \arctan\left[\frac{(1+\epsilon_s^2)\cos\alpha - 2\epsilon_s}{(1-\epsilon_s^2)\sin\alpha}\right] . \tag{F.14}$$

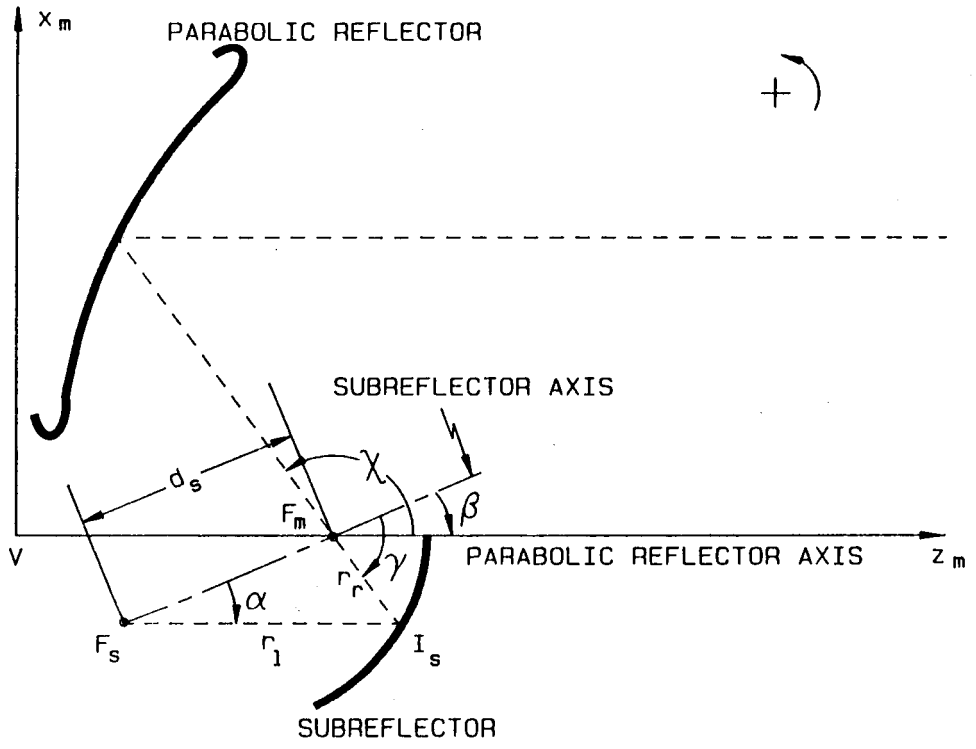

Figure 81: Geometry related to the angles α, β and χ.

APPENDIX G

EXPRESSIONS FOR THE GEOMETRIC TAPER OF THE REFLECTED FIELD

In this section some simple expressions for the taper of the reflected field (gro) of a single reflector and of a subreflector system are derived. The single reflector case is considered first for semplicity, and then the results are extended to the subreflector system through the principle of the equivalent reflector.

A parabolic reflector illuminated by a focussed uniform source is considered. The reference system is the polar reference system $F_m(r_m,\ \theta_m,\ \phi_m)$ introduced in Section 3.2. A line ℓ intersects the reflector axis z_m at a straight angle, and its distance from the paraboloid vertex V is d_l, R is a point of ℓ , and I_m is its z-projection (i.e., a projection parallel to the z_m axis) on the paraboloid, I_m has polar coordinates (r_m, θ_m, ϕ_m), ρ is the distance of R from the paraboloid axis z_m, ρ is also the distance of I_m from z_m (Figure 82).

Given two points P and Q, the symbol $P - Q$ indicates the vector starting at Q and ending at P, and $|P - Q|$ indicates its length.

The source considered has a vector pattern function **PF**

$$\mathbf{PF} = \mathbf{PF}\left(\frac{I_m - F_m}{|I_m - F_m|}\right) = \mathbf{PF}(\hat{\mathbf{r}}_m) \tag{G.1}$$

where the unit vector

$$\hat{\mathbf{r}}_m = \frac{I_m - F_m}{|I_m - F_m|} \tag{G.2}$$

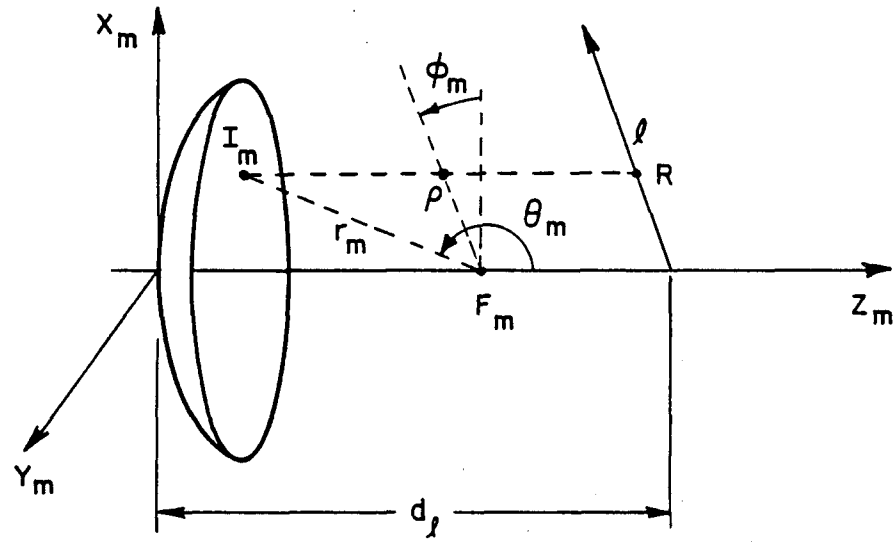

Figure 82: Geometry for the derivation of the gro.

represents the direction of propagation from the source at F_m to the point I_m. The vector pattern function $\mathbf{PF}(\hat{\mathbf{r}}_m)$ is completely determined by the direction of propagation from F_m to I_m, i.e., by $\hat{\mathbf{r}}_m$.

The field $\mathbf{U}^r(R)$, reflected at I_m and evaluated at R, is now computed. The field is generated by the uniform focussed source at F_m, it propagates as a uniform spherical wave, experiencing an attenuation of $1/r_m$, until it reaches the reflection point I_m, after reflection it propagates as a plane wave with no attenuation. The field incident at I_m is given by

$$\mathbf{U}^i(I_m) = \mathbf{PF}(\hat{\mathbf{r}}_m)\,\frac{e^{-jk|I_m-F_m|}}{|I_m-F_m|}\,, \tag{G.3}$$

consequently $\mathbf{U}^r(R)$ is given by

$$\mathbf{U}^r(R) = \mathbf{PF}(\hat{\mathbf{r}}_m)\,\frac{e^{-jk|I_m-F_m|}}{|I_m-F_m|}\cdot\overline{\overline{\boldsymbol{R}}}\,e^{-jk|R-I_m|} \tag{G.4}$$

$$\mathbf{U}^r(R) = \mathbf{PF}(\hat{\mathbf{r}}_m)\cdot\overline{\overline{\boldsymbol{R}}}\,\frac{e^{-jk(|I_m-F_m|+|R-I_m|)}}{r_m} \tag{G.5}$$

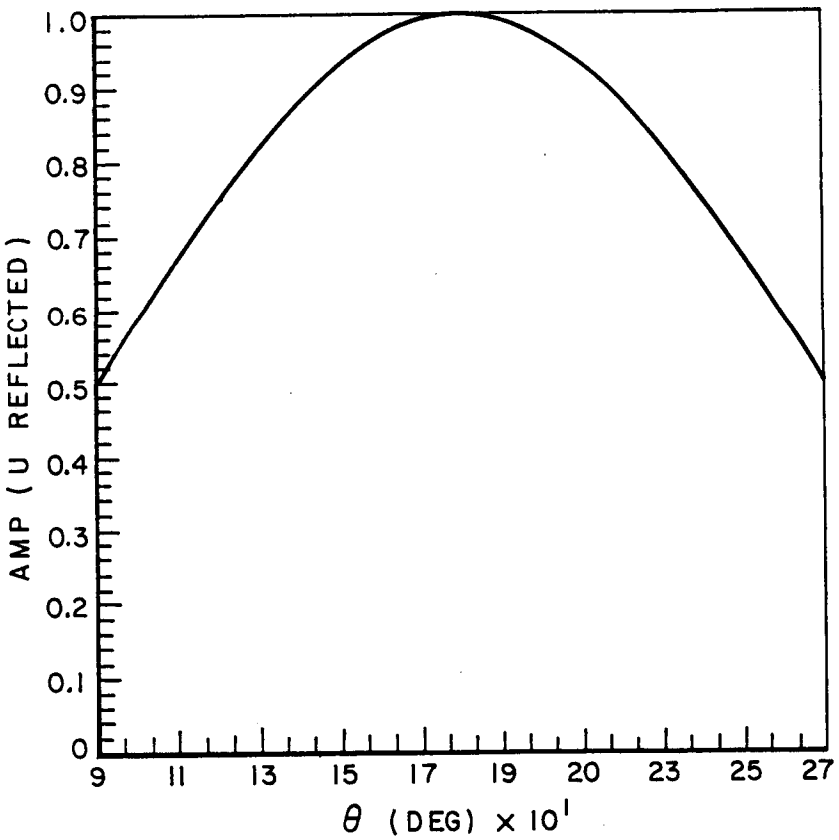

Figure 83: Plot of $|\mathbf{U}^r|$ versus θ_m.

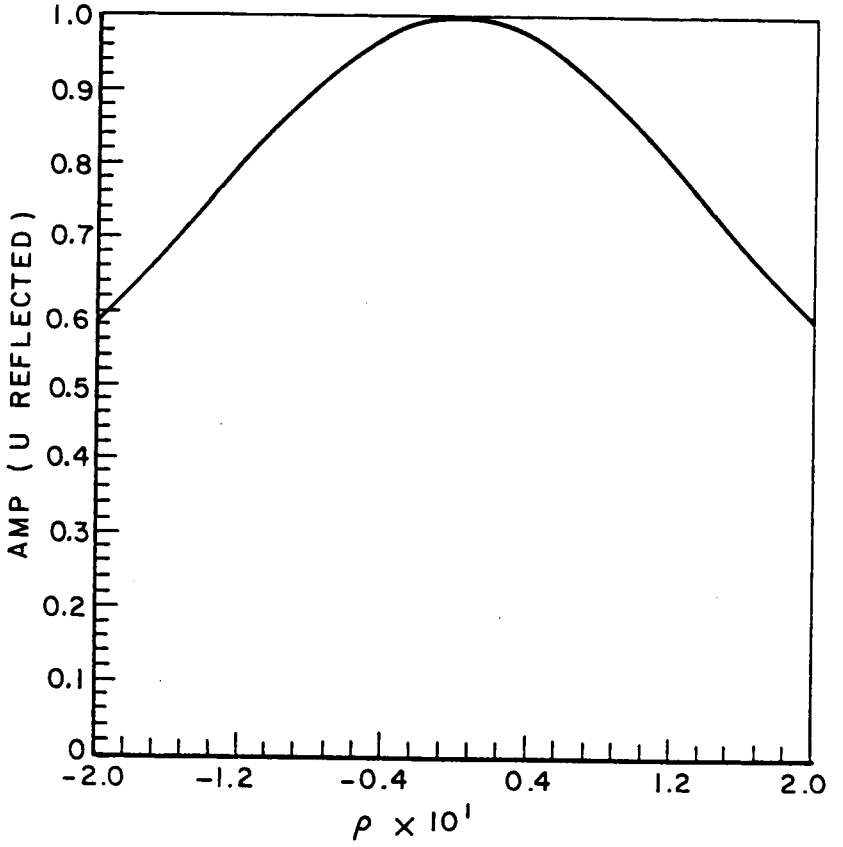

Figure 84: Plot of $|\mathbf{U}^r|$ versus ρ.

since $r_m = |I_m - F_m|$. The $\overline{\overline{\boldsymbol{R}}}$ is the dyadic reflection coefficient.

By the properties of the parabola, the distance $|I_m - F_m| + |R - I_m|$ is constant if R varies on the line ℓ previously defined, and, since the system is rotationally symmetric, this distance is also constant if ℓ is rotated around the axis z_m in a perpendicular fashion, generating a plane perpendicular to the parabolic axis, consequently the phase of the reflected field is constant on any plane perpendicular to the paraboloid axis, the reflected field is a (nonuniform) plane wave, the difference in phase of the fields on two such planes depends on the distance between the planes.

For a paraboloid

$$r_m = \frac{2f}{1 - \cos\theta_m} = \frac{4f}{\sin^2(\theta_m/2)} \tag{G.6}$$

consequently

$$\mathbf{U}^r(R) = \mathbf{PF}(\hat{\mathbf{r}}_m) \cdot \overline{\overline{\boldsymbol{R}}} \frac{\sin^2(\theta_m/2)}{4f} e^{-jk(|I_m - F_m| + |R - I_m|)} \tag{G.7}$$

$$|\mathbf{U}^r(R)| = |\mathbf{PF}(\hat{\mathbf{r}}_m) \cdot \overline{\overline{\boldsymbol{R}}}| \frac{\sin^2(\theta_m/2)}{4f} \tag{G.8}$$

For a uniform source the term $|\mathbf{PF}(\hat{\mathbf{r}}_m) \cdot \overline{\overline{\boldsymbol{R}}}|$ is a constant

$$|\mathbf{PF}(\hat{\mathbf{r}}_m) \cdot \overline{\overline{\boldsymbol{R}}}| = K \tag{G.9}$$

and a typical plot of $|\mathbf{U}^r(R)|$ versus θ_m is shown in Figure 83, the maximum is for $\theta_m = 180^o$ and the reflected field decreases monotonically for θ_m decreasing towards 0^o or increasing towards 360^o, in other words, $|\mathbf{U}^r(R)|$ is maximum when the reflection point coincides with the vertex of the paraboloid V and the distance ρ is zero, and monotonically decreases for increasing ρ. The same ρ represents both the distances of I_m and of R from the paraboloid axis. A typical plot of $|\mathbf{U}^r(R)|$ versus ρ is shown in Figure 84.

As the previous considerations suggest, the reflected field $\mathbf{U}^r$ can be expressed in terms of ρ instead of θ_m, where ρ is a function of the field point R,

$$\rho = \rho(R) \tag{G.10}$$

in fact

$$\rho(R) = \frac{2f}{1-\cos\theta_m}\sin\theta_m \tag{G.11}$$

and this equation can be solved for θ_m in terms of $\rho(R)$, as follows

$$\frac{\rho(R)}{2f} = \frac{\sin\theta_m}{1-\cos\theta_m} = \frac{1}{\tan(\theta_m/2)} \tag{G.12}$$

consequently

$$\frac{\theta_m}{2} = \arctan\left(\frac{2f}{\rho(R)}\right) \tag{G.13}$$

and

$$\sin^2\left(\frac{\theta_m}{2}\right) = \sin^2\left[\arctan\left(\frac{2f}{\rho(R)}\right)\right] \tag{G.14}$$

but

$$\sin^2 x = \frac{\tan^2 x}{\tan^2 x + 1} \tag{G.15}$$

consequently

$$\sin^2\left(\frac{\theta_m}{2}\right) = \frac{[2f/\rho(R)]^2}{[2f/\rho(R)]^2+1} \tag{G.16}$$

and the equations

$$\mathbf{U}^r(R) = \mathbf{PF}(\hat{\mathbf{r}}_m)\cdot\overline{\overline{\boldsymbol{R}}}\,\frac{1}{4f}\frac{[2f/\rho(R)]^2}{[2f/\rho(R)]^2+1} \tag{G.17}$$

$$\mathbf{U}^r(R) = \mathbf{PF}(\hat{\mathbf{r}}_m)\cdot\overline{\overline{\boldsymbol{R}}}\,\frac{1}{4f}\frac{(2f)^2}{(2f)^2+\rho^2(R)} \tag{G.18}$$

$$|\mathbf{U}^r(R)| = \frac{K}{4f}\frac{[2f/\rho(R)]^2}{[2f/\rho(R)]^2+1} \tag{G.19}$$

$$|\mathbf{U}^r(R)| = \frac{K}{4f}\frac{(2f)^2}{(2f)^2+\rho^2(R)} \tag{G.20}$$

give the required expressions.

A target zone is defined, in a general sense, as a finite part of a solid cylinder having generatrixes parallel to the paraboloid axis and delimited by planes perpendicular to the cylinder axis. A target plane-section, (TPS for short), is defined as the intersection of a plane perpendicular to the paraboloid axis with the target zone (Figure 28). A target plane-section is characterized by its distance z_l from the paraboloid vertex, on any other respect all target plane-sections are identical. By the previous considerations, the phase of the reflected field is constant on a target plane-section, while its amplitude varies (nonuniform plane wave).

The taper of the reflected field (gro) is defined as

$$\text{gro} \stackrel{\text{def}}{=} \frac{\min_{R\in TPS} |\mathbf{U}^r(R)|}{\max_{R\in TPS} |\mathbf{U}^r(R)|} \tag{G.21}$$

$$\text{gro} = \frac{\min_{R\in TPS} \left\{(K/4f)(2f)^2 \,/\, [(2f)^2 + \rho^2(R)]\right\}}{\max_{R\in TPS} \left\{(K/4f)(2f)^2 \,/\, [(2f)^2 + \rho^2(R)]\right\}} \tag{G.22}$$

$$\text{gro} = \frac{\min_{R\in TPS}[(2f)^2 + \rho^2(R)]}{\max_{R\in TPS}[(2f)^2 + \rho^2(R)]} \tag{G.23}$$

$$\text{gro} = \frac{(2f)^2 + \rho_{min}^2}{(2f)^2 + \rho_{max}^2} \tag{G.24}$$

$$\text{gro} = \frac{(2f/\rho_{max})^2 + (\rho_{min}/\rho_{max})^2}{(2f/\rho_{max})^2 + 1} \tag{G.25}$$

where

$$\rho_{max} = \max_{R\in TPS} \rho(R) \tag{G.26}$$

$$\rho_{min} = \min_{R\in TPS} \rho(R) \tag{G.27}$$

and R is the field point, and TPS (target plane-section) represents the set of the points obtained by intersecting the target zone with a plane perpendicular to the axis of the parabolic reflector. It is not been necessary to specify on which target plane-section the maximum and minimum are considered, in fact $|\mathbf{U}^r(R)|$ depends on $\rho(R)$ only and not on the coordinate z_l of the target plane-section, and then it does not depend on any specific target plane-section.

Also

$$\mathrm{gro}_{dB} = 20\log(\mathrm{gro}) \tag{G.28}$$

since the gro is defined as a ratio of field values.

Equation (G.24) can be solved for f in terms of the gro

$$(2f)^2\mathrm{gro} + \rho_{max}^2\mathrm{gro} = (2f)^2 + \rho_{min}^2 \tag{G.29}$$

$$(2f)^2(1-\mathrm{gro}) = \rho_{max}^2\mathrm{gro} - \rho_{min}^2 \tag{G.30}$$

$$f = \frac{1}{2}\sqrt{\frac{\rho_{max}^2\mathrm{gro} - \rho_{min}^2}{1-\mathrm{gro}}} \tag{G.31}$$

$$f = \frac{\rho_{max}}{2}\sqrt{\frac{\mathrm{gro} - (\rho_{min}/\rho_{max})^2}{1-\mathrm{gro}}}\,. \tag{G.32}$$

For a subreflector system, f must be replaced by f_e, the equivalent focal distance of the subreflector system, and

$$f_e = M\,f \tag{G.33}$$

consequently

$$\mathrm{gro} = \frac{(2M\,f)^2 + \rho_{min}^2}{(2M\,f)^2 + \rho_{max}^2} \tag{G.34}$$

$$f = \frac{1}{2M}\sqrt{\frac{\rho_{max}^2\mathrm{gro} - \rho_{min}^2}{1-\mathrm{gro}}} \tag{G.35}$$

$$f = \frac{\rho_{max}}{2M}\sqrt{\frac{\mathrm{gro} - (\rho_{min}/\rho_{max})^2}{1-\mathrm{gro}}}\,, \tag{G.36}$$

where ρ_{max} and ρ_{min} are the max and min of the distances of the points of a target plane-section from the central ray (the axis of the equivalent reflector).

A simple case important in practice is a target zone having rectangular xy cross section and centered on the reflector axis (or on the central ray, for the subreflector system case) (Figure 85). Let ρ_d is the length of the semidiagonal of the rectangle, for this case

$$\rho_{min} = 0 \tag{G.37}$$

and the previous equations become, for a single reflector

$$\text{gro} = \frac{(2f/\rho_d)^2}{(2f/\rho_d)^2+1} \tag{G.38}$$

$$f = \frac{\rho_d}{2}\sqrt{\frac{\text{gro}}{1-\text{gro}}}\,, \tag{G.39}$$

and for a subreflector system

$$\text{gro} = \frac{(2M\,f/\rho_d)^2}{(2M\,f/\rho_d)^2+1} \tag{G.40}$$

$$f = \frac{\rho_d}{2M}\sqrt{\frac{\text{gro}}{1-\text{gro}}}\,. \tag{G.41}$$

For a target zone centered on the reflector axis (or on the central ray, for the subreflector system case), having a circular cross-section, the previous equation holds if ρ_d is the radius of the circle.

For a target zone centered on the reflector axis (or on the central ray), having an elliptical cross-section with semiaxes a, b, the previous equation holds if $\rho_d = \max\{a, b\}$.

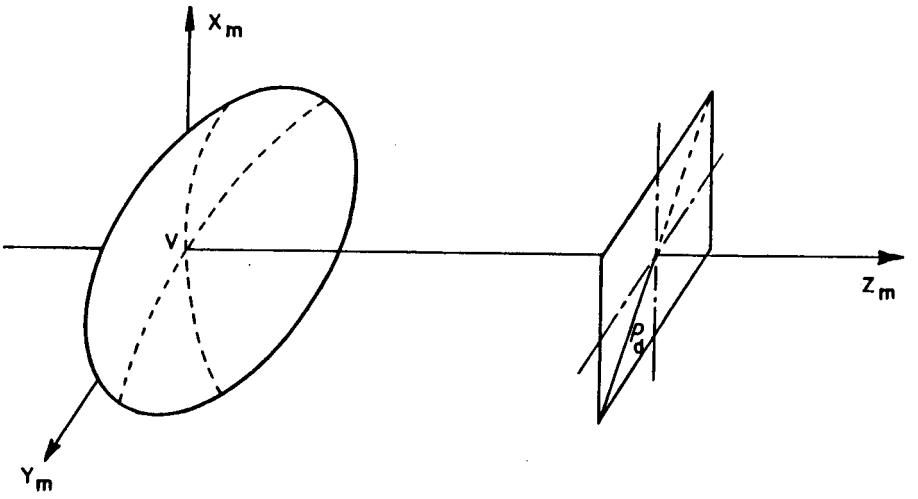

Figure 85: Geometry of a rectangular target zone.

REFERENCES

[1] W. D. Burnside, M. C. Gilreath, B. M. Kent, G. C. Clerici "Curved Edge Modification of Compact Range Reflector," IEEE Transactions on Antennas and Propagation, Vol. AP-35, No 2, February 1987.

[2] C. W. I. Pistorius, W. D. Burnside, "New Main Reflector, Subreflector, and Dual Chamber Concepts for Compact Range Applications," Tech. Report 716148-22, The Ohio State University ElectroScience Laboratory, August 1987.

[3] N. F. Chamberlain, "Radar Object Classification Using Full Polarization Scattering Matrix Data," The Ohio State University ElectroScience Laboratory, Department of Electrical Engineering, Columbus, Ohio, February 1988.

[4] W. D. Burnside, L. Peters, Jr., "Target Illumination Requirements for Low RCS Target Measurements," 1985 AMTA Symposium, Melbourne, Florida, 1985.

[5] M. D. Rader, W.D. Burnside, "A Cassegrain Reflector System for Compact Range Applications," Tech. Report 716148-14, The Ohio State University ElectroScience Laboratory, July 1986.

[6] C. Dragone, "Offset Multireflector Antennas with Perfect Pattern Symmetry and Polarization Discrimination," B.S.T.J., 57, No.9, pp. 2663-2685, September 1978.

[7] I. J. Gupta, W. D. Burnside, "Electromagnetic Performance Study of a New Compact Range Reflector," Report 718331-1, The Ohio State University ElectroScience Laboratory, prepared under Contract No. GR9300, Boeing Aerospace Co., June 1986.

[8] A. C. Ludwig, "The Definition of Cross Polarization," IEEE Transactions on Antennas and Propagation, Vol. AP-21, No 1, January 1973.

[9] C. Dragone, "Conformal Mapping and Complex Coordinates in Cassegrainian and Gregorian Reflector Antennas," B.S.T.J., 60, No. 10, pp. 2397-2420, December 1981.

[10] I. Koffman, "Feed Polarization for Parallel Currents in Reflectors Generated by Conic Sections," IEEE Trans. on Antennas and Propagation, Vol. AP-14, pp. 37-40, January 1966.

[11] M. R. Spiegel, "Mathematical Handbook," McGraw-Hill Book Co., Inc., New York, N.Y., 1968.

[12] W. V. T. Rusch, Y. Rahmat-Samii and R. A. Shore, "The Equivalent Paraboloid of an Optimized Off-Set Cassegrain Antenna," Digest IEEE Intl. Symp. Antennas and Prop., 1986.

[13] R. A. Shore, C. J. Sletten, "Dual Offset Reflector Antenna Systems With Rotationally Symmetric Aperture Distributions," Rome Air Force Development Center, RADC-TR-84-140, In-House Report, June 1984.

[14] E. K. Walton and J. D. Young, "The Ohio State University Compact Radar Cross-Section Measurement Range," IEEE Trans. on Antennas and Propagation, Vol. AP-32, No.11, pp. 1218-1223, November 1984.

[15] G. Clerici, J. D. Young, "Pattern Processing and Feed Simulation by Interpolation over Measured Data," Report 719267-7, The Ohio State University ElectroScience Laboratory, prepared under Contract No. GU0160, Boeing Aerospace Co., November 1987.

[16] P. Joseph "A UTD Pyramidal Absorber Scattering Analysis for Design of Compact Ranges," Ph. D. Dissertation, Department of Electrical Engineering, The Ohio State University, September 1988.

[17] W. D. Burnside, G. C. Clerici, J. D. Young, "First Status Report on Contract OR-549651-B28 to Elizabeth Stark," The Ohio State University ElectroScience Lab, June 1985.

[18] "The Modern GTD Short Course, September 1980," The Ohio University ElectroScience Laboratory, Department of Electrical Engineering, Columbus, Ohio.

[19] S. Silver, "Microwave Antenna Theory and Design," Peter Peregrinus Ltd., London, U.K., pp. 342-343; 1984 Reprint.

50272-101

REPORT DOCUMENTATION PAGE	1. REPORT NO.	2.	3. Recipient's Accession No.

4. Title and Subtitle

GEOMETRICAL OPTICS DESIGN OF A COMPACT RANGE GREGORIAN SUBREFLECTOR SYSTEM BY THE PRINCIPLE OF THE CENTRAL RAY

5. Report Date January 1989

6.

7. Author(s) Giancarlo Clerici, Walter D. Burnside

8. Performing Organization Rept. No. 719493-4

9. Performing Organization Name and Address

The Ohio State University
ElectroScience Laboratory
1320 Kinnear Road
Columbus, Ohio 43212

10. Project/Task/Work Unit No.

11. Contract(C) or Grant(G) No.

(C)

(G) NSG 1613

12. Sponsoring Organization Name and Address

National Aeronautics and Space Administration
Langley Research Center
Hampton, VA 22217

13. Type of Report & Period Covered Technical Report

14.

15. Supplementary Notes

16. Abstract (Limit: 200 words)

In recent years, the compact range has become very popular for measuring Radar Cross Section (RCS) and antenna patterns. The compact range, in fact, offers several advantages due to reduced size, a controlled environment, and privacy. On the other hand, it has some problems of its own, which must be solved properly in order to achieve high quality measurement results. For example, diffraction from the edges of the main reflector corrupts the plane wave in the target zone and creates spurious scattering centers in RCS measurements. While diffraction can be minimized by using rolled edges, the field of an offset single reflector compact range is corrupted by three other errors: the taper of the reflected field, the cross polarization introduced by the tilt of the feed and the aperture blockage introduced by the feed itself. These three errors can be eliminated by the use of a subreflector system. A properly designed subreflector system offers very little aperture blockage, no cross-polarization introduced and a minimization of the taper of the reflected field. A Gregorian configuration has been adopted in order to enclose the feed and the ellipsoidal subreflector in a lower chamber, which is isolated by absorbers from the upper chamber, where the main parabolic reflector and the target zone are enclosed. The coupling between the two rooms is performed through a coupling aperture. The first cut design for such a subreflector system is performed through Geometrical Optics ray tracing techniques (GO), and is greatly simplified by the use of the concept of the central ray introduced by Dragone. The purpose of the GO design is to establish the basic dimensions of the main reflector and subreflector, the size of the primary and secondary illuminating surfaces, the tilt angles of the subreflector and feed, and estimate the feed beamwidth. At the same time, the shape of the coupling aperture is initially determined. The design of the subreflector system is performed through some design equations which have been derived from geometrical considerations and from the zero cross polarization equation. These design equations are used to specify a subreflector system for the next generation compact range with improved reflected field taper, cross-polarization and aperture blockage performance. The design of the coupling aperture is performed by considering the reflection shadow boundaries of the overextended subreflector.

17. Document Analysis a. Descriptors

b. Identifiers/Open-Ended Terms

c. COSATI Field/Group

18. Availability Statement	19. Security Class (This Report) Unclassified	21. No. of Pages 231
	20. Security Class (This Page) Unclassified	22. Price

(See ANSI-Z39.18) See Instructions on Reverse

OPTIONAL FORM 272 (4-77)
(Formerly NTIS-35)
Department of Commerce